

**Design for Polymer Additive Manufacturing Processes with Coupled  
Process Responses Using Novel Numerical and Empirical Based Modelling  
and Optimization Tools**

By  
Khaled Mostafa

A thesis submitted in partial fulfillment of the requirements for the degree of  
Doctor of Philosophy

Department of Mechanical Engineering  
University of Alberta

© Khaled Mostafa, 2022

# ABSTRACT

Additive manufacturing (AM) is a process of joining materials to make parts from 3D model by successive layer by layer material addition. AM has triggered a paradigm shift towards parts and assemblies design methodologies, materials development and utilization, and additional part functionalization. The workflow to produce an additively manufactured part consists of three steps: preprocessing, build cycle, and post-processing. Design for additive manufacturing (DfAM) or the preprocessing is crucial in additive manufacturing and significantly impacting the process outcomes like part's strength, geometry, and manufacturing time which translates to cost. DfAM consists of different sub-steps, which are part design, process parameters optimization, and path planning. The promised advantages of AM will not get realized, and the results can be significantly costly unless the rules for DfAM are implemented. Additionally, new design strategies should be developed to overcome the inherent limitations of each AM processes.

Functional additively manufactured parts are evaluated based on three main criteria; mechanical performance, geometrical accuracy, Physical efficiency (thermal, fluid, and weight), and cost. Part design, process parameters, and path planning required to produce cost-effective and successful functional parts must be carefully designed and optimized to overcome the inherent tradeoffs of the selected process. The ultimate goal of DfAM is to produce parts with "as built" geometrical measurements and mechanical performance that match the "as designed" CAD part design specifications. The challenges facing design for polymer additive manufacturing process outcomes are coupled, process parameters are interdependent, commercially promised resolution is different from manufacturing resolution, and lack of simulation, modelling and optimization tools.

The thesis main research question is "Can the use of the DfAM tools and optimized process parameters produce a feasible as-built part comparable to the as-designed CAD part specifications?". The research domain of this thesis includes two subdomains. The first subdomain is the process parameter optimization, and the second domain is part design optimization to improve mechanical properties, geometrical accuracy and minimize cost and weight. Two polymer AM processes are studied in this thesis to apply and investigate the different challenges, namely Projection stereolithography (PSLA) and fused deposition modelling (FDM).

For the first subdomain, the thesis investigates the effect of the PSLA process parameters on the mechanical properties, geometric accuracy, and surface roughness of the manufactured part in light of a novel introduced curing model to estimate the accumulated exposure energy per each layer. Developed analytical and empirical models are integrated to predict the final part geometrical distortion, material properties, and surface roughness. Newly introduced terminologies like irradiance affected zone and critical energy for mechanical properties are used to develop curing schemes to improve geometrical accuracy while maintaining the mechanical properties to ensure the part integrity during manufacturing. Then mechanical properties can be enhanced during post-curing. A novel high-resolution fluorescence induced irradiance measurement methodology is introduced to measure and capture the irradiance profile projected from one micromirror and quantify the effect of building plat irradiance map non-uniformity on geometrical accuracy. The effect of part location on the geometrical accuracy and the effect of grayscale pixels on minimizing that effect is experimentally explored. A novel 3D geometry prediction algorithm capable of simulating the geometrical distortion in different features and surface roughness is developed. A three-stage integrated optimization algorithm with a newly introduced cross-layers optimization method and irradiance compensation algorithm is presented.

For the second subdomain, the thesis investigates the effect of part 2D design parameters on the mechanical properties and cost of manufactured parts by FDM process. A cost-based methodology is used while considering the part design parameters to manufacture parts optimized for strength and cost. A novel algorithm called the reverse CAD algorithm is introduced, which converts the machine input G-code file back to a CAD model. The Reverse CAD provides an accurate assessment of the geometric and mechanical behaviour of the printed part as it also incorporates the effect of slicing parameters. Finally, a novel framework to grade both the size and relative density of standard and custom unit cells simultaneously within a lattice structure as a function of the cell spatial coordinates. It was found that dual grading enhances compressive strength, modulus of elasticity, absorbed energy, and fracture behaviour of the lattice structure at the same part weight.

# PREFACE

This thesis presents an account of the original research work by Khaled Mostafa. Research articles originating from this thesis have been published in reputed journals and conference proceedings and are listed below. List of journal articles and proceedings: Publications and presentations resulting from this thesis:

## **Chapter 2:**

1. Mostafa, K. G., Arshad, M., Ullah, A., Nobes, D. S., and Qureshi, A. J., 2020, “Concurrent modelling and experimental investigation of material properties and geometries produced by projection microstereolithography,” *Polymers*, 12(3), p. 506.
2. Mostafa, K. G., Nobes, D. S., and Qureshi, A. J., 2020, “Investigation of light-induced surface roughness in projection micro-stereolithography additive manufacturing (PμSLA),” *Procedia CIRP*, 92, pp. 187–193.

## **Chapter 3:**

3. Mostafa, K., Qureshi, A. J., and Montemagno, C., 2017, “Tolerance control using subvoxel gray-scale dlp 3D printing,” *Proceedings of the ASME 2017 International Mechanical Engineering Congress and Exposition. Volume 2: Advanced Manufacturing*, American Society of Mechanical Engineers, Tampa, Florida, USA, p. V002T02A035.

## **Chapter 5**

4. Mostafa, K. G., Montemagno, C., and Qureshi, A. J., 2018, “Strength to cost ratio analysis of FDM nylon 12 3D printed parts,” *Procedia Manuf.*, 26, pp. 753–762.

## **Chapter 6**

5. Rupal, B. S., Mostafa, K. G., Wang, Y., and Qureshi, A. J., 2019, “A reverse cad approach for estimating geometric and mechanical behavior of FDM printed parts,” *Procedia Manuf.*, 34, pp. 535–544.

## **Chapter 7**

6. Mostafa, K. G., Momesso, G. A., Li, X., Nobes, D. S., and Qureshi, A. J., 2021, “Dual graded lattice structures: generation framework and mechanical properties characterization,” *Polymers*, 13(9), p. 1528.



*Dedicated to my family...*

# ACKNOWLEDGEMENTS

First and foremost, I would like to sincerely thank my advisors, Dr. Ahmed Jawad Qureshi and Dr. David Nobes, for their valuable academic and personal guidance and continuous support for my doctoral program. Their mentoring and encouragement during different phases of this journey have helped me become more independent in research and develop professionally. I would like to thank Dr. Aman Ullah for providing access to their lab facilities and assistance with material characterization. I would like to express my appreciation to the employees of the mechanical department workshop and the NanoFAB at the University of Alberta for providing training and assistance with the characterization techniques. I would like to thank my colleagues for their continuous support throughout my research. Finally, none of this would have been possible without the support of my father, my mother, my sisters and my wife for their endless love, support and inspiration.

# TABLE OF CONTENTS

1	INTRODUCTION.....	1
1.1	Background.....	1
1.2	Design for Additive Manufacturing .....	2
1.3	Principles of Operation .....	4
1.3.1	Projection Stereolithography Process.....	4
1.3.2	Fused Deposition Modelling Process .....	7
1.4	Problem Statement .....	8
1.5	Research Question and Objectives.....	11
2	Modelling and Experimental Investigation of Material Properties and Geometries Produced by Projection Stereolithography (PSLA).....	16
2.1	Introduction.....	16
2.1.1	Photopolymerization .....	16
2.1.2	Literature Review and Problem Statement.....	18
2.1.3	Research Motivation and Objectives.....	21
2.2	Curing Analytical Models .....	22
2.2.1	Vertical Multilayer Model for Accumulated Energy.....	22
2.2.2	Horizontal Curing Model .....	24
2.2.3	Surface Roughness Model.....	27
2.3	Materials and Methods.....	28
2.3.1	Material .....	28
2.3.2	Manufacturing Platform .....	28
2.3.3	Irradiance Measurement.....	29
2.3.4	Working Curve.....	30

2.3.5	Design of experiments for material and geometric characterization .....	31
2.3.6	Degree of Monomer Conversion.....	32
2.3.7	Mechanical Tensile Test .....	33
2.3.8	Dynamic Mechanical Analysis (DMA).....	34
2.3.9	Geometrical Feature Measurement .....	34
2.3.10	Surface Roughness Measurements.....	35
2.4	Results and Discussion.....	36
2.4.1	Irradiance Characterization .....	36
2.4.2	Working Curves .....	37
2.4.3	Material properties characterization.....	38
2.4.4	Geometrical Features Characterization .....	42
2.4.5	Surface Roughness Results .....	45
2.5	Conclusion .....	50
3	Assessment of Irradiance Map Non-Uniformity across Build Platform .....	52
3.1	Introduction.....	52
3.2	Irradiance Map Characterization.....	56
3.2.1	System Components and Operation .....	56
3.2.2	Calibration Methodology .....	58
3.2.3	Results.....	61
3.3	Assessment of Dimensional Deviation.....	68
3.3.1	Methods and Materials.....	68
3.3.2	Results.....	71
3.4	Conclusions.....	74
4	3D Modelling and Optimization of Projection Stereolithography (PSLA).....	75
4.1	Introduction.....	75
4.1.1	Literature review .....	75

4.1.2	Research gap .....	77
4.2	3D Geometry Prediction .....	79
4.3	3D Geometry Optimization.....	83
4.4	Results.....	87
4.4.1	Geometry Prediction Evaluation .....	87
4.4.2	Optimization Algorithm Evaluation.....	90
4.5	Conclusion .....	97
5	Effect of Design Parameters on Mechanical Properties and Cost of Fused Deposition Modeling (FDM) Parts .....	98
5.1	Introduction.....	98
5.2	Methodology .....	101
5.2.1	FDM Design Parameters .....	103
5.2.2	Materials and test Specimen.....	104
5.2.3	Design of experiment.....	104
5.2.4	Test procedure.....	105
5.3	Results.....	105
5.3.1	Data Analysis .....	106
5.4	Optimization model .....	109
5.5	Conclusion .....	112
6	Mechanical Properties Modelling Using Reverse CAD Methodology .....	114
6.1	Introduction.....	114
6.2	Methodology .....	116
6.2.1	Validation.....	119
6.3	Mechanical Behavior Prediction .....	120
6.4	Conclusion .....	125

7	Dual Graded Lattice Structures: Generation Framework and Mechanical Properties	
	Characterization .....	126
7.1	Introduction.....	126
7.2	Dual Grading Generation Algorithm.....	130
7.2.1	Development Environment .....	131
7.2.2	DGLS Input Parameters .....	131
7.2.3	Lattice structure operations .....	133
7.2.4	Shell operations and part finishing.....	136
7.2.5	Case Studies .....	137
7.3	Dual Grading Experimental Investigation.....	141
7.3.1	Lattice Structure Design.....	142
7.3.2	Specimen Manufacturing .....	147
7.3.3	Compression test and digital image correlation .....	147
7.3.4	Results.....	148
7.4	Conclusion .....	160
8	Conclusions .....	163
8.1	Research Work Limitations.....	166
8.2	Future work scope.....	167
	References .....	168

# LIST OF TABLES

Table 2-1 Values of the process parameters for three designed experiments.....	32
Table 2-2 Measured irradiance values across the build area (mW/cm <sup>2</sup> ).....	37
Table 2-3 Constants values for material property regression model .....	42
Table 2-4 Average measured horizontal (H) and vertical (V) diameters of the horizontal Channels and width of the vertical bars.....	43
Table 2-5 Average measured width of the vertical square channels and the thickness of the overhangs.....	43
Table 2-6 Average experimental measurements versus predicted results surface roughness in the <i>z</i> direction.....	47
Table 2-7 Average experimental measurements of surface roughness in <i>x</i> the direction at different layer thickness values .....	49
Table 3-1 Summary of the current state of the art in PSLA irradiance measurement .....	53
Table 3-2 Measured Gaussian profile parameters to fit equation (2-9).....	63
Table 3-3 Measured irradiance profile.....	67
Table 3-4 L9 Fractional factorial array .....	70
Table 3-53 Average diameters of each set per specimen .....	72
Table 4-1 Literature review .....	76
Table 4-2 Dimensions comparison between predicted and physically manufactured geometries	90
Table 4-3 Comparison between the different stage of the optimization and the raw images .....	95
Table 5-1 Summary of the FDM design and process parameters studied in the literature .....	99
Table 5-2 Level values for each parameter .....	105
Table 5-3 L-18 Orthogonal array with corresponding measured results .....	106
Table 5-4. Parameter significance rank.....	108
Table 5-5. Optimum Configurations.....	109
Table 6-1 Part design parameters for validation .....	120
Table 6-2 FDM process parameters for configuration (i) and (ii).....	121
Table 6-3 Material properties used in the FEA .....	121
Table 7-17 Average mechanical properties result for boundary lattice structure designs .....	149
Table 7-2 Average mechanical properties results for dual graded lattice structure designs.....	150

# LIST OF FIGURES

Figure 1-1 Additive manufacturing workflow.....	2
Figure 1-2 Pre-processing or design for additive manufacturing workflow .....	3
Figure 1-3 Schematic of a typical projection-based stereolithography additive manufacturing system (PSLA). ....	6
Figure 1-4 (a) Micromirror diamond arrangement [37], (b) micromirror diamond assignment decision, (c) Orthogonal mirror resampling over Diamond arrangement [38], and (d) Available build space (black) for orthogonal arrangement [39] .....	7
Figure 1-5 Schematic of a typical fused deposition modelling process.....	8
Figure 1-6 Example of PSLA process coupled outcomes .....	9
Figure 1-7 Illustration showing the difference between the as designed, the commercially promised, and the as-built parts based on the PSLA process.....	10
Figure 1-8 Flow chart of the thesis research domain.....	13
Figure 2-1 Illustration of the vertical energy accumulation model.....	23
Figure 2-2 Effect of exposure time, while with one micromirror turned off, on (a) superposition energy (b) lateral dimensions, and effect of exposure time, while with three micromirrors turned off, on (c) superposition energy (d) lateral dimensions. ....	26
Figure 2-3 (a) The effect of staircase phenomena on surface roughness, (b) The combined effect of staircase and process physics on surface roughness, and (c) Trigonometric illustration of the average surface roughness model.....	27
Figure 2-4(a) A projected image with nine 10×10 mm squares having 155 grayscale pixel value, (b) measuring the irradiance of the Ember machine using a power meter.....	29
Figure 2-5 (a) experiment 1: grayscale tiles for the continuous exposure-based working curve, (b) experiment 2: white tiles for the sequential discrete exposure-based working curve, (c) illustration of the specially designed vat, (d) CMM probe measuring the cured depth of tiles height.....	30
Figure 2-6 FTIR peaks considered in calculating the degree of monomer conversion.....	33
Figure 2-7 Geometric artifact to determine the minimum feasible feature size manufactured	35
Figure 2-8 Relation between the grayscale level of the pixels and irradiance level .....	36



Figure 2-9 Working Curve from (a) continuous exposure pattern (b) discrete sequential pattern .....	38
Figure 2-10 The effect of exposure time, layer thickness, and LED power on (a) Ultimate tensile strength, (b) Storage modulus, and (c) Degree of monomer conversion .....	39
Figure 2-11 Brittle failure of the UTS specimen from the top view for (a) 50 $\mu\text{m}$ and (b) 10 $\mu\text{m}$ layer thickness, from the section view for (c) 50 $\mu\text{m}$ and (d) 10 $\mu\text{m}$ layer thickness .....	40
Figure 2-12 (a) Effect of exposure time and layer thickness on accumulated energy, Relation between accumulated energy per layer ET and (b) Ultimate tensile strength, (c) Storage modulus, (d) DOC .....	41
Figure 2-13 Selected optical microscope measurement images for different sizes of horizontal circular channels, vertical square channels, vertical square bars, and rectangular overhangs .	44
Figure 2-14 (a) A fitted surface plot representing the relation between surface profile angle, exposure time, and layer thickness, (b) a surface plot showing the predicted relation between average surface roughness, exposure time, and layer thickness .....	46
Figure 2-15 (a), (b), and (c) are confocal microscopy images for surfaces build at layer thickness values of 50, 25, and 10 $\mu\text{m}$ respectively; (d), (e), and (f) are a 3D rendering of the confocal microscope scanning corresponding to layer thickness values of 50, 25, and 10 $\mu\text{m}$ . respectively; (g), (h), and (i) are 2D plots of surface profile in the lay in the z direction at layer thickness values of 50, 25, and 10 $\mu\text{m}$ . respectively; (j) 2D plot of a section of surface profile in the lay in the x direction at different layer thickness values; (k) SEM image of a conical shape build with 50 microns layer thickness; (l) Close up SEM image of 4 layers showing the surface profile angle .....	48
Figure 3-1 Irradiance induced fluorescence imaging setup .....	57
Figure 3-2 Absorption and emission spectrum of ZnOEP dissolved in DCM.....	58
Figure 3-3 Irradiance characterization calibration methodology .....	59
Figure 3-4 Captured image of the micro-scale targets of 4.5mm square grid and 0.25 mm spacing at the maximum zoom of the lens, (a) 20-micron line width and (b) 10-micron line width .....	59
Figure 3-5 Correlation between (a) Machine projected irradiance and normalized irradiance setting, and (b) projected irradiance and the captured image grayscale value .....	61

Figure 3-7 (a) Captured image of irradiance profiles projected from individual micromirrors, (b) Processed image of the individual adjacent micromirror irradiance profiles and sections across the individual micromirrors irradiance profile along the (c) X-axis and (d) Y-axis .....	62
Figure 3-8 Simulated irradiance Gaussian profiles from one micromirror compared to the measured irradiance profiles with different peak irradiances in (a) $x$ -axis and (b) $y$ -axis.....	63
Figure 3-9 Irradiance map across the build platform.....	64
Figure 3-10 Captured image and the corresponding analyzed irradiance profile of annulus cross-section with dimensions of (a) OD 3 mm with ID 1 mm (b) OD 1 mm with ID 0.35 mm projected at the first location (defined in Figure 3-9).....	65
Figure 3-11 Captured image and the corresponding irradiance profile of cylindrical cross-section with the dimensions of (a) OD 0.5 mm with ID 0.25mm (b) OD 0.25 mm at the third location (defined in Figure 3-9).....	66
Figure 3-12 Cross sectional irradiance profile across the projected 2D circular shapes with the following dimensions of (a) OD 3 mm with ID 1 mm, (b) OD 1 mm with ID 0.35 mm projected at the first location (defined in Figure 3-9), (c) OD 0.5 mm with ID 0.25mm, and (d) OD 0.25 mm at the third location (defined in Figure 3-9) .....	67
Figure 3-12 Designed specimen with four sets of cylinders with three replications for each set distributed across the build platform .....	68
Figure 3-14 Illustration of the different grayscale rings sets .....	69
Figure 3-15 Photoshop editing for the PNG slice images.....	70
Figure 3-16 CMM measurement while measuring the different cylinder specimens .....	71
Figure 3-17 Main effects plot for the cylinders sets (a) unedited cylinders, (b) 1 ring configuration, (c) 2 rings Configuration, and (d) 3 rings configuration .....	73
Figure 4-1 layout of the geometry prediction algorithm.....	79
Figure 4-2 Determining the position of the micromirror based on the input images .....	80
Figure 4-3 Sub-voxelizing of layers .....	82
Figure 4-4 Proposed 3D geometry optimization methodology .....	83
Figure 4-5 Layout of the optimization algorithm .....	84
Figure 4-6 Determining the distorted voxels.....	84
Figure 4-7 Illustration of the IAZ affected voxels and effective pixels selections .....	85

Figure 4-8 Comparison between manufactured vertical square bars at (a) $dz = 50 \mu\text{m}$ and 2 s and (b) $25 \mu\text{m}$ and 1.8 s, against the prediction results of $dz = 50 \mu\text{m}$ and 2 s (c) top view and (d) front view of the square bars.....	87
Figure 4-9 Comparison between manufactured vertical square holes at (a) $dz = 50 \mu\text{m}$ and 2 s and (b) $25 \mu\text{m}$ and 1.8 s, against the prediction results of $dz = 50 \mu\text{m}$ and 2 s (c) top view of the square bars.....	88
Figure 4-10 Comparison between manufactured horizontal circular holes at (a) $dz = 50 \mu\text{m}$ and 2 s and (b) $dz = 25 \mu\text{m}$ and 1.8 s, against the prediction results showing the front view of (c) $dz = 50 \mu\text{m}$ and 2s and (c) $dz = 25 \mu\text{m}$ and 1.8.....	89
Figure 4-11 Optimization algorithm evaluation test specimen.....	91
Figure 4-12 Machine input image example showing (a) raw sliced image (black and white pixels) only and (b) pixel blending output with grayscale pixels on the boundaries .....	91
Figure 4-13 3D predicted geometry of the raw images (a) isometric view, (b) front view, and (c) top view .....	92
Figure 4-14 Illustration of the target layers to be optimized with the Cross Layers Optimization (CLO) algorithm.....	93
Figure 4-15 Processed images through (a) Pixel blending + CLO, the three optimization stages at the location identified in Figure 3-9 (b) 1 <sup>st</sup> position, (c) 2 <sup>nd</sup> position, and (d) 3 <sup>rd</sup> position..	94
Figure 4-16 3D predicted geometry after applying pixel blending and CLO (a) front view and (b) top view .....	95
Figure 4-17 (a) uncompensated white image projected across the build platform for 2s and (b) exposure energy per each location in the build platform as a result of projecting image in (a), (c) compensated image using the developed algorithm projected for 3.3 , and (d) a uniform exposure energy per each location in the build platform as result of projecting the image in (c) .....	96
Figure 5-1 Flow chart showing the different steps in the methodology proposed .....	102
Figure 5-2 Illustration of different parameters values .....	103
Figure 5-3. Box plots for (a)ultimate tensile strength and (b) ultimate flexure strength.....	108
Figure 5-4. Main effects plot for (a) ultimate tensile strength, (b) manufacturing time for tensile samples, (c) tensile modulus, (d) volume, (e) ultimate flexure strength, and (f) flexure modulus .....	110

Figure 5-5. Stress-strain curves for the validation sample.....	111
Figure 6-1A flowchart depicting the output property prediction methodology based on the Reverse CAD algorithm.....	116
Figure 6-2 The Reverse CAD algorithm .....	117
Figure 6-3 Reverse CAD model VS manufactured part of (a) Cube and b) Cylinder .....	120
Figure 6-4 Half cross section of the shoulder area showing the meshing of configuration (i) and (ii).....	122
Figure 6-5 (a) Mechanical test results of both Nylon-12 and PC with printing configuration i and ii (b) Results up to 1 mm displacement compared to the FEA prediction.....	123
Figure 6-6 von Mises stress FEA results for Configuration (i) and (ii) made of Nylon-12. Corresponding section views are shown to depict infills.....	124
Figure 7-1 Different unit cells types and shapes: (a) simple cube, (b) back-centred cubic BCC, (c) diamond, (d) octet-truss, (e) IWP Schoen, (f) Schwartz diamond, (g) Gyroid, (h) Schwartz primitive, (i) and (j) topology optimized face-centred cubic cells, (k) hybrid (Neovius+Schwartz P), and (l) custom artistically designed unit cell .....	127
Figure 7-2 Dual grading generation framework .....	132
Figure 7-3 Constant size and relative density generated lattice structure for (a) skull implant partially filled with a cubic diamond lattice structure, and (b) spline-based revolved artifact filled gyroid.....	137
Figure 7-4 Size graded lattice structures: (a) side view and (b) isometric view of a sphere filled with TO FCC unit cell, and (c) top view and (d) isometric view of multi-domain hip joint implant partially filled with Schwartz D unit cell.....	138
Figure 7-5 Dual graded lattice structure: (a) Front view and (b) Isometric view of a sinusoidal-based revolved parts filled with a cubic unit cell, and (c) Top-down view and (d) Isometric view of GE bracket filled with IWP Schoen unit cell .....	140
Figure 7-6 Shell generation and perforation: (a) Cubic shell perforated with a diamond pattern and filled with the artistic unit cell, (b) spline-based revolved Shell perforated with a circular pattern and filled with multi-domain sized graded unit cells, and (c) two-step size graded gyroid shell for a sinusoidal revolved shape.....	141
Figure 7-7 Generation of the dual graded lattice structure using a BCCZ grading gallery for compression test specimens.....	142

Figure 7-8 Front views of the boundary lattice structure designs for compression test specimen .....	143
Figure 7-9 Front view of the dual graded lattice structure designs for compression test specimens.....	146
Figure 7-10 Stress-strain curves for (a) different cell size at LD, (b) different cell size at HD .....	149
Figure 7-11 Stress-strain curves for (a) Different cell size grading designs at D1, (b) Different cell size grading designs at D2, (c) Different cell size grading designs at D3, and (d) Modulus of elasticity and absorbed energy versus the 15 graded lattice designs .....	151
Figure 7-12 Digital Image Correlation (DIC) results depicting the two common engineering strain distribution patterns in the vertical direction at 10% compressive strain (a) unidirectional and (b) concentric strain distributions pattern .....	153
Figure 7-13 Digital Image Correlation (DIC) results of the boundary lattice designs depicting the engineering strain distribution in the horizontal direction at 10% compressive strain for (a) LDSS, (b) LDLS, (c) HDSS, and (d) HDLS boundary designs.....	154
Figure 7-14 Deformation of the boundary lattice designs: (a) LDSS at 30%, (b) LDLS at 30%, (c) HDSS at 30%, (d) HDLS failed before reaching 30%, (e) LDSS after test ended, (f) LDLS after test ended, (g) HDSS after test ended, and (h) HDLS after test ended.....	155
Figure 7-15 Digital Image Correlation (DIC) results of the functionally graded lattice designs depicting the strain distribution in the horizontal direction at 10% compressive strain: (a) D1S1, (b) D2S1, (c) D3S1, (d) D1S2, (e) D2S2, (f) D3S2, (g) D1S3, (h) D2S3, (i) D3S3, (j) D1S4, (k) D2S4, (l) D3S4, (m) D1S5, (n) D2S5, and (o) D3S5 .....	156
Figure 7-16 Deformation of the dual graded lattice designs at 30% compressive strain: (a) D1S1, (b) D2S1, (c) D3S1 failed before 30%, (d) D1S2, (e) D2S2, (f) D3S2 failed before 30%, (g) D1S3, (h) D2S3, (i) D3S3 failed before 30%, (j) D1S4, (k) D2S4, (l) D3S4, (m) D1S5, (n) D2S5, and (o) D3S5 .....	157
Figure 7-17 DGLS Deformation at the end of test: (a) D1S1, (b) D2S1, (c) D3S1, (d) D1S2, (e) D2S2, (f) D3S2, (g) D1S3, (h) D2S3, (i) D3S3, (j) D1S4, (k) D2S4, (l) D3S4, (m) D1S5, (n) D2S5, and (o) D3S5 .....	158

# 1 INTRODUCTION

This chapter introduces the polymer additive manufacturing workflow and focuses on the design for polymer additive manufacturing. Also, the principle of operation of the two polymer additive manufacturing machines used in this research is explained. The problem statement is discussed and the thesis global research question is presented. Moreover, the objectives of the thesis are laid out and how each chapter addresses those objectives is demonstrated. Due to the broad scope of this research, the literature review and scientific principles related to each chapter are introduced at the beginning of each chapter individually.

## 1.1 Background

Additive manufacturing (AM) is a process of joining materials to make parts from 3D model data by successive layer by layer material addition according to ISO/ASTM 52900:2015(E) [1]. AM technology was introduced in the early '80s as a rapid prototyping technology. With significant advancement in AM research, it started to be involved in functional parts manufacturing [2]. Several initial patents for the AM technology have ended, which allowed many technology manufacturers to compete in this area. Consequently, AM became affordable technology, which provided colossal inertia to AM research and development.

Additive Manufacturing has triggered a paradigm shift towards parts and assemblies design methodologies, materials development and utilization, and supporting the parts' additional functionalization [3,4]. With the increasing number of successful case studies in biomedical, aerospace, and automotive sectors [5], AM revolutionizes more industrial sectors from confectionaries [6] and shoemaking [7] to oil and gas [8] and constructions [9]. Several polymer and metal additive manufacturing processes can manufacture parts with significant geometrical and dimensional accuracy [10–14]. AM unleashes the manufactured parts' geometric freedom, enabling designers to fully utilize topology optimization and complex lattice structures to design functional parts while reducing their weight or tailoring their thermos-mechanical properties [15–18].

AM technology evolved into different sub-AM technologies; each has its unique physics, principles of operation, range of available materials, accuracy, and resolution. [1]. These technologies are classified by the material used to build the parts; either metals, polymers, or ceramics. Another classification is the principle of operation; either material extrusion, material

jetting, powder bed fusion, binder jetting, vat photopolymerization, or directed energy deposition. Some AM principle of operation allows utilizing more than one material type. For example, powder bed fusion can be used for all three material types.

The workflow to produce an additively manufactured part consists of three steps: preprocessing, build cycle, and post-processing, as shown in Figure 1-1. The preprocessing step consists of different sub-steps: part design, process parameters optimization, and path planning. The second step is the build cycle, in which one or more components are built up in layers in the process chamber of the additive manufacturing system. The last step is post-processing, which is a process taken to achieve the desired surface finish of the final product, for example, support material removal, chemical or mechanical finishing, or applying paint or primers.

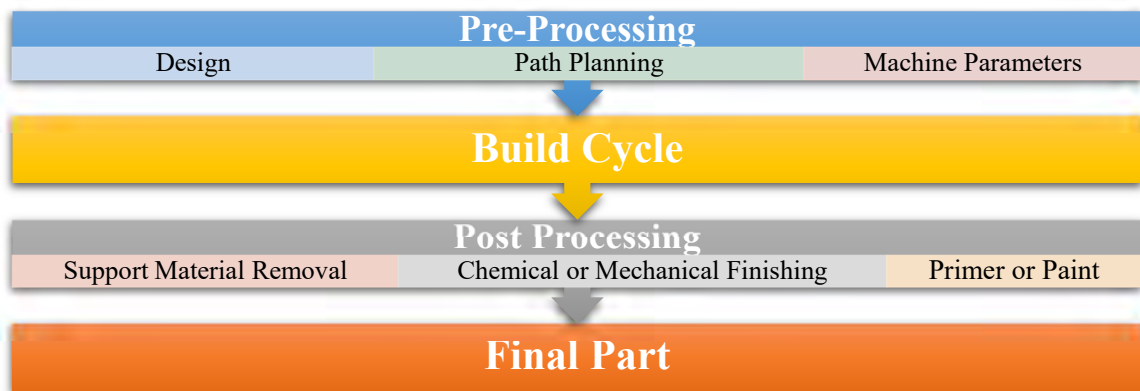


Figure 1-1 Additive manufacturing workflow

## 1.2 Design for Additive Manufacturing

Design for additive manufacturing (DfAM) or the preprocessing step is crucial in additive manufacturing, with a significant impact on process outcomes. It dictates the part's strength, geometry, and manufacturing time which translates to cost. Each sub-step in the part design affects the next step and sets some constraints on the different processes within each sub-step.

The part design process, which is the first step in the DfAM, as shown in Figure 1-2, starts by selecting the proper material that fits the function of the final part then selecting the proper additive manufacturing process that can handle the selected material and accommodate the required accuracy. The part preliminary design is carried out using computer-aided design software (CAD), which allows the design of the preliminary part envelop based on the design specifications and the functional requirements while keeping in mind the capabilities and limitations of additive manufacturing processes. The degree of geometrical freedom provided by AM allowed for further

shape geometry optimization to maximize mechanical properties, minimize weight, minimize fluid turbulence, and maximize heat transfer. This can be achieved by either using a generative design based on topology optimization algorithms or by using lattice structures, which is provided by numerous finite elements software. The last process in the part design is to export a CAD file readable by the computer-aided manufacturing software (CAM) dedicated to the additive manufacturing machine selected. One of the most popular CAD files is the STL file format, which is the first additive manufacturing compatible file developed initially for the stereolithography process. STL stands for Standard Tessellation Language file, and it describes the CAD model data as a surface geometry of an object in the form of a tessellation of triangles.

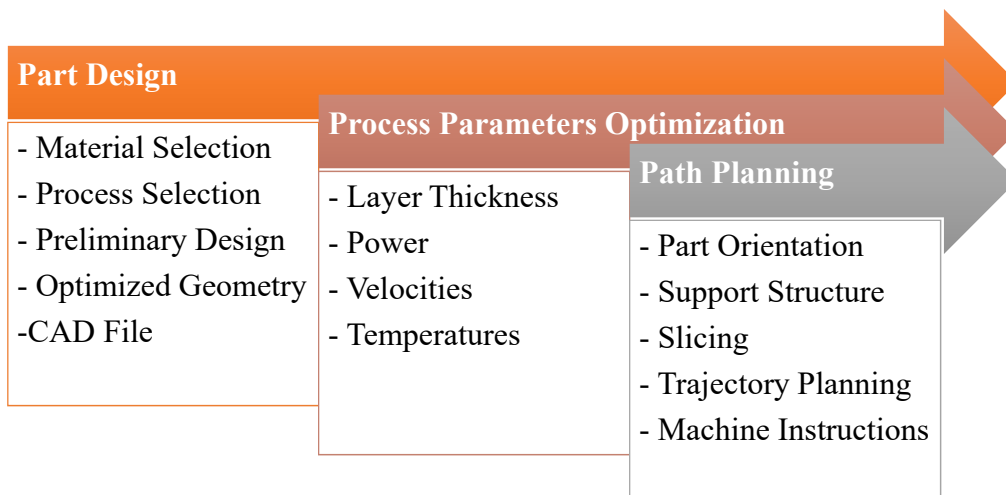


Figure 1-2 Pre-processing or design for additive manufacturing workflow

Process parameters are defined as the set of operating parameters and system settings used during the build cycle. The process parameters need to be optimized to ensure that the final part has a near-net-shape, where the part requires little to no post-processing to meet the required functional dimensions within the process promised accuracy or better. Layer thickness is one of the critical process parameters that affect the geometrical accuracy of the part. It also affects the fusion efficiency of the layers, thus affecting the strength of the part and directly translates to manufacturing time and cost. Properly selecting the power value of the fusing/heating/curing element is essential to ensure the part's integrity and prevent failure. The value range set for the different components velocities within the AM machine affects the manufacturing time, part quality. The environment temperature inside the AM machine can ensure that the part does not warp and can minimize the generated stress during the manufacturing process.



The last sub-step within the preprocessing is the path planning, which translates both the part design in the form of a CAD file and process parameters into machine-readable instructions (G-code), except projection stereolithography which reads images instead of G-code. Orienting the part within the build volume of the AM machine influence the quality of different feature types within the part. In order to ensure that each new layer to be manufactured is supported and not hanging in the air, the support structure is used to support those areas and ensure the part does not warp during manufacturing. The use of support structures will increase material usage and require post-processing steps to remove it and its marks from the part. Then based on the chosen, layer thickness the part is sliced into layers, and a path plan for each layer is generated, and the trajectory plan for the different machine components is computed.

### **1.3 Principles of Operation**

Since this thesis focuses on polymer additive manufacturing, two of the most popular polymer AM processes are studied to demonstrate the different DfAM research scopes in the thesis. The first process is the projection stereolithography process (PSLA), and the second process is the fused deposition modelling (FDM).

#### **1.3.1 Projection Stereolithography Process**

Projection stereolithography (PSLA) systems belong to the vat photopolymerization process, which is defined as the "process in which liquid photopolymer in a vat is selectively cured by light-activated polymerization" according to ISO/ASTM 52900:2015(E) [1]. SLA systems were introduced in the late 1980s as rapid prototyping equipment [2]. Currently, these systems are used for different applications like fully functional mechanical parts [19], microfluidics and lab on chip devices [20], and patient-specific medical applications [21–24]. A wide range of materials is compatible with SLA systems, such as pure polymers, mixed polymers, and ceramically loaded polymers [25,26]. The main advantage of the projection-based systems over the laser scanning systems is the lower manufacturing time. The projection systems simultaneously expose the whole build area with the desired UV pattern instead of a laser tracing each point of the pattern [27,28].

Like other additive manufacturing processes, the first step in PSLA is to slice the solid model of the desired part to be manufactured. The output of this slicing process is a stack of black and white pixelated Portable Network Graphics (PNG) images and a settings file. Each image

represents a cross-sectional projection for the corresponding layer. The white and black colours of the pixels represent the areas where the prepolymer resin should be polymerized or not, respectively. The number of images depends on the selected layer thickness and the part height. The minimum achievable layer thickness is determined by the minimum vertical resolution achieved by the driving system of the machine, which ranges from 1 to 100  $\mu\text{m}$  in the case of PSLA systems [8]. The input settings file contains the numerical values for the optical power (typically a UV LED), layer thickness, exposure times, the approach and separation velocities, and many other parameters.

As outlined in the schematic of a typical PSLA system shown in Figure 1-3, the build cycle starts with the PNG stack and the settings file are read by the machine controller. Then the controller sends signals to the pulse width modulation (PWM) driver of the UV LED (1) to control the average LED power. The light then passes through light conditioning and expanding optics (2) for the light to be distributed equally and uniformly on the entire digital micromirrors array device (DMD) (3) [29,30]. A black pixel on the PNG image will position the corresponding micromirror to reflect the light towards a heat sink (4). A white pixel will position the corresponding micromirror to reflect the light towards the photosensitive prepolymer resin (5) in the vat (6), passing through the clear transparent PDMS window (7). The PNG image is projected via the micromirrors on the DMD to cure a complete layer of prepolymer squeezed between the previously cured layers of the part (8) and the PDMS window. The manufactured part is attached to the vertically translating build platform (9). After curing one layer, the vat moves laterally to separate the cured part from the PDMS window then the build platform moves upwards by a distance equal to the layer thickness. PDMS inhibits free-radical polymerization by an insignificantly thin layer above its surface [27], which facilitates the separation of the part at a low separation force and minimizes the part distortion [27,31]. The accuracy of the manufactured parts depends on the minimum voxel size that can be achieved. Instead of using white and black pixels, grayscale pixels can control the average irradiance transmitted by each micromirror to achieve sub-voxel resolution [32].

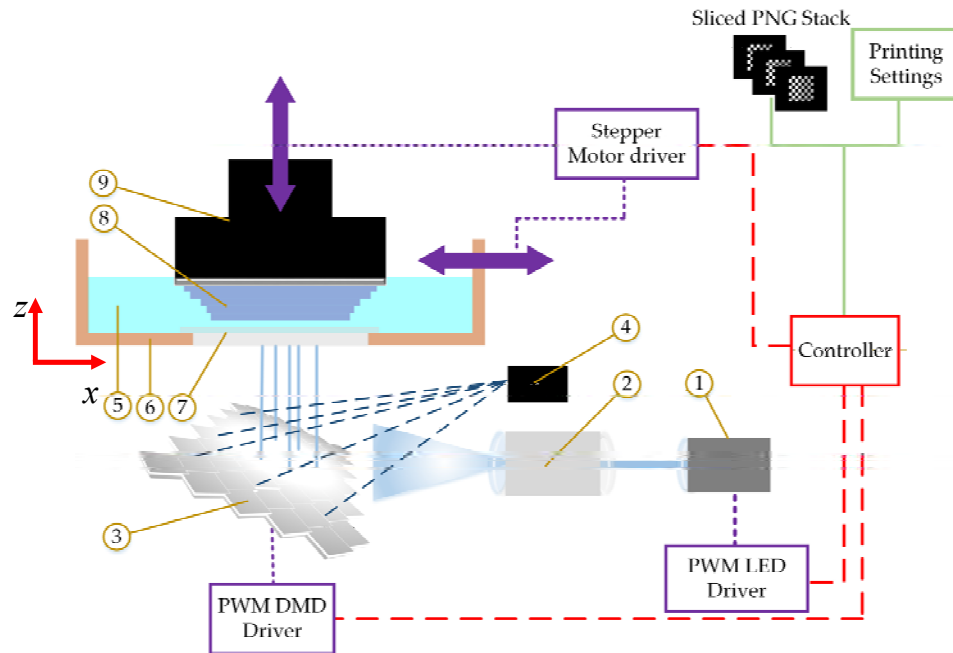


Figure 1-3 Schematic of a typical projection-based stereolithography additive manufacturing system (PSLA).

By adding, expanding or reducing optics, the resolution achievable and the build area size changes. As the reduction ratio increases, the resolution increases while the build area decreases; there is always a tradeoff between them [33]. Different manufacturing scales have studied in the literature, from microscale to mesoscale application targets with a resolution of 1  $\mu\text{m}$  to 250  $\mu\text{m}$  [34].

The current DLP has its micromirrors arranged in a diamond-oriented array, as shown in Figure 1-5 (a), to fit more mirrors within the same space than the orthogonally arranged micromirrors [35,36]. A weighted calculation must be performed to decide which micromirror in the projector diamond array will correspond to a pixel in an image with a square array, as shown in Figure 1-4 (b). This micromirror arrangement was developed to advance the video projection with higher resolution, but in additive manufacturing, this will distort the geometry, mainly if the target application is a microstructure. The part has to be rotated 45°, and the diamond resampling option must be disabled in the settings file to print with the square arrangement on the diamond micromirror array. Each pixel in the image file will now correspond to a certain micromirror; however, this compromises the available build area to manufacture a part on, as shown in Figure 1-4 (c) and (d).

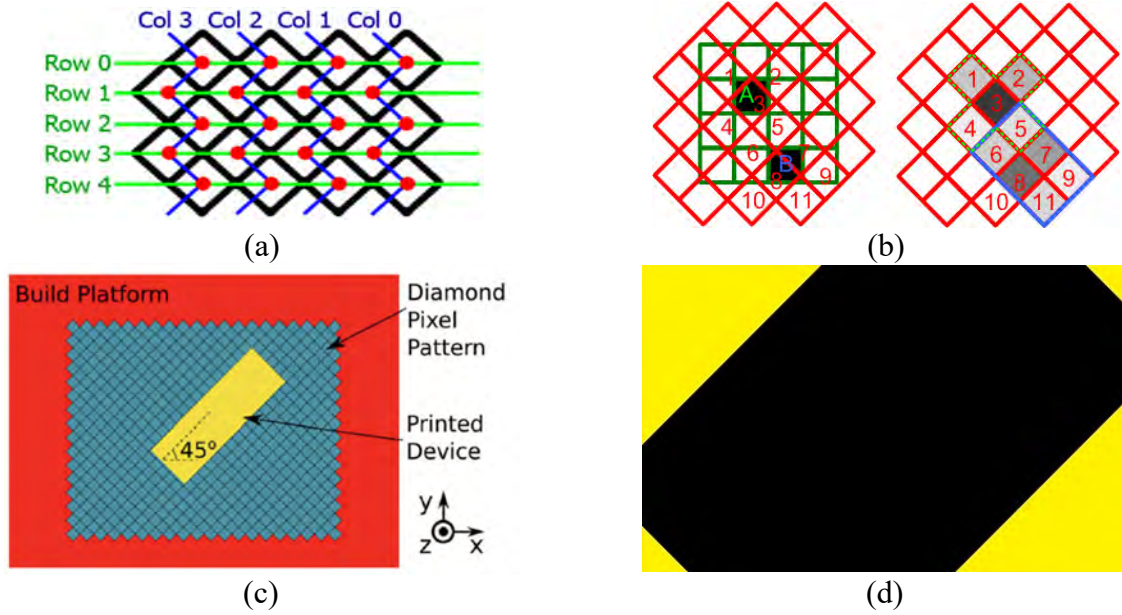


Figure 1-4 (a) Micromirror diamond arrangement [37], (b) micromirror diamond assignment decision, (c) Orthogonal mirror resampling over Diamond arrangement [38], and (d) Available build space (black) for orthogonal arrangement [39]

### 1.3.2 Fused Deposition Modelling Process

Fused deposition modelling (FDM) belongs to the material extrusion AM process category, which is defined as the "process in which material is selectively dispensed through a nozzle or orifice" according to ISO/ASTM 52900:2015(E) [1]. The build cycle starts when the FDM machine receives the G-code describing the movements and actions required to produce the desired part. Then the drive wheels, gripping the used build material, rotates and forces the thermoplastic filament to be extruded through the extrusion nozzle after passing through a heating element contained in the printing head, as shown in Figure 1-5.

The extruded material should reach the softening temperature range, which is above the recrystallization temperature and below its melting temperature. The machine controller ensures that the material has the extrusion velocity and is capable of stopping extrusion completely; this allows to deposit material on the desired locations selectively. For the first layer, the material is deposited on the build platform, while in the next layers, the material is deposited on the previous layers. The extruded material must both fully solidify while maintaining the original deposited shape and bond to the material of the previous layer. The printing head moves in both the  $X$  and  $Y$  direction while depositing any layer; after material for that layer is extruded, extrusion stops and

the build platform moves down in the Z direction by a value corresponding to the layer thickness. For parts with overhang features, supports with weaker or water/solvent dissolvable materials, which eases the support removal process. This can be done by using printing heads with dual extrusion nozzles, and the machine controllers select which material to be extruded.

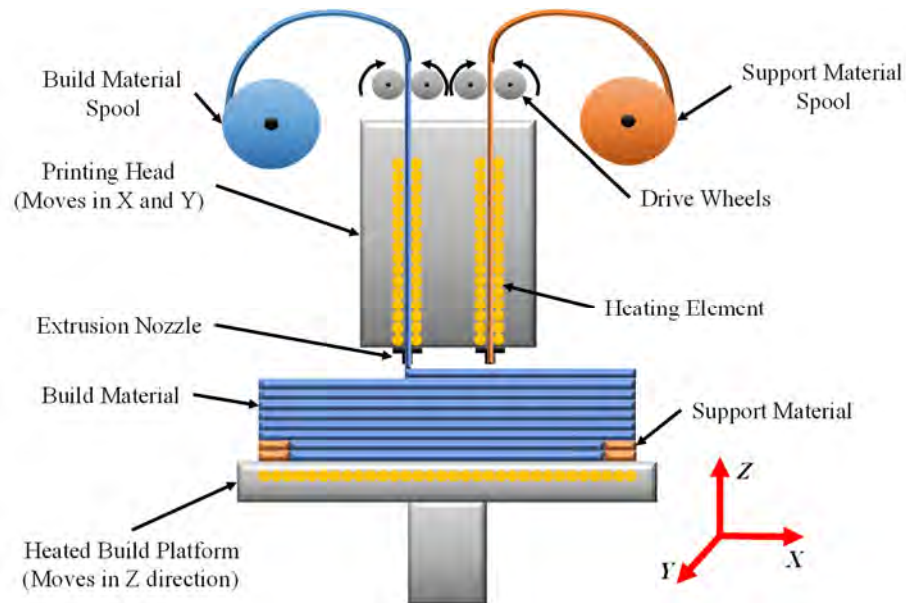


Figure 1-5 Schematic of a typical fused deposition modelling process

The consistency of shape and dimensions of the extruded filament depends on the material flow rate, extrusion nozzle diameter, and the printing head velocity. The extrusion nozzle diameter limits the minimum feature size to be manufactured, where no feature with a size smaller than the nozzle diameter can be created. FDM is more convenient for larger parts with features at least double the nozzle diameter. To ensure the integrity of the manufactured part, the material should be heated to the point to adhere properly to the previous layer without leaving a distinctive layer boundary which can lead to fracture and without melting and distorting geometry of the previous layer. The Parts' warping is an issue for most AM processes; in FDM, heating the build platform minimizes the thermal gradients and minimizes warpage.

#### 1.4 Problem Statement

While AM had leveraged part and assembly design freedom, it added new constraints on the design for additive manufacturing (DfAM). The promised advantages of AM will not get realized, and the results can be significantly costly unless the rules for DfAM are implemented. Additionally, new design strategies should be developed to overcome the inherent limitations of

each AM processes. AM processes. Functional additively manufactured parts are evaluated based on three main criteria; mechanical performance, geometrical accuracy, Physical efficiency (thermal, fluid, and weight), and cost. Efficient part design, process parameters, and path planning required to produce cost-effective and successful functional parts must be carefully designed and optimized to overcome the inherent tradeoffs of the selected process. The ultimate goal of DfAM is to produce parts with "as-built" geometrical measurements and mechanical performance that match the "as designed" CAD part design specifications.

The first challenge is that the process outcomes, namely, geometry, mechanical properties, and cost, are significantly sensitive to part design, process parameters, and path planning decisions. What complicates this issue is that the process outcomes mentioned are coupled, and some of the process parameters are interdependent. For instance, if all the process parameters are optimized to maximize one of the outcomes, the other outcomes are not usually maximized; however, it can negatively affect them. If one parameter is changed, other interdependent parameters will be changed accordingly so that the manufactured part does not fail. In projection-based stereolithography (PSLA), as shown in Figure 1-6, like all other AM processes, the building material constituents, the CAD and CAM parameters, the individual machine components specifications, and several noise sources affect the coupled process outcomes.

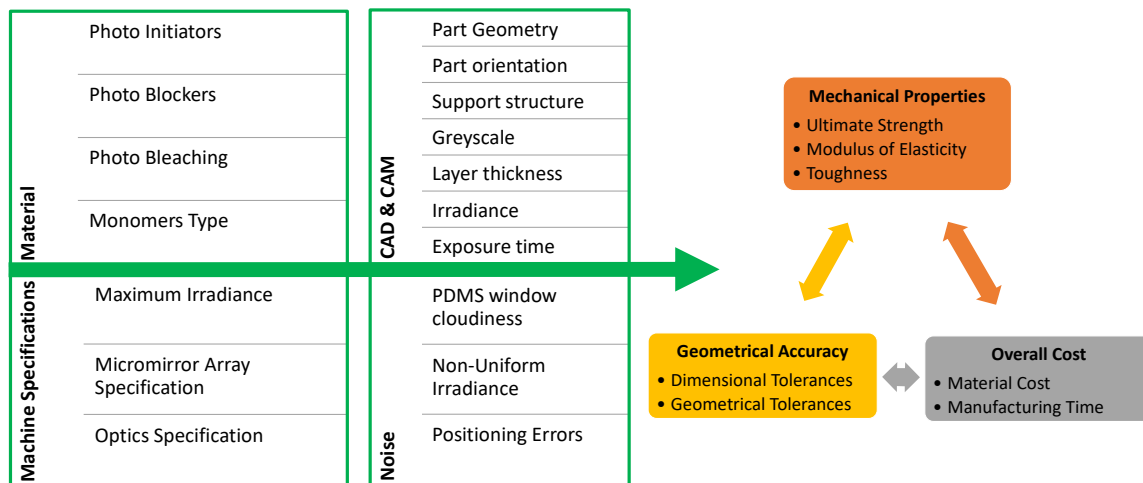


Figure 1-6 Example of PSLA process coupled outcomes

Decreasing the layer thickness value improves the geometrical accuracy and resolution of features built in the vertical direction, the average surface roughness, and the strength; however, it increases the manufacturing time by more than the decrease in the layer thickness percentage

increases the cost. Decreasing the layer thickness without decreasing the exposure time will distort the horizontal dimension, polymerize the resin within the horizontal holes in the part, and cause layers to stick to the PDMS window, resulting in complete part failure. This scenario of process outcome coupling and parameters interdependency are valid for the different parameters stated in Figure 1-6. The process outcomes coupling and the process parameters interdependency impose constraints on manufacturing a functional part that meets both geometrical and material properties requirements. Therefore, development of numerical or empirical models is needed to understand the aforementioned relationships between parameters and process outcomes.

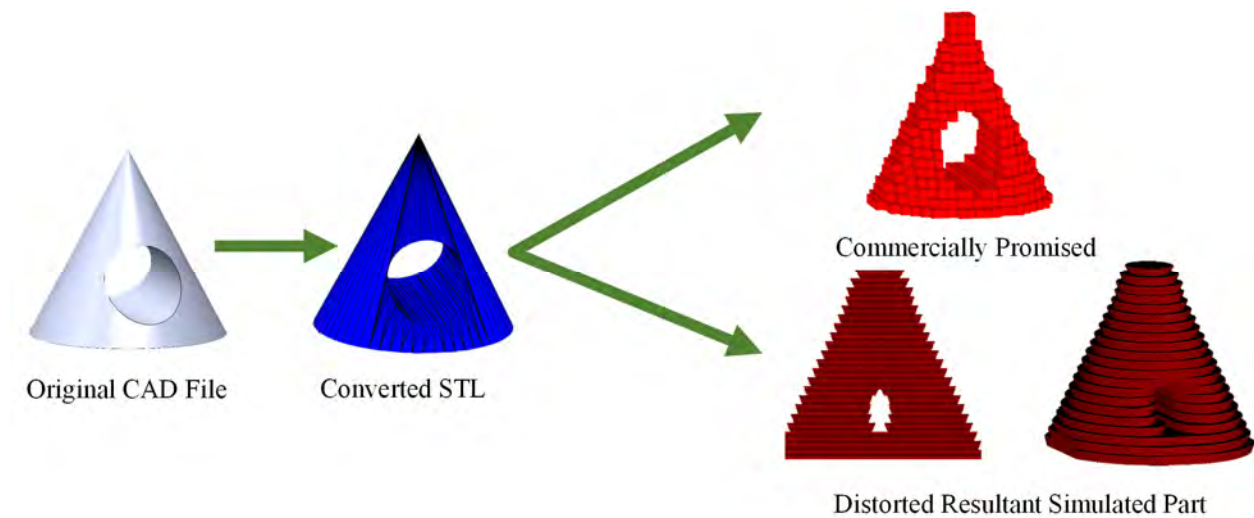


Figure 1-7 Illustration showing the difference between the as designed, the commercially promised, and the as-built parts based on the PSLA process

The second challenge that faces DfAM is that the commercially promised resolution either describes the physical machine electric driver's resolution, nozzle diameter, or laser spot size but not the overall manufacturing resolution, which reflects the process physics. Both the part with commercially promised resolution and the as build resolution deviate from both the STL geometry and the original CAD geometry, as shown in Figure 1-7. Different process parameters values in a different geometrical errors. Therefore, there is a need for geometry prediction algorithm to estimate the geometrical deviation in terms of material properties, process parameters, and process physics.

The third challenge is that the manufacturing accuracy promised is only guaranteed while using specific materials and manufactured at the pre-defined set of settings optimized for those materials. This limits the use of different materials available in the market that were not sold by

the AM machine producer. Most of the machine producers lock the settings change to prevent users from not using their materials. This can be reasoned with two main reasons. The first is the financial aspects of profit generation, while the second and most important one is that not all the users can calibrate the machine parameters safely to use new materials as there is no straightforward, standardized procedure to acquire the optimum process parameters. Therefore, the need for a deterministic calibration and characteristics measurement methods is required to ensure the accuracy is maintained for different materials.

The fourth challenge is lack of software tools predicting and correcting geometrical distortion and mechanical performance ahead of starting the build cycle. Building parts without simulating their performance will lead to costly outcomes requiring multiple manufacturing trials. Metal additive manufacturing has several reliable commercial software packages, while polymer additive manufacturing does not have much. A simulation and prediction modelling can be used along with optimization algorithms to optimize the DfAM parameters to maximize the part performance ahead of the build cycle start. An optimization methodology is required to ensure that the final part will meet the geometrical and mechanical properties requirements.

The geometrical freedom provided by AM facilitated the utilization of 2D and 3D lattice structures and infill patterns to replace the bulky solid material to tailor customized mechanical and thermal performances. The fifth challenge is that the available design software packages have a closed library with a predefined lattice while new lattices shapes are introduced frequently. The currently available software packages also limit the control over the unit cells' size and density variation across the lattice structure. At the same time, new patterning strategies are introduced to achieve specific goals like shock and energy absorption and stiffness tuning. There is a need for a framework that allows manipulating user defined unit cells within a lattice structures to enable further mechanical properties enhancement beyond what the process parameters can achieve.

## **1.5 Research Question and Objectives**

This thesis attempt to answer the following research question:

*“How to improve the mechanical and geometric quality of as built parts produced by PSLA and FDM additive manufacturing processes to meet the as designed part specifications through research and development of DfAM models and tools?”*



The thesis research project has been designed to address many fundamental issues facing the additive manufacturing process and construct the knowledge and understanding related to the design for polymer additive manufacturing. This research studies two of the most common polymer additive manufacturing processes, namely projection-based stereolithography (PSLA) and fused deposition modelling (FDM) processes, to answer the thesis research question. The objectives of this research are as the following:

1. Investigate the significance of the different process parameters' effect on the process outcomes, study process and design parameters' interdependency, and identify possible solutions to minimize process outcomes coupling.
2. Develop numerical and empirical models to capture the process physics and represent the process outcomes
3. Develop methodologies to extract constants for material and AM machine to be used to model the manufactured part and optimize the process parameters.
4. Develop prediction and simulation tools to assess the geometrical accuracy and mechanical performance of the manufactured parts.
5. Develop optimization algorithm to improve the manufactured geometry to minimize deviation from the as-designed part dimensions.
6. Develop a 3D modelling tool to facilitate using generic user-defined unit cells to be propagated within a designed part to form a spatially variable size and density lattice structure.

This thesis consists of eight chapters, including the introduction and the thesis conclusions chapters, with six chapters in the middle discussing the different aspects of design for polymer additive manufacturing. As shown in Figure 1-8, the thesis research domain is split into two main subdomains, process parameters, and design parameters optimization. Chapters two to four investigate the process parameters subdomain and target to improve the manufactured part's mechanical and geometrical accuracy. While chapter 5 to chapter 7 investigate the design parameters domain and target to enhance the mechanical properties, cost, and part weight. After optimizing the process parameters, the mechanical properties reach a saturation state. Then optimizing part design parameters to tune mechanical properties further and reduce cost by reducing material usage and minimizing weight becomes the only option.

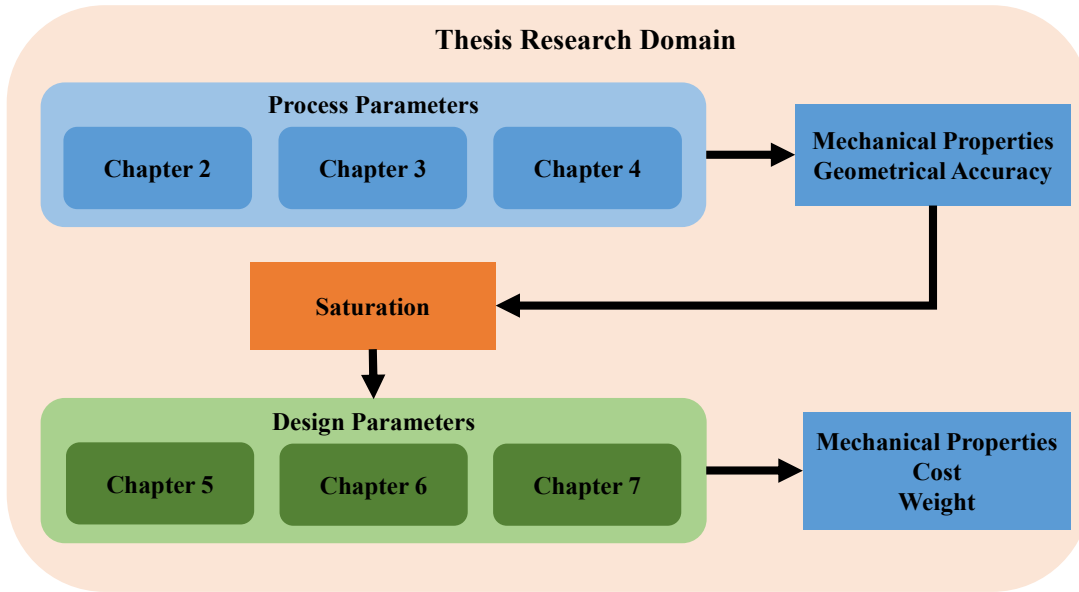


Figure 1-8 Flow chart of the thesis research domain

**Chapter 2** investigates the effect of the PSLA process parameters on the mechanical properties, geometric accuracy, and surface roughness of the manufactured part. Along with a novel introduced curing model to estimate the accumulated exposure energy per layer. The numerical, analytical model is combined with empirical models to predict material properties and surface roughness. Newly introduced terms like irradiance affected zone and critical energy for mechanical properties are used to develop curing schemes to improve geometrical accuracy. At the same time, the mechanical properties is set to a value that ensures the part integrity during manufacturing, and then mechanical properties will be enhanced during post-curing. This chapter answers part of the thesis research question that process parameters can improve the as-built part to achieve comparable measurements to the as-designed part. This chapter provides the foundation on which a modelling and optimization tool can be built.

**Chapter 3** investigates the effect of process noise on the geometrical accuracy of the part. In other words, this chapter quantifies the effect of build platform irradiance map non-uniformity on geometrical accuracy. A novel high-resolution fluorescence-induced irradiance measurement methodology is introduced to measure and capture the irradiance profile projected from one micromirror. The effect of part location on the geometrical accuracy and the effect of a grayscale pixel on minimizing that effect is experimentally explored. This chapter answers another part of the research question in which process parameters can minimize the geometrical deviation across the build platform, bringing the as-built part closer one more step towards the designed part.

**Chapter 4** utilizes the material and machine constants from chapter 2 and chapter 3 to develop a 3D geometry prediction algorithm capable of simulating the geometrical distortion in different features and surface roughness. The second part of this chapter integrates the existing pixel blending optimization algorithm with a newly introduced cross-layer optimization method and the irradiance compensation algorithm. This chapter provides a design for additive manufacturing tool to virtually assess the geometrical deviation between the as build and the design parts. Also, provide the optimization tool to improve the accuracy of the as build while minimizing the effect of irradiance map irregularities and maintain the part mechanical properties at a level to ensure the structural integrity of the part during manufacturing.

**Chapter 5** investigates the effect of part 2D design parameters on manufactured parts' mechanical properties and cost by fused deposition modelling. A cost-based methodology is used while considering the part design parameters to manufacture parts optimized for strength and cost. The study focuses on a systematic design of experiments to measure the ultimate tensile strength, ultimate flexural strength, modulus of elasticity, time, and volume. This chapter investigates a different type of process outcomes coupling, namely the mechanical properties and cost, and how to minimize such coupling using part design parameters which answer another aspect of the main thesis hypothesis compared to the previous chapters. This chapter uses empirical modelling to predict the mechanical properties and cost of FDM manufactured parts.

**Chapter 6** presents a novel algorithm capable of converting the machine input G-code file back to a CAD model (called the Reverse CAD model). The Reverse CAD model can provide an accurate assessment of the geometric and mechanical behaviour of the printed part as it also incorporates the effect of slicing parameters. In order to validate the algorithm, primitive geometries are printed, and mass properties are compared to the Reverse CAD model. This chapter approaches the thesis hypothesis by providing a numerical 3D modelling tool to predict the mechanical behaviour and geometrical Quality of the part ahead of manufacturing which can cut manufacturing costs. Therefore by using the developed tool presented, the process outcomes coupling can be minimized.

**Chapter 7** introduces a framework to grade both the size and the relative density or porosity of standard and custom unit cells simultaneously within a lattice structure as a function of the cell spatial coordinates. Moreover, it investigates the effect of lattice structure dual grading strategies on the mechanical properties experimentally. It was found that combining both relative density

and size grading enhances compressive strength, modulus of elasticity, absorbed energy, and fracture behaviour of the lattice structure at the same part weight.

This chapter approaches the thesis research question by providing a 3D modelling tool to tune mechanical properties beyond the process parameter optimization limits, such as improving toughness, ultimate strain, and ultimate compression strength at lower material usage.

## **2 Modelling and Experimental Investigation of Material Properties and Geometries Produced by Projection Stereolithography (PSLA)\***

In projection stereolithography (PSLA), the material properties are coupled with geometrical accuracy, implying that optimizing one response will affect the other. Material properties can be enhanced by the post-curing process, while geometry is controlled during manufacturing. This chapter investigates the effect of process parameters on the green material properties (after manufacturing and before applying post-curing) and the geometrical accuracy of the manufactured parts concurrently using designed experiments and analytical curing models. It also presents a novel accumulated energy model that considers the light absorbance of the liquid resin and solid polymer. An essential definition named the irradiance affected zone (IAZ) is introduced to estimate the accumulated energy per layer and assess geometries feasibility. Innovative methodologies are used to minimize the effect of irradiance irregularities on the studied responses and to characterize the light absorbance of liquid and cured resin. Analogous to the working curve, an empirical model is proposed to define the critical energies required to start developing the different material properties. The results obtained in this chapter can be used to develop an appropriate curing scheme to approximate an initial solution and to define constraints for projection stereolithography geometry optimization algorithms.

### **2.1 Introduction**

#### **2.1.1 Photopolymerization**

A successful P $\mu$ SLA system, in general, requires an optimized resin formulation. The current available photosensitive resins consist of a single or a mixture of monomers and oligomers, photoinitiator, photoblocker, and enhancing additives [26,38,40,41]. The concentration of each

---

\* Part of this chapter is published in:

- i. Mostafa, K. G., Arshad, M., Ullah, A., Nobes, D. S., and Qureshi, A. J., 2020, "Concurrent modelling and experimental investigation of material properties and geometries produced by projection microstereolithography," *Polymers*, 12(3), p. 506.
- ii. Mostafa, K. G., Nobes, D. S., and Qureshi, A. J., 2020, "Investigation of light-induced surface roughness in projection micro-stereolithography additive manufacturing (P $\mu$ SLA)," *Procedia CIRP*, 92, pp. 187–193.

component influences the process parameter values selected to achieve the desired material properties and geometrical accuracy [42].

When the prepolymer starts to receive the transmitted light from the DMD, the photoinitiator absorbs the light at a specific wavelength till it reaches its molar excitation threshold, then an intermolecular photocleavage occurs and the photoinitiator decomposes to its active radicals. These radicals attack the double bonds of the surrounding monomers and oligomers, starting a chain reaction and bonding of the active monomers and oligomers with the other unsaturated ones and forming polymer chains [43]. Due to this, a state of coexistence of gel and liquid appears. As more UV energy is absorbed, the gel further solidifies while retaining unconverted prepolymer trapped within the solid. The full conversion cannot be achieved during the  $\mu$ SLA process itself and may require post-curing [26]. An effective curing scheme achieves an acceptable amount of monomer conversion and solid phase per layer before starting a new subsequent layer to prevent shape distortion or even complete part failure.

The ideal photosensitive prepolymer resin absorbs most of the projected irradiance for each layer while allowing a small amount to penetrate to the previously manufactured layer to ensure interlayer adherence. However, in practice, a significant amount of the projected irradiance penetrates the current layer and polymerizes the uncured areas in the previous layers; thus, the photoblocker is added to minimize the irradiance penetration effect. The overall absorbance coefficient  $\alpha$ , at position and time  $(x, t)$ , which quantify the absorbance of the light at a specific wavelength by the resin and is a function of the concentrations of the different components of the material and can be described by:

$$\alpha(x, t) = \alpha_I \times C_I(x, t) + \alpha_B \times C_B(x, t) + \alpha_P \times DOC(x, t) + \alpha_o \times (1 - DOC(x, t)) \quad (2-1)$$

where  $\alpha_I$  and  $\alpha_B$  are the light absorption coefficient of the photoinitiator and photo blocker, respectively, while  $C_I$  and  $C_B$  are their concentrations. The photodecomposition rate of the photoinitiator or blocker, known as the photobleaching, is described by:

$$\frac{\partial C_j(x, t)}{\partial t} = \beta_j \times I(x, t) \times C_j \quad (2-2)$$

where  $\beta_j$  is the photodecomposition coefficient of molecule  $j$ , which in this case can be either the photoinitiator or the photoblocker, and  $I$  is the irradiance. As the absorbed energy increases,

the concentrations of both the photoinitiator and blocker decrease, which will increase the amount of the penetrating and non-absorbed energy [43,44]. As the degree of monomer conversion (DOC) increases, the number of prepolymer molecules decreases and the number of polymer molecules increases; usually, polymer absorption  $\alpha_p$  is much higher than the prepolymer molecules absorption ( $\alpha_o$ ).

The Beer-Lambert equation expresses the light absorption/penetration through the material as:

$$I(x, z) = I_o(x) \times e^{-\alpha z} \quad (2-3)$$

This equation is used to derive Jacob's working curve equation (2-4) [2,38]. The  $I(x, z)$  is the irradiance at position  $x$  at depth  $z$  and  $I_o$  is the projected irradiance at depth equals to zero and located above the PDMS window surface and just below the prepolymer resin. The cured depth ( $C_d$ ) described by:

$$C_d(x) = D_p \cdot \ln\left(\frac{I(x) \times t}{E_c}\right) \quad (2-4)$$

is more practical and specially tailored for SLA as it is described in terms of material constants that can be evaluated experimentally, namely characteristic penetration depth  $D_p$  and critical energy  $E_c$ . The critical energy is the energy at which the prepolymer start to polymerize without developing any cured depth ( $C_d = 0$ ), while the characteristic penetration depth is the depth at which the exposure energy reaches  $e^{-1}$  of its original value. The variables are exposure energy delivered represented by  $I(x) \cdot t$ , where  $t$  is the exposure time per layer.

## 2.1.2 Literature Review and Problem Statement

### 2.1.2.1 Material properties

Projection stereolithography possesses highly coupled process responses. For example, the geometrical accuracy and the material properties of the manufactured parts, which are the focus of this study, are intimately connected [45]. Manipulating the process parameters, for example, the layer thickness, the exposure time, and the irradiance, to optimize one response will significantly affect all the other responses. Minimizing the effect of this coupling is one of the motivations of

this study. The literature review section summarizes some of the research efforts to optimize the P $\mu$ SLA process parameters to achieve different optimal responses.

Aznarte et al. [46,47] studied the significance of twelve process parameters on the green mechanical properties of parts. It was found that the layer thickness, the exposure time, the part orientation, and the wait time between two successive exposures are the top most significant parameters. Also, the manufactured parts showed major properties anisotropy, which is confirmed by Dizon et al. [48].

Chockalingam et al. [49] studied the effect of layer thickness, orientation, and post-curing time effect on the strength of the part using the L18 orthogonal array and developed a second-order polynomial regression model. It was found that the layer thickness is the most significant parameter; however, the post-curing time levels chosen for this experiment were causing over-curing of the polymer, which decreased its strength as time increased.

Monzón et al. [50] studied the effect of post-curing on the anisotropy of the manufactured parts. The results showed that with proper post-curing time, the anisotropy diminishes completely along all axes with a notable increase in the mechanical strength. Also, Monzón et al. [50] showed that the position of the part on the build platform affects the mechanical properties significantly, which can be reasoned by the irradiance irregularities of the DMD device depicted by Zheng et al. and Warburg et al. [51,52].

Wu et al. [43] developed a curing kinetic model for acrylates-based photopolymers to predict different material properties. The test specimen was made of a single-layer part using a mould and curing light source. Yang et al. [53] developed a multi-layer curing model to estimate a theoretical average degree of curing and developed a regression model relating material properties to the degree of cure. The previous two models require extensive and expensive experimentation to evaluate all the required constants and also require detailed information about the resin components and their concentration, which is not available for most industrial resins.

#### **2.1.2.2 Geometrical Accuracy**

Zhou et al. [54,55] used a pixel blending optimization algorithm to improve the geometrical accuracy of the horizontal shapes. This algorithm enabled higher accuracy and sub-voxel resolution, but it did not manipulate the exposure time. Mitteramskogler et al. [56] studied the lateral growth of the dimensions with curing time experimentally.



Gong et al. [38,57] developed a multi-layer curing model to calculate the exposure time for each layer independently to improve the accuracy of the horizontal microchannel against the light penetration challenge. O'Neill et al. [58] studied the effect of the number of layers manufactured after a microchannel on the deviation of the microchannel dimensions. These models treat the light penetration/absorption for both the liquid prepolymer and the solid polymer as the same. However, they are different, as indicated by (2-1). Because as the monomer converts into a polymer, the absorption changes.

Mostafa et al. [32] studied the effect of exposure time, grayscale, and layer thickness on the accuracy and tolerance control of cylindrical features and showed that exposure time is the most significant parameter.

Optimizing the concentrations of the material components will improve the material properties and the features' geometrical accuracy. However, the excessive addition of photoblockers to minimize light penetration through the material improves geometry but decreases strength. On the other hand, increasing photoinitiator concentration improves the material properties but decreases the critical energy for the prepolymer, which makes it highly sensitive and will result in distorted geometries [38,59–61]. Increasing both concentrations by insignificant amounts also increases material toxicity significantly, which makes the material unsuitable for medical applications.

### ***2.1.2.3 Surface Roughness***

Surface roughness is a major challenge for most additive manufacturing processes due to the addition of discretized layers. The surface roughness varies significantly with the change of process parameters [62]. For most AM processes, the surface roughness is a combined result of the staircase phenomena and the characteristic physics of the process. A model based on the staircase only will predict the surface roughness when the part surface is inclined [63]. The experimental results presented in [62,64–66] show that vertical surfaces have an average surface roughness of significant value but are less than that of the inclined surfaces. There are several studies dedicated to optimizing the inclined surface quality resulting from the staircase phenomena using the PμSLA physical models; however, these models did not predict the vertical surface roughness [67,68].

Baltej et al. [11] used geometry-based modelling and were able to predict the surface quality of both inclined and vertical surfaces of the FDM process. Krishnan and Gurunathan [69] presented an analytical physics-based model that considers both the intrinsic polyjet AM process surface roughness and the staircase phenomena. The theoretical model proposed in this chapter is shown in Figure 2-3(b), where both the inclined and vertical surfaces have surface roughness with a characteristic form due to the curing light diffractions.

### **2.1.3 Research Motivation and Objectives**

The motivation of this study is to determine the appropriate curing scheme producing accurate geometries with sufficient green materials properties before the post-curing process to withstand the manufacturing process and the subsequent post-processing. The geometry is mainly controlled during the manufacturing process itself, while material properties can be further enhanced with post-curing to reach the optimum properties.

The coupling of the process responses entails the analysis of the effect of process parameters, namely layer thickness, exposure time, and irradiance, on both the material properties and the geometrical accuracy of the manufactured parts using a series of designed experiments. The irradiance irregularities across the building platform are identified, and their effect on the measured properties is accounted for in the experiments. A novel multi-layer curing model that differentiates between the absorbance of light through the liquid prepolymer resin and the solid polymer while calculating the accumulated energy per layer is developed and presented. A new terminology called the irradiance affected zone (IAZ) is introduced to define the number of previously cured layers affected by the exposure light of the current layer. An innovative experimental methodology for evaluating the constants of the working curve required for the developed model is presented. Analogous to the working curve, this chapter defines the critical energy to develop different material properties using an empirical model, which is a result of a logarithmic fit between the measured material properties and the numerical computed accumulated exposure energy per each layer. An experimental geometric artifact was designed to evaluate the manufacturability of different features at different sizes. Both the horizontal curing model and the vertical accumulated model are also used to assess the feasibility of manufacturing different parts.

Based on the proposed vertical and horizontal curing models, the average surface roughness is modelled using a curing model as a function of the significant process parameters, namely the

exposure time per layer and the layer thickness. A prediction model based on both the curing and the staircase models is introduced. The surface roughness is characterized experimentally using both the confocal microscope and scanning electron microscope. The main surface lay directions are identified. Both the predicted and the experimental results are compared to evaluate model performance.

The results obtained from this study allow a new methodology to estimate the proper curing scheme for successful functional parts. By knowing the different material critical energies defined by the empirical model, the process parameters can be tuned to achieve such energies as a minimum energy constraint while focusing on achieving the required geometrical accuracy using the different pixel blending optimization algorithms.

## **2.2 Curing Analytical Models**

In this section, two analytical curing models that will be used in the analysis of the results are presented. The first model, which is a novel model, is called the vertical multilayer model along the  $z$ -axis. This model estimates the accumulated energy received per layer. The novelty in this model is that it differentiates between the irradiance absorbance in liquid prepolymer and solid polymer. The accumulated energy per layer is further used to model the material properties. The second model is a horizontal curing model along the  $x$ -axis, which is used to study the effect of process parameters on the dimensions of different features. Both models are used to assess the manufacturing feasibility of different geometric features.

### **2.2.1 Vertical Multilayer Model for Accumulated Energy**

Various vertical energy accumulation models have been presented in different studies [57,67,70]. However, these studies consider that the irradiance absorbance is the same across liquid prepolymer and cured polymer. In reality, the absorbance coefficient differs as suggested by (2-1) and is shown experimentally in the next sections. The proposed new model uses two working curves to simulate the irradiance penetration through both liquid resin and cured polymer. As shown in Figure 2-1, the first layer of prepolymer receives its initial exposure energy  $E_1$  which equals to the multiplication of the irradiance  $I$  projected just above the PDMS window, for layer  $i$ , which in this case equals one, and exposure time  $t$ . During the curing of the second layer, the squeezed resin between the PDMS window and the cured layer receives the initial exposure  $E_2$

and the first cured layer receives a portion of this exposure energy  $E_{12}$  which passes through the liquid resin of layer two. Then the third layer receives  $E_3$  and a portion of it  $E_{23}$  penetrates through liquid resin of the third layer and exposes the second layer, then sub-portion of it  $E_{13}$  penetrates through the cured second layer and exposes the first layer, and so on.

As described by (2-5), each layer receives total exposure energy of  $E_{Ti}$  which is the summation of the initial exposure  $E_i$  of the layer  $i$ , and accumulation of the penetrating exposure energy  $E_{ij}$  received by layer  $i$  from the initial exposure of the subsequent layer  $j$ . The subsequent layers considered in the energy accumulation estimation are only within the irradiance affected zone (IAZ), described by (2-7). The IAZ is the number of layers having a thickness  $d_z$  and penetrated by irradiance  $I$  for time  $t$  before the exposure energy decreases below the critical energy  $E_c$ . For a certain layer thickness value, the IAZ is a material-dependent property and defined by the characteristic penetration depth  $D_{P_1}$  and the critical energy  $E_c$  of the resin. The penetrating exposure energy  $E_{ij}$  from layer  $j$  to layer  $i$ , described by (2-8), is defined as the exposure energy penetrating through one layer of liquid resin, defined by  $D_{P_1}$ , and the previously cured layers between  $i$  and  $j$ , defined by  $D_{P_2}$ . The IAZ also defines the minimum horizontal channel size; in which any horizontal gaps smaller or equal to the depth of the IAZ will cease to exist, and the vertical dimensions of the horizontal channel will deviate depending on the layer thickness used and exposure time.

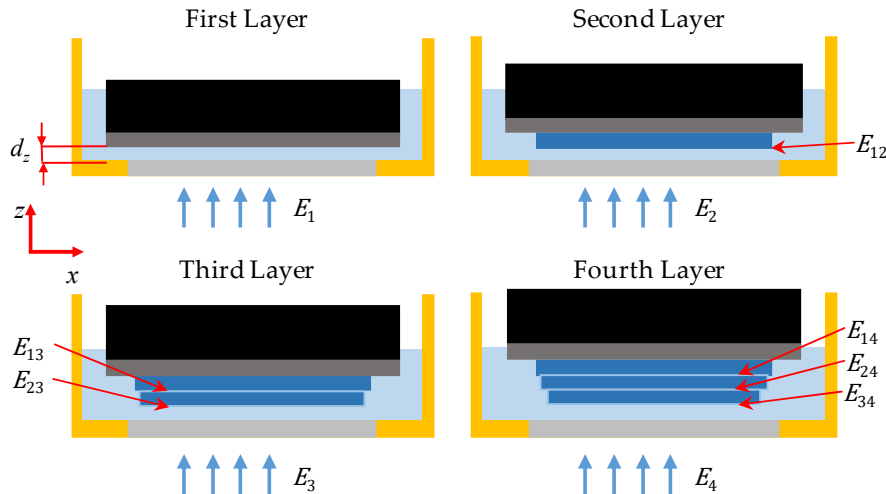


Figure 2-1 Illustration of the vertical energy accumulation model

$$E_{Ti} = E_i + \sum_{j=i+1}^{i+IAZ} E_{ij} \quad (2-5)$$

$$E_i = I \times t \quad (2-6)$$

$$IAZ = \frac{D_{P1}}{d_z} \times \ln\left(\frac{I \times t}{E_c}\right) \quad (2-7)$$

$$E_{ij} = E_j \times e^{-\left(\frac{d_z}{D_{P1}} + (j-i-1) \times \frac{d_z}{D_{P2}}\right)} \quad (2-8)$$

### 2.2.2 Horizontal Curing Model

Horizontal curing models have been presented before in several studies to optimize or evaluate horizontal geometries of a single layer [54,71–73]. Due to light dispersion, the projected irradiance from one micromirror on to the PDMS surface  $I(x)$  at any distance  $x$  is represented by a Gaussian profile with a Gaussian radius of  $\omega_o$  and maximum irradiance per micromirror of  $I_m$  as presented by (2-9). The projector consists of a 2D array of micromirrors; however, the presented model simulates only a 1D array only. The Gaussian irradiance distribution is assumed to be axisymmetric around the center of each micromirror, thus reduced into a 2D distribution. The maximum irradiance of each micromirror is assumed to be the same for the micromirrors in the model. The irradiance profile projected from a linear series of micromirrors is simulated by the superpositioning of the Gaussian profiles of all the micromirrors using (2-10), where  $I_T(x)$  is the superpositioned irradiance, at any distance  $x$ , projected by  $N$  micromirrors and,  $P$  is the pitch distance between two consecutive micromirrors. This model is used to simulate the constrained surface process, where the maximum value for the cured depth cannot exceed the layer thickness  $d_z$ . The cured depth at any distance  $x$  can be estimated by using (2-11) and (2-12).

$$I(x) = I_m \times e^{-\frac{2 \times x^2}{\omega_o^2}} \quad (2-9)$$

$$I_T(x) = \sum_{k=1}^N I_m \times e^{-\frac{2 \times (x - k \times P)^2}{\omega_o^2}} \quad (2-10)$$

$$E_T(x) = I_T(x) \times t \quad (2-11)$$

$$C_d(x) = \begin{cases} D_{P_1} \times \ln\left(\frac{E_T(x)}{E_C}\right) & D_{P_1} \times \ln\left(\frac{E_T(x)}{E_C}\right) < d_z \\ d_z, & D_{P_1} \times \ln\left(\frac{E_T(x)}{E_C}\right) \geq d_z \end{cases} \quad (2-12)$$

To simulate the effect of exposure time on the buildup exposure energy and the lateral dimensions of simple linear features, equations (2-9) to (2-12) are used. The outcome of this simulation is depicted in Figure 2-2. Figure 2-2(a) shows the results of projecting light from a linear series of nine micromirrors, with all of them turned on when the middle mirror is turned off. The dashed blue lines represent the individual Gaussian profiles reflected by each micromirror, while the solid blue line with triangles represents the superpositioned irradiance profile. The red line represents the corresponding exposure energy evaluated at different exposure times ranging from 1.2 to 2 seconds. The horizontal black solid lines represent the critical energy, and the other dashed black lines represent the minimum energy required to achieve a cured depth of 10, 25, and 50  $\mu\text{m}$ .

The cured depth for the different exposure energies is evaluated and presented in Figure 2-2(b). The black dashed line is the ideal shape, while the black horizontal lines represent the maximum height for the layer thickness of 10 and 25  $\mu\text{m}$ . Figure 2-2(c) and (d) show the effect of exposure time on exposure energy and lateral dimensions for a line projected by nine micromirrors with all of them turned on when the middle three mirrors are turned off. For the outer dimensions, as the exposure time increases, the exposure energy increases, leading to an increase in the lateral dimensions and deviations from the ideal shape.

For internal dimensions, as the exposure time increases, the exposure energy increases, leading to a decrease in the size of the internal gap until it ceases to exist, especially at lower layer thickness values. It is theoretically not possible to create an internal gap by turning off one mirror in the middle of a series of turned-on mirrors; however, it is theoretically possible that an internal gap can be developed by turning off three micromirrors. This is due to the resultant energy being above the critical energy for each layer thickness; therefore, the gap will get cured. For the three micromirrors case, the resultant energy is below the critical energy for all the layer thickness values, which means it is possible to create this gap at the studied exposure time. The superposition

of irradiance in the case of linear features has lower values compared to 2D horizontal superposition, which means that a 2D gap created within a 2D feature is more challenging than within linear features. The conclusion is that there is some restriction in achieving the commercially promised horizontal resolution. An experiment is designed to evaluate the performance of these models and to study the effect of the layer thickness, exposure time, and irradiance on the dimensions of vertical and horizontal microchannels, vertical bars, and overhangs.

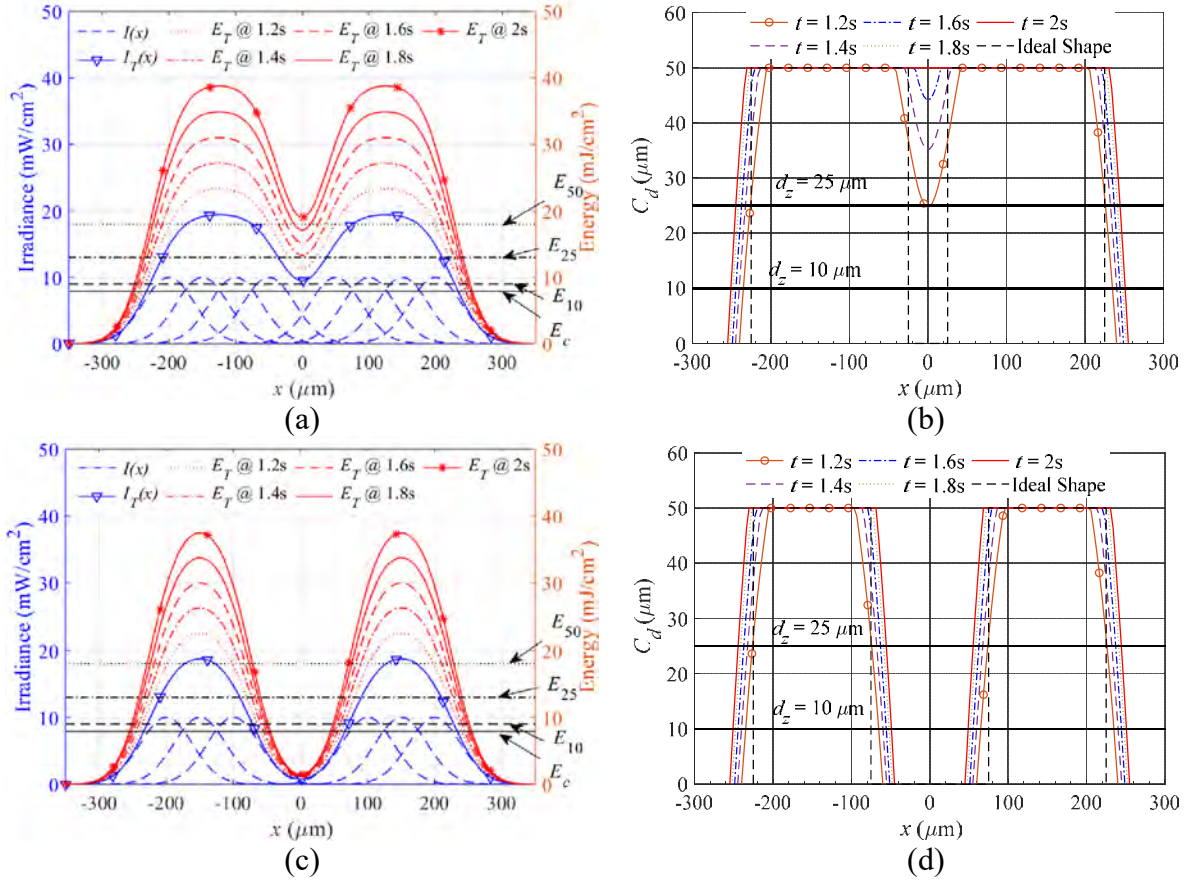


Figure 2-2 Effect of exposure time, while with one micromirror turned off, on (a) superposition energy (b) lateral dimensions, and effect of exposure time, while with three micromirrors turned off, on (c) superposition energy (d) lateral dimensions.

### 2.2.3 Surface Roughness Model

A model based on the staircase only will predict the surface roughness when the part surface is inclined, as shown in Figure 2-3(a). While in reality, the manufactured parts have surface roughness similar to Figure 2-3(b).

According to ASME B46.1 [74], the surface quality can be described by the average surface roughness, which is defined as the summation of the peaks and valleys areas divided by the evaluation length. According to the staircase theoretical model presented in [65], the value of shaded area  $A$  is divided by the evaluation length  $W$ , as shown in Figure 2-3(c). Where the surface angle  $\theta$  describes the surface inclination, the layer thickness is  $d_z$ , and the surface profile angle is  $\phi$ . The process physics model will be used to evaluate the  $\phi$  as suggested by [69]. If the process parameters are kept fixed, the  $\phi$  value will also be fixed, and equation (2-13) can be used to describe the average surface roughness of both the inclined and the vertical surfaces. However, in the usual case, each part has its optimized process parameters to achieve different functional requirements. Thus, another model that can relate the process parameters to the surface profile angle  $\phi$  is required.

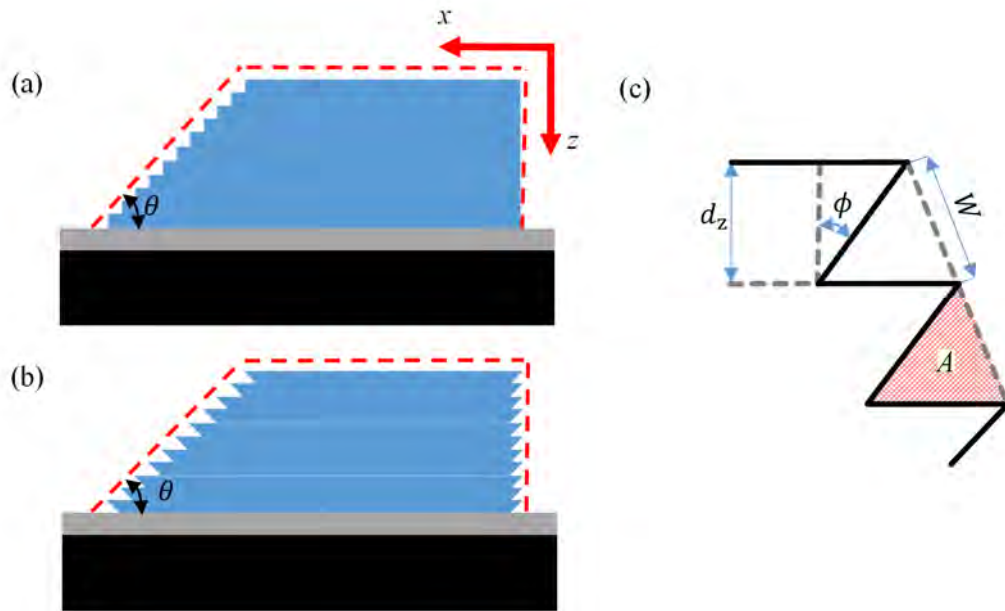


Figure 2-3 (a) The effect of staircase phenomena on surface roughness, (b) The combined effect of staircase and process physics on surface roughness, and (c) Trigonometric illustration of the average surface roughness model



$$R_a = \frac{A}{W} = \frac{d_z}{2} \times \left| \frac{\cos(\theta - \phi)}{\cos(\phi)} \right|, \quad (0^\circ < \theta < 180^\circ) \quad (2-13)$$

By using both the vertical and horizontal curing schemes, the cured shape can be estimated, as shown in Figure 2-2. The slope and the nominal width of the cured shapes increase as the layer thickness value decrease and as the exposure time increase. The surface profile angle  $\phi$  is the angle of the cured shape slope.

## 2.3 Materials and Methods

In order to study the concurrent influence of significant process parameters, suggested by the literature review, on the degree of monomer conversion, ultimate tensile strength, storage modulus, and geometrical accuracy, a series of characterizations are carried out based on a design of experiments. Since this work aims to relate the manufactured part characteristic to the independent process parameters, a set of experiments is carried out to determine the working curve constants of the used material and assess the irradiance of the machine at different grayscale levels and LED power.

### 2.3.1 Material

The prepolymer liquid resin used in this study is called PR48 clear resin, Colorado Photopolymer Solutions, LLC. This resin was chosen because it is optimized for macro and micro-scale features, commercially available with defined chemical composition allowing development and optimization in labs. PR48 clear resin consists of Allnex Ebecryl 8210 with a 39.776 wt%, Sartomer SR 494 with a 39.776 wt% as oligomers, Esstech TPO+ with 0.4 wt% as a photoinitiator, Rahn Genomer 1122 with 19.888 wt% as a reactive diluent, and Mayzo OB+ with 0.16 wt% as a UV blocker [75].

### 2.3.2 Manufacturing Platform

The machine used in this study is the Ember<sup>®</sup> DLP 3D printer, a machine developed by Autodesk. The LED has a maximum of 5 W and emits light at 405 nm wavelength. The DLP system has 912×1140 micromirrors. The build area has a maximum volume of 64×40×130 mm. The machine vertical minimum resolution/layer thickness is 5  $\mu$ m, and the horizontal commercial

resolution is 50  $\mu\text{m}$ . The machine is an open-source platform that allows complete user control over all the process parameters.

### 2.3.3 Irradiance Measurement

There are two sets of experiments performed to characterize the irradiance of the machine. The first experiment aims to measure the irradiance projected on the PDMS top surface, corresponding to 3 different LED power values at different input image grayscale values. The result of this set is used to correlate the values of the LED power and grayscale value to the irradiance value. The results will also be used in the working curve evaluation. These measurements were done by projecting a sequence of images containing nine mono-colour grayscale squares of  $10 \times 10$  mm, where the colour of the images ranges between 0 (Black) to 255 (White), as shown in Figure 2-4(a). Then the irradiance of the Ember printer (1) was measured by Thorlabs PM100 power meter (2) with a photodiode power sensor Thorlabs S121C (3), as shown in Figure 2-4(b). These measurements were repeated at three different LED power values corresponding to the pulse width modulation integer values of 255 for the maximum available power, 225, and 215; zero means the LED is off.

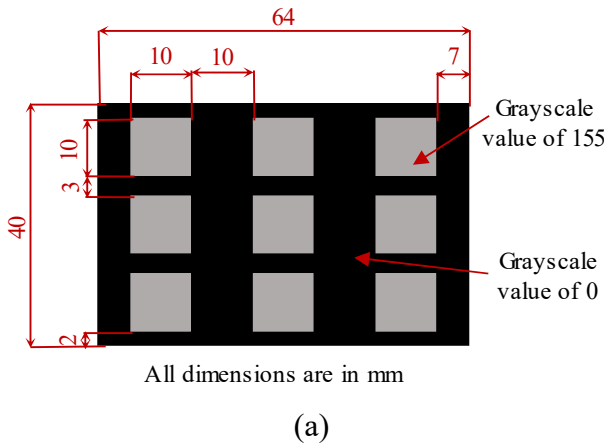


Figure 2-4(a) A projected image with nine  $10 \times 10$  mm squares having 155 grayscale pixel value,  
(b) measuring the irradiance of the Ember machine using a power meter

The second experiment is to evaluate the irradiance map irregularities across the building area in order to choose a suitable manufacturing region on the build platform with consistent irradiance for the manufacturing of the different parts. By using the same image shown in Figure 2-4(a) while

projecting it at the maximum LED power and white (255) squares and measuring the irradiance of each area.

### 2.3.4 Working Curve

In order to study the effect of exposure energy on the curing depth and light penetration through the polymer, two experiments were carried out. For each of the experiments, characteristic penetration depth and critical energy are determined. The first experiment is used to measure the cured depth of the polymer formed after continuous light expose for six seconds at different irradiance levels. This experiment is achieved by projecting an image consisting of different 24 grayscale tiles that were projected continuously for six seconds, as shown in Figure 2-5(a). The lowest irradiance corresponds to a dark grey with an integer value of 11, while the highest irradiance corresponds to the white tile with an integer value of 255. This method will evaluate the light penetration and cured depth evolution through the liquid at the initial exposure of the layer.

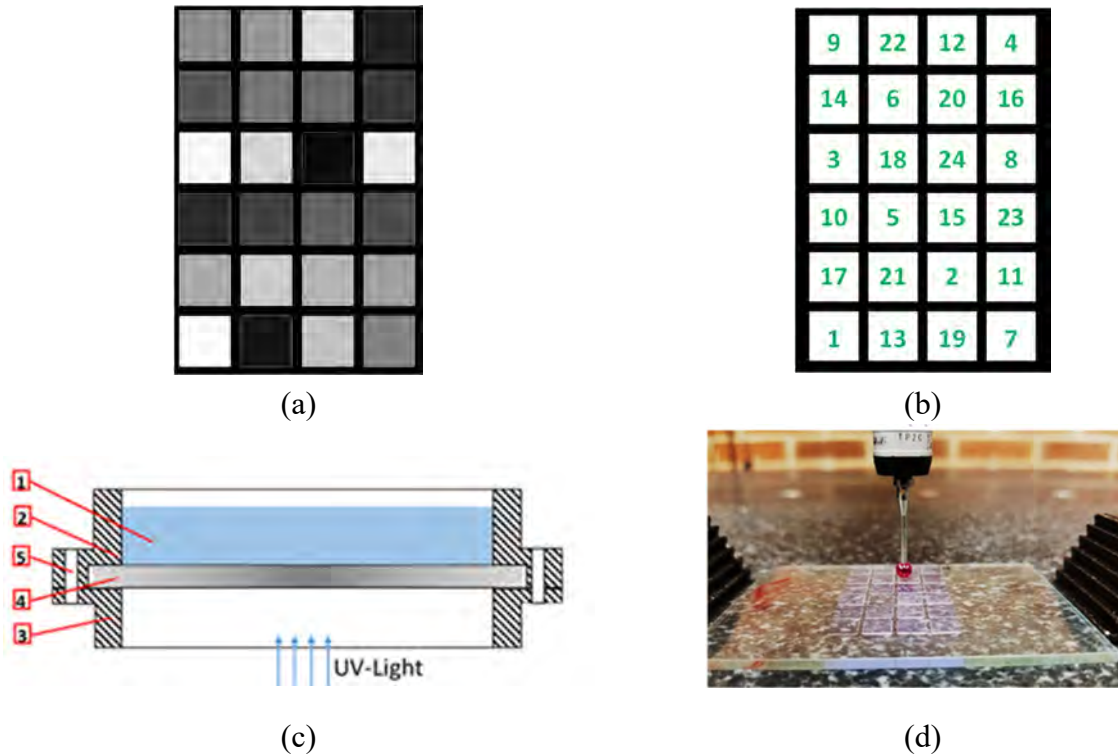


Figure 2-5 (a) experiment 1: grayscale tiles for the continuous exposure-based working curve, (b) experiment 2: white tiles for the sequential discrete exposure-based working curve, (c) illustration of the specially designed vat, (d) CMM probe measuring the cured depth of tiles height.

The second experiment, which was inspired by the technique used in [76], will evaluate the cured depth and light penetration through the cured polymer. It is achieved by projecting a sequenced stack of the 24 images containing white tiles (255) only, as shown in Figure 2-5(b). The number on each tile represents the number of images out of the 24 images that would project the specific white tile. For example, the first image will contain all the 24 tiles whereas the second image will contain all the tiles except the tile number 1, the third image will contain all the tiles except 1 and 2, and similarly, the last image will only contain the tile number 24. The exposure time for each image is 200 ms, and the wait time between every two successive exposures equals the typical wait time during the normal process, which is set to its optimal value of 1 s [47].

Both sets are carried out at two different LED power; 255 (HI) and 215 (LO). Each tile is 5×5 mm, and the distance between any two tiles is 1 mm. The total area occupied by the 24 tiles is 23×35 mm. The positioning of tiles in both sets is randomly assigned. The area where the tiles are distributed is limited to around 1/3 of the total build area so that the tiles are placed within an area of a tolerable irradiance map difference. A specially designed vat was used in this experiment, as shown in Figure 2-5(c), to carry the liquid resin (1). The vat consists of the upper body (2) and lower body (3) enclosing a quartz plate (4), and the two bodies are tightened together with bolt and nut through aligned through hole (5). The upper and lower bodies were 3D printed. The unique design allows removing the quartz plate after each experiment, cleaning the uncured resin using isopropyl alcohol spray and also facilitating the measurements of the cured depth. The average cured depth based on three measurements on different locations per cured polymer tile was evaluated. The machine used for measurement is the Crysta-Plus M443 Mitutoyo CMM machine, which has a 0.5  $\mu\text{m}$  resolution and repeatability of 4  $\mu\text{m}$ . The measurement setup is shown in Figure 2-5(d).

### **2.3.5 Design of experiments for material and geometric characterization**

Three experiments were designed using a  $2^2$  full factorial array, as shown in Table 2-1. Three different layer thicknesses are studied with a value of 10, 25, and 50  $\mu\text{m}$ . For each experiment, the exposure time and LED power are the only variables, while the layer thickness value is kept constant.

The reason for doing three separate experiments is that as the exposure time increases at lower layer thickness, the printed part adheres to the PDMS window, which halts the process in the

middle and produces distorted shapes. The exposure time values were adjusted in each experiment to ensure that the maximum limit will not cause PDMS separation problems, and its lower limit will not cause part failure due to layers separation caused by incomplete curing. The LED power values used are the maximum available power at 255 and 215 below, which requires prolonged exposure time. For each of the three experiments, the responses measured are the degree of monomer conversion, tensile strength, storage modulus, and the dimensions of several geometric features.

Table 2-1 Values of the process parameters for three designed experiments

Layer Thickness								
50 $\mu\text{m}$			25 $\mu\text{m}$			10 $\mu\text{m}$		
#	Time (s)	Power	#	Time (s)	Power	#	Time (s)	Power
1	2	HI	1	1.8	HI	1	1.6	HI
2	2	LO	2	1.8	LO	2	1.6	LO
3	1.6	HI	3	1.4	HI	3	1.3	HI
4	1.6	LO	4	1.4	LO	4	1.3	LO

### 2.3.6 Degree of Monomer Conversion

The degree of monomer conversion (DOC) is calculated using Fourier transform infrared spectroscopy (FTIR) with attenuated total reflection (ATR) to scan both the cured polymer samples for all the experiments and the uncured prepolymer resin. Six cubes of 5 mm each were manufactured for each configuration and then appropriately cleaned with isopropyl alcohol. Then the cubes were finely ground before the scanning. The machine used is Nicolet iS50, ThermoFisher Scientific, with a build-in ATR module. Each sample was scanned 32 times with a wavenumber resolution of  $2\text{ cm}^{-1}$ . During polymerization, the double bond  $\text{C}=\text{C}$  is opened and converted to a single bond in the polymer chain. The degree of conversion can be estimated by comparing the absorbance spectra of the  $\text{C}=\text{C}$  stretching vibration peaks at  $1620\text{ cm}^{-1}$  and  $1635\text{ cm}^{-1}$  in the cured polymer to the same peaks in the liquid resin, as shown in Figure 2-6. The measured values are normalized against a non-variable standard bond during the reaction to account for the differences in the amount of the scanned samples. The  $\text{C}=\text{O}$  bond is chosen as the non-variable reference based on the material we have. The  $\text{C}=\text{O}$  has a stretching vibration at  $1725\text{ cm}^{-1}$ . The DOC is calculated using equation 13, where  $A$  is peak absorbance area of the cured sample at a specific wavenumber

and  $A_o$  is the peak absorbance area for the uncured prepolymer resin at the same specific wavenumber.

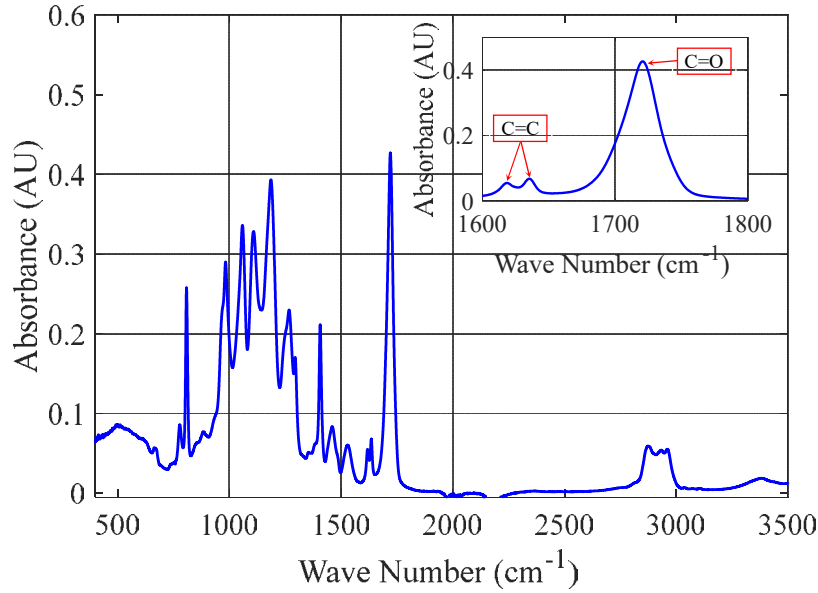


Figure 2-6 FTIR peaks considered in calculating the degree of monomer conversion

$$DOC = 1 - \frac{(A_{@1635} + A_{@1620}) / A_{@1725}}{(A_{o@1635} + A_{o@1620}) / A_{o@1725}} \quad (2-14)$$

### 2.3.7 Mechanical Tensile Test

The ultimate tensile strength (UTS) was determined experimentally by manufacturing a standard dog bone specimen 1 BB, according to ISO 527-1:2012(E) [77,78]. This specimen was explicitly chosen due to its short overall length, which is around 30 mm and also its tight width of 4 mm with a narrow cross-section of 2×2 mm, which makes it the smallest specimen compared to the other specimens in the ISO or ASTM. Three replicates were manufactured for each experimental configuration. The dog bones were positioned in a defined location on the build area to minimize the irradiance irregularities effects, which will allow more consistency in the results. The printing location is defined based on the irradiance measurements, which are discussed in section 4.1. The specimens were orientated flat on the build platform, and the specimen edges were parallel to the micromirror edges. The specimens were conditioned for seven days at room

temperature of 22 C° and room humidity of 23% [79]. The machine used is the 3360 series universal testing system by Instron. The specimens were tensioned at an elongation rate of 0.125 mm/min.

### **2.3.8 Dynamic Mechanical Analysis (DMA)**

A dynamic mechanical analysis (DMA) with a three-point bending test is used to measure the storage modulus corresponding to each experimental configuration. The machine used in this test is DMA Q50, produced by TA instruments. The test was performed at a temperature range from 0 C° to 100 C° at 1 Hz cycle. The specimen size is 35×12.5×4 mm. The specimens were manufactured within the same location that was used for the tensile test specimens in order to be manufactured to minimize the effect of irradiance irregularities and tests were conducted in duplicate.

### **2.3.9 Geometrical Feature Measurement**

A geometrical artifact was designed to study the effect of process parameters on the size of different geometrical features. The artifact is designed to include four different features at different sizes to determine the minimum feasible sizes for each feature and assess the accuracy of the manufacturing process [80]. The four features included are the horizontal circular channels (the channel axis is parallel to the  $x$ - $z$  plan), vertical square channels (the channel axis is parallel to the  $z$ -axis), overhangs, and vertical square bar, as shown in Figure 2-7. Six sizes of horizontal and vertical channels are included in the artifact ranging between 150  $\mu\text{m}$  to 750  $\mu\text{m}$ . While seven sizes for the square vertical bars and overhangs ranging from 100 to 1000  $\mu\text{m}$ . For each size per each feature, there are two replicates.

The input images to the machine consist of black and white pixels only with no grayscale pixels in order to study the effect of the process parameters selected without interference from any grayscale pixels. The artifact was positioned on the platform within a defined location with tolerable irradiance irregularities. The base of the artifact was oriented flat above the build area, and the edges of the features were aligned with the micromirror edges to avoid geometrical distortion caused by the diamond orientation of the micromirrors array. The features were measured using Stemi-508 Carl Zeiss optical microscope equipped with ZEISS Axiocam 105

colour camera with  $2560 \times 1920$  pixels, which provides a resolution of  $2.5 \mu\text{m}$  at the selected optical zooming level.

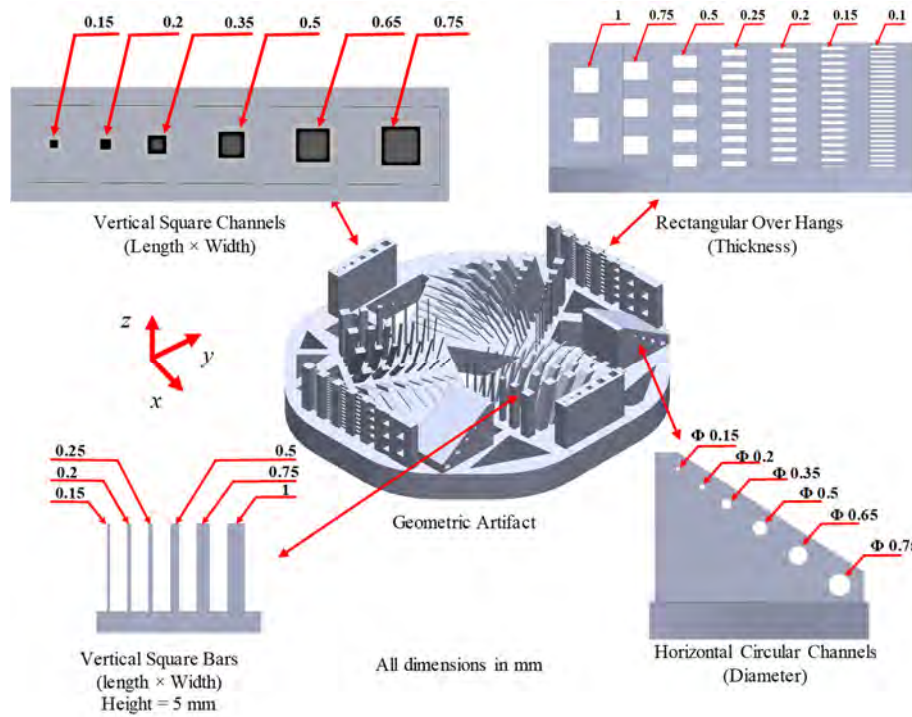


Figure 2-7 Geometric artifact to determine the minimum feasible feature size manufactured

### 2.3.10 Surface Roughness Measurements

In order to characterize the effect of the process parameters on the surface roughness induced by light diffraction, the sidewalls of a  $5 \times 5$  mm cube were characterized. The sidewalls of each manufactured cube are characterized using the Olympus LEXT OLS3000 confocal laser scanning microscope. The microscope is equipped with a 20x objective lens with a numerical aperture of 0.46 and a 408 nm wavelength laser source, which achieves an optical resolution of 0.44 microns. The system over nominal horizontal resolution is 0.625 microns, while the vertical stepping resolution was set to 0.64 microns. The acquired raw image was filtered using a median image filter with a  $4 \times 4$  pixels neighborhood area surrounding each target pixel to remove noise spikes. A 3D surface was constructed out of the filtered images, and then it was compensated for surface inclination due to the mounting setup. The surface roughness was evaluated in two main lay directions. The vertical direction is defined as the direction perpendicular to the layers' surface and parallel to the layers' surface. For each lay direction per each scanned surface, the surface



roughness of three equally spaced sections distributed across the surface were analyzed. Each surface profile is a result of high pass filtering of the primary profile with a cut-off wavelength ( $\lambda_c$ ) of 80 microns and a low pass filtering with a cut off wavelength ( $\lambda_s$ ) of 2.5 microns, according to ASME B46.1, 2009 [74]. The use of the confocal microscope in the surface roughness characterization of AM parts compared to other techniques was discussed in [81,82]. Zeiss EVO MA10 scanning electron microscope was also used to capture a magnified image of the surface profile angle and to identify the main lay directions.

## 2.4 Results and Discussion

### 2.4.1 Irradiance Characterization

The irradiance across the build area was found to be significantly variable, as shown in Table 2-2. The maximum difference between the highest and the lowest regions is 6.5 mW/cm<sup>2</sup>. The region with the most consistent irradiance is the center column with an average of 18.2 mW/cm<sup>2</sup> and was selected to manufacture the specimens of the different experiments within it. The value of the average irradiance of this region is used to measure the irradiance value corresponding to the different pixel grayscale colours and the LED power value. The relationship between the grayscale level of the input image's pixels and the irradiance value, as shown in Figure 2-8. The relation between the grayscale and the irradiance is linear. As the grayscale integer value increases, the irradiance increases. As the LED power increases, the irradiance value increases but not in a proportional trend.

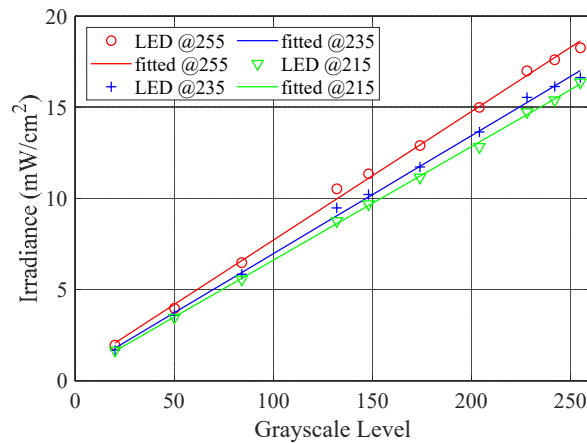


Figure 2-8 Relation between the grayscale level of the pixels and irradiance level

Table 2-2 Measured irradiance values across the build area (mW/cm<sup>2</sup>)

Position	Left	Center	Right
Top	12.5	17	12.5
Middle	14.3	18.7	14.7
Bottom	15.6	19	16.2

### 2.4.2 Working Curves

The results for the continuous light exposure pattern are depicted in Figure 2-9(a). The critical energy ( $E_c$ ) required to initiate the photopolymerization ( $C_d = 0$ ) equals to 9.5 mJ/cm<sup>2</sup> for both LED power, while the characteristic penetration depth ( $D_p$ ), which is the slope of this curve, if plotted on a semi-log plot, is different for the different LED power. The  $D_p$  of the continuous pattern at high LED power equals to 71  $\mu$ m and at the lower power is 62  $\mu$ m. Figure 2-9(b) depicts the results for the sequential discrete pattern. The critical energy ( $E_c$ ) for this pattern equals to 6.5 mJ/cm<sup>2</sup> for both LED power. The  $D_p$  of the discrete pattern at high LED power equals to 43  $\mu$ m and for the lower power is 41  $\mu$ m. The continuous exposure generally shows a higher  $C_d$  for the same amount of received energy compared to the discrete pattern. The average critical energy of the two curves equals to 8 mJ/cm<sup>2</sup>, and this energy is used in the curing models to simulate the different scenarios. The logarithmic fitted curves have an average  $R^2$  equals to 0.93. The deviation between the fitted lines at the two LED power within the same the exposure pattern starts to significantly increase after 20 mJ/cm<sup>2</sup> to reach around 15  $\mu$ m at 100 mJ/cm<sup>2</sup> for the continuous pattern while 5  $\mu$ m at 100 mJ/cm<sup>2</sup> for the sequential discrete pattern. These results show that the cured depth is sensitive to the irradiance level. The cured depth of the polymer resulting from the initial exposure is different from the cured depth formed by subsequent exposures through cured layers, for the same amount of received energy. For example, at 60 mJ/cm<sup>2</sup>, the difference between the cured depth for continuous exposure and the one for the sequential discrete exposure is around 50  $\mu$ m. These results show that there is a difference between the absorbance of the prepolymer and the cured polymer.

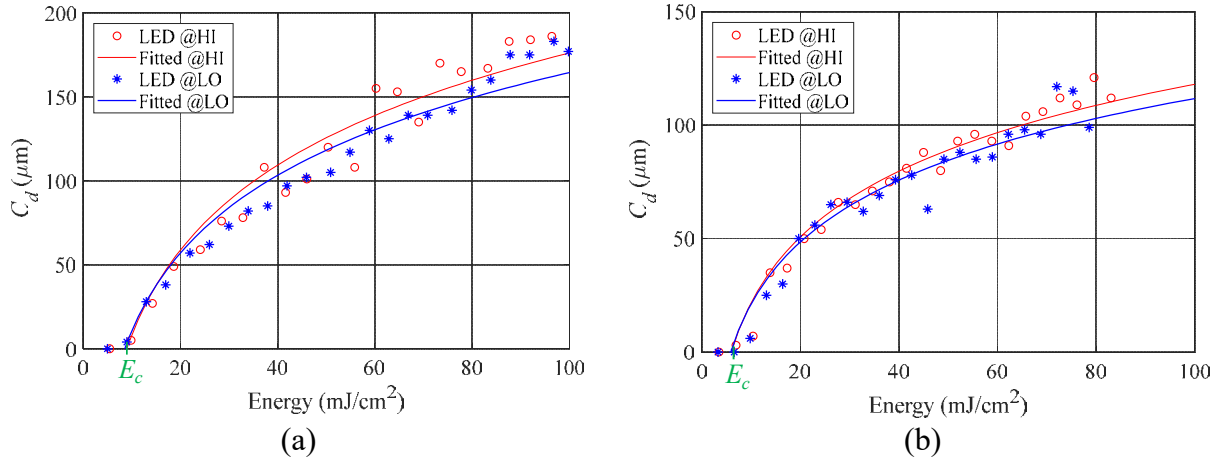


Figure 2-9 Working Curve from (a) continuous exposure pattern (b) discrete sequential pattern

### 2.4.3 Material properties characterization

Figure 2-10 (a), (b), and (c) depict the effect of the exposure time and the ultimate tensile strength (UTS), storage modulus, and degree of monomer conversion (DOC), respectively. Each plotted line within each figure represents a particular layer thickness and LED power. There is a general trend that can be easily determined in the three figures; as the layer thickness decreases, the material properties increase, and within the same layer thickness, as the exposure time or the LED power increase, the material properties increase. For all of the properties measured, the layer thickness was found to be the most significant parameter followed by exposure time and LED power

For ultimate tensile strength, the maximum green strength achieved is 24 MPa at 10  $\mu\text{m}$  layer thickness and 1.6 s exposure time at HI power, while the lowest achieved UTS was 4 MPa at 50  $\mu\text{m}$  layer thickness and 1.6 s at a LO LED power. The average error is around 1.7 MPa, with a standard deviation of 0.68 MPa. The maximum achieved storage modulus is 1250 MPa at 10  $\mu\text{m}$  layer thickness and 1.6 s exposure time at HI power, while the lowest achieved storage modulus was 860 MPa at 50  $\mu\text{m}$  layer thickness and 1.6 s at a low LED power. The average error is around 37 MPa with a standard deviation of 19.5 MPa. For the degree of monomer conversion, the maximum achieved degree is 0.84 at 10  $\mu\text{m}$  layer thickness and 1.6 s exposure time at HI power, while the lowest achieved UTS was 0.43 a 50  $\mu\text{m}$  layer thickness and 1.6 s at a low LED power.

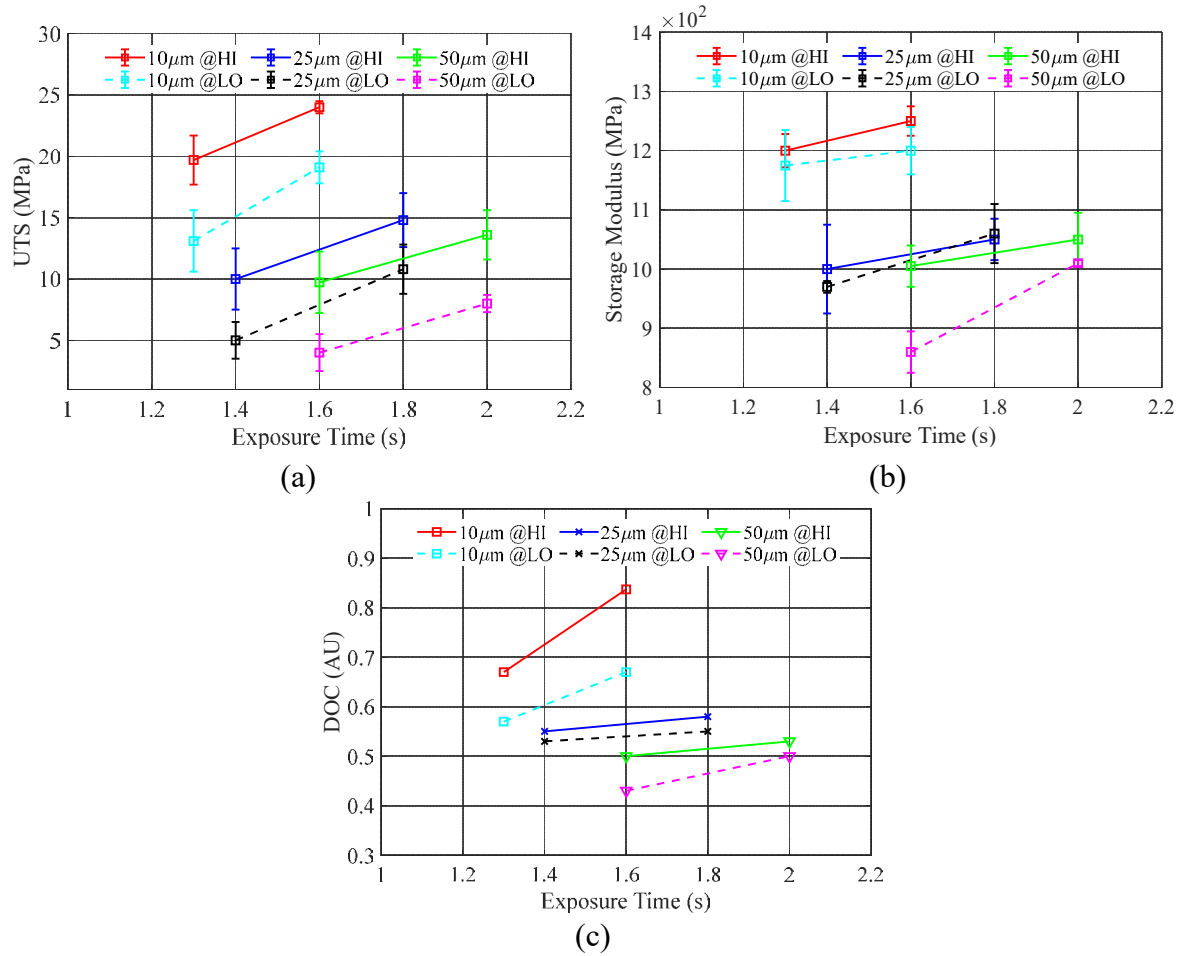


Figure 2-10 The effect of exposure time, layer thickness, and LED power on (a) Ultimate tensile strength, (b) Storage modulus, and (c) Degree of monomer conversion

During the tensile testing, the material showed a consistent brittle failure for all the tested specimens and their replicates, as shown in Figure 2-11 (a) and (b). The breakage is perfectly straight, with no signs of necking. The breakage happens to align with the edges of the micromirrors square array footprint on the specimen. The layers lines are visible in the cross-section of the 50  $\mu\text{m}$  layer thickness manufactured specimen as shown in Figure 2-11(c), while the cross-section of the 10  $\mu\text{m}$  layer thickness manufactured specimen, as shown in Figure 2-11(d), is almost seamless with no layers lines as it was not manufactured with the AM process.

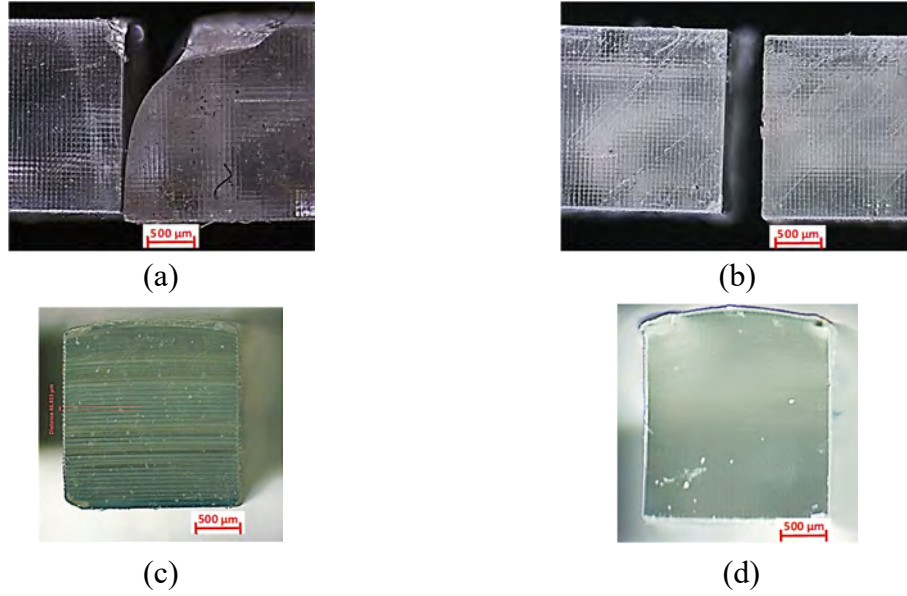


Figure 2-11 Brittle failure of the UTS specimen from the top view for (a) 50  $\mu\text{m}$  and (b) 10  $\mu\text{m}$  layer thickness, from the section view for (c) 50  $\mu\text{m}$  and (d) 10  $\mu\text{m}$  layer thickness

The accumulated energy per each layer  $E_T$ , calculated using the vertical energy accumulation model (2-5), is plotted against exposure time, layer thickness, and LED power, as shown in Figure 2-12(a). This plot shows the same trend as the material properties trend with the same process parameters, as shown in Figure 2-10, which indicates a significant relationship between them. The maximum calculated accumulated energy per layer equals to 140  $\text{mJ}/\text{cm}^2$  and achieved at 10  $\mu\text{m}$  layer thickness and 1.6 s exposure time at HI power while the lowest is 42  $\text{mJ}/\text{cm}^2$  at 50  $\mu\text{m}$  layer thickness and 1.6 s at a low LED power. By plotting the experimental results for any material property against the corresponding calculated accumulated energy per layer, two distinctive visible point sets are found where one of the point sets belong to the HI irradiance while the other set belongs to LO irradiance. These results suggest that for each irradiance level, there is a different trend line. Therefore, two different regression models are estimated for each LED power level per each material property. For the UTS and DOC, this separation is easily determined; however, for the storage modulus, it seems that one regression model for both power level is enough, as shown in Figure 2-12.

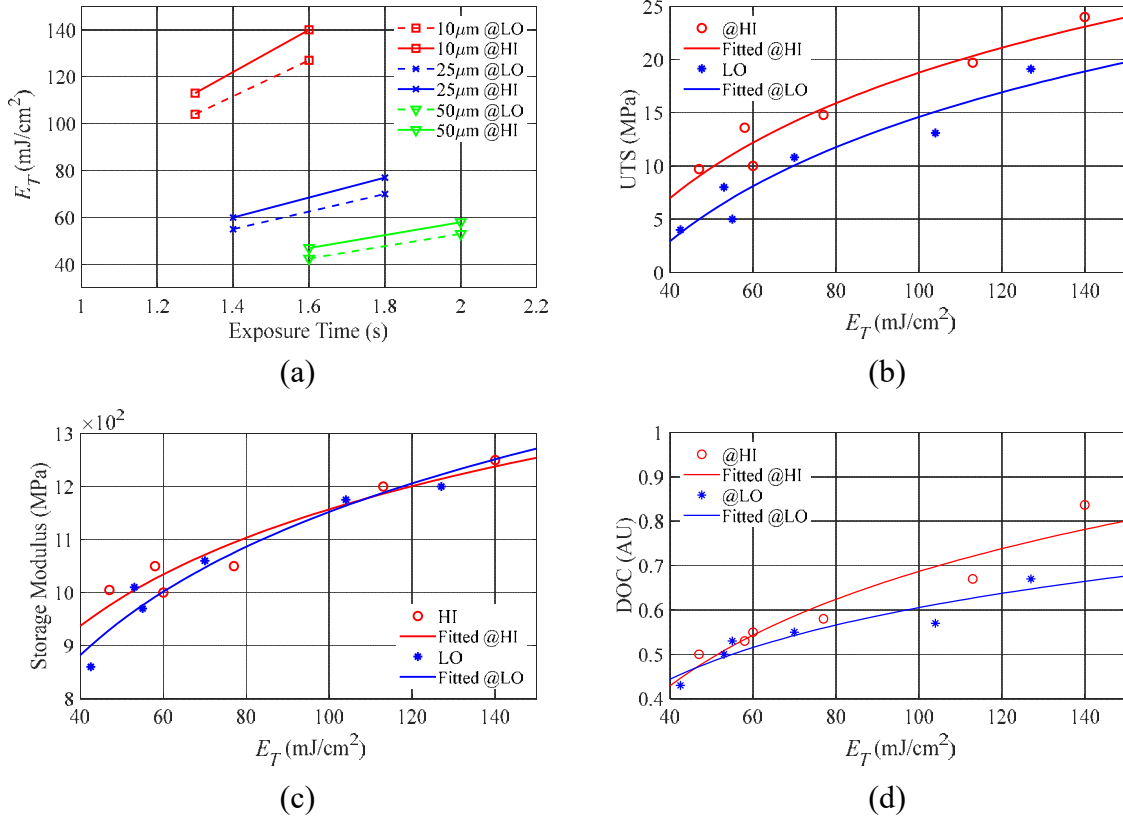


Figure 2-12 (a) Effect of exposure time and layer thickness on accumulated energy, Relation between accumulated energy per layer  $E_T$  and (b) Ultimate tensile strength, (c) Storage modulus, (d) DOC

The empirical regression model suggested is based on a logarithmic fitting resembling to the working curve model, and depicted by:

$$\gamma = C_1 \times \ln\left(\frac{E_T}{C_2}\right) \quad (2-15)$$

where  $\gamma$  is a general output variable for any material property and  $E_T$  is the calculated accumulated energy per layer (2-5), while  $C_1$  and  $C_2$  are the regression model constants. By analogy with the working curve equation (2-4),  $C_1$  will be the characteristic material property constant while  $C_2$  is the critical energy to for this property to start evolving. Using MATLAB least-squares fit function for nonlinear curves, the different constants for each material property were obtained and presented in Table 2-3. The average  $R^2$  for all the fitted model is around 0.9. The new defined critical energies can be used towards defining better optimization constraints other than the cured depth critical energy, which does not guarantee that the part will withstand the separation forces or even its weight during printing. By knowing the projected irradiance value, the exposure

time corresponding to the critical energy can be calculated and should be treated as the minimum bound for exposure time value.

Table 2-3 Constants values for material property regression model

Material Property ( $\gamma$ )	Constant	HI Power	LO Power
UTS (MPa)	$C_1$ (MPa)	12.86	12.7
	$C_2$ (mJ/cm <sup>2</sup> )	23.27	31
Storage Modulus (MPa)	$C_1$ (MPa)	240	294
	$C_2$ (mJ/cm <sup>2</sup> )	0.806	2
DOC (AU)	$C_1$ (AU)	0.281	0.176
	$C_2$ (mJ/cm <sup>2</sup> )	8.7	3.2

#### 2.4.4 Geometrical Features Characterization

The process parameters affect the size and the form of the different features in the artifact. Figure 2-13 shows some optical microscope images for different sizes of horizontal circular channels, vertical square channels, vertical square bars, and rectangular overhangs, manufactured at different curing schemes. Table 2-4 and Table 2-5 present all the measured dimensions for all the manufactured features per all the experimental configurations. The features that failed to be manufactured are denoted by the symbol ( $\times$ ).

For horizontal channels, the horizontal and vertical diameters were measured, with a noticeable oblong aspect ratio distortion in the manufactured geometry along the horizontal plane, as shown in Table 2-4. As the exposure time independently increases, the horizontal diameter of the channels decreases, as predicted by the horizontal curing model previously. Moreover, as the exposure time increases and the layer thickness decreases, the vertical diameter decreases. The minimum horizontal manufacturable channel was 350  $\mu\text{m}$  diameter, achievable only by using the 50  $\mu\text{m}$  layer thickness configuration. The channels with 200  $\mu\text{m}$  and 150  $\mu\text{m}$  diameters were not manufactured for any of the configurations. It was found that the channel with the 500  $\mu\text{m}$  diameter was not achieved within the 10  $\mu\text{m}$  layer thickness configuration. The 150  $\mu\text{m}$  and the 200  $\mu\text{m}$  channels are theoretically predicted to be manufacturable from the view of the horizontal curing model; however, from the accumulated energy vertical model, these channels are entirely within the IAZ, which make them infeasible. In the configurations with a layer thickness of 50  $\mu\text{m}$ , the staircase effect is visible, as shown in Figure 2-13. For the vertical bars, the minimum bar achieved was 100  $\mu\text{m}$ , but it was not stiff enough to stand vertically, and the bar was flexible to be bent

without getting broken. As the exposure time decreases, the dimension of the vertical bar also decreases, which was predicted by the horizontal curing model.

Table 2-4 Average measured horizontal (H) and vertical (V) diameters of the horizontal Channels and width of the vertical bars

$d_z$	#	Horizontal circular channels ( $\mu\text{m}$ )								Vertical square bars ( $\mu\text{m}$ )					
		750H	750V	650H	650V	500 H	500V	350H	350V	1000	750	500	250	200	150
50 $\mu\text{m}$	1	705	614	636	564	471	468	343	323	1022	769	509	261	200	×
	2	752	669	640	623	501	468	339	333	1034	776	503	240	175	×
	3	733	683	634	637	505	488	349	356	1017	773	505	257	199	138
	4	762	666	683	656	544	500	390	×	1002	748	474	229	×	×
25 $\mu\text{m}$	1	732	624	575	573	×	×	×	×	1055	796	519	263	220	×
	2	766	660	643	660	541	495	×	×	996	751	428	209	×	×
	3	665	665	602	588	×	×	×	×	1027	767	506	240	202	×
	4	667	671	613	584	472	443	×	×	1057	791	517	258	207	×
10 $\mu\text{m}$	1	747	626	681	586	×	×	×	×	979	726	409	×	×	×
	2	782	666	758	587	×	×	×	×	929	710	374	×	×	×
	3	738	646	663	584	×	×	×	×	993	749	450	×	×	×
	4	805	675	707	575	×	×	×	×	980	730	445	×	×	×

Table 2-5 Average measured width of the vertical square channels and the thickness of the overhangs

$d_z$	#	Vertical square channels ( $\mu\text{m}$ )						Over hangs ( $\mu\text{m}$ )							
		750	650	500	350	200	150	1000	750	500	250	200	150	100	
50 $\mu\text{m}$	1	775	666	511	362	201	127	1050	790	570	270	234	176	105	
	2	756	673	501	353	179	×	1038	787	554	263	226	129	83	
	3	784	676	511	345	200	142	1011	778	543	256	220	133	×	
	4	776	677	519	370	199	168	1002	775	533	249	208	132	60	
25 $\mu\text{m}$	1	778	657	501	296	×	×	1024	811	562	301	235	177	111	
	2	813	701	534	387	223	167	1091	787	544	268	246	177	90	
	3	777	689	527	361	196	125	1053	809	526	261	210	181	122	
	4	775	662	492	339	178	×	1074	821	557	260	200	120	×	
10 $\mu\text{m}$	1	866	738	577	406	×	×	1074	817	600	293	229	145	×	
	2	864	768	624	441	×	×	1060	805	583	286	216	×	×	
	3	833	706	555	357	×	×	1055	796	584	279	230	×	×	
	4	853	701	570	390	229	×	1081	822	525	264	177	×	×	



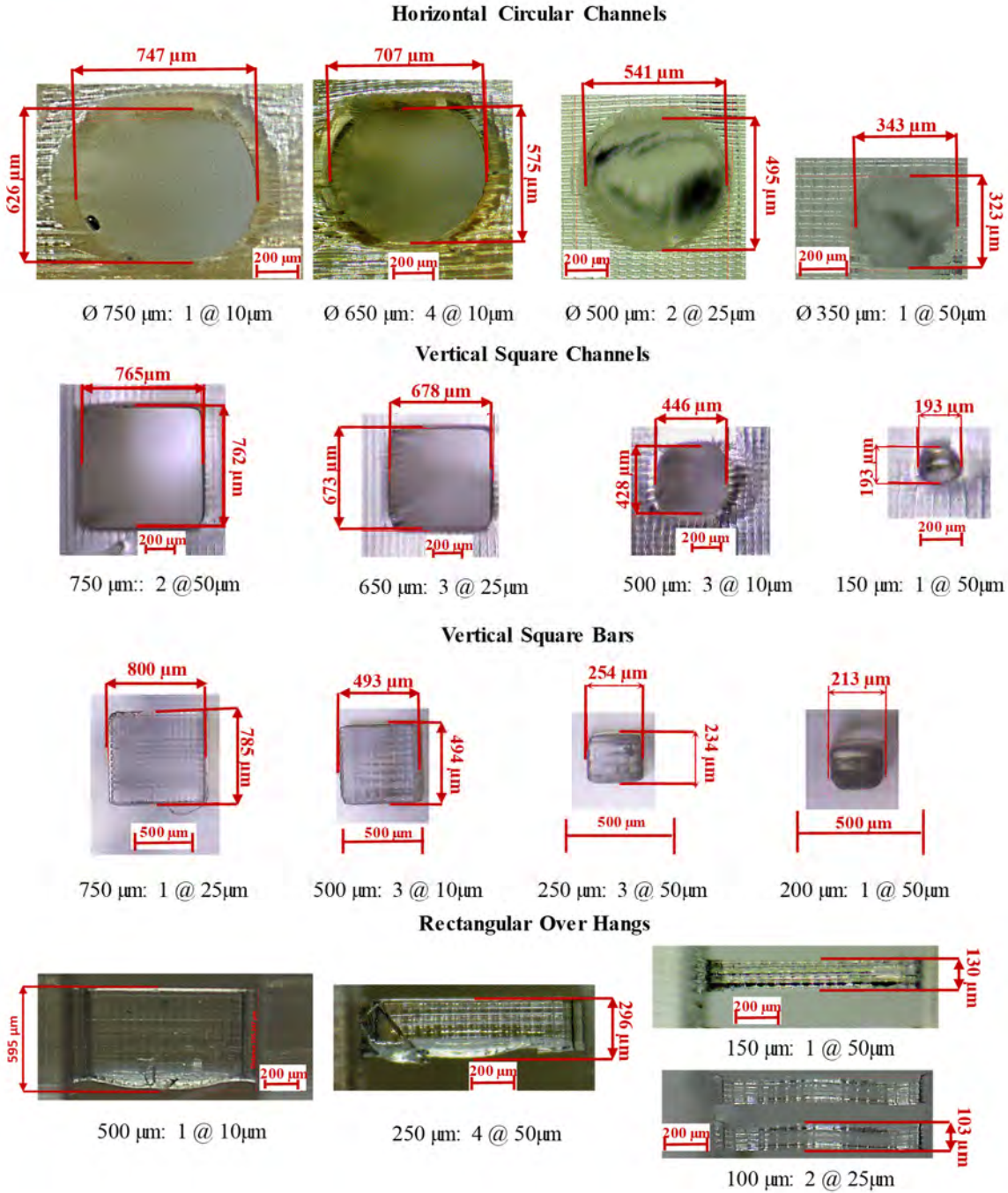


Figure 2-13 Selected optical microscope measurement images for different sizes of horizontal circular channels, vertical square channels, vertical square bars, and rectangular overhangs

The vertical square channels are more accurate and manufacturable compared to the horizontal channels. The minimum created channel was 150  $\mu\text{m}$  diameter and achieved within the 25 and 50  $\mu\text{m}$  layer thickness configurations but not within 10  $\mu\text{m}$  layer thickness ones, as shown in Table 2-5. It was found that as the exposure time decreases, the dimensions of the vertical

channels increase. The vertical channel dimensions depend mainly on the horizontal curing model as there is no projected irradiance from any layer within the channel gap, which makes the layer thickness not significantly affecting compared to the exposure time. Also, as the size of the channel decreases, its shape tends to be circular rather than a square as designed. For the overhang structures, the minimum size achieved was 100  $\mu\text{m}$  for both the 25 and 50  $\mu\text{m}$  layer thickness configurations but not for the 10  $\mu\text{m}$  layer thickness, as shown in Table 2-4. It was found that as the exposure time increases and the layer thickness decreases, the overhang thickness increases. An interesting phenomenon is shown in Figure 2-13 under the overhang section for configuration number 4 at 50  $\mu\text{m}$  layer thickness while manufacturing the 250  $\mu\text{m}$  over-hang, the first layer was weak and got torn during the separation. The reason for this phenomenon is that configuration 4 has the lowest exposure time and LED power for all experiments. The layer thickness and exposure time are the most significant parameters for both the horizontal channels and overhangs, while the exposure time is the most significant for vertical channels and bars. The LED power was the least significant parameter for all the features.

#### 2.4.5 Surface Roughness Results

The curing model presented earlier was used to evaluate the slope angle of the cured shapes simulated at different layer thickness and exposure time values. A total of 25 discrete points was evaluated and plotted against the process parameters, plotted as black asterisks, as shown in Figure 2-14(a). Then a polynomial surface fit, between the surface profile angle, layer thickness, and exposure time, was plotted in Figure 2-14(a) and is described by equation (2-16). By substituting equation (2-16) into equation (2-13), the average surface roughness is computed based on the values of the studied process parameters. Figure 2-14(b) depicts the relation between the average surface roughness of a vertical surface ( $\theta = 90^\circ$ ), layer thickness, and exposure time. The surface can be considered to be a linear surface than a nonlinear one. The highest predicted  $R_a$  is about 11 microns and is due to a  $25^\circ$  surface profile angle as a result of using 50 microns a layer thickness at 1.2 s exposure time. The lowest  $R_a$  is about 0.75 microns and has a  $7^\circ$  surface profile angle as a result of using 10 microns a layer thickness at 2 s exposure time.

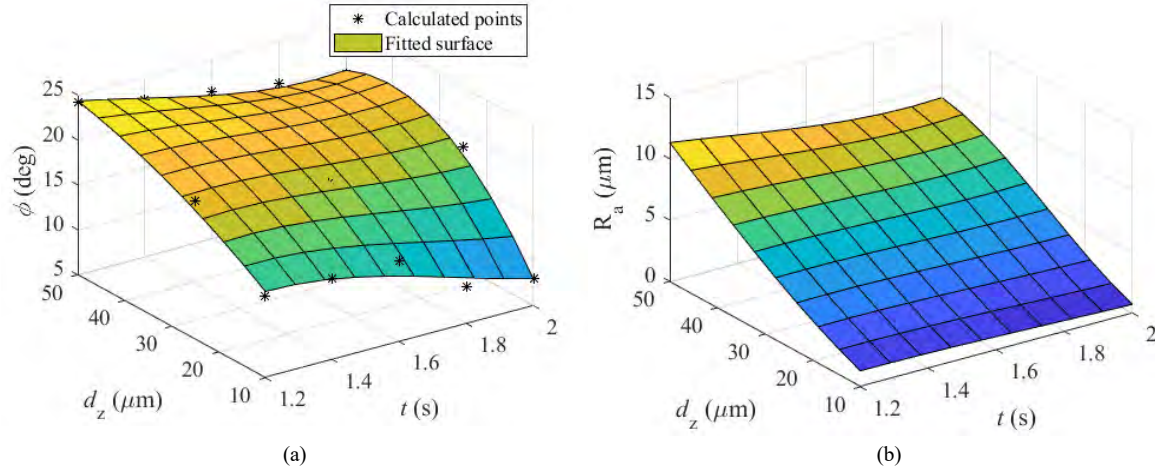


Figure 2-14 (a) A fitted surface plot representing the relation between surface profile angle, exposure time, and layer thickness, (b) a surface plot showing the predicted relation between average surface roughness, exposure time, and layer thickness

$$\phi = 11.4 \times t^3 - 64.5 \times t^2 + 0.33 \times t^2 \times d_z + 0.013 \times d_z^2 - 0.013 \times d_z^2 \cdot t - 0.18 \times t \times d_z + 101 \times t + 0.16 \times d_z - 37.38 \quad (2-16)$$

Some selected confocal microscope scanned images are presented in Figure 2-15(a), (b), and (c), which correspond to 50, 25, and 10 microns layer thickness, respectively. The images show a visible and easily recognizable pattern in both  $x$  and  $z$  directions. The pattern in the  $z$  direction, which is the perpendicular direction to the layers' surface, varies in their wavelength with the variation of the layer thickness value. While the surface profile wavelength in the  $x$  direction seems to be independent of the layer thickness. The scanned surface was converted into 3D surface plots. Figure 2-15(d), (e), and (f) present the surface plots corresponding to 50, 25, and 10 microns layer thickness, respectively. The presented surface plots are a small part cropped from the full surface to allow for a better illustration of the surface profile. The surface plots confirm that there are two primary lay directions, the  $x$  and the  $z$  axes, with a periodic surface profile in both directions.

Selected sections in the  $z$  direction from each specimen are presented in Figure 2-15(g), (h), and (i). Each figure represents a certain layer thickness at two different exposure times, where Figure 2-15(g), (h), and (i) correspond to 50, 25, and 10 microns layer thickness, respectively. The mean of each surface profile was vertically shifted to align with the zero on the surface profile axis of each plot to facilitate the comparison between the different profiles. The surface profiles in the  $z$  direction manufactured with 25 and 50 microns layer thickness values show a periodic behaviour

with a wavelength close to the layer thickness value; however, the profiles manufactured at 10 microns show more of a random profile. The peak to valley distance decrease as the layer thickness value decrease. The exposure time seems to have no significant effect on the surface profile. Three sections at equally spaced locations were studied per each lay direction per each specimen. For each section, the measured parameters are as follow:

- $R_a$ : The summation of the peaks and valleys areas divided by the evaluation length.
- $R_z$ : The average of the successive values of the maximum vertical distance peak to valley distances within a sample length calculated over the evaluation length.
- $R_{sm}$ : The mean value of the spacing between profile irregularities within the evaluation length.
- $R_{sk}$ : The measure of the asymmetry of the profile about the mean line calculated over the evaluation length.

Table 2-6 Average experimental measurements versus predicted results surface roughness in the  $z$  direction

$d_z$ ( $\mu\text{m}$ )	$t$ (s)	Measurements				Prediction			Error	
		$R_a$ ( $\mu\text{m}$ )	$R_z$ ( $\mu\text{m}$ )	$R_{sm}$ ( $\mu\text{m}$ )	$R_{sk}$	$\phi$ ( $^\circ$ )	$R_a$ ( $\mu\text{m}$ )	$\phi$ ( $^\circ$ )	$R_a$ (%)	$\phi$ (%)
10	1.2	1.8	10.4	16.8	0.3	13.0	1.3	14.6	27.8	12.3
	1.6	1.5	9.7	15.9	0.4	12.0	1.1	14.0	25.7	16.7
25	1.4	2.8	12.5	24.2	0.3	22.0	3.9	18.9	37.3	14.1
	1.8	2.4	10.0	25.3	0.1	17.0	3.3	17.2	40.4	1.4
50	1.6	6.4	21.9	47.4	0.2	24.0	9.2	20.6	43.8	14.2
	2.0	5.9	18.7	49.4	0.1	17.0	8.6	19.0	45.8	11.8

Table 2-6 shows the average of the measured values, the predicted values of  $R_a$  and  $\phi$ , and the error between the measured and the predicted values. The  $R_a$ , the  $R_z$ , the  $R_{sm}$ , and the  $\phi$  increase as the layer thickness value increases while decrease with the increase of the exposure time within the same layer thickness value. The predicted  $R_a$ ,  $\phi$  values follow the same trend as the corresponding experimental values. The  $R_{sm}$  values is close to the layer thickness values in both the 25 and 50 microns layer thickness; however, in the 10 microns layer thickness, the value significantly deviates. The  $R_{sk}$  values are above zero for all the specimens and decrease as the layer thickness value increase. The layer thickness significantly influences the surface roughness parameters compared to the exposure time values selected for this experiment.



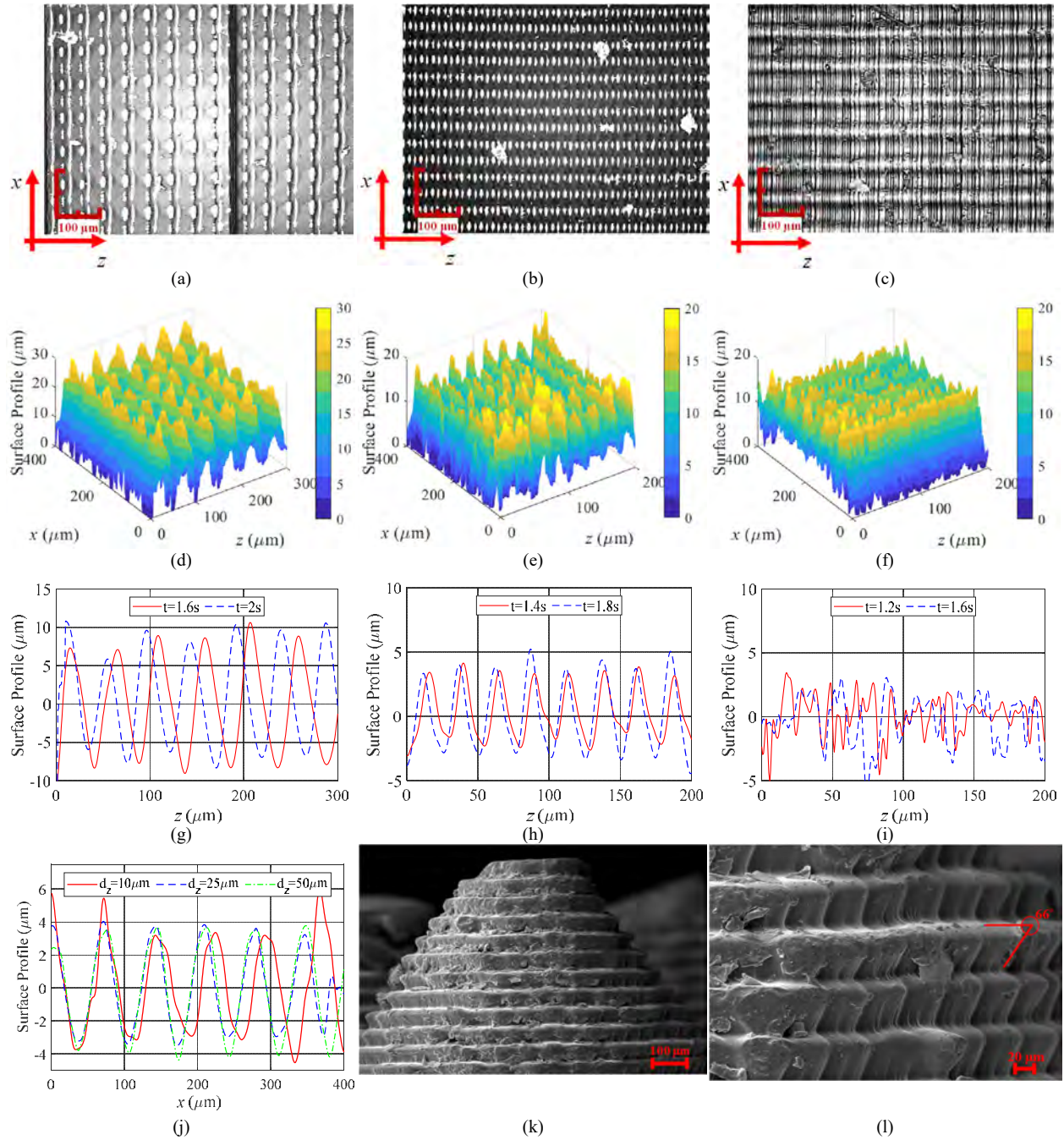


Figure 2-15 (a), (b), and (c) are confocal microscopy images for surfaces built at layer thickness values of 50, 25, and 10  $\mu\text{m}$  respectively; (d), (e), and (f) are a 3D rendering of the confocal microscope scanning corresponding to layer thickness values of 50, 25, and 10  $\mu\text{m}$ . respectively; (g), (h), and (i) are 2D plots of surface profile in the lay in the z direction at layer thickness values of 50, 25, and 10  $\mu\text{m}$ . respectively; (j) 2D plot of a section of surface profile in the lay in the x direction at different layer thickness values; (k) SEM image of a conical shape build with 50 microns layer thickness; (l) Close up SEM image of 4 layers showing the surface profile angle

The predicted values of  $\phi$  match the measured values with an average error of 14% with a maximum of 16.7% and a minimum of 1.4%. The  $R_a$  values deviated from the measured values by an average error of 37% with a maximum of 45.8% and a minimum of 25.7%. In order to put the error values in perspective, it is worth mentioning that the maximum deviation error of the  $R_a$  is equivalent to an error of 2.7 microns.

The measured layer thickness values were found to deviate from the nominal value from one layer to another. For the 50 microns nominal layer thickness, the error was found to be of +0/-3 microns. In comparison, for the 25 microns nominal layer thickness, the error was found to be +2/-2 microns, and for the 10 microns nominal layer thickness, the error was found to +4/-0 microns. The variation in the layer thickness values was used to recalculate the average surface roughness values, but the prediction error was not significantly improved. The authors' hypothesis for the error between the predicted model and the measured data is that there is further polymerization happens near the valleys' vertices which results in filleted valleys instead of the sharp-angled ones as shown in Figure 2-15(l); contrary to the model proposed in Figure 2-3(c).

Selected sections in the surfaces, along the  $x$  direction, of parts manufactured at different layer thickness values, are presented in Figure 2-15(j). The surface roughness profile in the  $x$  direction shows a particular trend with disregard to the layer thickness value and exposure time. The average measured surface roughness parameters are presented in Table 2-7. The average  $R_a$  value is approximately 2.4 microns, and it did not significantly vary by changing the process parameters. The average  $R_z$  is 7.8 microns and slightly decrease with the increase of the layer thickness values. The variation in the average values of both the  $R_a$  and the  $R_z$  from one specimen to another is very close to the vertical stepping resolution of the confocal microscope. The average  $R_{sm}$  is around 70 microns and its value decreases as the layer thickness value increases. The average  $R_{sk}$  is 0.17 and the value decrease with the increase of layer thickness. The authors' hypothesis for the surface profile in the  $x$  direction is due to the 45° diamond orientation of the micromirrors in the DMD [37].

Table 2-7 Average experimental measurements of surface roughness in  $x$  the direction at different layer thickness values

$d_z (\mu m)$	$R_a (\mu m)$	$R_z (\mu m)$	$R_{sm} (\mu m)$	$R_{sk}$
10	2.4	8.6	74	0.2
25	2.2	7.8	69.8	0.17
50	2.4	7.1	67.5	0.1

To further confirm the different lay direction and to visualize the surface profile angle, a 2×2 mm cone was manufactured with 50 microns layer thickness at 2 seconds exposure time. The specimen was scanned using the SEM, and the result is shown in Figure 2-15(k) and l. The complementary angle of the surface profile angle is more direct to measure. The complementary angle is 66°, which gives a surface profile angle of 24°, which aligns with the previous measurements for the same process parameters. A periodic surface profile is visible in the direction going into the image, the *x* direction.

## 2.5 Conclusion

This chapter provides a comprehensive analytical and experimental investigation on the projection stereolithography additive manufacturing process. It studies the effect of the process parameters, namely, the layer thickness, the exposure time, and the LED power on the ultimate tensile strength, storage modulus, degree of monomer conversion, and different micro geometrical features. A novel multilayer vertical energy accumulation model is presented, which considers the difference between the light absorbance through the liquid prepolymer resin and the solid cured polymer. This model is used to explain why a part manufactured with 10 μm layer thickness has double or more the strength, the storage modulus, or the degree of monomer conversion of a part of 50 μm layer thickness for the same exposure time and LED power. An original terminology called the Irradiance affected zone (IAZ) is introduced, which defines the number of layers affected by the projected irradiance for particular exposure time and is a function of the process parameters and the material working curve constants. The IAZ sets a limit on the number of layers considered in calculating the accumulated energy for each of the previously cured layers and also defines the minimum feasible size of horizontal channels to be manufactured for a specific material at a process parameters. A horizontal curing model is discussed and used to assess the minimum feasible size for different geometrical results and also to show that as the exposure time increases, the diameters of the channels decrease, and the diameters of solid bars increase.

Using the Curing models developed a surface roughness model is developed as function of the layer thickness and the exposure time. The prediction results were compared to the experimental results obtained from parts manufactured with a different combination of process parameters. The surface profile angle was predicted with a maximum error of 2° and the average surface roughness was predicted with an error of 2.7 microns.

An innovative experimental methodology to evaluate the constants of the working curve for the multi-layer curing model is presented. The results show that LED power affects the cured depth for the same exposure time. Also, the light penetration through a liquid prepolymer was found to be higher than through a cured polymer, which explains the necessity to consider these differences in the accumulated energy model. The machine irradiance was characterized, and it was found that the P $\mu$ SLA have significant irradiance irregularities. To minimize the effect of the irradiance irregularities on the measured responses, a distinct region on the build area with tolerable irradiance difference was used strictly to manufacture all the test specimens. For the material properties, the layer thickness was found to be the most significant parameter controlling the process outcomes followed by the exposure time then the LED power was the least significant process parameter. It is crucial to select the proper process parameter to achieve the geometrical dimensions required while having enough green strength for the part to hold self against its weight, separation force, and post-processing. A generic empirical logarithmic regression is proposed to predict the different material properties based on the process parameters and the material working curve constants, represented by the accumulated energy. The proposed model facilitates the development of prediction models based on simple experimental procedures. Due to the analogy of this model to the working curve equation, it can define the critical amount of energy required to start developing the different material properties.

A geometry artifact was designed to study the effect of the process parameters on various features of different sizes. It was found that horizontal channels smaller than the irradiance affected zone will not be feasible physically to be manufactured. The layer thickness and exposure time are the most significant parameters for both the horizontal channels and overhangs, while the exposure time is the most significant for vertical channels and bars. The LED power was the least significant parameter for all the features.

The results of this chapter can be used towards the general optimization of the process in terms of geometry, speeding up the process by decreasing the exposure time without harming the strength. It also can be used towards estimating an initial solution for dedicated geometry optimization algorithms.



### **3 Assessment of Irradiance Map Non-Uniformity across Build Platform<sup>\*</sup>**

One of the required decisions in preprocessing is selecting the location of the part on the build platform as the geometrical accuracy of the manufactured part is influenced by the location on the build platform. This issue is due to the intrinsic characteristics of the used additive machine and is considered as a process noise. In the case of projection stereolithography, this noise is directly correlated to the projection irradiance map irregularities, which can be due to the manufacturing of the micromirrors or light source irradiance profile. This chapter is inspired by “You cannot control/improve what you cannot measure”. In the first part of this chapter, the irradiance profile projected from individual micromirrors is imaged and analyzed, and the irradiance map non-uniformity is quantified using a novel proposed irradiance-induced fluorescence imaging technique. The first part of the chapter answers the thesis question by investigating one of the significant reasons why the as build part is different from the as designed part; namely irradiance non-uniformity across the build platform. While the second part of this chapter investigates experimentally the effect of irradiance map / part location on the dimensional accuracy while varying the exposure time, layer thickness, and the gray scale value of shape boundary pixels in the projected images. The results obtained in this chapter are the inputs to geometry simulation and optimization algorithms discussed in the next chapter.

#### **3.1 Introduction**

There are several imaging-based measurement setups and methodologies for the projection stereolithography (PSLA) documented in the literature, as shown in Table 3-1. The main characteristics to assess the practicality of each of the methodologies studied in the literature are the following:

1. The camera type and its resolution
2. The projected size of the micromirror
3. The lens and optical filters,

---

<sup>\*</sup> Part of this chapter is published in. “Mostafa, K., Qureshi, A. J., and Montemagno, C., 2017, “Tolerance control using subvoxel gray-scale dlp 3D printing,” Proceedings of the ASME 2017 International Mechanical Engineering Congress and Exposition. Volume 2: Advanced Manufacturing, ASME, Tampa, Florida, USA, p. V002T02A035.”.

4. The projection plane medium
5. The overall measurement resolution,
6. The measurement Calibration methods
7. The objective of the measurement method.

Table 3-1 Summary of the current state of the art in PSLA irradiance measurement

#	Year	Projector Resolution ( $\mu\text{m}$ )	Camera Type	Camera Resolution (Mega Pixels)	Lens	Medium	Filter	Measurement Resolution ( $\mu\text{m}/\text{pixel}$ )	Calibration	Ref
1	09	265	CMOS ProScope	1.3	50X	Paper	N/A*	N/A	Irradiance	[83]
2	12	1.3	CCD	N/A	6:1	Resin	N/A	N/A	N/A	[51]
3	18	50	Machine vision CMOS	N/A	N/A	N/A	UV	N/A	N/A	[52]
4	18	50	CMOS Nikon D810	35.9	N/A	Resin	N/A	4	N/A	[61]
5	20	21.6	Sony CCD with UV sensor	1.4	1:1	Substrate	N/A	5.4	N/A	[84]
6	21	N/A	CCD	1.9	N/A	Paper	N/A	N/A	N/A	[85]

\*N/A means either the component was not used or authors did not provide enough information about it in their manuscript

Zhou et al. proposed a measurement system to measure the geometry and intensity of the projected irradiance from one micromirror [83]. The theoretical projection of one micromirror at the projection plane is 265 microns. The setup consists of ProScope HR digital microscope device while using white paper as a projection medium. The system has an integrated 50X lens and does not have any optical lens or filters. A proposed methodology to calibrate the system using a generic photo-sensor to correlate the captured coloured image to the irradiance value. It was shown that the projected irradiance from on micromirror has a Gaussian profile with an elliptical base.

Zheng et al. proposed an overall irradiance map measurement system implemented in a bottom-down PSLA layout [51]. The theoretical projection of one micromirror at the projection plane is 1.3 microns. The setup consists of a charge-coupled device (CCD) based camera and a resin medium as a reflection surface. The camera's field of view is set to cover the whole build platform measure the overall irradiance from the resin surface. The acquired measurements input the projection normalization algorithm to minimize the irradiance difference across the build platform. There is no correlation between the pixel reading and the irradiance value, and the normalization is based on the captured image intensity.

Warburg et al. used a complementary metal-oxide-semiconductor (CMOS) based camera equipped with a UV filter and looking towards the projection plane [52]. The objective of this setup is to capture the irradiance map non-uniformity. There was no further detail provided regarding the camera resolution, lens, or medium.

Kowsari et al. used a high-resolution Nikon CMOS Camera and captured the irradiance projected through the used resin medium [61]. The used system is not equipped with any optical filters. The overall measurement resolution is 4 microns/pixel. The experiment has assessed the profile of the projected irradiance from one micromirror and 10×10 micromirrors. The irradiance profile was approximated to a conical shape.

Emami et al. used a CCD camera with an ultraviolet wavelength sensitive sensor with a 1:1 magnification lens and without optical filters [84]. The system's overall resolution is 5.4  $\mu\text{m}$ /pixel. The objective of the measurement is to assess the irradiance profile at different planes away from the projection focal plane. There was no irradiance calibration, and a normalized intensity was adopted. The irradiance profile was assumed to be a Gaussian profile. The intensity decreased as the imaging plane was far from the focal projection plan and the Gaussian radius increased. Deng et al. used a CCD camera to capture the Gaussian profile projected through a paper medium [85]. The irradiance was normalized, and no calibration methods were used.

It is worth mentioning that all of the studies analyzing the irradiance map non-uniformity did not test the effect of the irradiance map non-uniformity on the geometrical deviations. Based on the literature review on the irradiance measurement methods, several research gaps are identified. One of the major concerns is the projection medium, whether it is paper or resin. Using paper as a projection medium will not give an accurate profile measurement and irradiance map non-uniformity since paper sheets have an intrinsic paper texture. The projected irradiance on paper is distorted with an ellipse shape due to reflection and refraction, and the paper density itself might not be uniform. Using resin as a projection medium will not produce same irradiance over time as it contains several molecules that absorb the projected irradiance, like photo-initiator and phot-blocker; therefore, the projected irradiance from the resin is not equal original projected one from the micromirror array. The photobleaching phenomena affect the irradiance projected from the resin, and the value will increase as the photoinitiator breaks after absorbing a certain amount of irradiance (critical energy).

Cameras normally are not sensitive to the Ultra-violet (UV) and near UV wavelength, and their quantum efficiency is low compared to the wavelength between 500 and 700 nm. Therefore, looking directly at the projected irradiance, the camera will capture the curing wavelength, usually around 360 to 405 nm, poorly while the other non-curing wavelengths with a strong signal in case of using a lamp as the light source. The same goes for using a UV filter which rejects the curing range of the emitted light.

The last concern is measurement system calibration which is crucial to establish confidence in the acquired results. Cameras are not calibrated for irradiance measurement because it is not their primary purpose; therefore, each light receptor on the camera does not respond to light similarly, requiring calibration. The lens adds a vignette effect on the captured image due to high zoom values and low aperture value, which cause the measured irradiance value to decrease as it moves away from the image center. Calibrating the pixel to physical distance using calibration targets to ensure the profile geometric measurements are correct.

In the first part of the chapter, a novel irradiance measurement method is proposed to overcome the literature gaps identified. This method is inspired by the laser-induced fluorescence technique used in particle imaging velocimetry (PIV) [86]. A fluorescent dye is used as a projection medium in which it absorbs the near UV projected light and emits a corresponding wavelength that the camera can capture with high quantum efficiency. The filter usage eliminates two of the major concerns related to mediums and filters. A multi-step rigorous calibration is proposed to ensure that the camera sensor is calibrated for irradiance measurement, the vignette is removed, and physical measurements are reliable. The measurements acquired in this part will be used in the next chapter to develop a geometry simulation algorithm. The second part of the chapter investigates the effect of irradiance map non-uniformity of the dimensions. The irradiance map non-uniformity is tested at different process parameters like exposure time, layer thickness, and grayscale pixel blending. This chapter sheds light on one of the reasons why the as build part is different from the as-designed part as a result of irradiance non-uniformity, which is the main research question of this thesis.

## 3.2 Irradiance Map Characterization

### 3.2.1 System Components and Operation

The measurement system's different components are shown in Figure 3-1. The projection stereolithography (PSLA) manufacturing platform used is Ember 3D printer (1) from Autodesk, USA, which is described in detail previously in section 2.3.2. A monochrome camera TM-4200 GE, Jai, Denmark, (2) with an 8-bit color depth and 2048×2048 pixels resolution. The camera is equipped with a macro TV zoom lens, Navitar, Japan (3) with up to 6X magnification power. The lens has a 500 nm long-pass filter (4) from ThorLabs, USA. The whole camera assembly is assembled on a 3D printed bracket mounted on a vertical traverse (5) attached to the vertical aluminum frame. On the aluminum frame below the camera assembly, the flow cell assembly is mounted. The flow cell assembly consists of an in-line flow cell 45-Q-0.1 (6) from Starna, USA, with a path thickness of 100  $\mu\text{m}$ , a width of 10 mm, and a length of 40 mm. the flow cell is securely mounted on by a 3D printed bracket (7) and rubber cushions. For its superior solvent resistance, the flow cell's inlet and outlet ports are connected to a Viton tubing from Cole-Parmer, USA. The flow cell is located over the projection window (8) of the Ember 3D printer (1). The Viton tubing passes through MasterFlex L/S peristaltic pump (9) from Cole-Parmer, USA, then both ends of the tubing end in the glass container (10) of the zinc-octa-ethyl-porphyrin (ZnOEP) fluorescent dye from Sigma Aldrich, USA. The dye container is covered by silver duct tape to prevent room light from affecting the dye.

The ZnOEP in DCM solution absorbs the 405 nm wavelength and emits light at 570 nm and 620 nm, as shown in . The ZnOEP is mixed with DCM at a concentration of 5 mg/l [87]. The peristaltic pump circulates the dye solution at a flow rate of 15 ml/min. The dye circulation prevents the dye from absorbing enough energy to break down the dye molecules; however, increasing the flow rate will cause a shadow of the projected pattern shape in the flow directions, especially with long camera shutter times.



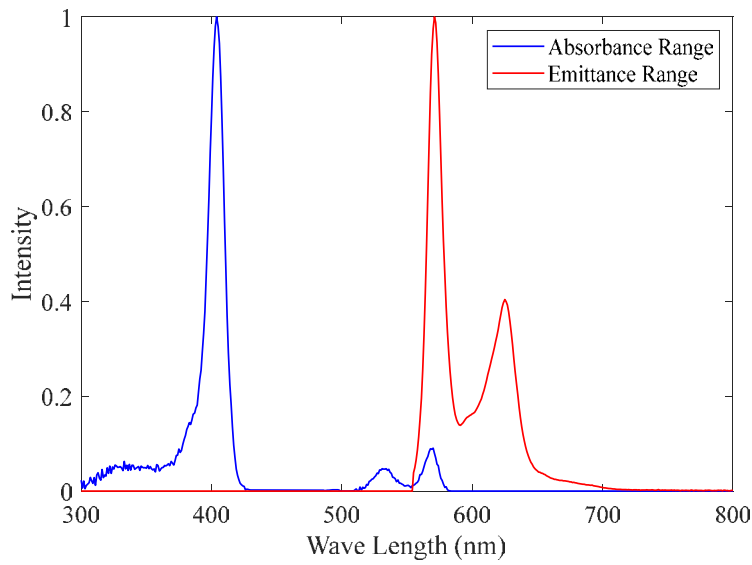


Figure 3-2 Absorption and emission spectrum of ZnOEP dissolved in DCM

### 3.2.2 Calibration Methodology

The calibration methodology consists of four main stages, as shown in Figure 3-3. The calibration methodology ensures that the acquired measurements are reliable and have high confidence. The four stages are

1. Dimensions calibration
2. Camera calibration
3. AM machine irradiance calibration
4. Camera VS AM machine irradiance

The first stage is correlating the physical dimensions with the captured image pixels by using microscale targets. After adjusting the zoom and focus of the lens, different microscale targets are captured, as shown in Figure 3-4. The first target has a 20  $\mu\text{m}$  line width, and the second target has a 10  $\mu\text{m}$  line width. By analyzing the captured images, it was found that the overall system resolution is 3  $\mu\text{m}/\text{pixel}$  with both targets

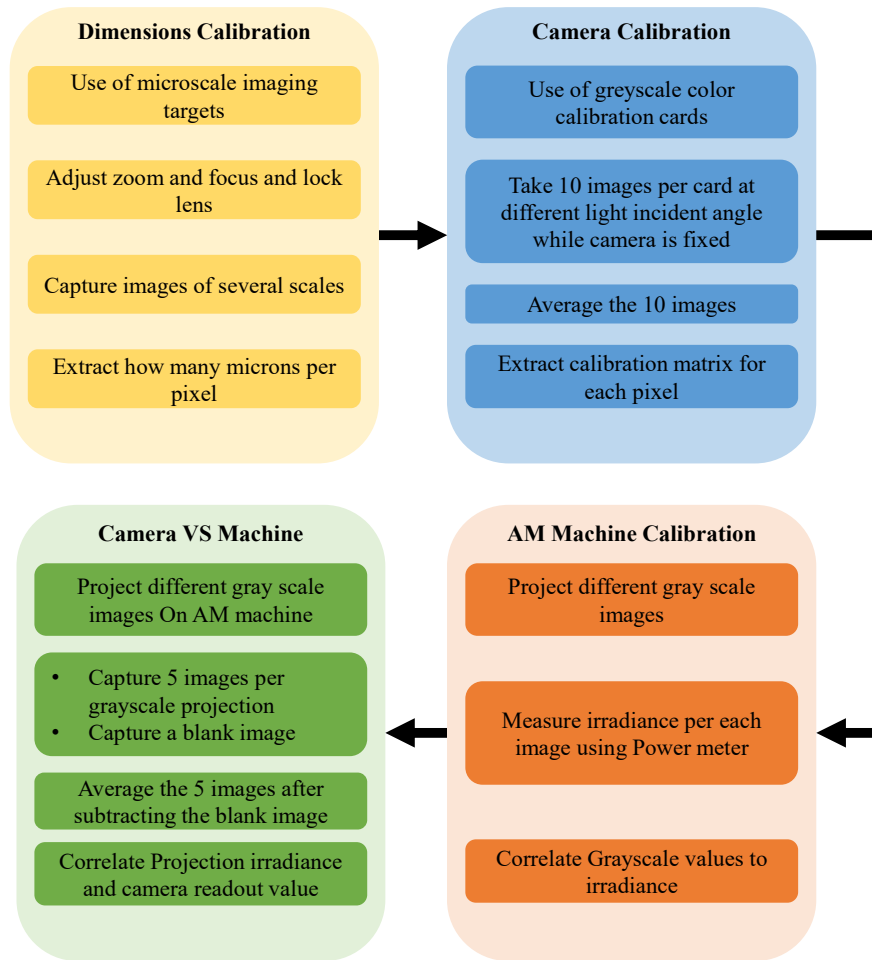


Figure 3-3 Irradiance characterization calibration methodology

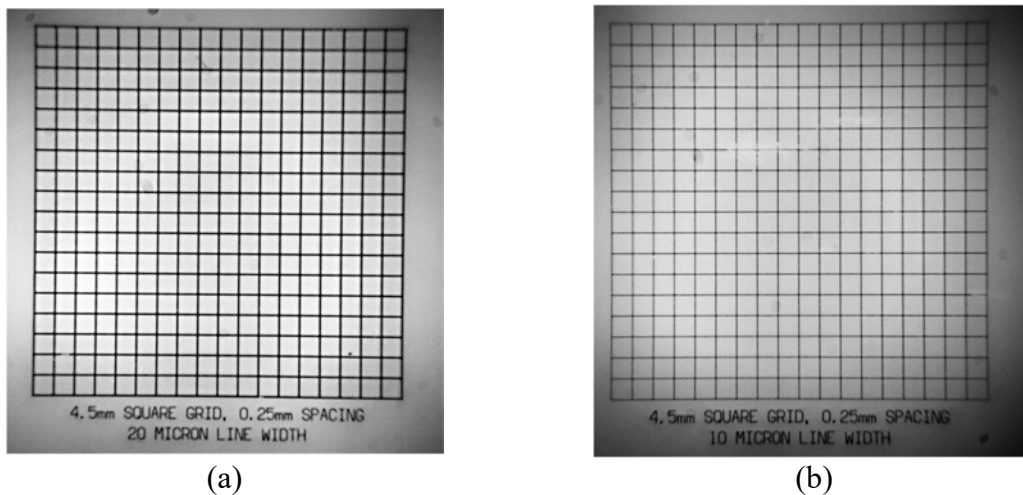


Figure 3-4 Captured image of the micro-scale targets of 4.5mm square grid and 0.25 mm spacing at the maximum zoom of the lens, (a) 20-micron line width and (b) 10-micron line width



The second stage is to ensure that the camera is calibrated so that each light receptor in the CCD sensor will respond to the light in the same behaviour and ensure that the lens vignette effect is minimized. White, grey (60%) and black nonglossy colour calibration cards were used in this calibration stage. The aperture value is adjusted so that the maximum irradiance projected from the AM machine will achieve 70% of the color depth and will not saturate the captured image. With the 8-bit color depth images the irradiance measurement resolution of the used setup is 0.15 mW/cm<sup>2</sup>. After the card is placed below the camera, a handheld white ring lamp is used to illuminate the cards. A total of ten images per card is captured, and for each image, the light incident angle and orientation are changed to cover 360° around the card, and one position is in line with the camera direction. The mean of the ten captured images per card is computed. Calibration matrices are obtained based on a linear regression between the captured image and the expected average greyscale value using equation (3-1).

$$G_{ij} = (P_{ij} - B_{ij}) \times a_{ij} + b_{ij} \quad (3-1)$$

where  $G_{ij}$  is the expected average grayscale value for each pixel in the captured image and  $i$  and  $j$  is the position index of the pixel in the image.,  $P_{ij}$  is the averaged captured image of each card,  $B_{ij}$  is the background noise of the camera without light, and  $a_{ij}$  &  $b_{ij}$  are the linear regression coefficient and constant, respectively.

The third stage is calibrating the irradiance value of the Ember 3D printer. The procedure used in this stage is similar to the procedure discussed previously in 2.3.3. The only difference is that the measurement is done directly on the projection window and not on the PDMS window. All of the measurements are taken at the center of the projection window. The projection pattern is a 10×10 mm square and projected at different irradiance levels defined the machine settings. A linear regression (3-2) correlated the normalized irradiance settings and the corresponding measured irradiance. The results from this stage are presented in Figure 3-6 (a).

$$I_p = I_s \times a_s + b_s \quad (3-2)$$

where  $I_p$  the average is projected irradiance,  $I_s$  is the normalized irradiance value in the machine settings, and  $a_s$  &  $b_s$  are the regression coefficients.

The last stage captures the same projected patterns in the third stage using the flow cell and camera assembly while the fluorescent dye flows through the flow cell. Five images were captured

per each projected pattern and then averaged. The grayscale value in the captured image is correlated to the projected irradiance value using linear regression as presented in (3-3). The evaluated relation is shown in Figure 3-5 (b).

$$I_{fij} = I_{p_{ij}} \times a_{f_{ij}} + b_{f_{ij}} \quad (3-3)$$

where  $I_{f_{ij}}$  is the fluorescence irradiance emitted from the flow cell,  $I_{p_{ij}}$  is the projected irradiance from the Ember 3D printer,  $a_{f_{ij}}$  &  $b_{f_{ij}}$  are the regression coefficients.

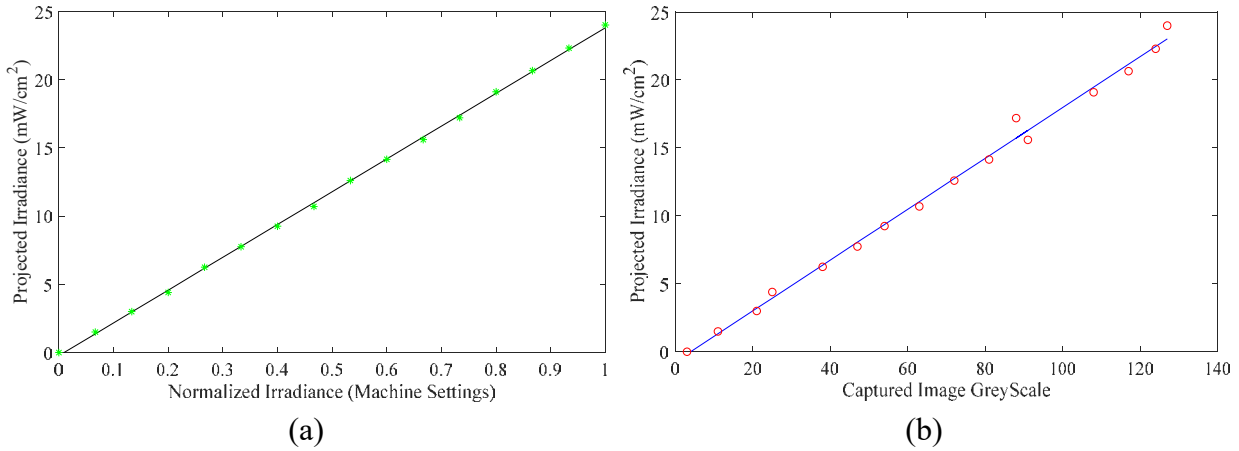


Figure 3-5 Correlation between (a) Machine projected irradiance and normalized irradiance setting, and (b) projected irradiance and the captured image grayscale value

### 3.2.3 Results

#### 3.2.3.1 Micromirror irradiance profile

In order to characterize the irradiance profile projected from micromirrors, a pattern with one micromirror was set on (white pixel), and the seven subsequent micromirrors were set off (black pixels). The pattern was repeated periodically in both directions. The pattern spacing eliminates the interactions between the neighbouring micromirrors; therefore, the camera captures the micromirror's true profile while minimizing the superposition between neighbouring micromirrors. The pattern occupies a total of 5×5 mm square, and the average captured image is shown in Figure 3-6 (a). The captured pattern was projected in the center of the projection window.

The processed captured image is shown in Figure 3-6 (b) after implementing the calibration methods discussed in section 0Error! Reference source not found.. Three sections were taken

along the  $x$ -axis and  $y$ -axis at several locations as annotated in Figure 3-6 (b) and the profiles at those sections are shown Figure 3-6 (c) and (d). It is noticed that the micromirrors' peak irradiance ( $I_m$ ) varies based on the micromirror position. The average peak irradiance was found per micromirror was found to be  $2.8 \text{ mW/cm}^2$  with a maximum of  $3.25 \text{ mW/cm}^2$  and a minimum of  $1.45 \text{ mW/cm}^2$ . The pitch between any two consecutive micromirrors projections is between  $48$  to  $51 \mu\text{m}$ .

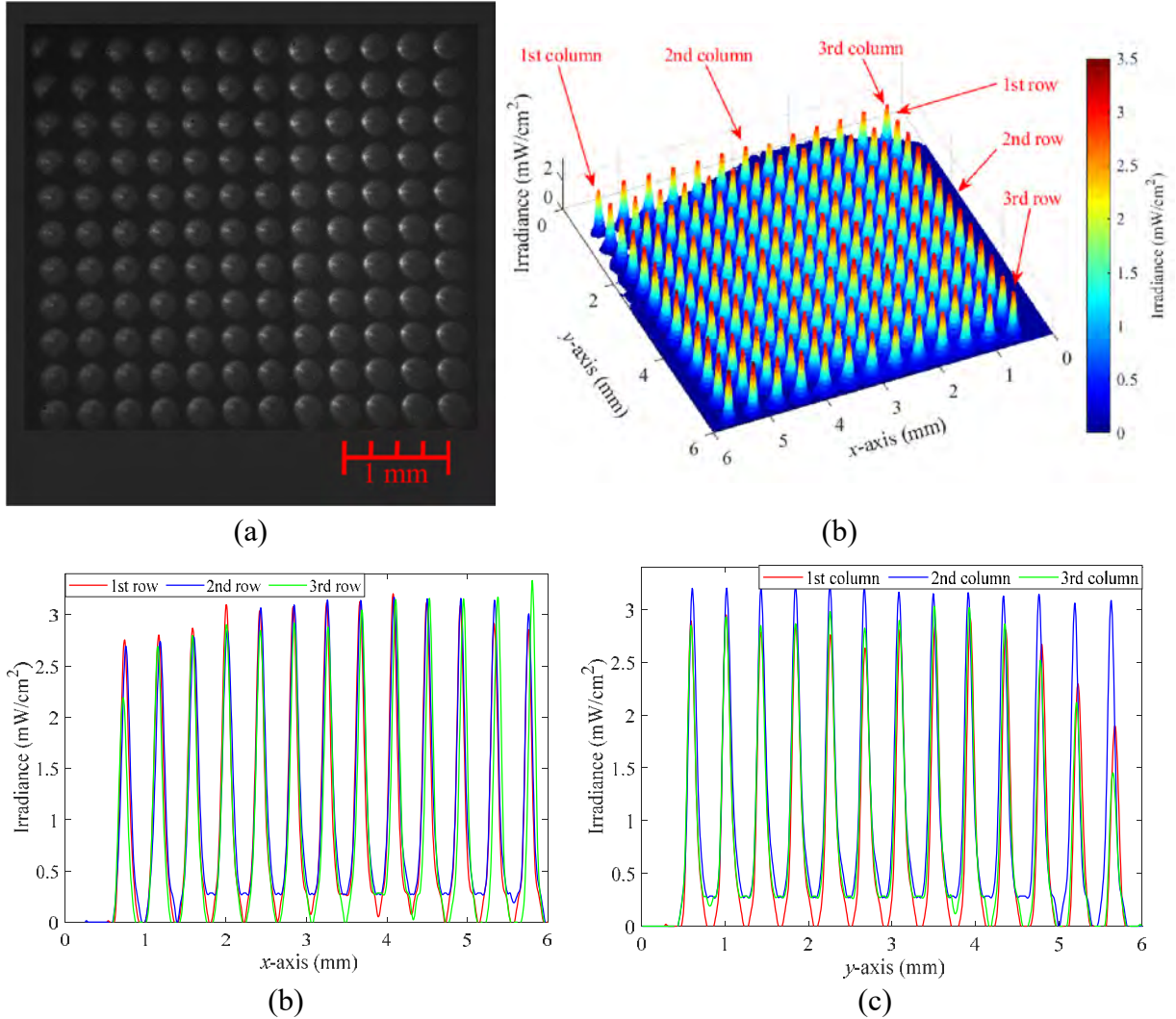


Figure 3-6 (a) Captured image of irradiance profiles projected from individual micromirrors, (b) Processed image of the individual adjacent micromirror irradiance profiles and sections across the individual micromirrors irradiance profile along the (c) X-axis and (d) Y-axis

In order to analyze the individual micromirror projected irradiance profile closely, individual profiles with different peak irradiance ( $I_m$ ) in both the  $x$  and  $y$  axis are plotted in Figure 3-7 (a)

and (b). The plotted profiles are compared to a simulated Gaussian profile using the measured parameter from each of the experimentally captured profile as tabulated in Table 3-2.. The captured irradiance profile was found to match the form of the simulated Gaussian profile as shown in Figure 3-7 (a) and (b). The Gaussian radius ( $\omega_o$ ) is measured at  $1/e^2$  of the peak irradiance of the Gaussian profile. On average, the Gaussian radius in both directions is  $96\mu\text{m}$  with a maximum value of  $98\mu\text{m}$  and a minimum value of  $94\mu\text{m}$  as depicted in Table 3-2.

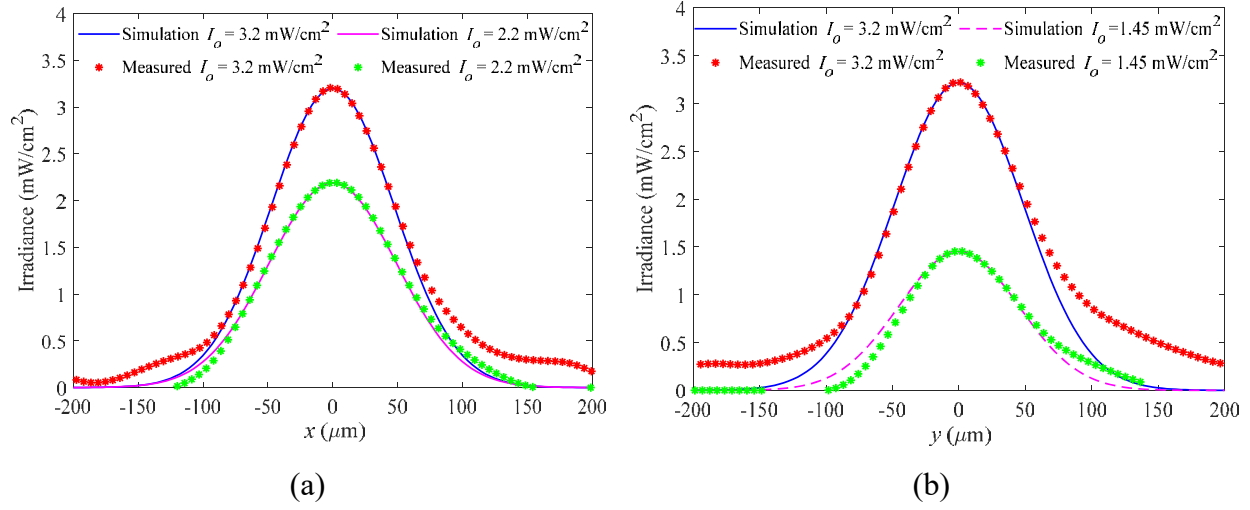


Figure 3-7 Simulated irradiance Gaussian profiles from one micromirror compared to the measured irradiance profiles with different peak irradiances in (a)  $x$ -axis and (b)  $y$ -axis

Table 3-2 Measured Gaussian profile parameters to fit equation (2-9)

Axis	Peak Irradiance $I_m$ (mW/cm <sup>2</sup> )	$\frac{I_m}{e^2}$ (mW/cm <sup>2</sup> )	Gaussian Radius $\omega_o$ ( $\mu\text{m}$ )	Average Gaussian Radius $\omega_o$ ( $\mu\text{m}$ )
$x$	3.2	0.433	94	96
$y$	3.2	0.433	98	
$x$	2.2	0.3	98	
$y$	1.45	0.2	94	

### 3.2.3.2 Irradiance map

The overall irradiance was computed by superimposing 1024 captured images of individual micromirror irradiance profiles. The captured images covering  $32 \times (5 \times 5 \text{ mm}^2)$  locations spread across the whole projection. For each capturing location, the same pattern used in the previous section is used, but for each capture, the full pattern is shifted by two micromirror in both directions resulting in 32 images to cover each square. Any non-captured micromirror location is averaged from the surrounding neighbouring irradiance profiles. The analyzed projection map is shown in

Figure 3-8. The average irradiance across the build platform recorded is  $19.8 \text{ mW/cm}^2$  with a maximum of  $24.5 \text{ mW/cm}^2$  and a minimum of  $14 \text{ mW/cm}^2$ . Three areas at different positions are selected to analyze the average per area. The first position has average irradiance of  $19.6 \pm 1 \text{ mW/cm}^2$ , the second position has  $22.2 \pm 1 \text{ mW/cm}^2$ , and the third position has  $17.5 \pm 2.5 \text{ mW/cm}^2$ .

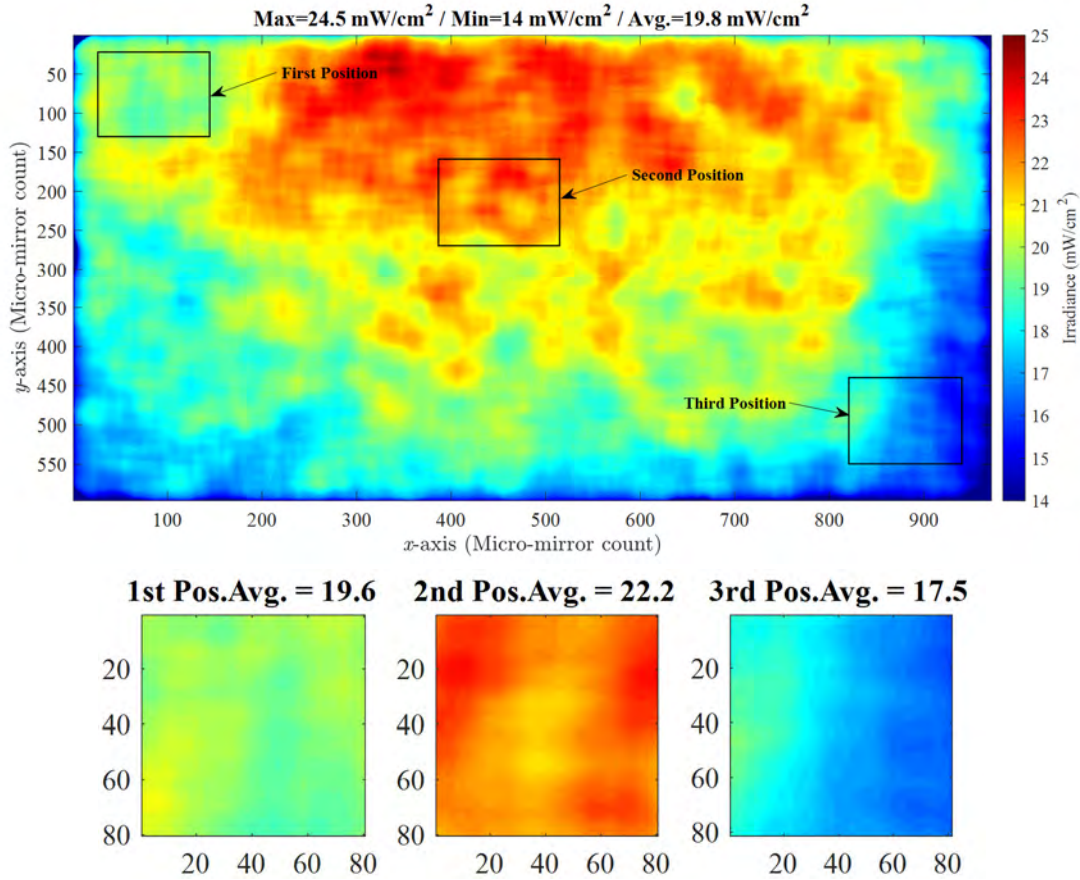


Figure 3-8 Irradiance map across the build platform

### 3.2.3.3 Irradiance profile of 2D shapes

Several two-dimensional shapes were projected, captured, and analyzed. Two locations were selected to project the circular patterns; the first and the third location as annotated on Figure 3-8. The first location's captured images and its corresponding analyzed irradiance profiles are shown in Figure 3-9. The first projected shape in the first location is a 3 mm diameter circle with a 1 mm hole, as shown in Figure 3-9 (a). The maximum irradiance is  $20 \text{ mW/cm}^2$ . The second projected shape in the first location is a 1 mm diameter circle with a 0.35 mm hole, as shown in Figure 3-9 (b). The maximum irradiance is  $18 \text{ mW/cm}^2$ . It is worth mentioning that the irradiance did not

reach zero inside the hole of the second shape, which means there is a possibility that this hole will not be created.

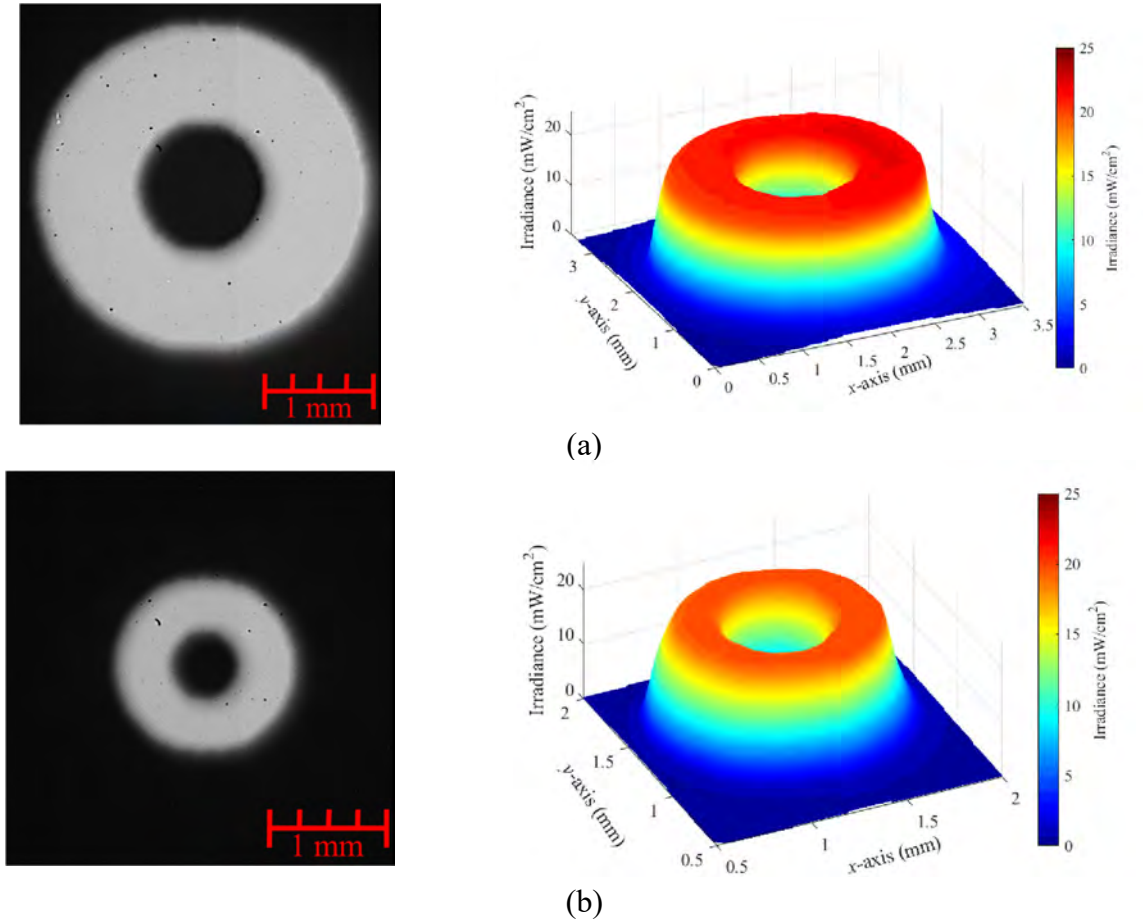


Figure 3-9 Captured image and the corresponding analyzed irradiance profile of annulus cross-section with dimensions of (a) OD 3 mm with ID 1 mm (b) OD 1 mm with ID 0.35 mm projected at the first location (defined in Figure 3-8)

The third location captured image and its corresponding analyzed irradiance is shown in Figure 3-10. The first projected shape in the third location is a 0.75 mm diameter circle with a 0.5 mm hole, as shown in Figure 3-10 (a). The peak irradiance is 16 mW/cm<sup>2</sup>. While the second projected shape in the first location is a 0.5 mm diameter circle, as shown in Figure 3-10 (b). The peak irradiance is 16 mW/cm<sup>2</sup>. It is worth mentioning that the irradiance is skewed in the third position, which might be due to the significant difference between the maximum and minimum irradiance in this position.



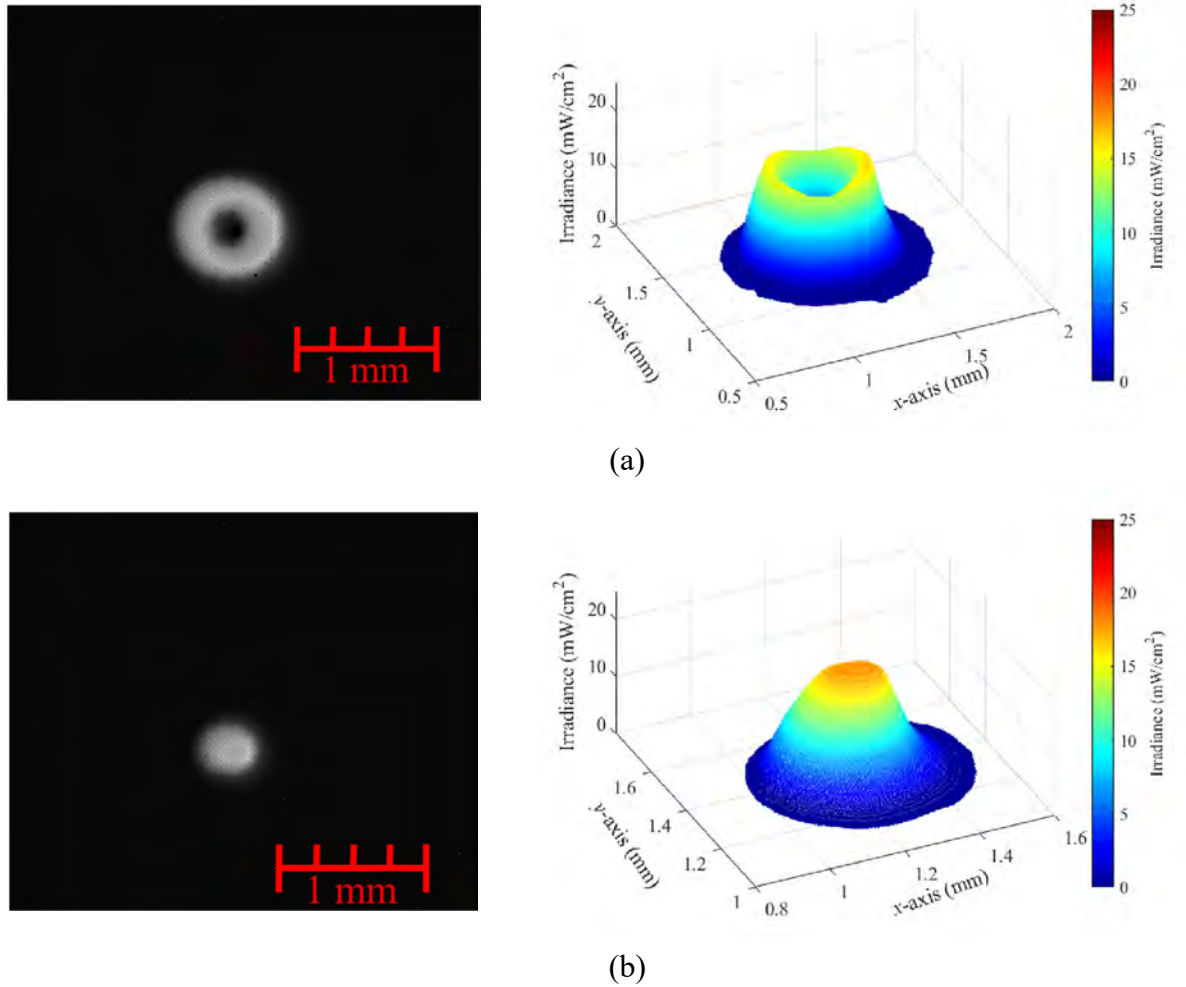


Figure 3-10 Captured image and the corresponding irradiance profile of cylindrical cross-section with the dimensions of (a) OD 0.5 mm with ID 0.25mm (b) OD 0.25 mm at the third location (defined in Figure 3-8)

Cross section profiles along the projected shapes are shown in Figure 3-11 (a) to (d). The critical irradiance value ( $I_c$ ) of  $4.75 \text{ mW/cm}^2$  corresponding to the critical curing energy ( $E_c$ ) of  $9.5 \text{ mJ/cm}^2$  at 2 seconds exposure time is marked as dashed red line on each figure. The diameter of the projected profiles at the critical irradiance corresponds to the maximum expected diameter after manufacturing. The expected diameter values are documented in Table 3-3. The outer diameter is expected to be larger than the nominal. In case of the 3 mm outer diameter (OD) the expected dimension is 3.1 mm and for 1 mm OD it is expected to be 1.15 mm. In case of the 0.5 mm outer diameter (OD) the expected dimension is 0.57 mm and for 0.25 mm OD it is expected to be 0.23 mm. For internal diameters (ID), the 1 mm becomes 0.88 and for a 0.35 mm the internal

diameter becomes 0.27. The outer diameter is expected to be larger. For internal diameters (ID) with 0.25 mm and less the internal hole will not be printed as the minimum irradiance value in the internal hole is higher than the critical irradiance.

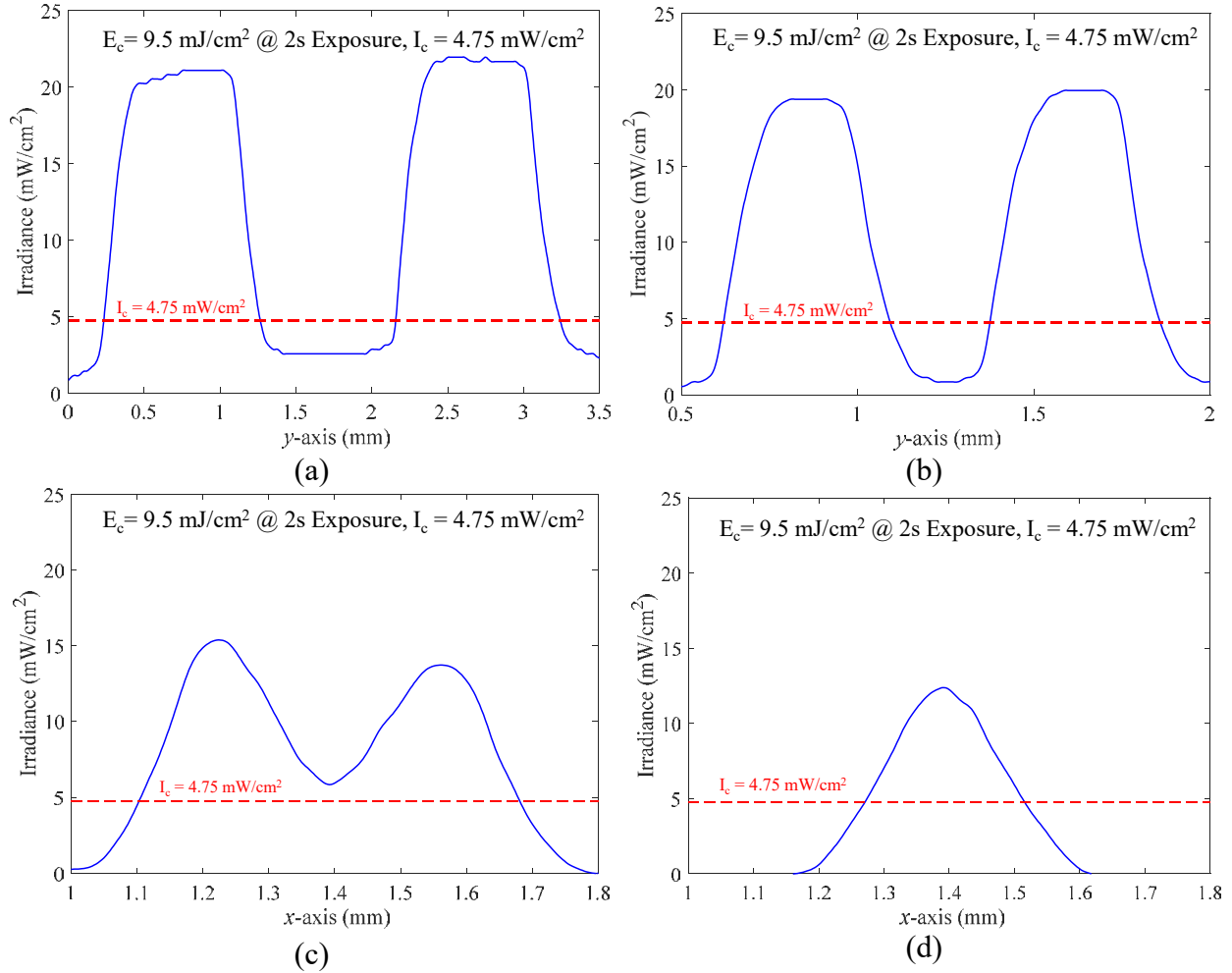


Figure 3-11 Cross sectional irradiance profile across the projected 2D circular shapes with the following dimensions of (a) OD 3 mm with ID 1 mm, (b) OD 1 mm with ID 0.35 mm projected at the first location (defined in Figure 3-8), (c) OD 0.5 mm with ID 0.25mm, and (d) OD 0.25 mm at the third location (defined in Figure 3-8)

Table 3-3 Measured irradiance profile

	OD (mm)	ID (mm)	T=2s	
1	3	1	3.1	0.88
2	1	0.35	1.15	0.27
3	0.5	0.25	0.57	0
4	0.25	N/A	0.23	N/A



In the first part of this chapter a reliable novel irradiance characterization technique is proposed using the irradiance-induced fluorescence technique. The irradiance profile projected from individual micromirrors is captured and analyzed, and the average Gaussian radius was found to be 96  $\mu\text{m}$ . The overall irradiance map was characterized, and the maximum and minimum irradiance was 24.5 and 14  $\text{mW}/\text{cm}^2$ . Several irradiance profiles of two-dimensional circular shapes were analyzed and presented. In the next part studies the effect of irradiance map on dimensional deviations.

### 3.3 Assessment of Dimensional Deviation

The objective of this experiment is to assess the effect of irradiance map non-uniformity represented by location on the build platform on the geometrical accuracy under different exposure time, layer thickness, and grayscale pixel blending values and strategies.

#### 3.3.1 Methods and Materials

##### 3.3.1.1 Specimen Design

The specimen is manufactured from a black resin called PR57 by Autodesk, USA. The specimen is a simple 8 mm cylinder distributed equally on the specimen base in order to assess the irradiance map irregularity on the dimensional accuracy. The specimen design allows the Coordinate Measurement Machine (CMM) with a 4 mm measuring probe to pass through the cylinders. Each specimen contains four sets of cylinders; each set consists of three replications, as shown in Figure 3-12.

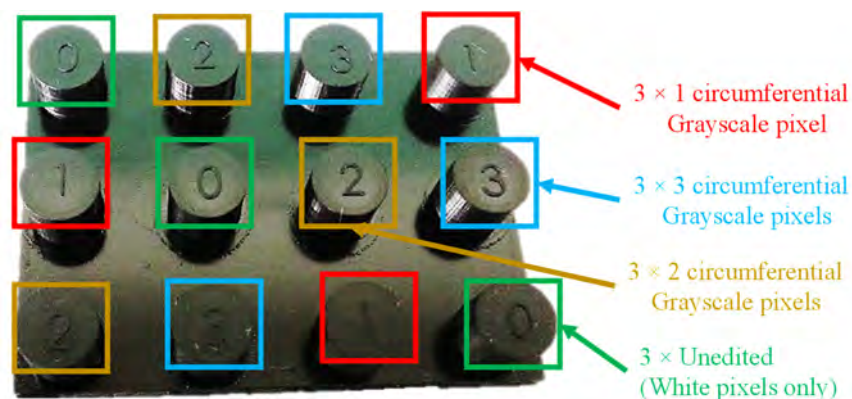


Figure 3-12 Designed specimen with four sets of cylinders with three replications for each set distributed across the build platform

The difference in the sets are shown in Figure 3-13 and described as follow:

1. The first set is unedited 8 mm cylinders with (0) notation.
2. The second set is the same cylinders but with only a one-pixel width ring circumferential from the inner side of the original 8mm cylinder circumference and has a notation of (1).
3. The third set has a two-pixel width circumferential ring, one ring is from the inner side of the original circumference, and the other is from the outside and has a notation of (2).
4. The fourth set has a three-pixel circumferential ring, two pixels are from the inner side of the original circumference, and the last pixel is on the outside and has a notation of (3)

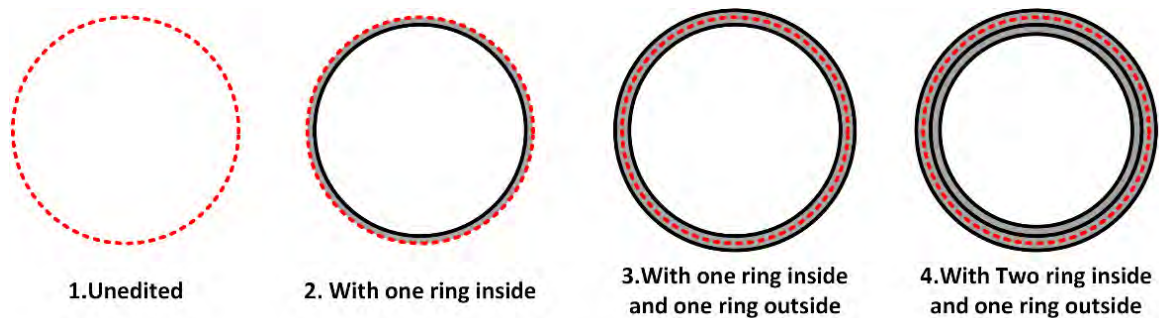


Figure 3-13 Illustration of the different grayscale rings sets

The difference between the different sets is only in the PNG stack. After slicing the basic specimen of twelve 8 mm cylinders, the PNG master slices, with only white and black pixels, were edited using Adobe Photoshop® to add pixel width rings with the required grayscale colour according to the designed experiment shown in Figure 3-14.

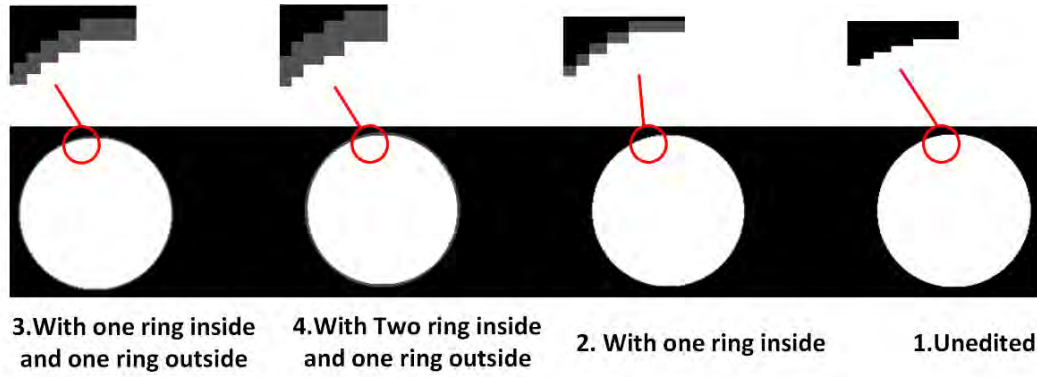


Figure 3-14 Photoshop editing for the PNG slice images

### 3.3.1.2 Design of Experiment

A fractional factorial experiment was designed using Taguchi L9 orthogonal array as shown in Table 3-4. The parameters studied are as follows:

1. The grayscale value for pixel width circumferential rings has three values of 105, 155, and 205.
2. The exposure time per layer has values of 1.8, 2, and 2.5 seconds.
3. The layer thickness has two values of 25 and 50  $\mu\text{m}$ , and the 50  $\mu\text{m}$  was replicated twice, as one of the three levels was dummy treated.

The recommended exposure for the resin for a 50  $\mu\text{m}$  layer thickness by Autodesk is 1.8 seconds. The grayscale pixels used in the antialiasing mode were in the range of 100 to 242. All values are based on slight variations around the normally used recommended settings for the PR57.

Table 3-4 L9 Fractional factorial array

Run#.	Gray Scale Value	Exposure Time (s)	Layer Thickness( $\mu\text{m}$ )
1	105	2	50
2	105	2.25	25
3	105	1.8	50
4	155	2	25
5	155	2.25	50
6	155	1.8	50
7	205	2	50
8	205	2.25	50
9	205	1.8	25

### 3.3.1.3 Dimensional Measurements

A calibrated Mitutoyo Crysta-Plus M443 Coordinates Measuring Machine (CMM) was used to measure the nine specimens with a total of 108 cylinders, as shown in Figure 3-15. Eight equally distributed points across the circumference of each cylinder were used to evaluate the value of mean diameter. Normally, a circle is defined by using only three points on the circumference, but for better representation with more confidence level, eight points were used.



Figure 3-15 CMM measurement while measuring the different cylinder specimens

### 3.3.2 Results

All the measured diameters for each set of cylinders per specimen were averaged. The difference between the maximum and minimum values was recorded and presented in Table 3-5. Results vary significantly by changes in the process parameters and cylinder location. All the measured cylinders have a circularity error of 50  $\mu\text{m}$ , which describes the distance between the farthest to nearest points to the center of the mean circle. It was found that the maximum error due to location is 0.237 mm. Many configurations can achieve both tight and loose clearance fit or achieve light or heavy shrink fitting. According to the tolerance tables, a shaft with 8 mm having a tolerance ranging between 20 to 90  $\mu\text{m}$  corresponds to the standard tolerance grades of IT8 to IT11. The other tolerance grades are harder to achieve using the current projection stereolithography machine used.

Table 3-53 Average diameters of each set per specimen

Run #	Unedited (mm)		1 ring (mm)		2 rings (mm)		3 rings (mm)	
	Average	±	Average	±	Average	±	Average	±
1	8.08	0.145	7.937	0.103	8.04	0.056	8.017	0.038
2	8.11	0.16	7.978	0.089	8.05	0.052	8.02	0.028
3	8.1	0.109	7.927	0.06	7.98	0.037	7.917	0.04
4	8.11	0.118	8.047	0.073	8.13	0.055	8.123	0.052
5	8.14	0.237	8.023	0.119	8.13	0.075	8.085	0.067
6	8.1	0.117	8.093	0.053	8.17	0.083	8.15	0.065
7	8.08	0.161	8.02	0.09	8.14	0.042	8.107	0.042
8	8.14	0.14	8.014	0.075	8.11	0.089	8.101	0.06
9	8.21	0.205	8.064	0.118	8.18	0.104	8.143	0.076
Avg.	8.12	0.155	8.011	0.087	8.1	0.066	8.073	0.052

The general overall trend depicted from Table 3-5 is that the mean diameter of the cylinders with inner circumferential one pixel grayscaled ring is the least compared to the other sets, followed by the cylinders with 3 pixels circumferential ring with two pixels inside and one pixel outside. The cylinders with two pixels ring and the unedited cylinders have the same rank. For the unedited cylinder set, the mean diameter ranges between 8.08 to 8.141mm, and the average is about 8.125 mm. This range of values does not offer much control on the dimensional tolerance around the mean of the cylinders. When one grayscale ring from inside is used, the average diameter decreases to be 8.012 mm, which is a reasonable value. The range of mean diameters varies between 7.927 to 8.064 mm, which allows for more control over the cylinder dimensions in both directions, either increasing or decreasing. In the case of using one greyscale ring inside and the other one outside, the range of achievable diameters ranges from 8.02 to 8.16, while in the case of the three pixels, the mean diameters range from 7.975 to 8.125 mm. Manipulating the three process parameters offers a dimensional control over the values of the mean diameters. Different tolerance grades for different fitting methods can be achieved; for example, using configuration two with the one ring set can achieve a mean diameter of 7.978 mm, a tight clearance fit with IT8 grade. For a loose clearance fit, configuration one with one grayscaled ring can achieve 7.937 mm, corresponding to IT10 grade. For light interference fit, configuration one with three rings set can achieve 8.17 mm, corresponding to IT 8. For IT 10 grade for interference fitting, either configuration two with two rings set or configuration nine with one ring set to achieve mean diameters equal to 8.47 and 8.49 mm, respectively.

In order to understand the process parameters' significance on the geometrical deviation across the build platform, main effects plots were used to study the different sets separately, as shown in Figure 3-16. The figures show, in general, that as the layer thickness increases, the mean diameter decreases. The mean diameter decreases as the exposure time increases only in one ring set, while for both the two and three rings set, it increases to 2 seconds and then decreases again. The mean diameter increases with a grayscale value till 155 and then starts to decrease in all the sets. In Figure 3-16 (b), the mean diameter decreases with the exposure time compared to the other two figures. The hypothetical theory behind it is that the set with the only one-pixel ring is more affected by the neighbouring white pixels of the main cylinder, making greyscaled one-pixel ring starts the crosslinking phase earlier than in the case of two or three pixels.

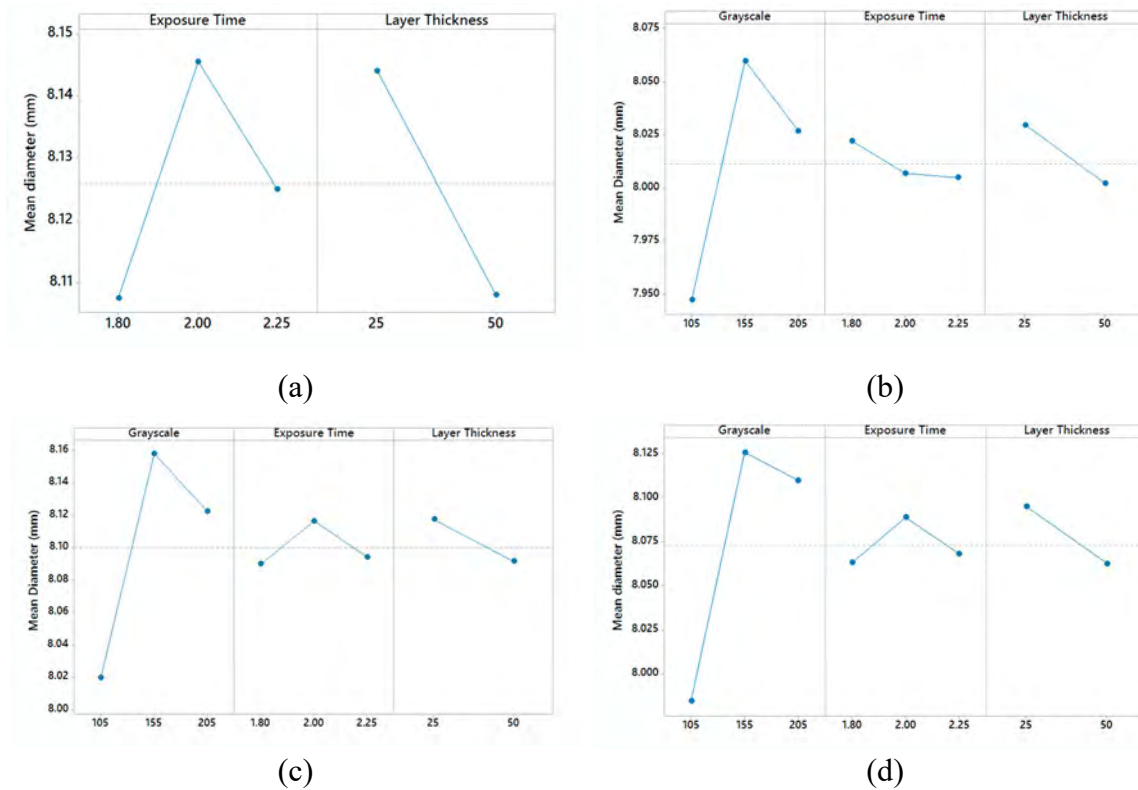


Figure 3-16 Main effects plot for the cylinders sets (a) unedited cylinders, (b) 1 ring configuration, (c) 2 rings Configuration, and (d) 3 rings configuration

The parameter significance was calculated, and it shows that the exposure time is the most influential parameter, followed by the grayscale value and then the layer thickness. This means that a slight change in the exposure time varies the dimensions significantly, but using the different

grayscale colours can adjust the dimensions smoothly, and it will not considerably affect the overall mechanical strength of the part.

### **3.4 Conclusions**

A reliable novel irradiance characterization technique is proposed in this chapter using the irradiance-induced fluorescence technique. The irradiance profile projected from individual micromirrors is analyzed, and the average Gaussian radius was 96  $\mu\text{m}$ . The overall irradiance map was characterized, and the maximum and minimum irradiance was 24.5 and 14  $\text{mW}/\text{cm}^2$ . Several irradiance profiles of two-dimensional circular shapes were analyzed and presented.

It was found that the maximum error due to location is 0.237 mm. However, the grayscale technique has proved its efficiency in controlling the dimensions of the 8mm cylinders by manipulating the layer thickness and exposure time with it. Three sets of grayscale configurations are used to adjust the mean diameter of the 8 mm cylinder to be within the normal IT Fitting tolerance grade. Taguchi design of experiments and analysis technique was used to design an experiment to determine the separate main effect of each parameter on the mean diameter. It was shown that the exposure time is the most influential parameter, followed by the grayscale value and then the layer thickness. Potential samples for tight and loose fittings were discussed.

This chapter sheds light on one of the reasons why the as build part is different from the as-designed part, which is the main research question of this thesis. The results obtained in this chapter are the inputs to geometry simulation and optimization algorithms discussed in the next chapter.

## **4 3D Modelling and Optimization of Projection Stereolithography (PSLA)**

The vertical resolution of the PSLA is affected by the minimum layer thickness achievable by the control system, along with the light penetration through the material, which is determined based on the overall absorbance of the used resin. On the other hand, the horizontal resolution depends on the size of the micromirrors in the DMD, reducing/spreading optics, and the curing light diffraction, which is represented by the point spread function. The currently available DMD facilitates the individual modulation of irradiance reflected from each micromirror. Irradiance manipulation improves the horizontal resolution with pixel blending algorithms. This chapter has two main objectives; the first is to develop an algorithm to simulate the expected manufactured part three-dimensional geometry and represent the shape using a voxel logical array. The second objective is to develop a 3D optimization methodology for PSLA that can be applied to the different resin types.

This chapter directly answers the main research hypothesis that the geometry can be optimized without affecting the mechanical properties by optimizing the process parameters. The optimization algorithm will improve the geometry while maintaining the mechanical properties at a level that ensures the part's structural integrity during manufacturing. After manufacturing, the mechanical properties can be enhanced further with the post-curing process. Predicting parts geometry ahead of manufacturing will minimize manufacturing costs by minimizing the manufacturing trials in case of part failure.

### **4.1 Introduction**

#### **4.1.1 Literature review**

Several research studies discussed and developed modelling and optimization algorithms; Table 4-1 demonstrates a chronological summary of the development in the geometry prediction and optimization for PSLA. The table shows whether the used model considers a single layer or Multilayers and the distribution assumed for the irradiance profile. The table shows whether the irradiance was superpositioned in the horizontal (H) or the vertical (V) plane, whether the profiles



were superpositioned in 1-D or a 2-D only, process parameters considered, and the studied response.

Table 4-1 Literature review

Year	#Layer	Irradiance Profile	Direction	Algorithm	Parameters	Response	Ref.
03	Multi	Constant	1-D V	Modelling	-	Curling	[88]
05	Single	Gaussian	1-D H	Modelling	-	Geometry	[71]
06	Multi	Constant	1-D V	Optimization	Exp. time	Features height	[67]
07	Single	Polynomial	2-D H	Modelling	-	Lateral dim.	[72]
09	Single	Gaussian	2-D H	Optimization	Greyscale	Geometry	[89]
09	Single	Gaussian	2-D H	Optimization	Greyscale	Flatness	[83]
12	Multi	Constant	2-D H	Optimization	Greyscale	Side roughness	[73]
12	Single	Rectangular	2-D H	Modeling	-	Geometry	[90]
12	Single	Random	2-D H	optimization	Pixel on/off	Map uniformity	[51]
14	Single	Rectangular	2-D H	Modelling	-	Geometry	[91]
15	Multi	Constant	2-D V	Modelling	Exposure	Dim. Of $\mu$ channels	[38]
18	Single	Random	2-D H	optimization	Greyscale	Map uniformity	[52]

Huang et al., in 2003, attempted to minimize the curl distortion due to the uneven accumulated absorbed energy by resin mix, which is reflected as an uneven elastic modulus and the temperature gradient across the part. They developed a 3D finite element model which simulates the deformation and curling based on the multilayer energy absorption model with a constant irradiance profile [88,92]. Sun et al., in 2005, proposed a single layer 1-D horizontal solidification model based on the superposition of the Gaussian irradiance distribution from each micromirror [71].

Limaye et al., in 2006, proposed a 1-D vertical solidification model based on a constant irradiance profile. This model considers the multiple exposures received by each layer from the successive layers. They developed a nonlinear optimization problem to minimize the error in the height of the feature by manipulating the exposure time of each layer individually [67]. In another work by the same authors in 2007, they proposed a 2D single layer non-Gaussian horizontal solidification model to estimate the lateral dimensions[72].

Zhou et al., in 2009, developed a linear integer optimization algorithm, called pixel blending algorithm, using a single layer 2-D model, based on the superposition of Gaussian irradiance profiles [54]. The objective function is to minimize the absolute difference between a target shape and a predicted shape; both are rendered at a resolution lower than the projector mirror's size by

manipulating the grayscale colour of each pixel at a fixed given exposure time. The target and predicted models are binary 2D matrices. An element in the estimated model will equal one if its position receives irradiance above the critical amount and zero if it has irradiance is below, while the binary elements of the target model depend on the PNG input file. The same authors, in 2009, studied the flatness of a horizontally manufactured surface. They found the surface has an intrinsic waviness, and the reason behind that was that each micromirror projects different peak irradiance. They developed a calibration algorithm to manipulate the greyscale to minimize the distortion in the horizontal flat surface [83].

Pan et al., in 2012, studied the staircase effect and proposed a process planning algorithm depending on the 2D pixel blending algorithm. It showed significant improvement to the side surfaces of a curved manufactured part [68,73].

Kang et al., in 2012, defined an irradiance rectangular orthotropic distribution for each mirror which was then implemented within a single layer 2D solidification model, and the result of the simulation was visually compared to an experimental result[90]. Ding et al., in 2014, optically simulated the irradiance profile based on considering the micromirror as a square aperture producing a rectangular distribution irradiance profile, and it was compared visually to a solidified layer [91].

Gong et al., in 2015, developed a 2D multilayer vertical solidification model with a constant irradiance profile to estimate the exposure time required to allow the manufacturing of a horizontal microchannel while considering the light penetration through the layers [38]. Moreover, in 2017, they enhanced the minimum manufactured microchannel [57].

Zheng et al., in 2012, studied the non-uniform light projection from the DMD, and he proposed a method to reduce projection non-uniformity from 16 to 5% by suppressing bright pixels. With several iterations, the brightness across the focus plan was within the average [93]. Warburg et al., in 2018, proposed a non -uniformity compensation model and introduced Christiansen's uniformity coefficient [94] to be used to judge the intensity uniformity of the DMD light projection[52].

#### **4.1.2 Research gap**

The current state of art discussed in the previous section contributed to individually improving and optimizing different geometric features for PSLA. Each algorithm optimizes a certain

geometric feature using only one process parameter, which messes with the coupled geometrical features. There are no general geometry optimization algorithms that can simultaneously handle multiple parameters to optimize and decouple the different geometrical features. The Literature gaps found can be summarized as follow:

1. The pixel blending algorithm, proposed in [54,83], optimized 2D single-layer geometries only and did not consider the exposure time, which controls the 3D multi-layer geometries deviations [38,67,72]. For example, in the case of non-vertical holes, as the light penetrates through the layers and cures the prepolymer remaining in these holes leading to feature failure.
2. The one and two-dimensional vertical optimization algorithms presented in [38,67,72,88,92] have two main issues:
  - a. It manipulates exposure time as the only process variable without integrating the pixel blending to solve the non-vertical holes failure problem. However, as the exposure time deviates from the nominal, the lateral dimensions of each layer will deviate accordingly.
  - b. It utilized a constant irradiance model only, which did not estimate the minimum feasible gaps to be created.
3. The current geometry optimization algorithms used the working curves as the only solidification criterion [38,54,67,68,72,73], which might lead to failure during manufacturing since accurate dimensions might be achieved within the early polymerized phase of the material and might not withstand the manufacturing forces or self-weight.
4. The current projection uniformity algorithms [52,93] utilize pixel blending to fix the irradiance map uniformity; therefore, the pixel blending will not be available to be used in optimizing horizontal features.

The main objective of this research is to develop a robust 3D geometry optimization algorithm that can optimize the geometry of different features types simultaneously. The algorithm will integrate different algorithms from the literature to simultaneously manipulate different process parameters while minimizing the effect of irradiance map irregularities effect. The objectives of this research are as follows: This chapter directly answers the main research hypothesis that by optimizing the process parameters, the geometry can be optimized without affecting the

mechanical properties. The optimization algorithm will improve the geometry while maintaining the mechanical properties at a level that ensures the part's structural integrity during manufacturing. Then after manufacturing, the mechanical properties can be enhanced further with the post-curing process. Predicting parts geometry ahead of manufacturing will minimize manufacturing costs by minimizing the manufacturing trials in case of part failure.

## 4.2 3D Geometry Prediction

In order to develop a geometry prediction algorithm, a 3D solidification model has to be established first, which will be based on the 2D solidification model discussed in 2.2. This algorithm should process the same input file to the machine without further manipulations for this algorithm to be convenient. As shown in Figure 4-1, after the algorithm reads the stack of the sliced images, it starts by calculating the overall irradiance profile of each layer independently, by superposition of the irradiance profile resulting from all the white pixels within each layer image. The next step is to accumulate the light penetrating from the successive layers to the previously manufactured layers. Then the cured shape is evaluated based on the accumulated energy for each layer. The last step is voxelizing of the cured shape at sub-voxel resolution. This resolution is lower than that of the theoretically achievable voxel.

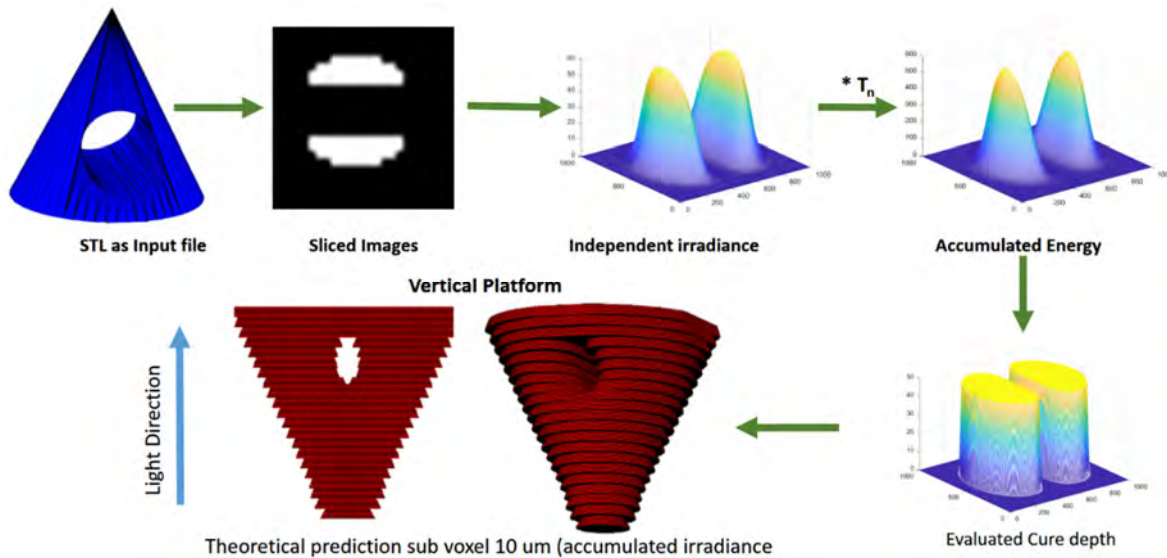


Figure 4-1 layout of the geometry prediction algorithm

This model is based on several assumptions:

1. Orthogonal micromirror sampling is used.
2. The polymerization terminates when there is no light immediately.

3. The light refraction within the cured layer thickness is negligible.
4. The prepolymer liquid level in the VAT is always higher than the irradiance penetrated zone.
5. The prepolymer liquid between microchannel walls and between the outer edges of layers remains in its place due to the viscosity of the liquid and the friction of the walls.

Before calculating the overall irradiance profile of each layer, the original input grayscale images -which are a 2D 8-bit integer matrix- are cropped by  $C_l \times C_m$  pixels to only include the region of interest shown in Figure 4-2; where  $C_l$  &  $C_m$  are the length and width of the cropped images represented by the numbers of pixels. The cropped matrices have  $l$  and  $m$  as indices to define the position of each pixel in the image. The value of the grayscale level of each pixel is stored in a 3D matrix called  $P_{lmn}$  which has dimensions of  $C_l \times C_m \times N$ , where  $N$  is the total number of input images and  $n$  is the layer (input image) index to define the position of the image in the 3D matrix. Each pixel is sub-pixelated by a factor  $G_d$  which stands for the Gaussian density to accurately render the Gaussian profile reflected from each micromirror. Gaussian density  $G_d$  is a physical distance by which the pitch ( $p$ ) between two consecutive micromirrors is divided in both the  $x$  and  $y$  direction;  $G_d$  represents the simulation resolution. The pitch is defined as the distance between the centers of two successive micromirror projections on the focus plane. Using both the Gaussian density value and micromirrors' pitch, a sub-pixelated matrix representing the physical horizontal dimensions of the irradiance profile of the whole layer is generated and has a maximum physical size of  $(G_d \times C_l) \times (G_d \times C_m)$ . The  $x$  and  $y$  are the indices of this matrix, and the values increments in  $G_d$  steps in the  $x$  and  $y$  direction from  $(0, 0)$  till its end.

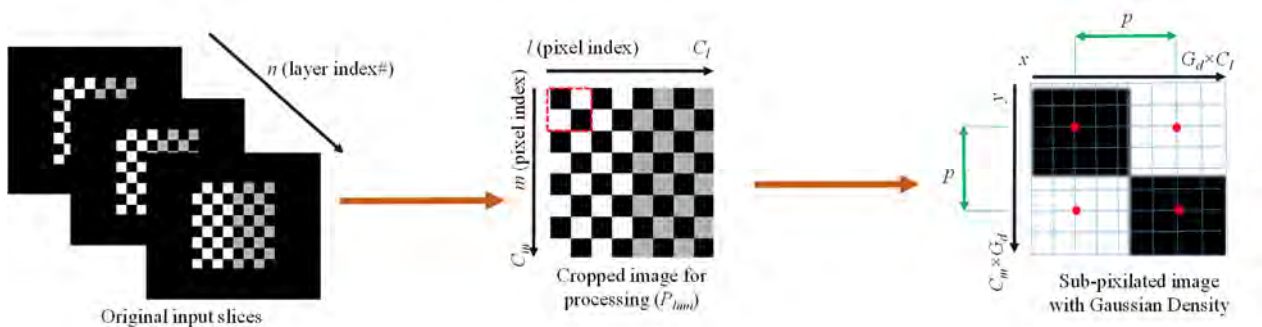


Figure 4-2 Determining the position of the micromirror based on the input images

The individual superpositioned irradiance profile of each layer. “ $I_{xyn}$ ” is described by (4-1), where  $\omega_o$  is the Gaussian radius,  $I_o$  is the maximum irradiance per micromirror,  $H_{lmn}$  is the irradiance map matrix for all the micromirrors.

$$I_{xyn} = I_o \sum_{l=1}^{c_l} \sum_{m=1}^{c_m} H_{lmn} \times P_{lmn} \times e^{\frac{-2 \times \left( \left( x \times G_d - (l-1) \times p - \frac{p}{2} \right)^2 + \left( y \times G_d - (m-1) \times p - \frac{p}{2} \right)^2 \right)}{\omega_o^2}} \quad (4-1)$$

$$IAZ = \frac{D_{P1}}{d_z} \times \ln \left( \frac{E_{max}}{E_c} \right) \quad (4-2)$$

$$E_{xyn} = t \times \left( I_{xyn} + \sum_{i=1}^{IAZ} I_{xy(n+i)} \times e^{-\left( \frac{d_z}{D_{P1}} + (i-1) \times \frac{d_z}{D_{P2}} \right)} \right) \quad (4-3)$$

$$z_{xyn} = \begin{cases} D_{P1} \times \ln \left( \frac{E_{xyn}}{E_c} \right) & , z_{xyn} < d_z \\ d_z & , z_{xyn} \geq d_z \end{cases} \quad (4-4)$$

In order to compute the accumulated energy received by each layer, a new definition was made under the name Irradiance Affected Zone (IAZ).  $IAZ$  is the number of previously printed layers affected/reached by the light exposing the current layer.  $IAZ$  Depends on the material characteristic working curve (2-4) and is described by (4-2). Where  $E_{max}$  is maximum saturated energy resulting from superposition of multiple micro mirrors irradiance ( $I_{max}$ ),  $d_z$  is the constant layer thickness.

The accumulated energy received by each subpixel in each layer is computed using (4-3), which is divided into two terms. The first term computes the energy received by the current layer from the current exposure, where  $t$  is the exposure time. The second term is the summation of the energy received by the current layer from all the subsequent layers within the  $IAZ$ , where  $i$  is an index counter for the layers with in the  $IAZ$ . The exposure time is considered to be variable in this solidification model in order to allow optimizing it, as discussed in the next section.

The next step is to evaluate the cured depth  $Z_{xyn}$  for each sub-pixel based on the accumulated energy using (4-4). Since this process is a constrained surface, the maximum cured depth within each layer cannot exceed the layer thickness.

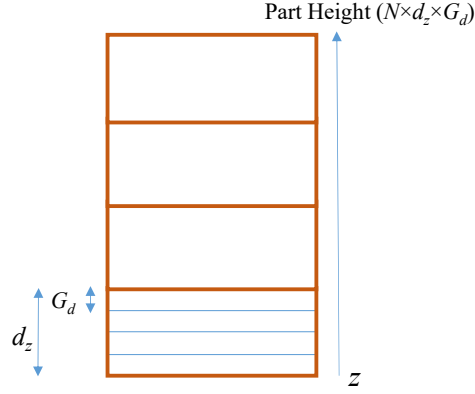


Figure 4-3 Sub-voxelizing of layers

After the cured depth is calculated for each layer, the layer thickness is sub-voxelized by the Gaussian density value  $G_d$ , as shown in Figure 4-3. The physical  $z$ -direction dimension of the whole part is realized in a new matrix called the voxel logical array (VLA)  $V_{xyz}$  matrix. The resultant VLA has the dimensions of  $(G_d \times C_l) \times (G_d \times C_m) \times (G_d \times N \times d_z)$ , and  $x$ ,  $y$ , and  $z$  as position indices of each voxel. Each element in the VLA is compared to the criteria described by (4-5) and (4-6). If the cured depth of a subpixel in a certain layer  $z_{xyi}$  is larger than the subtraction of height of the current position of part by the total height of previously processed layers, then the sub voxel well is “True” if it is lower than that value, then the sub voxel will be “False”. The index  $i$  represents the current layer position in the cured depth matrix.

$$V_{xyz} = \begin{cases} False, & z_{xyi} < z \times GD - ((i - 1) \times d_z) \\ True, & z_{xyi} \geq z \times GD - ((i - 1) \times d_z) \end{cases} \quad (4-5)$$

$$i = floor\left(z \times \frac{GD}{d_z}\right) \quad (4-6)$$

The code for the geometry prediction algorithm of constant layer thickness is written in the Matlab environment. The geometry prediction algorithm results are evaluated in section 4.4.1. Different features are compared against manufactured features at different layer thickness and exposure times.

### 4.3 3D Geometry Optimization

This part of the chapter aims to discuss the developed methodology to integrate three different optimization methodologies to achieve a 3D geometry optimization methodology. As shown in Figure 4-4, the first optimization stage is the pixel blending optimization, which is an existing optimization method [54] and is dedicated to enhancing horizontal manufacturing accuracy. The second stage is the cross-layer optimization (CLO), a novel proposed method dedicated to minimizing the cross-talk between the irradiance projected for one layer and affecting the empty volumes in the previously manufactured layers. The third and last stage is the irradiance map compensation method. The last stage is an upgrade to an existing method so it can be integrated with the whole algorithm and does not affect the enhancement from other stages contrary to the existing method.

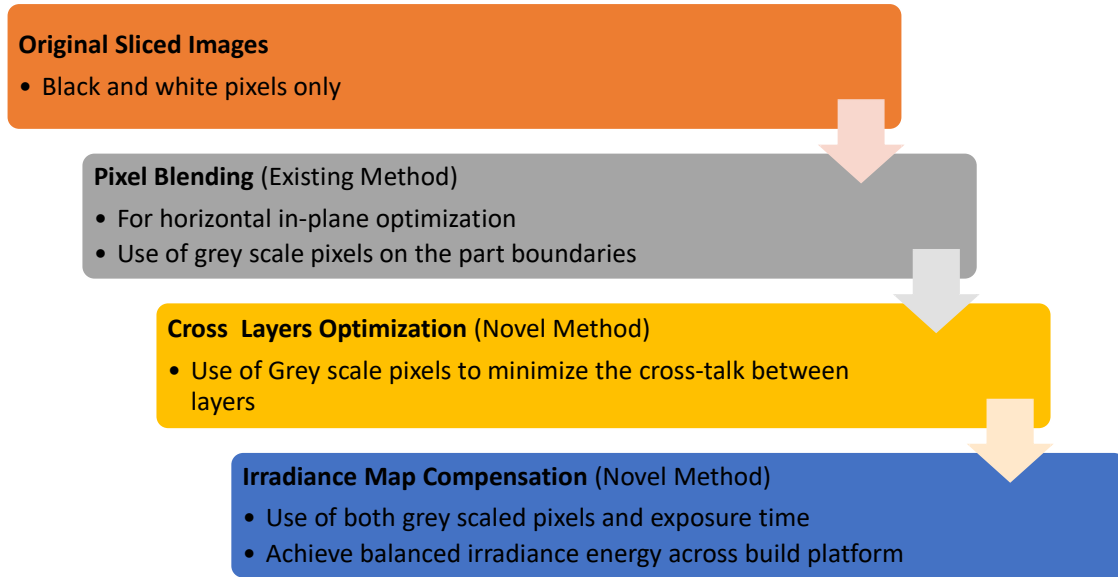


Figure 4-4 Proposed 3D geometry optimization methodology

As shown in Figure 4-5, the proposed optimization method global process starts by slicing the desired STL file with the required manufacturing layer thickness. The 3D geometry prediction algorithm converts these sliced files into a predicted voxelized geometry, as discussed in 4.2. In parallel, the same STL file gets voxelized at the target resolution, usually less than or at least equal to the commercially promised resolution. Then two voxelized geometries are compared together and distorted voxels are determined, as shown in Figure 4-6. The algorithm only handles the optimization of the differential voxels while ensuring that the other correct voxels maintain the



same state. The objective function minimizes the absolute difference between the predicted part and the target voxel logical array, as shown in Figure 4-5. The algorithm satisfies a minimal strength boundary condition to ensure that the solution is not at the gelation phase and that the part can withstand the manufacturing forces (see section 2.4.3. The output of the algorithm is a machine-ready grayscaled PNG image and the exposure time per layer.

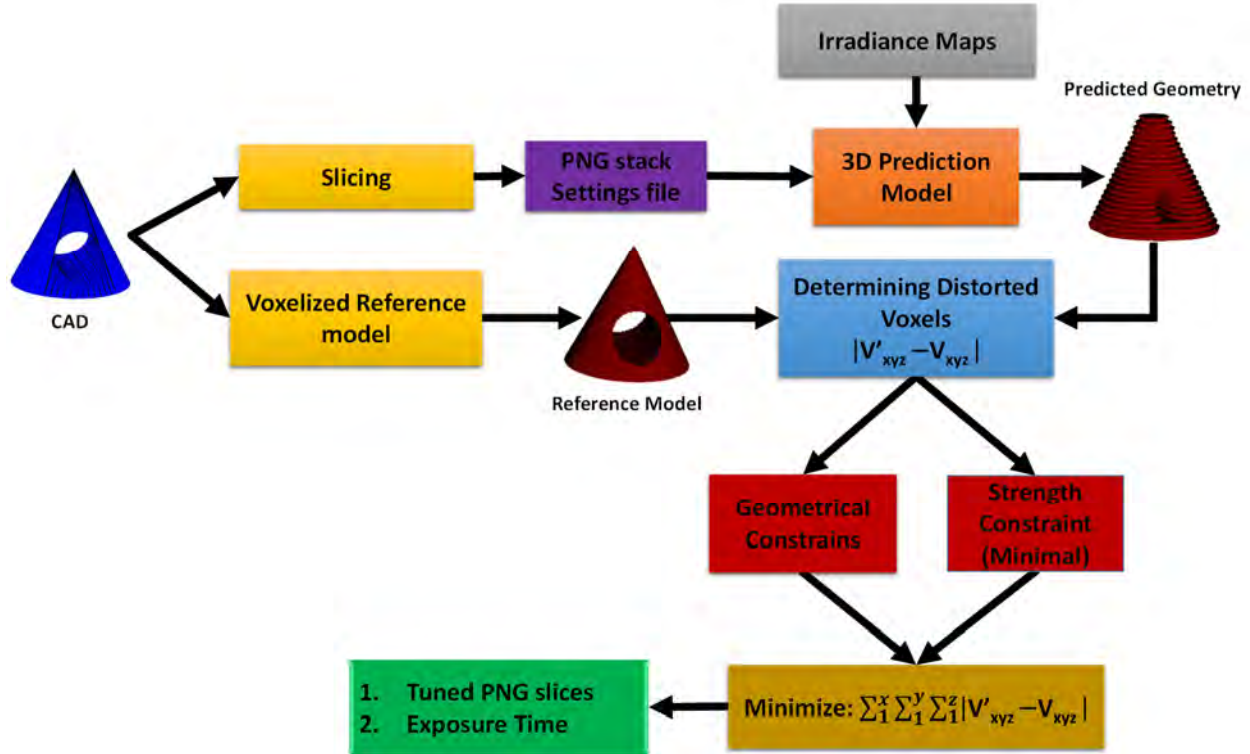


Figure 4-5 Layout of the optimization algorithm

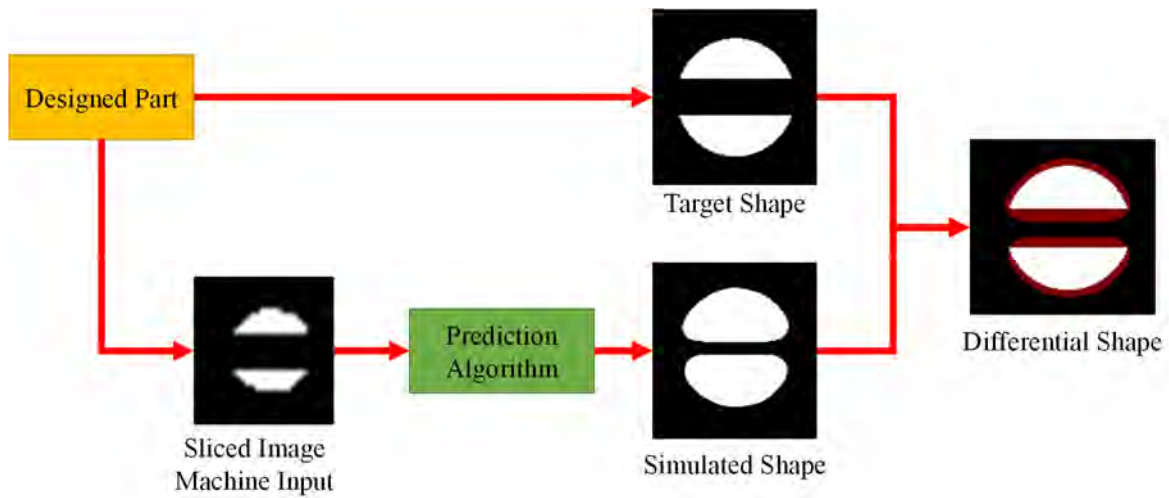


Figure 4-6 Determining the distorted voxels

The current method of optimization requires massive computing power and memory. For example, predicting the shape of the part with a bounding box of 5x5x5 mm and rendering size at 10 microns sub-voxel, there will be 125 Million voxels. As a result, the algorithm will have to satisfy at least the same number of equations. The proposed algorithm introduces a search approach for pixel tuning based on the irradiance affected zone concept, introduced in section 2.2.1. This will minimize the number of equations to be satisfied within the algorithm. The irradiance affected zone (IAZ) is a 3D bounding box. The creation of a voxel at any position within will affect the state of other neighbouring voxels within the IAZ bounded box. In order to define this boundary zone, first, the distance between the peak micromirrors irradiance of a micromirror and where this irradiance drops to nearly zero must be measured, see section 3.2.3.1. Secondly, the vertical penetration distance across the layers should be determined, 2.2.1. After acquiring the differential pixels as shown in Figure 4-6. The optimization algorithm will search for all the influencing pixels in the PNG input images affecting the distorted voxels. It will search for other neighbour voxels affected by those pixels within the IAZ and satisfy only the selected voxels/equations as shown in Figure 4-7.

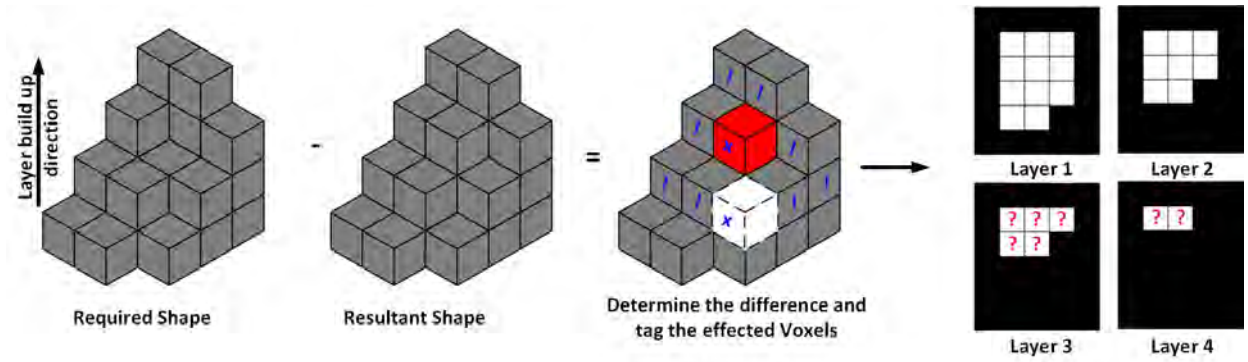


Figure 4-7 Illustration of the IAZ affected voxels and effective pixels selections

The results from the pixel blending optimization [54] are the input to the cross-layer optimization algorithm (CLO). The CLO searches vertically in the predicted part for distorted voxels. Depending on the number of layers in the IAZ, the CLO optimizes the grayscale colour for the pixels within IAZ layers affecting the distorted voxel. The objective function of this algorithm is to minimize the curing depth in the empty volumes where the next cured layer is exposed to irradiance directly below or near the empty volumes within the IAZ. The main constraint is that each layer below the empty volumes and within the IAZ receives at least the critical energy for

ultimate tensile strength on initial exposure, as defined in Table 2-3 in chapter 2. Then accumulates penetrating exposure energy from the subsequent layer to achieve at least a 5 MPa ultimate tensile strength, and then during post-curing, the part strength will increase. The algorithm assumes that irradiance from all micromirrors is equal and has the maximum peak irradiance value. The algorithm manipulates only the greyscale value of the pixels in each PNG slice. It does not interfere with the previous greyscale boundary pixels or exposure time from pixel blending stage unless the pixel directly affects the empty volume.

The last stage of the optimization is irradiance compensation. The inputs to this stage are the CLO output, the exposure time, and the irradiance map. The existing irradiance compensation algorithm manipulates the grayscale value of the pixels only to ensure an equal irradiance profile, which will interfere with the previous two optimization stages. The proposed algorithm manipulates both greyscale value and exposure time to ensure that each voxel will receive the optimized exposure energy decided from the previous two optimization stages. Hence, the proposed irradiance compensation works with exposure energy and not irradiance as the objective. The irradiance compensation uses a simple calculation procedure. The first step is to determine the lowest irradiance value in the irradiance map. Then the exposure time will be adjusted so that the exposure energy projected from this micromirror will be equal to the average exposure energy of the whole map, as shown in equation (4-7). Then the grayscale value of each pixel will be tuned to achieve the same exposure energy dictated from the previous two optimization stages, as shown in equation (4-8).

$$t_{new} = t \times N|_{I_{min}} \times \frac{I_{avg}}{I_{min}} \quad (4-7)$$

$$I_{newij} = I_{ij} \times N_{ij} \times \frac{t}{t_{new}} \quad (4-8)$$

Where  $t_{new}$  is the new calculated exposure time,  $t$  is the exposure time dictated by the pixel blending algorithm,  $H_{ij}$  is the normalized irradiance map value at location  $i$  and  $j$ ,  $I_{avg}$  is the average peak irradiance micromirrors,  $I_{min}$  is the lowest micromirror peak irradiance, and  $I_{newij}$  is the newly calculated peak irradiance value for micromirror at locations  $i$  and  $j$ .

## 4.4 Results

### 4.4.1 Geometry Prediction Evaluation

To evaluate the prediction accuracy of the developed algorithm, the prediction results are compared against the measured manufactured features studied in section 2.4.4. The studied features are vertical square bars, vertical square holes, and horizontal circular holes, and have nominal dimensions of 750, 500, 200  $\mu\text{m}$ . The prediction results were obtained at layer thickness of 50 and 25  $\mu\text{m}$  at exposure time of 2 and 1.8 seconds respectively. As previously concluded and documented in chapter 2, the measured dimensions of the manufactured features deviated from the nominal design dimensions; therefore, the prediction results shall forecast such deviation. The results comparison are depicted in Figure 4-8 through Figure 4-10 and tabulated in Table 4-2.

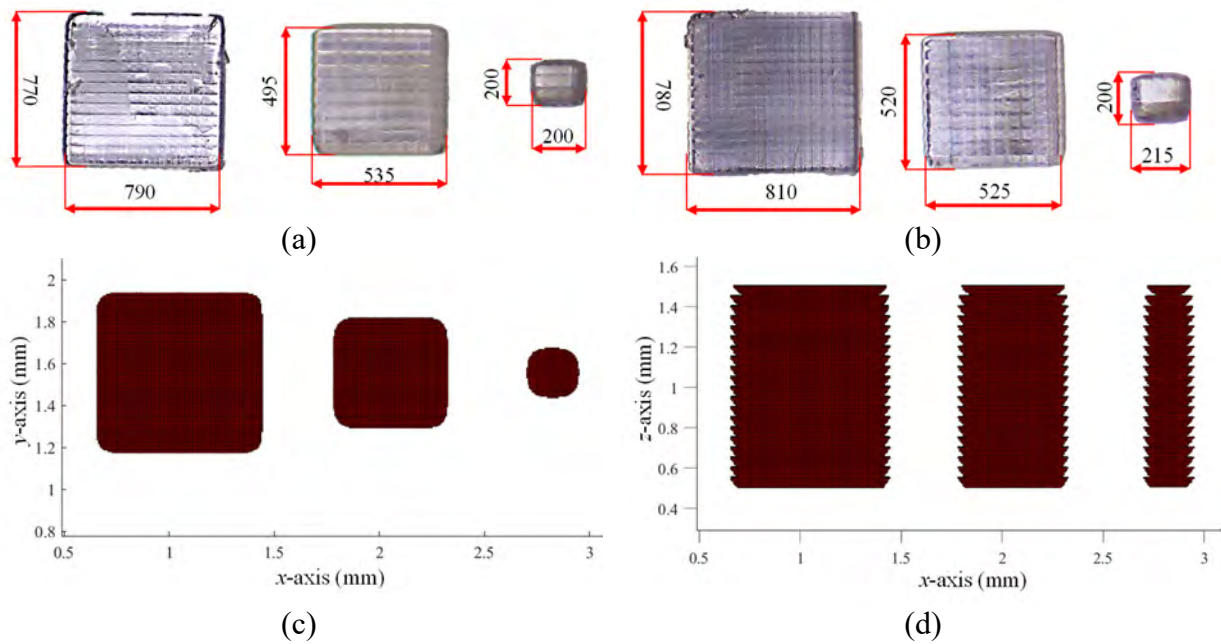


Figure 4-8 Comparison between manufactured vertical square bars at (a)  $d_z = 50 \mu\text{m}$  and 2 s and (b)  $25 \mu\text{m}$  and 1.8 s, against the prediction results of  $d_z = 50 \mu\text{m}$  and 2 s (c) top view and (d) front view of the square bars

Figure 4-8 shows a comparison between manufactured and prediction results of the vertical square bars with 750, 500, 200  $\mu\text{m}$  width and length. Qualitatively, the filleted corners in the manufactured part is captured by the prediction as shown in Figure 4-8 (c). The unique intrinsic surface roughness shape is captured by the prediction geometry as shown Figure 4-8 (d) which matches the electron and confocal microscope images presented and analyzed in section 2.4.5. Quantitatively, the deviation from the nominal design dimensions was captured by the predicted

parts within some errors as documented in Table 4-2. A general trend noticed is that the predicted geometries are slightly larger than the average measured dimensions of the manufactured part. The maximum error was found to be 40  $\mu\text{m}$  and occurred when predicting the 200  $\mu\text{m}$  square bare dimensions at both layer thickness values. The lowest error of 10  $\mu\text{m}$  occurred in predicting the 750  $\mu\text{m}$ . The layer thickness was not significantly affecting the both the manufactured and the predicted vertical square bar dimensions. It is worth mentioning that the prediction algorithm was running at a resolution of 6.25  $\mu\text{m}$ ; which is the value set to the Gaussian density parameter in the algorithm ( $G_d$ ).

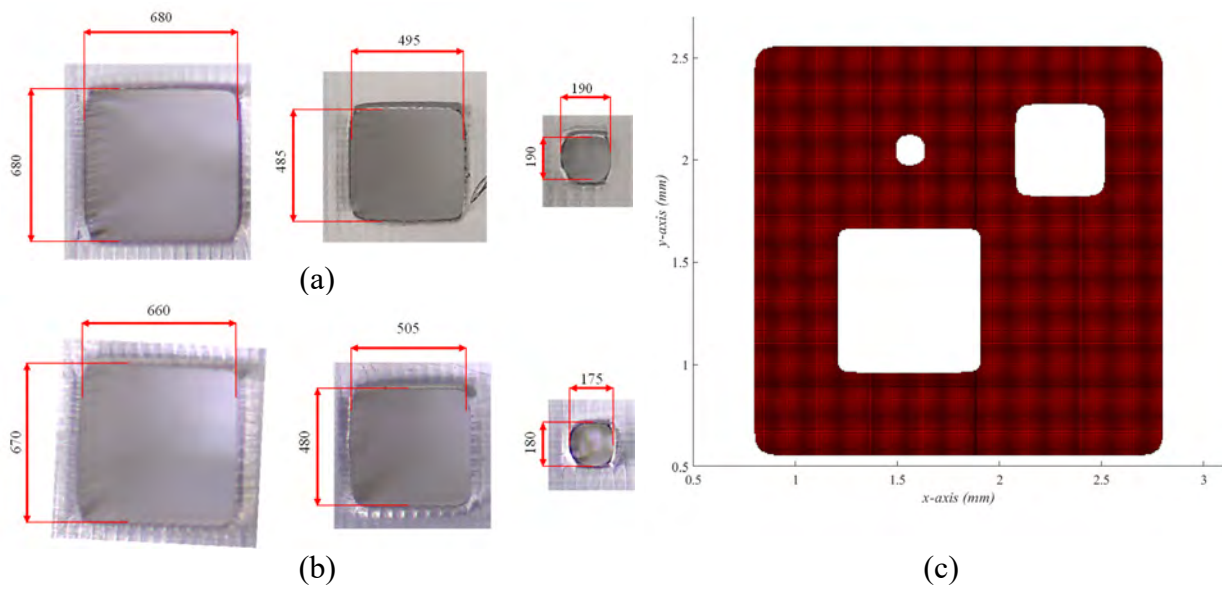


Figure 4-9 Comparison between manufactured vertical square holes at (a)  $d_z = 50 \mu\text{m}$  and 2 s and (b) 25  $\mu\text{m}$  and 1.8 s, against the prediction results of  $d_z = 50 \mu\text{m}$  and 2 s (c) top view of the square bars

Figure 4-9 shows a comparison between manufactured and prediction results of the vertical square holes with 750, 500, 200  $\mu\text{m}$  width and length. Qualitatively, the filleted corners in the manufactured part is captured by the prediction as shown in Figure 4-9 (c), in addition, the near circular shape of the 200  $\mu\text{m}$  in the manufactured part is simulated in the prediction shape. Quantitatively, the deviation from the nominal design dimensions was captured by the predicted parts within some errors as documented in Table 4-2. A general trend noticed is that the predicted vertical holes are slightly smaller than the average measured dimensions of the manufactured part, except for the 750  $\mu\text{m}$  holes the predicted hole was larger. The maximum error between the manufactured and predicted geometry occurred at the 500  $\mu\text{m}$  hole with 50  $\mu\text{m}$  error value, while the lowest error occurred at 750  $\mu\text{m}$  with 20  $\mu\text{m}$  error value.



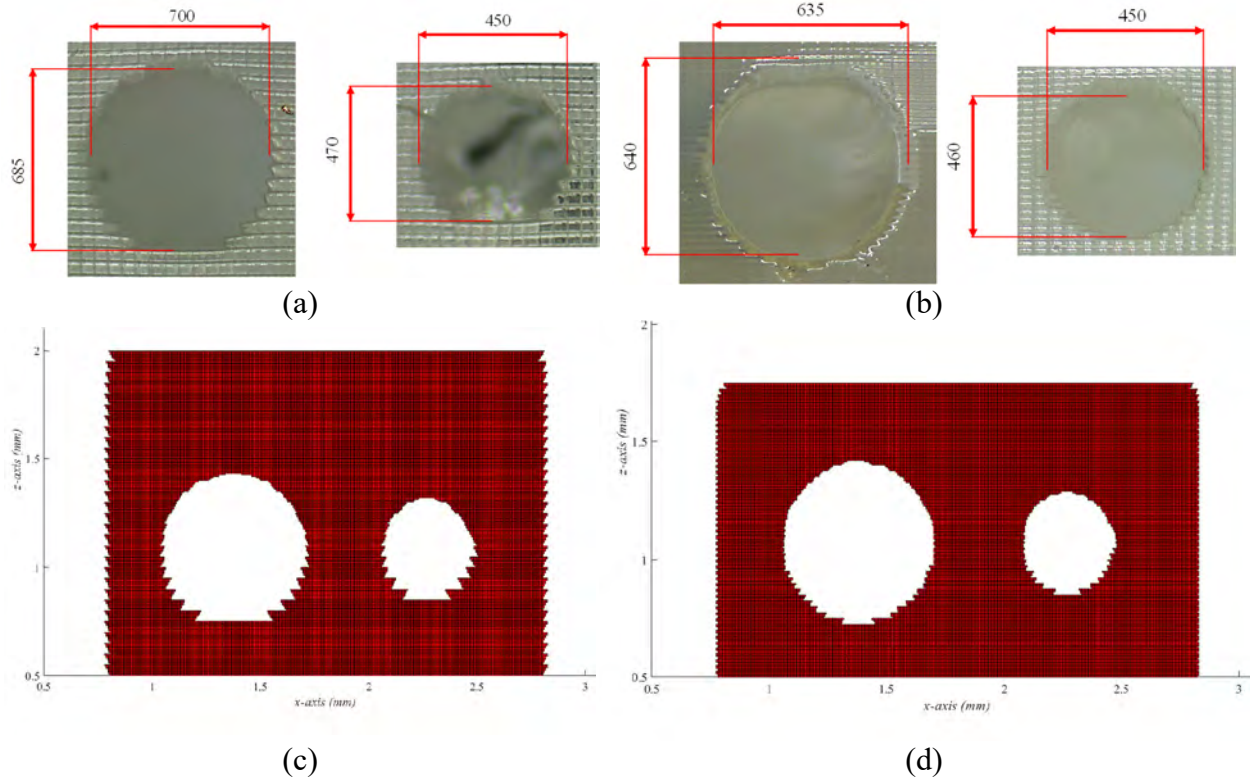


Figure 4-10 Comparison between manufactured horizontal circular holes at (a)  $d_z = 50 \mu\text{m}$  and 2 s and (b)  $d_z = 25 \mu\text{m}$  and 1.8 s, against the prediction results showing the front view of (c)  $d_z = 50 \mu\text{m}$  and 2s and (d)  $d_z = 25 \mu\text{m}$  and 1.8

Figure 4-10 shows a comparison between manufactured and prediction results of the horizontal circular holes with 750, 500, 200  $\mu\text{m}$  diameters. Qualitatively, the manufactured circular holes matches the predicted holes from the geometrical shaped deviation aspect, where the bottom half of the hole shows the intrinsic surface roughness shape of the PSLA process. While the top half of the hole has a smoother surface. Additionally, the top surface of the hole has a visible significant flat portion. Both the prediction and the manufactured part showed that holes less than 500  $\mu\text{m}$  are not manufactured for the used resin at the manufacturing settings selected. Quantitatively, the deviation from the nominal design dimensions was captured by the predicted parts within some errors as documented in Table 4-2. A general trend noticed is that the predicted horizontal holes are slightly smaller than the average measured dimensions of the manufactured part. The maximum error between the manufactured and predicted geometry occurred at the 750  $\mu\text{m}$  hole with 30  $\mu\text{m}$  error value, while the lowest error occurred at 500  $\mu\text{m}$  with 10  $\mu\text{m}$  error value. In contrary to the two previously analyzed features, the horizontal holes predicted dimensions, geometrical deviation, and prediction error depends on the axis, as the vertical dimension of the

hole is governed by the light penetration through the layers; while the horizontal dimensions of the hole are governed by the Gaussian profile.

Table 4-2 Dimensions comparison between predicted and physically manufactured geometries

Feature	$d_z$ ( $\mu\text{m}$ )	t (s)	Nom. Dim. 750 $\mu\text{m}$			Nom. Dim. 500 $\mu\text{m}$			Nom. Dim. 200 $\mu\text{m}$		
			Measured	Predicted	Error	Measured	Predicted	Error	Measured	Predicted	Error
Vertical Bars	50	2	770	790	20	510	540	30	200	240	40
	25	1.8	795	800	10	520	550	30	220	255	35
Vertical Holes	50	2	680	700	20	490	445	45	185	160	25
	25	1.8	665	690	25	470	420	50	175	135	40
Horizontal Holes	50	2	700/685	670/680	30/5	450/470	440/460	10/10			
	25	1.8	640/635	660/650	20/15	450/460	420/450	30/10			

With a maximum prediction error of 50  $\mu\text{m}$  and as low as 10  $\mu\text{m}$ , the prediction algorithm proves its worthiness in estimating the geometrical and dimensional deviation of different features. The errors are due to known limitations to the prediction algorithm, such as shrinkage modelling is not considered, resin flow and surface tension, and the geometrical distortion due to separation forces.

#### 4.4.2 Optimization Algorithm Evaluation

In order to evaluate the efficiency of the optimization methodology, a simple test specimen is developed which contains 3 different features. The test specimen is a  $2 \times 2 \times 2$  mm simple cube with two horizontal holes 0.75 mm and 0.5 mm diameters. On top of the cube, there are two hollow cylinders with different dimensions with OD 0.75mm / ID 0.35mm and OD 0.5 mm/ ID 0.2 mm, as shown in Figure 4-11. The testes specimen will be sliced without utilizing any optimization method to produce raw image with only black and white pixels and the dimensions will be predicted using the previously presented algorithm. Then the images produced after each optimization stage will be used to predict the dimension after each stage and the dimension measured are documented in Table 4-3.

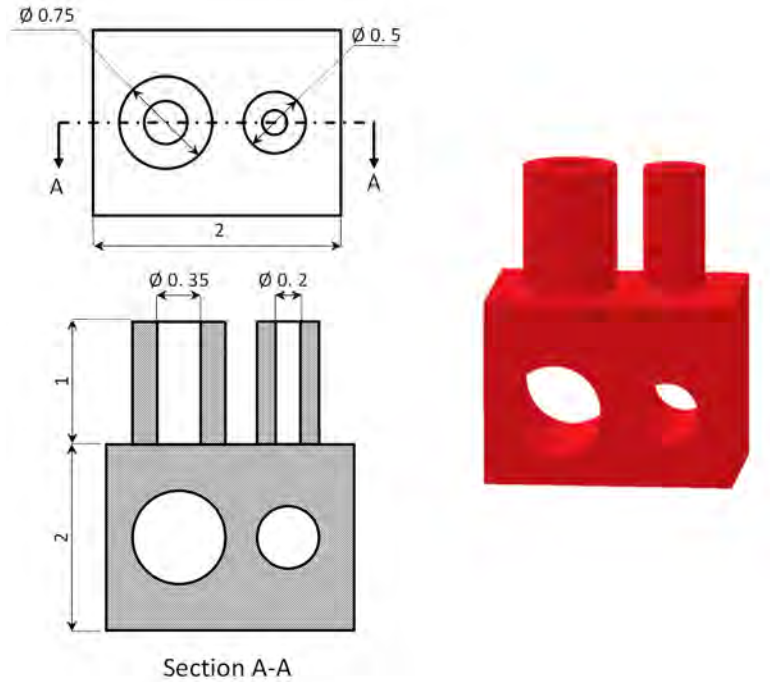


Figure 4-11 Optimization algorithm evaluation test specimen

A sample of the raw sliced image with only black and white pixels showing a section in the top cylinders with a rough and pixelated shape is shown in Figure 4-12 (a) and compared to the smoother processed image after applying the pixel blending algorithm as shown in Figure 4-12 (b).

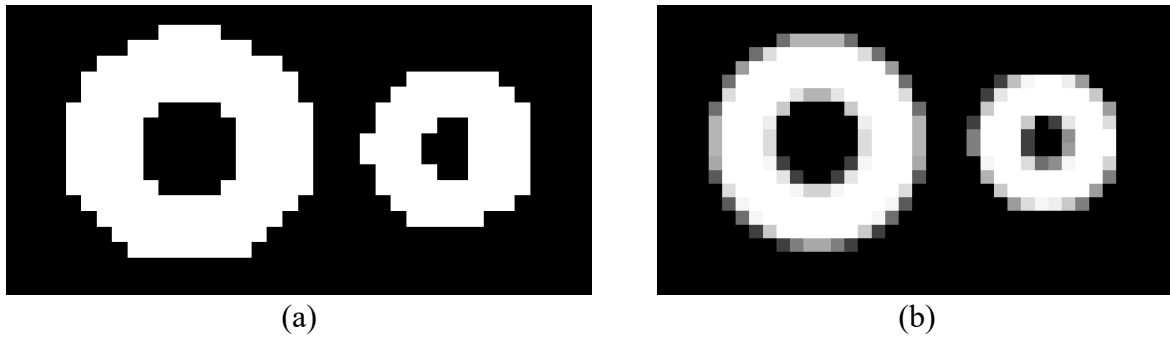


Figure 4-12 Machine input image example showing (a) raw sliced image (black and white pixels) only and (b) pixel blending output with grayscale pixels on the boundaries

The 3D prediction of the raw image at 50 $\mu$ m layer thickness and 2s exposure time is shown in Figure 4-13, while the 3D prediction of raw images sliced at 25 $\mu$ m layer thickness and 1.8s is evaluated, documented, and compared to other scenarios in Table 4-3. The vertical cylinders show a significantly distorted shape with a high circularity error as shown in Figure 4-13(c). The



maximum circularity error of  $25\text{ }\mu\text{m}$  was calculated for both the cylinders when manufactured at  $25\text{ }\mu\text{m}$  layer thickness, while the lowest recorded was for  $20\text{ }\mu\text{m}$  for the cylinders printed at  $50\text{ }\mu\text{m}$  layer thickness. The maximum deviation error from the design nominal diameter measured is  $100\text{ }\mu\text{m}$  for the cylinders manufactured with  $25\text{ }\mu\text{m}$  layer thickness, while the lowest is  $40\text{ }\mu\text{m}$ . Vertical holes also have the circularity issue and the smaller hole is partially manufactured. The circularity error is within  $7.5\text{--}10\text{ }\mu\text{m}$  and with deviation from the nominal design diameters around  $70\text{--}100\text{ }\mu\text{m}$ . The horizontal holes have a circularity error between  $20\text{--}30\text{ }\mu\text{m}$  and deviates from the nominal dimensions by  $40\text{--}110\text{ }\mu\text{m}$ .

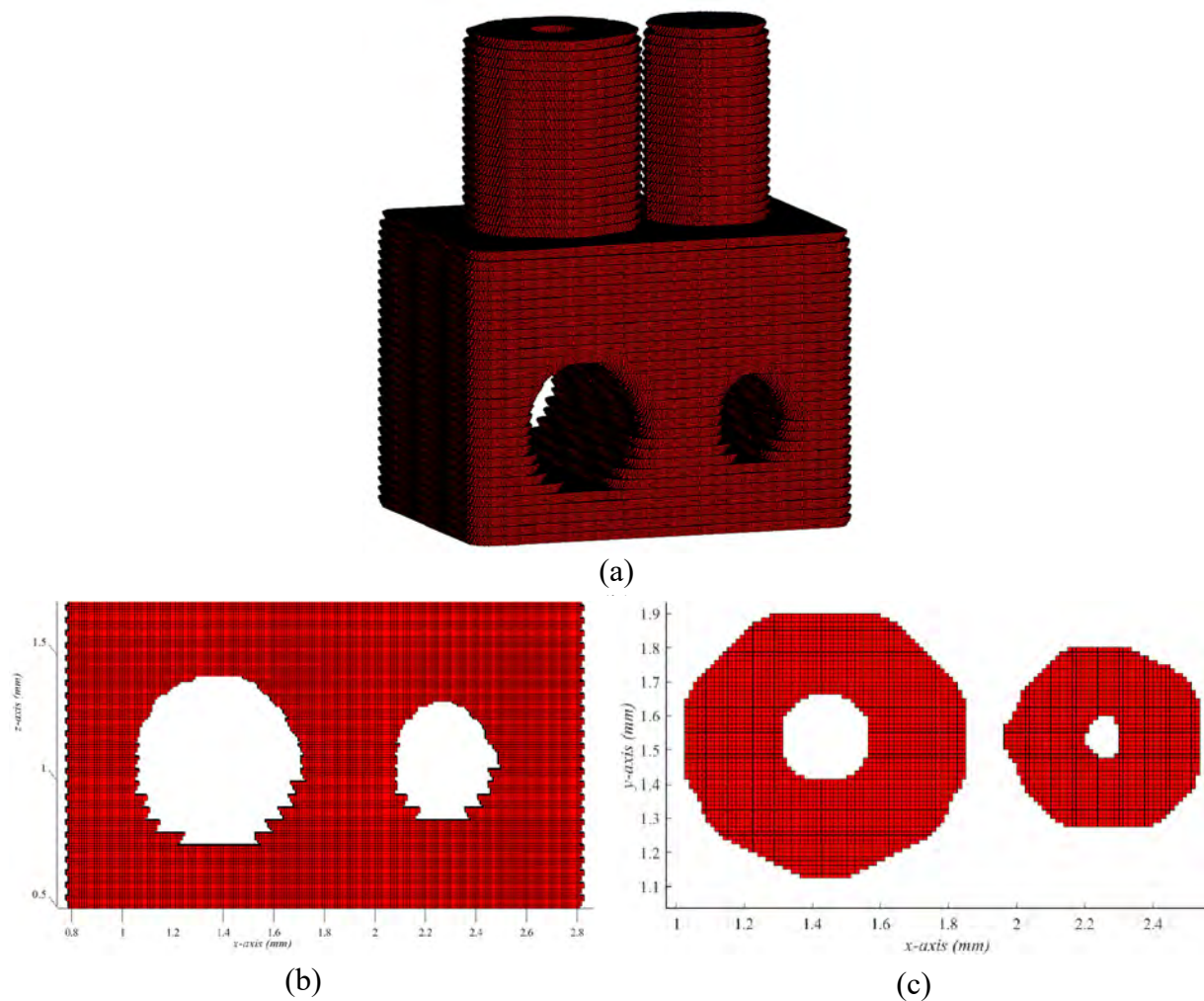


Figure 4-13 3D predicted geometry of the raw images (a) isometric view, (b) front view, and (c) top view

The first stage in the optimization is processing the initially sliced images with the pixel blending algorithm. The grayscaled output slicing image from the first stage is shown in Figure 4-12 (b) and the predicted geometry is shown in Figure 4-16 (b). Qualitatively, both the vertical cylinders and holes showed circularity improvements. The pixel blending, as documented in Table 4-3, has improved the circularity error to be within the 10-15  $\mu\text{m}$  for the vertical cylinders compared to the 20-25  $\mu\text{m}$  from the raw image. It also reduced the deviation error from the nominal dimensions to be within 30-80  $\mu\text{m}$  compared to the raw images which have

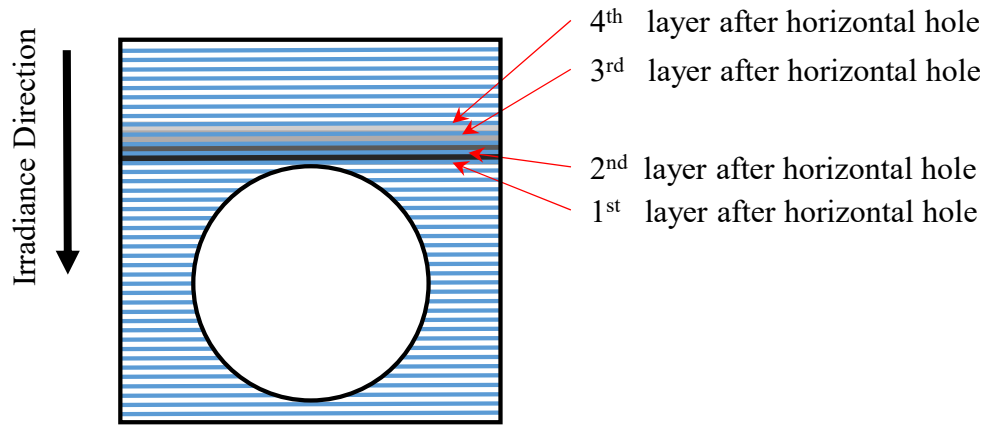


Figure 4-14 Illustration of the target layers to be optimized with the Cross Layers Optimization (CLO) algorithm

The cross layers optimization (CLO) algorithm optimizes the grayscale color of the layers within the irradiance affected zone (IAZ) which are manufactured just after the horizontal cavities/holes as illustrated in Figure 4-14. The output of the pixel blending is fed to the CLO algorithm, and the processed images after applying the CLO is compared to the raw images and presented in Figure 4-15. The CLO grayscale colors optimized for each layer above the 750  $\mu\text{m}$  hole are 75, 90, 120, and 180 bit out of 256 bit image in sequence starting from the first layer above the hole as shown in Figure 4-15 compared to the raw images which are all white (255 bit) above the hole. As the layer number progress, the area above the hole brightens from a dark grey till it reaches complete white. The predicted geometry is shown in Figure 4-16. Qualitatively, the horizontal holes circularity improved compared to the raw image and the pixel blended image while there were no improvement to the vertical cylinders beyond the enhancement of the pixel blending. Quantitatively, the circularity error for the horizontal holes reduced to be within 15-20  $\mu\text{m}$  compared to the 20-30  $\mu\text{m}$  of the raw image error. The deviation from the nominal dimensions in

the vertical diameter of the horizontal hole was reduced to be within 20-30  $\mu\text{m}$  compared to 30-50  $\mu\text{m}$  of the pixel blending and 40-70  $\mu\text{m}$  of the raw images. The vertical diameter did not improve beyond the pixel blending results. The dimensions of the vertical cylinder did not improve considerably compared to the horizontal hole beyond the pixel blending results.

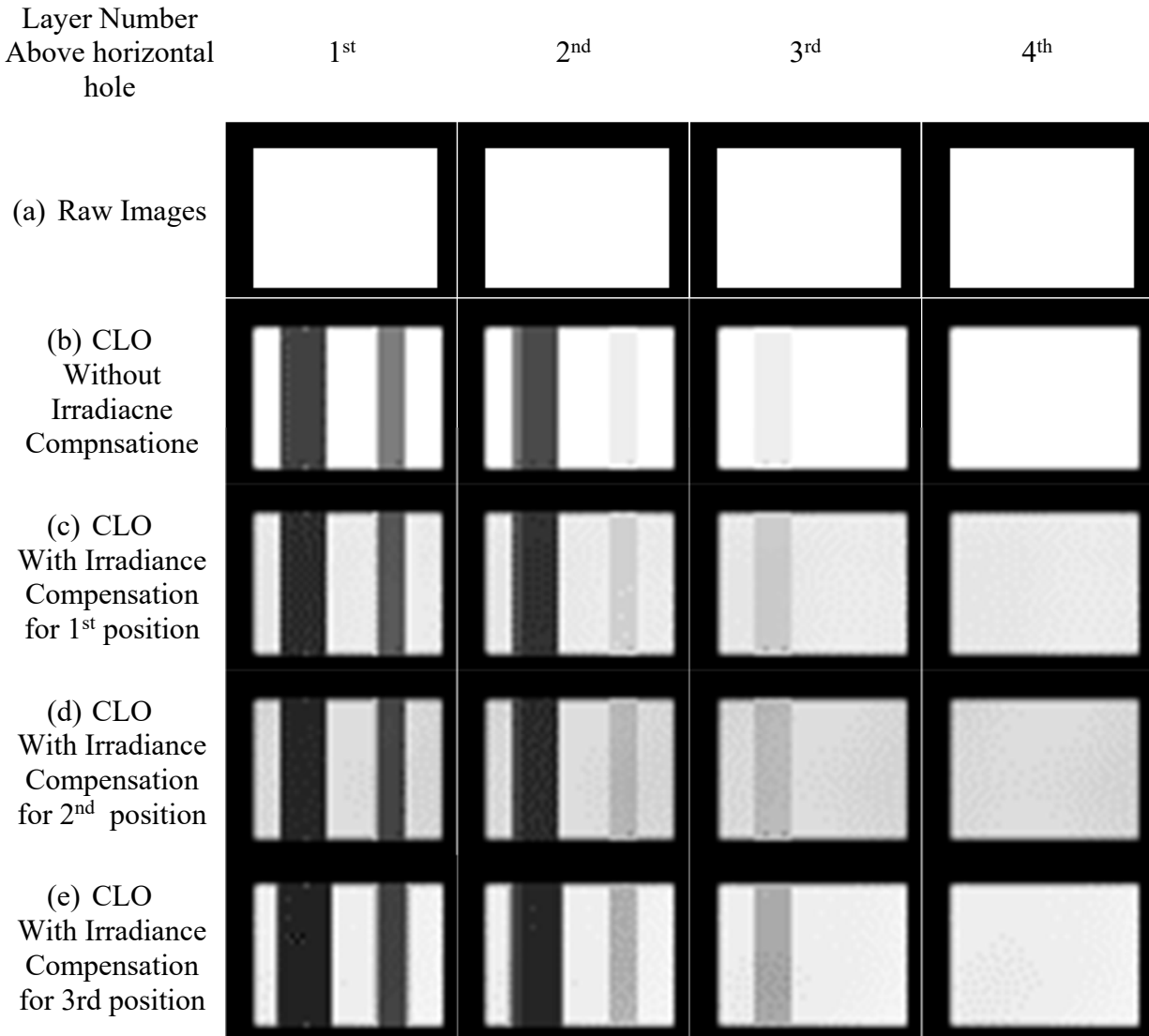


Figure 4-15 Processed images through (a)Raw image, (b) Pixel blending + CLO, the three optimization stages at the location identified in Figure 3-8 (c) 1<sup>st</sup> position, (d) 2<sup>nd</sup> position, and (e) 3<sup>rd</sup> position

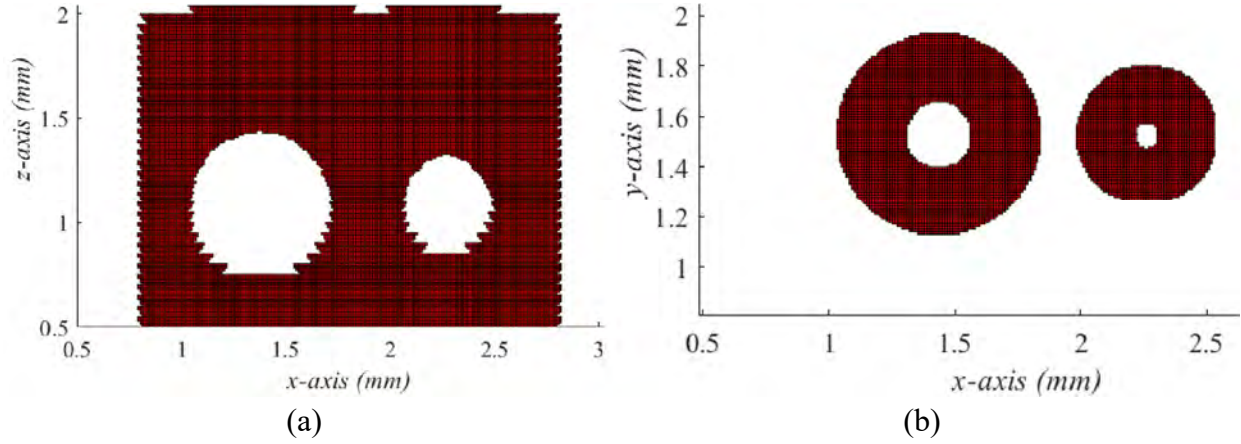


Figure 4-16 3D predicted geometry after applying pixel blending and CLO (a) front view and (b) top view

Table 4-3 Comparison between the different stage of the optimization and the raw images

Feature	$d_z$ ( $\mu\text{m}$ )	$t$ (s)	Raw image			Pixel Blending Error			CLO		
			Predicted ( $\mu\text{m}$ )	Circ. Error ( $\mu\text{m}$ )	Error from design	Predicted ( $\mu\text{m}$ )	Circ. Error ( $\mu\text{m}$ )	Error from design	Predicted ( $\mu\text{m}$ )	Circ. Error ( $\mu\text{m}$ )	Error from design
Vertical Cylinders (750 $\mu\text{m}$ )	50	2	830/790	20	80/40	800/780	10	50/30	800/780	10	50/30
Vertical Cylinders (500 $\mu\text{m}$ )	25	1.8	850/800	25	100/50	830/780	10	80/30	830/780	10	80/30
Vertical Cylinders (500 $\mu\text{m}$ )	50	2	580/540	20	80/40	550/530	10	50/30	550/530	10	50/30
Vertical Cylinders (500 $\mu\text{m}$ )	25	1.8	600/550	25	100/50	580/540	15	80/40	580/540	15	80/40
Vertical Holes (350 $\mu\text{m}$ )	50	2	270/250	10	80/100	290/270	5	60/80	290/270	5	60/80
Vertical Holes (350 $\mu\text{m}$ )	25	2	250/230	10	100/120	290/250	10	60/100	290/250	10	60/100
Vertical Holes (200 $\mu\text{m}$ )	50	1.8	130/100	10	70/100	140/120	7.5	60/80	140/120	7.5	60/80
Vertical Holes (200 $\mu\text{m}$ )	25	2	115/100	7.5	85/100	130/120	5	70/80	130/120	5	70/80
Horizontal Holes (750 $\mu\text{m}$ )	50	1.8	680/640	20	70/110	700/690	7.5	50/60	720/690	15	30/60
Horizontal Holes (750 $\mu\text{m}$ )	25	1.8	700/640	30	50/110	700/680	10	50/70	720/680	20	30/60
Horizontal Holes (500 $\mu\text{m}$ )	50	2	460/420	20	40/80	480/440	15	30/60	480/450	20	20/50
Horizontal Holes (500 $\mu\text{m}$ )	25	1.8	440/400	20	60/100	460/430	15	40/70	480/440	20	20/60

The last stage of the optimization methodology is the irradiance compensation algorithm. The algorithm was evaluated by calculating the exposure energy across the whole build platform when projecting a white image as shown in Figure 4-17 (a) for 2 seconds. The resultant accumulated energy varies between 27 and 49 mJ/cm<sup>2</sup> as shown in Figure 4-17 (b). By utilizing the irradiance compensation algorithm a compensated image was generated as presented in Figure 4-17 (c) and the equivalent exposure time was calculated to be 3.3 seconds. The resultant exposure energy

from the irradiance compensated image has a uniform energy of 49 mJ/cm<sup>2</sup> across the build platform as presented in Figure 4-17 (d). Finally, the algorithm was implemented to generate the images for the optimization test specimen presented in Figure 4-11 to be manufactured at 3 different on the three identified locations as shown in Figure 3-8 simultaneously. The resultant sliced image for each part is shown in Figure 4-15 (b), (c), and (d). Since the second location has more average irradiance than the other two locations, it has darker grey colours than the other two locations. The exposure time increased from 2s original time dictated by pixel blending to be 3s. The predicted shapes received approximately identical accumulative energy per pixel for the three different locations.

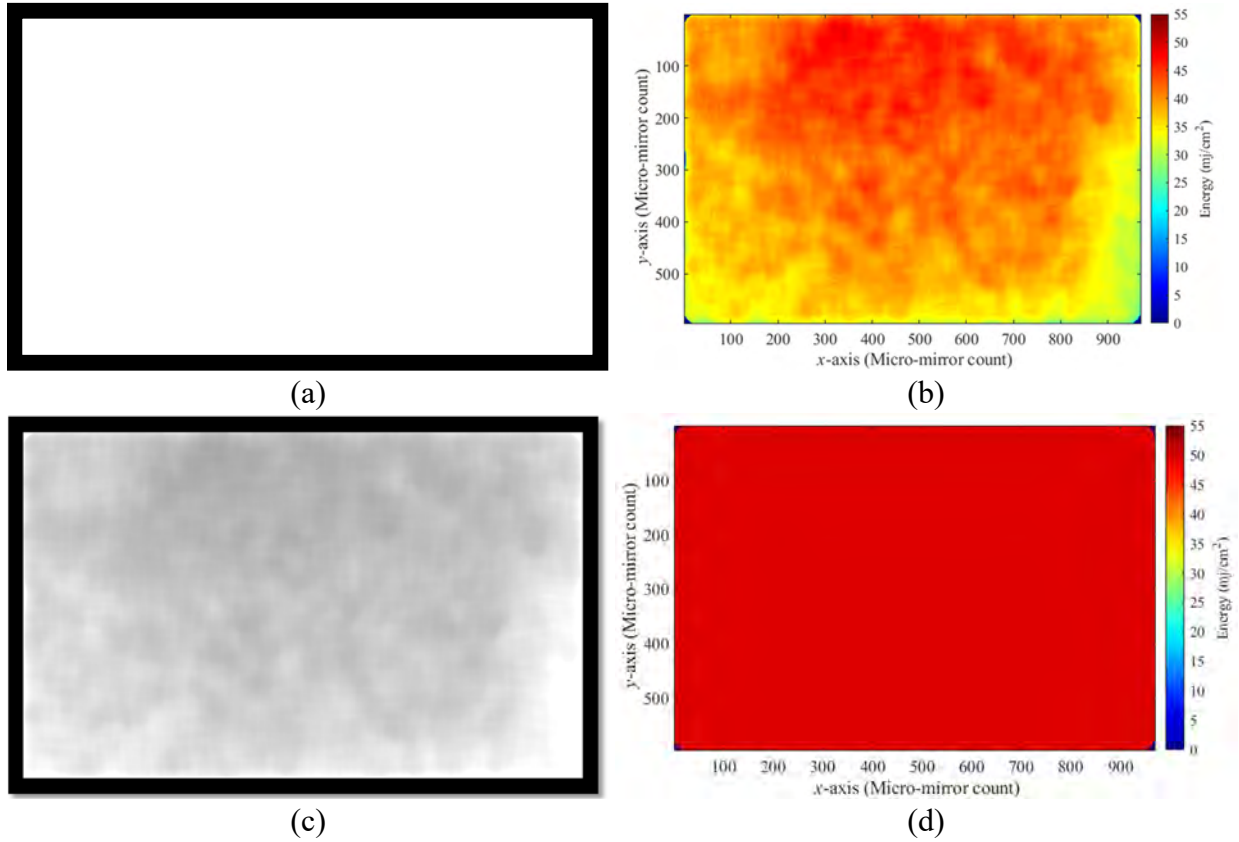


Figure 4-17 (a) uncompensated white image projected across the build platform for 2s and (b) exposure energy per each location in the build platform as a result of projecting image in (a), (c) compensated image using the developed algorithm projected for 3.3 , and (d) a uniform exposure energy per each location in the build platform as result of projecting the image in (c)

## 4.5 Conclusion

The main aim of this chapter is to provide a tool to optimize the geometry produced by the PSLA process. This chapter has two main objectives. The first is to develop an algorithm to simulate the expected manufactured part three-dimensional geometry and represent the shape using a voxel logical array. The second objective is to develop a 3D optimization methodology for PSLA that can be applied to the different resin types. This chapter directly answers the main research hypothesis that the geometry can be optimized without affecting the mechanical properties by optimizing the process parameters. The optimization algorithm will improve the geometry while maintaining the mechanical properties at a level that ensures the part's structural integrity during manufacturing. Then after manufacturing, the mechanical properties can be enhanced further with the post-curing process. Predicting parts geometry ahead of manufacturing will minimize manufacturing costs by minimizing the manufacturing trials in case of part failure.

It was shown that the 3D prediction algorithm is capable of predicting geometries using sliced images within 10 to 40 microns of error. The algorithm showed distorted shapes and dimensions that agreed with the measured values in chapter 2. The algorithm was also able to predict the distinctive surface roughness, which also agreed with the measured results in chapter 2.

A three-stage geometry optimization algorithm was proposed. The algorithm utilizes the concept of irradiance affected zone to minimize the number of pixels to be tuned. The algorithm was able to improve the circularity of vertical cylinders and enhance the dimensions of horizontal holes. The algorithm was able to account for the irradiance map irregularities while not interfering with other optimization steps. The overall circularity errors across the different studied features was reduced to be within 5-20 microns compared to 7.5 to 30 microns in the raw images. The deviation error from the nominal design dimensions was reduced to be within 20-80 microns compared to 40-110 microns in the raw images. The irradiance compensation algorithm improved the uniformity of the exposure energy across the build platform.

The optimization algorithm was not able to improve the horizontal dimensions significantly. The pixel blending algorithm efficiently improved the shape form but not the dimension; therefore, a more rigorous optimization algorithm should be developed to improve horizontal dimensions. The proposed methodology did not integrate the surface roughness optimization algorithms, and it should be the extent of this work in the future.

## **5 Effect of Design Parameters on Mechanical Properties and Cost of Fused Deposition Modeling (FDM) Parts\***

The Fused Deposition Modeling (FDM) process is the most commonly used additive manufacturing technique due to its simplicity and the range of available materials. The quality of the parts printed via FDM depends on several process parameters. These parameters are dependent on the Computer-Aided Design (CAD), Computer-Aided Manufacturing (CAM), and material. The variation in design and process parameters affects the ultimate strength and modulus of elasticity. It affects the manufacturing time and volume, which translates into the final cost of the part. This chapter aims to define a cost-based method, taking into account the product and part design parameters to manufacture parts optimized for strength and cost. The study focuses on a systematic design of experiments to measure the ultimate tensile strength, ultimate flexural strength, modulus of elasticity, time, and volume based on ISO-compliant specimens.

This chapter will investigate a different type of process outcomes coupling, namely the mechanical properties and cost, and how to minimize such coupling using part design parameters which answer another aspect of the main thesis hypothesis. This chapter uses empirical modelling to predict mechanical properties and cost of FDM manufactured parts.

### **5.1 Introduction**

The slicer software allows the manipulation of different design parameters: each layer's raster pattern, infill density, number of contours, number of shells, layer thickness, raster orientation, raster width, air gap, and part orientation. Other parameters control the printing process like printing speed, travelling speed, extruder temperature, and build plate temperature. Each printing parameter affects mechanical properties, quality, volume, printing time, and finally, cost of the printed part.

Researchers have studied different parameters combinations to optimize the FDM process parameters to get the best mechanical properties (M), cost (\$), dimensions (D), and time (T) as shown in Table 5-1. Raster orientation, raster width, layer thickness, part orientation, air gap are the most studied parameters among the other parameters. Table 5-1 shows the parameter

---

\* This chapter is published as "Mostafa, K.G.; Montemagno, C.; Qureshi, A.J. Strength to cost ratio analysis of FDM Nylon 12 3D Printed Parts. *Procedia Manuf.* 2018, 26, 753–762."

significance in each work. The most significant parameter equals one, and as this value increases, the significant decrease. The most studied material for FDM process optimization is the ABS. The parameters' significance reported in the literature vary based on the other parameters included in the experiment and the parameter's value range selected for the experiment.

Table 5-1 Summary of the FDM design and process parameters studied in the literature

Reference No.	Year	Material	Raster Width	Layer Thickness	Contour Width	Air Gap	Nozzle Temp.	Raster Pattern	Raster Ort.	Part ort.	Feed rate	Scale	Location	Extrusion Speed	Build plate Temp	Peeling Temp	Infill Density	Number of shells	Shell Spacing	Response
[95]	01	ABS	3			2	4		1											M
[96]	01	ABS	3	2				1												TD
[97]	05	ABS	4	1		2			3											M
[98]	10	PC	2					1	3											M
[99]	12	ABS							•											M
[100]	14	ABS	2			1			3	4										M
[101]	14	ABS	3			2				1										\$
[102]	15	ABS		6			12	11	3			1	10	5	4	7	8	2	9	M
[103]	15	PEEK		1					2											M
[104]	16	ABS						2									1			M
[105]	17	PC							2	1										M
[106]	17	ABS	•	•	•	•			•	•										\$
[107]	17	ABS	4	1		5			3	2										D
[108]	17	ABS	4	1	6	3			5	2										T
[109]	17	PLA		2						1	3									M

The effects of raster width, air gap, nozzle temperature, raster orientation, and filament colour on the tensile strength of ABS were studied in [95]. The raster width and nozzle temperature do not significantly affect the strength, while the raster orientation and air gap are the main significant parameters. The raster width and nozzle temperature do not significantly affect the strength, while the raster orientation and air gap are the main significant parameters.

Multi-objective optimization to minimize printing time and decrease dimensional accuracy was performed in [96]. The parameters used in this research are layer thickness, raster width, and filling strategy, which represent both the infill percentage and raster pattern. The flexibility of a 3D printed catapult, made of ABS, measured in terms of throw distance, was significantly improved in [3] by optimizing the air gap, raster angle, layer thickness, and raster width. The raster



width was the least significant, the layer thickness was the most significant, while the other two parameters were semi-equal in their significance. The raster pattern, raster angle, and raster width values were manipulated to result in higher tensile strength of polycarbonate (PC) material [98]. The 3D printed PC Specimen, compared to an injected one, has a tensile strength of 70-75% of the tensile strength of the injected PC. The effect of raster orientation on different mechanical responses has been studied in [99]. The ultimate compressive strength seems slightly affected for the compression test, while the ultimate tensile and flexure strength are significantly affected by the raster orientation. The optimization of the tensile strength of 3D printed ABS was also studied in [100] in the light of the part orientation, raster angle, air gap, and raster width, and the optimum levels were also concluded using the group method for data handling and differential evolution. The effect of part orientation, air gap, layers, and raster width on printing cost is studied in [101]. The part orientation was the major contributor, as different part orientations may result in printing more support materials and may increase the number of layers, increasing the support material volume and printing time.

An extensive experiment consisting of 12 printing, 3-levels, factors, and one scalability factor was designed in [102] to determine the parameters' significance and optimize them for higher ultimate tensile strength and elastic modulus. As the parts scale up, their strength decreases, unlike other manufacturing processes. The influence of the layer thickness and raster angle of 3D printed polyether-ether-ketone (PEEK) was studied in a comparative study with the ABS in [103]. The mechanical properties of 3D printed PEEK is higher than that of the 3D printed ABS. Different infill patterns and densities impact the tensile strength and modulus of elasticity of 3D printed dog bones specimens made of ABS in [104]. The rectilinear (double sparse) and honeycomb patterns show a competitive result at different densities, and the infill density fits as a second-order polynomial function. The effect of part orientation and raster angle on 3D printed ABS and PC specimens [105]. The different orientations studied are flat, on edge, and upright orientations, while the raster angles are 0°, 15°, 30°, and 45°. With a 45° raster angle, the flat orientation has the higher ultimate tensile strength for the PC specimens and the flat orientation, with a 0° raster angle, for the ABS Specimen.

The response surface method is used in the multiobjective optimization of the build time and volume to minimize the printing cost [106]. This study included the raster width, angle, part orientation, and air gap as the printing parameters and the signs were not discussed. Fuzzy logic

has been integrated with a Taguchi DOE to predict the external dimension accuracy of rectangular specimens [107]. The effect of part orientation on building time only was experimented with [108].

Different materials have been developed and standardized as feedstock filaments. Some of the standard materials in the market are ABS, polyethylene, polypropylene, PC, ABS-M30i, ABSi, ASA, PLA, PCL, PLGA, PC-ABS, PC, PC-ISO, PPSF/PPSU, ULTEM 9085, FE-Nylon, FE-ABS, AL<sub>2</sub>O<sub>3</sub>-Nylon, Nylon 6, and Nylon 12 [110]. The choice of the printing material is influenced by its characteristics that are suitable for a target application. The characteristics can include biocompatibility, UV resistance, static charge resistance, flexibility, endurance under cyclic loads, optical properties, and heat resistance [110].

Previous research studies focused on optimization of the FDM printing of ABS with limited work done on PC. Many other materials that are available for FDM still need characterization. Nylon 12, for example, is used in aerospace and automotive applications due to its mechanical properties, fatigue endurance, impact resistance, vibration absorption, low friction coefficient, and flexibility under low temperature, besides its chemical resistance. Limited literature is available on the effect of FDM parameters on the mechanical properties of Nylon in general and Nylon 12 specifically.

There are several successful multi-objective optimization studies in the literature to optimize printing time, dimensional accuracy, printing time, and printing volume. Besides the many studies to optimize the mechanical properties, geometrical accuracy, or cost independently. The influence of FDM parameters on mechanical properties while considering cost and time has not been studied before. This chapter studies the effect of seven FDM parameters, selected from previous research work as shown in Table 5-1, on the mechanical properties of Nylon 12 printed specimens, along with printing time and total volume, which reflect the product cost. The mechanical properties considered in this study are the ultimate tensile strength (UTS), tensile modulus (TE), ultimate flexure strength (UFS), and flexure modulus (FE). The parameter's significance of each response is determined. Taguchi's method is implemented to optimize each response based on the estimated parameters' optimum levels. The strength to cost ratio is optimized using a meta-model predicted based on Taguchi mean responses.

## **5.2 Methodology**

The study follows a systematic experimental design methodology based on Taguchi's Design of Experiment (DOE). This method reduces time and money spent on experimental work and

provides a consistent experimental approach, ensuring repeatability. The responses considered in the experiment are tensile and flexure ultimate strength, tensile and flexure modulus of elasticity, time and printed part volume. The material used for the experiments is the standard Nylon 12 produced by Stratasys. Figure 5-1 shows the methodology used, in which two CAD files are created in STL format for the tensile and flexure tests. Insight<sup>®</sup> is the slicer software (CAM) used to convert the CAD files into G-code corresponding to each configuration per each test type as specified in the DOE. The Stratasys Fortus 900mc FDM machine is used to print five replicates for each configuration. The printed specimens are conditioned for 88 hours before they are tested for either tensile or flexure. The ultimate strength is then determined using the stress-strain curves obtained from the testing. By analyzing the parameters at different levels and the corresponding response, the parameters' significance and optimum levels are determined. Using the responses from Taguchi's method, a full factorial array is predicted to determine the configuration of the highest strength to cost ratio specimen.

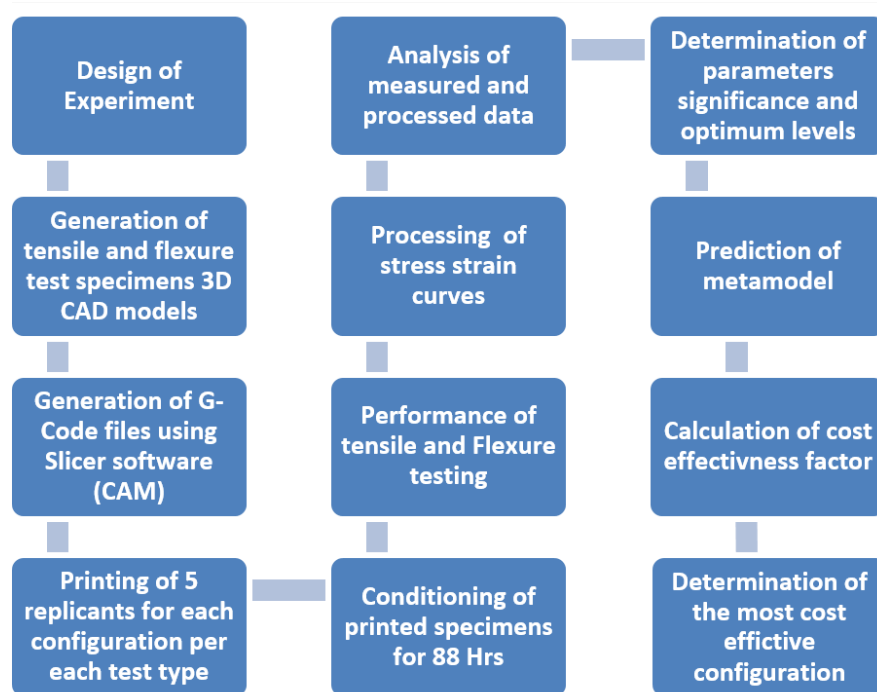


Figure 5-1 Flow chart showing the different steps in the methodology proposed

### 5.2.1 FDM Design Parameters

This chapter investigates seven FDM parameters highly significant on the ultimate tensile strength and printing time based on literature, as shown in Table 1. All of the selected parameters were ranked as the first or the second most influential parameter, at least in one cited research. Despite the high significance of the air gap parameter, it was not included in the study, as it is usually used to describe the material overlap. The infill density defines the percentage of filling effortlessly. This study aims to minimize the volume of material to decrease the cost while having a high strength-to-cost ratio. The part orientation has a high significance, but it is set to be flat in the direction of the x-axis, as the parts have more strength than either on edge or in the upright orientations [105]. Insight software limits the number of variables controlled by the user, for example, temperature, feed rate, and speed parameters. The unstudied parameters are fixed at default settings from the insight.

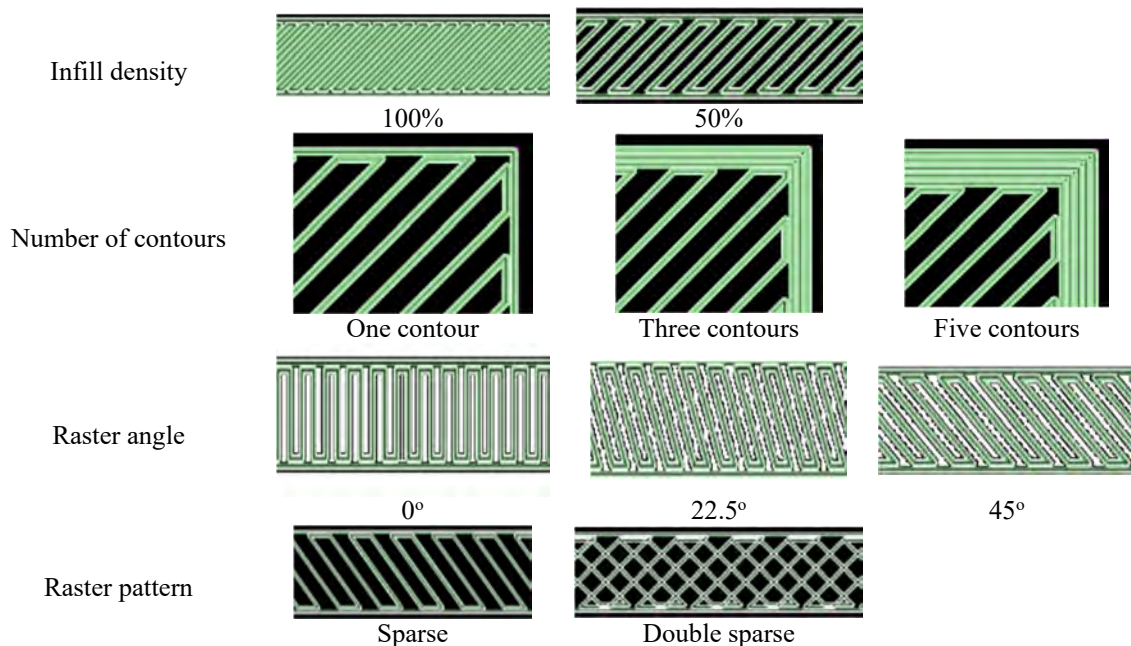


Figure 5-2 Illustration of different parameters values

The parameters considered are described below and shown in Figure 5-2.

1. Infill density specifies the percentage of the printed region of each core layer.
2. Number of Contours is the number of borders surrounding the infill (raster) in each layer.
3. Raster orientation refers to the angle between the raster direction and the x-axis.

4. Raster pattern could be either sparse or double sparse. Sparse means that the first layer will have the raster with specified orientation, and the successive layer is printed with a 90° shift, while double sparse means that each layer will contain both the sparse and the 90° shifted-sparse.
5. Number of shells describes the number of upper and lower surfaces of the printed body, which has 100% infill density.
6. Raster width refers to the width of the extruded filament material.
7. Layer thickness refers to the thickness of each layer.

### **5.2.2 Materials and test Specimen**

The material investigated in this study is Nylon 12, which is a thermoplastic material. The ultimate tensile strength is 46 MPa, while the ultimate compressive strength is 167 MPa, with the elongation percentage at failure at 30%. It poses an impact resistance of 135 J/m for the notched specimen while 1656 J/m for the unnotched specimen. The melting point of Nylon 12 is 178°C. These properties are based on Stratasys Nylon 12 datasheet [111], in which they used a specimen that follows ASTM D638 and has printing settings of 100% infill density, 0.01" (0.254 mm) layer thickness, and flat orientated. The chemical resistance chart of Nylon 12 shows that it is resistant to various acids, bases, oils, and grease.

Standard tensile and flexure tests were performed to evaluate the stress-strain relation of the printed Nylon 12 specimens. The tensile test specimens selected follow ISO 527-2:2012(E) standard of a dog-bone shape of type 1B. The flexural test specimens follow ISO 178:2010(E). Before the testing, the dimensions of each specimen are measured three times at equidistant positions, and nominal dimensions are considered.

### **5.2.3 Design of experiment**

Systematic design of experiments was carried out to evaluate the relationship between the responses and parameter changes within the prescribed ranges [112]. The infill density has six levels, while the other parameters have three levels, except the raster pattern has only two levels, as shown in Table 2-1. A full factorial design of experiments for such a configuration would result in 2916 experimental trials. Taguchi's design of experiment method was used for an L-18 orthogonal array covering a different combination of levels for each parameter, with a total of 18

experiments, to reduce the experimental effort. Taguchi orthogonal arrays provide unique, balanced, and minimum experimental trials and are capable of determining the significance and optimum levels for each parameter. The raster pattern has only two levels due to a software limitation. Therefore a dummy level technique was used to degrade its column from two degrees of freedom to one degree of freedom; by repeating the sparse level as the first and second level with the double sparse as the third level.

Table 5-2 Level values for each parameter

	<b>Parameter</b>	<b>L1</b>	<b>L 2</b>	<b>L 3</b>	<b>L 4</b>	<b>L 5</b>	<b>L 6</b>
X <sub>1</sub>	Infill Density (%)	10	28	46	64	82	100
X <sub>2</sub>	Layer thickness (mm)	0.178	0.254	0.33			
X <sub>3</sub>	No. of contours	1	3	5			
X <sub>4</sub>	Raster Pattern	Sparse	Sparse	Double			
X <sub>5</sub>	Raster width (mm)	0.457	0.584	0.71			
X <sub>6</sub>	No. of shells	2	3	4			
X <sub>7</sub>	Raster orientation (°)	0	22.5	45			

#### 5.2.4 Test procedure

After printing using Fortus 900mc, the test specimens are conditioned at room condition for 88 hours after printing at a temperature of 23°C and about 35% average humidity. The machine used in both the tensile and flexure testing is the MTS 810 testing machine. The tensile tests run at an extension speed of 1 mm/min according to ISO 527 standards, while the 3-point flexure tests are at a loading speed of 2 mm/min according to ISO 178 standards. All the testing was considered completed when a sign of failure/breakage or excessive necking occurred in the test specimen.

### 5.3 Results

The L18 orthogonal array along with the corresponding mean values of the measured responses are shown in Table 5-3. The mean of the measured UTS values range from 9.9 to 43.6 MPa; the uncertainty ranges between 0.26 to 2.37% with a mean of 0.9% and the standard deviation of 0.93%. The mean measured UFS values range from 16.1 to 62.9 MPa; the uncertainty within each trial over the whole experiment ranges 0.85 to 3.82% with an average of 1.53% and a standard deviation of 0.72%, as shown in Figure 5-3.

The output of each test is a stress-strain data from which all the material properties are estimated. The modulus of elasticity is the slope of the straight line between the stress points at a strain of 0.05% and 0.25%. The ultimate strength is the maximum stress at failure.

The build time and volume of the tensile specimen are calculated using the Insight software. The cost is estimated based on the building time and the volume of material required using (5-1).

C1 is the price per time and equals 0.33 \$/min, while C2 is the price per unit volume and equals 0.348 \$/cm<sup>3</sup>. The price rates are obtained based on average quoted prices from the Canadian market. The strength per unit cost (MPa/\$) defines the strength to cost ratio for each trial.

$$C = C1 * t + C2 * V \quad (5-1)$$

Table 5-3 L-18 Orthogonal array with corresponding measured results

#	X1	X2	X3	X-4	X5	X-6	X7	UTS (MPa)	Time (min)	V (cm <sup>3</sup> )	TE (MPa)	FE (MPa)	UFS (MPa)	C (\$)	Z (MPa/\$)
1	10	0.178	1	1	0.457	2	0	9.9	16	5.70	364	492	16.1	7.32	1.36
2	10	0.254	3	2	0.584	3	22.5	25.9	12	8.21	821	957	44.5	6.86	3.78
3	10	0.33	5	1	0.711	4	45	36.9	12	11.27	1100	1168	59.7	7.92	4.66
4	28	0.178	1	2	0.584	4	45	18.7	19	8.75	588	854	37.1	9.38	2
5	28	0.254	3	1	0.711	2	0	27.0	12	8.64	844	929	44.7	7	3.86
6	28	0.33	5	1	0.457	3	22.5	30.8	14	10.05	949	1087	54.9	8.16	3.78
7	46	0.178	3	1	0.711	3	45	24.7	21	10.42	846	931	44.7	10.62	2.33
8	46	0.254	5	2	0.457	4	0	34.9	17	10.49	1041	1148	57.7	9.31	3.75
9	46	0.33	1	1	0.584	2	22.5	18.6	11	9.36	642	928	41.8	6.92	2.69
10	64	0.178	5	1	0.584	3	0	28.5	26	11.47	1098	1083	55.5	12.65	2.26
11	64	0.254	1	1	0.711	4	22.5	29.6	13	10.95	943	1089	55.6	8.14	3.64
12	64	0.33	3	2	0.457	2	45	26.3	14	10.73	772	1008	47.9	8.4	3.14
13	82	0.178	3	1	0.457	4	22.5	30.3	30	12.19	1012	1102	55.9	14.24	2.13
14	82	0.254	5	1	0.584	2	45	38.6	17	11.77	1193	1212	59.0	9.76	3.96
15	82	0.33	1	2	0.711	3	0	29.7	12	11.83	983	1082	55.5	8.12	3.61
16	100	0.178	5	2	0.711	2	22.5	40.8	26	13.22	1358	1265	62.4	13.26	3.08
17	100	0.254	1	1	0.457	3	45	43.6	19	12.59	1298	1231	62.9	10.71	4.08
18	100	0.33	3	1	0.584	4	0	38.9	14	12.73	1151	1135	60.6	9.1	4.28

### 5.3.1 Data Analysis

#### 5.3.1.1 Parameter Significance

The Taguchi analysis method is implemented within Minitab software to analyze the orthogonal array and the corresponding measured values. The ranking method, based on both the signal-to-noise ratio and mean of means, is used to determine the significance of each parameter on the different responses. Parameters ranking is shown in Table 5-4.

The infill percentage is the most significant for all measured responses except for the time, which is ranked second. For the UTS, the four leading significant parameters are infill percentage, number of contours, layer thickness, and the number of shells, respectively, and they control 80% of the UTS value.

The most significant printing parameters influencing the build-time are the layer thickness, infill percentage, number of contours, and raster width, respectively, with a total percentage of 81%. The volume and the UFS share the same most significant three parameters that are as follows, the infill percentage, the number of contours, and the number of shells, the fourth significant parameter for the volume is the orientation and for the UFS is the layer thickness.

The parameter significance rank of the tensile and flexure modulus matches those of the UTS.

The box plots in Figure 5-3 are sorted based on the two most significant parameters; infill density and number of contours. It can be noticed in both Figure 5-3(a) and b, the number of contours significantly affects the UTS and UFS in the lower infill densities, and this effect decrease as the infill percentages increase. At the infill densities of 82% and 100%, the effect of the number of contours becomes less, and the other parameters seem to control the values of UTS

#### **5.3.1.2 *Optimum parameters levels***

For each response, there is a set of optimal printing parameter values which results in the highest or the lowest response value. The optimal level for each printing parameter is depicted from either the signal-to-noise ratio or the main effects plots, depending on the goal of the analysis. The signal to noise ratio predicts the optimum level for a robust response, while the main effects plot predicts the optimum levels for a high or low mean response. In this study, the optimum levels were chosen based on the larger, better selection method for all the parameters except for the time and volume which are smaller the better. In this study, both the mean effects and the SN ratio plots show the same optimum levels. Only the main effects plots are shown in Figure 5-4 and Table 5-4.

In the main effects plot in Figure 5-4, the horizontal dash line shows the mean result of the corresponding measured response values, while the dots show the average of the corresponding response values at each parameter's level.



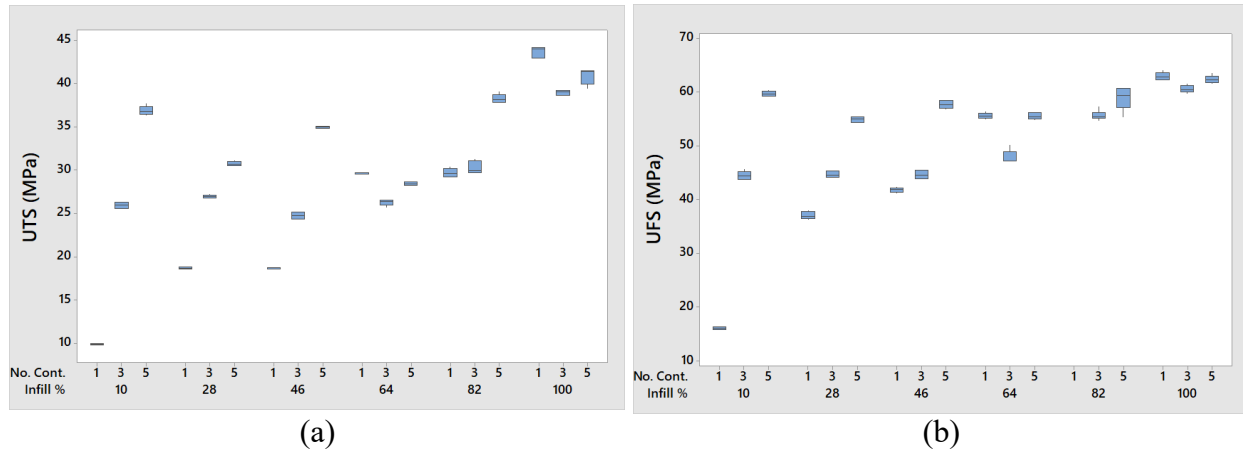


Figure 5-3. Box plots for (a)ultimate tensile strength and (b) ultimate flexure strength

To maximize one response only, the levels of the parameters corresponding to the highest values for this response are selected from the main effects plot. In contrast, to minimize one of the responses the levels of the parameters corresponding to the lowest values are selected. Then by using the Taguchi prediction method as shown in equations (5-3) to (5-6)., the optimum response can be predicted. The ultimate tensile strength of mould injected Nylon 12, which equals to 46 MPa [111], is set as a bounding constraint for the optimization problem. The configuration that has the highest ultimate tensile strength can be predicted based on optimum levels from Figure 5-4.a, which equals 54.4 MPa with a cost of 11.2 \$ using equation (5-7). This value exceeds the ultimate strength stated; therefore, a saturation threshold was implemented on the configurations, giving more than 46 MPa.

Table 5-4. Parameter significance rank

	Infill Density	Layer Thickness	No. of Contours	Raster Width	Number of Shells	Raster Angle	Raster Pattern
UTS	1	3	2	5	4	6	7
Delta	16.8	7.79	10.04	0.4	3.24	4.71	3.31
Time	2	1	3	4	5	6	7
Delta	6.33	10.17	3.67	0.42	2.33	1.4	1.6
Volume	1	6	2	5	3	4	7
Delta	0.27	0.042	0.092	0.033	0.046	0.071	0.047
UFS	1	4	2	6	3	7	5
Delta	21.8	8.8	13.36	0.11	4.5	9.11	4.16
TE/FE	1	3	2	5	4	6	7
Delta	338	139.8	214.7	19.9	66.4	110.3	93.3

## 5.4 Optimization model

This study aims to maximize the strength to cost ratio as shown in equation (5-2). The ultimate tensile strength is the only mechanical response considered for the optimization, but different objective criteria can be directly adopted, for example, flexure strength to cost or tensile strength to volume ratio. The UTS, volume, and time are evaluated by the Taguchi response prediction method using equations (5-3) to (5-6). The predicted cost is calculated based on (5-7). The prediction method used is valid only within the experimented parameters levels combination only; this limit is described by (5-8). The predicted volume is limited to the volume of a full solid specimen (5-9). The predicted UTS is limited to the ultimate tensile strength of the mould injected Nylon 12 specimen (5-10).

The optimum solution is based on the predicted responses of the UTS, volume, time, and cost from the full factorial array, 2916 combinations, which contains all the experimented parameters combinations. The combination with the highest strength to cost ratio is selected. The optimum strength to cost ratio is 5.3 MPa/ \$, where the UTS is 33.9 MPa, and the cost is 6.4 \$, as shown in . Five contour lines and the three shell layers develop the strength of the part. The optimum configuration is validated by printing and testing five replicates. The stress-strain curves of the five samples are shown in Figure 5-5. The average ultimate tensile strength is 36.4 MPa, while the average actual printing time is 10.5 min, and the average actual volume is 10.5 cm<sup>3</sup>. Therefore the cost is 7.12\$. The strength to cost ratio is 5.1 MPa/\$. The Prediction error for the UTS is 6.8 %, for the time is 15.2 %, and for the volume is 6.6%. The overall error in the strength to cost ratio is 4%.

Table 5-5. Optimum Configurations

Infill %	L. Th.	N. Contours	Pattern	R. Width	N. Shell	R. Angle	UTS (MPa)	Time (min)	VOLUME (cm <sup>3</sup> )	Cost (\$)	TE (MPa)	UFS (MPa)	FE (MPa)	UTS/ \$
10	0.33	5	1	0.71	3	45	33.9	8.9	9.8	6.4	1028	53	1064	5.3

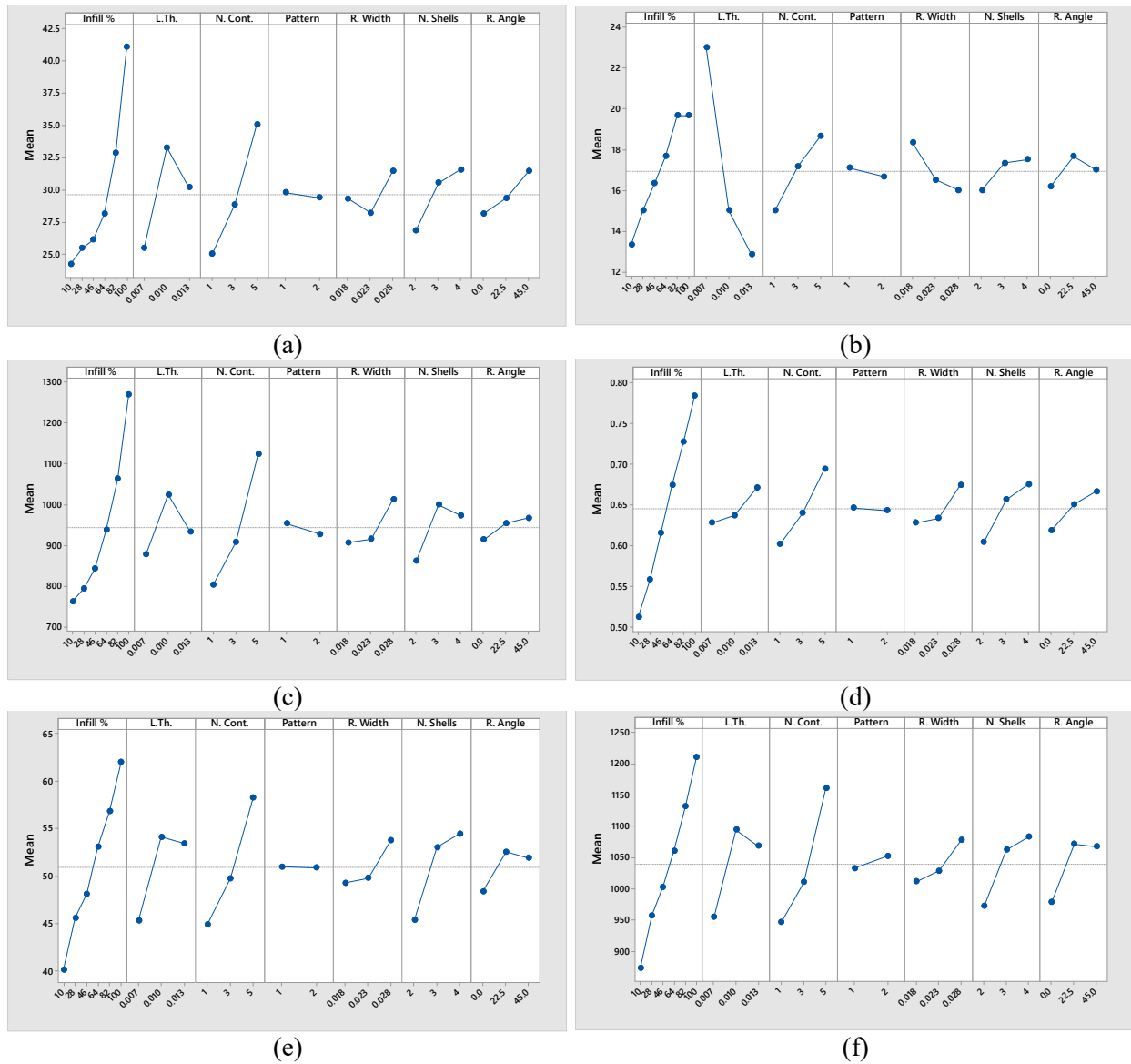


Figure 5-4. Main effects plot for (a) ultimate tensile strength, (b) manufacturing time for tensile samples, (c) tensile modulus, (d) volume, (e) ultimate flexure strength, and (f) flexure modulus

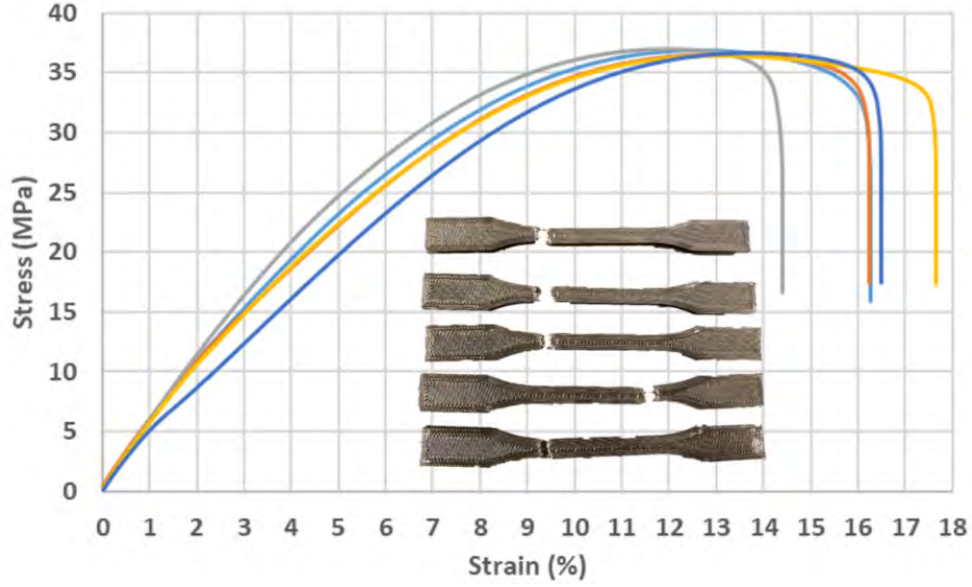


Figure 5-5. Stress-strain curves for the validation sample

$$\max: Z_p = \frac{UTS_p}{C_p} \quad (5-2)$$

*Subjected to:*

$$UTS_p = \overline{UTS} + (\overline{UTS}_{x1i} - \overline{UTS}) + (\overline{UTS}_{x2j} - \overline{UTS}) + (\overline{UTS}_{x3k} - \overline{UTS}) + (\overline{UTS}_{x3l} - \overline{UTS}) + (\overline{UTS}_{x3m} - \overline{UTS}) + (\overline{UTS}_{x6n} - \overline{UTS}) + (\overline{UTS}_{x7q} - \overline{UTS}) \quad (5-3)$$

$$V_p = \bar{V} + (\bar{V}_{x1i} - \bar{V}) + (\bar{V}_{x2j} - \bar{V}) + (\bar{V}_{x3k} - \bar{V}) + (\bar{V}_{x3l} - \bar{V}) + (\bar{V}_{x3m} - \bar{V}) + (\bar{V}_{x6n} - \bar{V}) + (\bar{V}_{x7q} - \bar{V}) \quad (5-4)$$

$$T_p = \bar{T} + (\bar{T}_{x1i} - \bar{T}) + (\bar{T}_{x2j} - \bar{T}) + (\bar{T}_{x3k} - \bar{T}) + (\bar{T}_{x3l} - \bar{T}) + (\bar{T}_{x3m} - \bar{T}) + (\bar{T}_{x6n} - \bar{T}) + (\bar{T}_{x7q} - \bar{T}) \quad (5-5)$$

$$\overline{UTS} = \frac{\sum UTS}{N}, \bar{T} = \frac{\sum T}{N}, \& \bar{V} = \frac{\sum V}{N} \quad (5-6)$$

$$C_p = C_1 V_p + C_2 T_p \quad (5-7)$$

$$i \in \{1,2,3,4,5,6\}, j, k, n, m, q \in \{1,2,3\}, \& l \in \{1,2\} \quad (5-8)$$

$$V_p \leq V_{max} \quad (5-9)$$

$$UTS_p \leq UTS_{max} \quad (5-10)$$

All variable are of a non-negative value

where :

$UTS_p$  : The predicted ultimate tensile strength.

$\overline{UTS}$  : The average of the grand total of UTS response over the 18 experiment.

$\overline{UTS}_{X_{1i}}$  : The Average of all the UTS responses corresponding to level  $i$  of parameter  $X_1$ .

$V_p$ : The predicted Volume.

$\bar{V}$ : The average of the grand total of Volume response over the 18 experiments.

$\bar{V}_{X_{3k}}$ : The Average of all the volume responses corresponding to level  $k$  of parameter  $X_3$ .

$V_p$ : The predicted volume.

$T_p$ : The predicted time.

$\bar{T}$ : The average of the grand total of time response over the 18 experiments.

$\bar{T}_{X_{7q}}$ : The Average of all the time responses corresponding to level  $q$  of parameter  $X_7$ .

$i, j, k, l, m, n, q$ : , Level index of each parameter.

## 5.5 Conclusion

The effect of seven FDM process parameters was studied on the ultimate tensile and flexure strength, tensile and flexure modulus of elasticity, building time, and volume of 3D printed Nylon 12 using Taguchi's L18 orthogonal array. The infill density was shown to be the most significant parameter for all responses, except the building time for which the infill density ranks second after the layer thickness. The number of contours is the second most significant parameter for all the responses except for building time, for which it ranks third after the infill density. The layer thickness ranks the third for most of the parameters except for the time it ranks the sixth. The number of shells is the fourth significant parameter for most of the parameters. The raster pattern has the lowest significance of all parameters, while for the volume, it ranks sixth. The first four significant parameters control about 80% of the response value.

The cost is calculated based on the volume, time, and recent price rates in the Canadian market, and then the strength to cost ratio is evaluated. The optimum level for each parameter was determined using the mean effects plot, and the response at the optimum levels was estimated using Taguchi's response prediction method.

An optimization model to maximize the strength to cost ratio based on predicting the responses for a full factorial array consisting of 2916 printing configuration were used. The optimized configuration was validated by the stress-strain curves of five replicates of the optimum configuration specimen. The optimum configuration recommends that lowering the infill density to the minimum will decrease the build volume, time, and UTS as well. However, the UTS is compensated by using the UTS optimum levels for all parameters except for infill density, for example, setting the number of contours, number of shells, layer thickness, and raster width to the maximum value available. The modulus of elasticity increased by increasing the ultimate strength in general. This research showed that with the Taguchi experimentation technique, a cost-based analysis could be developed to allow for the manufacture of 3D printed parts with high strength to cost ratio.

One of the limitations of this work is that the measured properties correspond to the strength of the specific test specimens, which can be altered if the specimen is scaled in the width or thickness directions. The FDM products are highly orthotropic materials; therefore, for each printing configuration, the modulus of elasticity, Poisson's ratio, and shear modulus for the three-main axis are entirely different. This issue is addressed in the next chapter. The cost model used in this study is limited, in which the printed material and machine costs are only considered, while the support material, pre-processing, and post-processing costs were not included in the model.

## 6 Mechanical Properties Modelling Using Reverse CAD

### Methodology\*

Fused Deposition Modeling (FDM) printed parts are widely used in various applications. It is necessary to assess the geometric and mechanical behaviour of the part beforehand to avoid material and time wastage. The CAD model is converted to a toolpath (sliced) before it is sent to manufacturing. The difference between the CAD and the toolpath model creates a research gap for estimating the part properties accurately. Since the manufactured part is not the replica of the original CAD model but of the sliced model, which is dependent on various slicing parameters, this chapter presents a novel algorithm, which is capable of converting the machine input G-code file back to a CAD model (called the Reverse CAD model). The Reverse CAD model is capable of providing an accurate assessment of the geometric and mechanical behaviour of the printed part as it also incorporates the effect of slicing parameters. In order to validate the algorithm, primitive geometries are printed, and mass properties are compared to the Reverse CAD model. Standardized tensile test specimens are also printed with two different materials to compare the experimental mechanical behaviour with the finite element analysis of the Reverse CAD model. Comparative studies validate the Reverse CAD model as a better and more accurate estimator of the FDM manufactured part properties

This chapter approaches the thesis hypothesis by providing a numerical 3D modelling tool to predict the mechanical behaviour and geometrical Quality of the part ahead of manufacturing which can cut manufacturing costs. While this chapter addresses only the mechanical behaviour prediction, the same algorithm was successfully used in predicting geometric deviations; for more information, see\*\*. Therefore by using the developed tool presented, the process outcomes coupling can be minimized.

### 6.1 Introduction

The FDM process introduces mechanical anisotropic behaviour to the manufactured part even when the filament used is of isotropic material. These anisotropic mechanical properties are

---

\* This chapter is part of the published article “Rupal, B.S.; Mostafa, K.G.; Wang, Y.; Qureshi, A.J. A Reverse CAD Approach for Estimating Geometric and Mechanical Behavior of FDM Printed Parts. *Procedia Manuf.* **2019**, *34*, 535–544.”

variable, and each of them is a function of the part orientation, infill percentage, raster orientation, raster pattern, and layer thickness[99,109,113]. Currently, to predict the mechanical behaviour of FDM manufactured parts, researchers use either use the design of experiments approaches to find best-fit regression [95]models or finite element analyses (FEA) with 100% solid CAD models. Each technique has its advantages and disadvantages, but neither of them can predict mechanical behavior generically and conveniently without depending on specific geometries or a certain range of parameters.

A constitutive model was presented to predict the mechanical behavior based on an orthotropic behavior stiffness matrix, and the constants are evaluated experimentally in[114]. Also, several analytical models to predict the strength of the part in terms of the bonding between filaments, raster, and part orientation were developed and experimentally validated in[102,115–117]. Various studies used FEA with different modeling philosophies to simulate the stresses along simple tensile test specimens[118]. The orthotropic material stiffness matrix was experimentally evaluated, and the FEA model used was a complete solid part. The effective stress for the overall part was estimated by performing an FEA for several single-layered FDM parts, where each layer had a different raster orientation, and then calculated overall part stresses [119]. A semi-realistic approach was presented in[120] ,in which a full standard tensile specimen was 3D modeled using 100% infill density layers with two alternating raster orientations per layer, where the 3D air gaps were geometrically included. The main disadvantages of the previously discussed FEA methods include that they require extensive material characterization to represent the orthotropic behavior and that they are limited to simple linear raster patterns and 100% infill density parts. A tool path generation using cladding and milling commercial software was presented in [121]to visualize the part exteriors and interiors for any geometry, but it was applied to visualize the toolpath only.

This chapter focuses on modeling the part design parameters and its effect on the final part mechanical properties without the need for experimentations. This will be realized by developing an algorithm which is capable of converting the sliced file (toolpath) back into a solid CAD model called the Reverse CAD model. The methodology for the work is shown in Figure 6-1. The generic AM process chain is modified. A geometric and mechanical analysis is performed on the Reverse CAD model to check the model for design requirements. If the conditions are met, then the sliced file is sent to print. Otherwise, design changes or parametric variations are made to meet the design



criteria. This chapter discusses only the mechanical properties prediction using the reverse CAD algorithm. For detailed information about the geometric analysis using the reverse CAD, see [11].

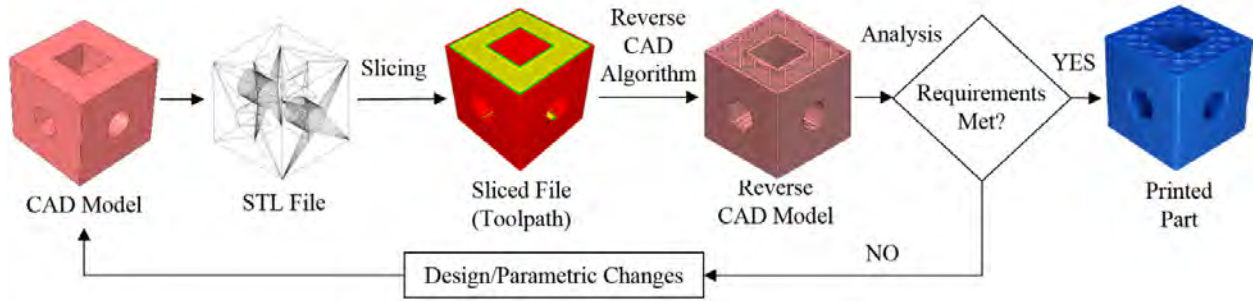


Figure 6-1A flowchart depicting the output property prediction methodology based on the Reverse CAD algorithm

## 6.2 Methodology

The FDM process starts by slicing the CAD file in order to be additively manufactured with respect to the required process parameters using pre-processing slicer software. The output of the slicing software is a G-code for the extruder nozzle path. The reverse CAD algorithm, which is demonstrated in Figure 6-2 The Reverse CAD algorithm, is written in the MATLAB environment. It reads the output G-code and the constants values; for example, the layer thickness and the road width are fed into it. It then calculates the deposited filament cross section parameters using equations (6-1) to (6-7). The deposited filament is assumed to ellipse, as shown in Figure 6-2, based on previous studies which used microscopy imaging to analyze the filament profile and used the ellipse to model mechanical and geometrical behavior [122] analytically. The deposited filament has  $l_a$  as the major radius and  $l_b$  as the minor radius of the ellipse, while  $w$  is the road width and  $r$  is the overlap ratio between adjacent filaments.  $lth$  is the layer thickness value used for FDM printing. Where  $S_1$  is the surface area of the filament before deposition, where  $D$  is the extruder nozzle diameter, and  $f$  is the shrinkage value after deposition and cooling off.  $S_2$  is the surface area of the ellipse of the deposited filament. By equating  $S_1$  and  $S_2$  and using equation (6-1) and (6-2), the ellipse radii and the overlap ratio are computed.

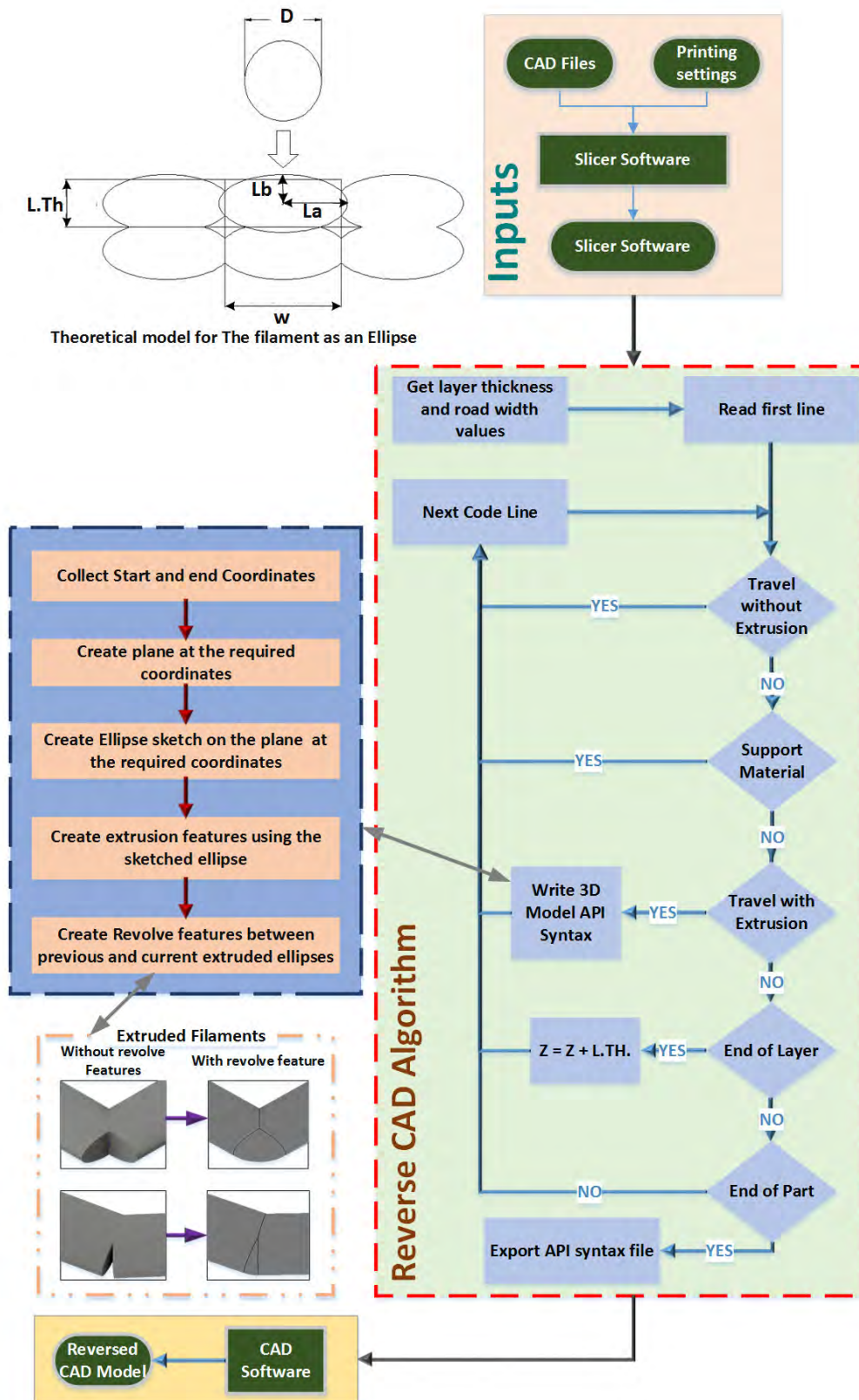


Figure 6-2 The Reverse CAD algorithm

$$l_a = \frac{w \times r}{2} \quad (6-1)$$

$$l_b = \frac{lth \times r}{2} \quad (6-2)$$

$$S_1 = \frac{D^2 \times \pi}{4} \times f \quad (6-3)$$

$$S_2 = l_b \times l_a \times \pi \quad (6-4)$$

$$r = \sqrt{\frac{D^2 \times f}{w \times lth}} \quad (6-5)$$

$$l_a = \sqrt{\frac{D^2 \times f \times w}{4 \times lth}} \quad (6-6)$$

$$l_b = \sqrt{\frac{D^2 \times f \times lth}{4 \times w}} \quad (6-7)$$

The algorithm scans the code line by line and searches for the different G-codes that correspond to different printing actions. There are two main modes in the FDM process: in the first mode, the extruder moves without printing in a fast approach motion, while in the second mode, it extrudes material with a certain linear speed. If the Reverse CAD model is required without the support materials, the code will discard any path for the support or the interface material. If the second printing mode is detected and the path is either a contour, a raster infill, or a shell, an Application Programming Interface (API) sequence syntax writing function is called in order to export the syntax used by the CAD software to generate a corresponding 3D model for the extruded path. The API collects the starting and end points of the current printing path and writes a syntax to create a plane at the start point and perpendicular to the required path. Then another syntax is created to sketch an ellipse on the previous plane using the previously calculated parameters. After that, a syntax is written for the extrusion boss/base of the created ellipse with an extrusion length correspondent to the difference between the start and end point of the printed line trajectory. The

extruded ellipse geometries are combined together as one part only at their intersection areas as shown in Figure 6-2, while the resultant voids between the non-intersecting ellipses are kept in the reverse CAD model. The last syntax is written to create a revolve feature between the currently printed line and the previous line, fill in the sharp gap developed, and to simulate the filament bending between two tool paths intersecting at an angle. After a layer ends in the G-code, the algorithm shifts the z coordinates in the vertical direction by the layer thickness value.

The algorithm exports a file containing sequenced API syntaxes after it determines that the printing of the part is finished in the G-code. In the CAD software, the API launcher is used to open the syntax file and the part is 3D modeled as instructed in the initial G-code. Finally, a CAD file is exported and can be opened with any CAD software and used to analyze the properties of the part. The time to convert the exported G-code into an API syntax file is negligible compared to the time to convert the API syntax into a reversed CAD model. The time consumed to create a reversed CAD model consisting of 700 features, like extrusions and revolves, with their sketches is around 1 hour. It was noticed and then experimented that as the number of features per part increase the time consumed to create the next feature within the same part takes longer time, for example the creation time of the feature with the sequence number of 100 is 1 s while the feature with the sequence number 400 is 3 s and the 700th features takes 8 s. The whole operation was done on a computer of 16 GB memory and Core I7 Processor with 4GHz capacity.

### 6.2.1 Validation

CAD models of primitive geometries were selected to demonstrate the capabilities of the algorithm. Reverse CAD models were generated for the designed models using the algorithm. A cube was modeled, saved as an STL file, and a slicing file was created. A sparse infill pattern was selected for the cubical part as well as a 45° raster angle. Similarly, a cylindrical part was modeled and saved as a slicing file. The critical process part design parameters for both of the parts are depicted in Table 6-1. The comparison between the manufactured parts and the reverse CAD models is presented in Figure 6-3. By comparing the masses of the reverse CAD model and the manufactured parts, the average error was found to be 14.1%.

Table 6-1 Part design parameters for validation

Parameters	Cube	Cylinder
Infill pattern	Sparse	Double sparse
Number of contours	5	4
Raster angle	45°	0°
Layer thickness (mm)	0.33	0.33
Number of shells	1	1
Infill density	50%	100%

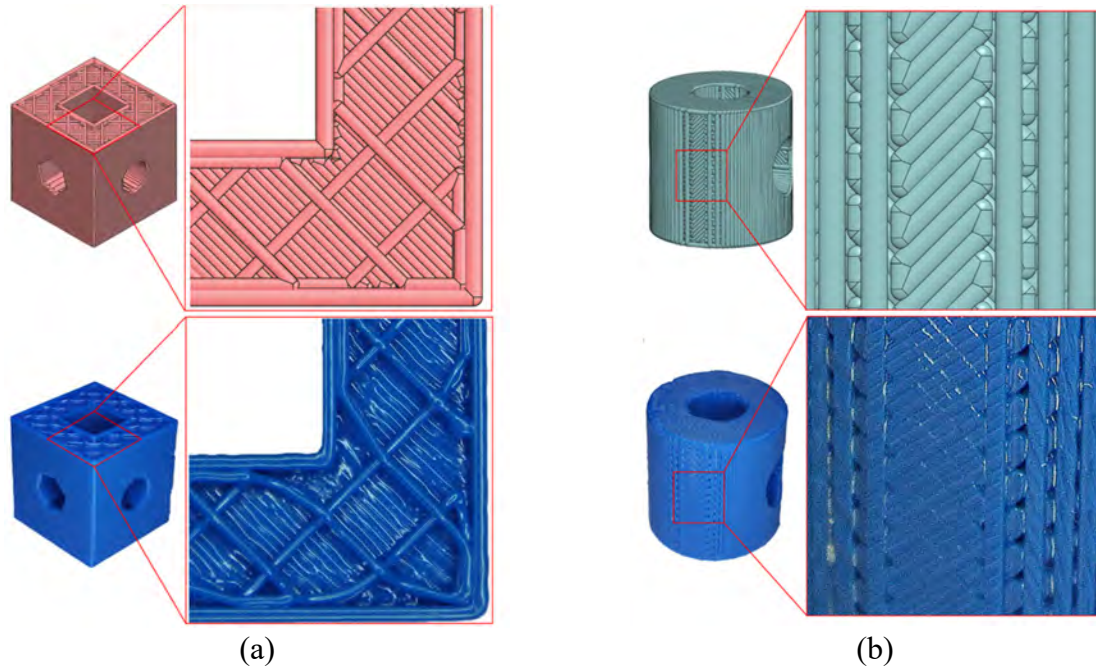


Figure 6-3 Reverse CAD model VS manufactured part of (a) Cube and b) Cylinder

### 6.3 Mechanical Behavior Prediction

One of the direct applications of the reverse CAD algorithm is to predict the mechanical behavior of FDM additively manufactured parts while considering the process parameters using FEA. Two different configurations were selected as shown in

Table 6-3, based on the previous experimental investigation in [122], to manufacture tensile test specimens (dog bones) with two different materials. The test specimen selected follows ISO 527-2:2012(E), type 1B. The G-codes for these two configurations were also used as an input for the reverse CAD algorithm to generate the Reverse CAD file that has the exact same slicing parameters of the specimen manufactured by the FDM process.

Table 6-2 FDM process parameters for configuration (i) and (ii)

Configuration	(i)	(ii)
Layer thickness (mm)	0.25	0.33
Filling density (%)	28	10
Number of Contours	3	5
Road width (mm)	0.71	0.71
Raster angle (degrees)	0	45
Number of shells	2	4
Raster Pattern	Double Sparse	

The two materials selected were Nylon-12 and PC. The mechanical behavior of the materials used is assumed isotropic, and the extruded ellipse geometries are combined together as one part only at the intersection areas as shown in Figure 6-2, while the resultant voids between the non-intersecting ellipses are kept in the reverse CAD model. The influence of the inter-layer adhesion will not affect the geometric characteristics of the part as a theoretical ideal reference, but it will certainly affect the accuracy of the prediction of the mechanical characteristics in the printing direction. The isotropic properties used in this study are presented in

Table 6-3.

Table 6-3 Material properties used in the FEA

Material Property	Nylon-12	PC
Elastic Modulus (MPa)	1000	2050
Poisson's Ratio	0.38	0.32
Density (gm/cm <sup>3</sup> )	1	1.3

For the FEA analysis, the two parts representing the two configurations were meshed using quadratic tetrahedrons with minimum and maximum element sizes of 0.1 and 0.5 mm respectively. The quadratic tetrahedrons capture the bending deformation in the elements on the contrary to the linear ones, and also show competitive results compared to the hexahedrons elements. It is also easier and faster to mesh complex shapes with tetrahedrons in general. The resultant mesh is shown in Figure 6-4, with a total of around 9.5 million elements for both configurations. The overall quality of the generated mesh was assessed by different parameters, with an average mesh quality of 0.9 (where 1 is the maximum quality), the average aspect ratio of 2, and the average element skewness of 0.05 (where 0 is the best skewness).

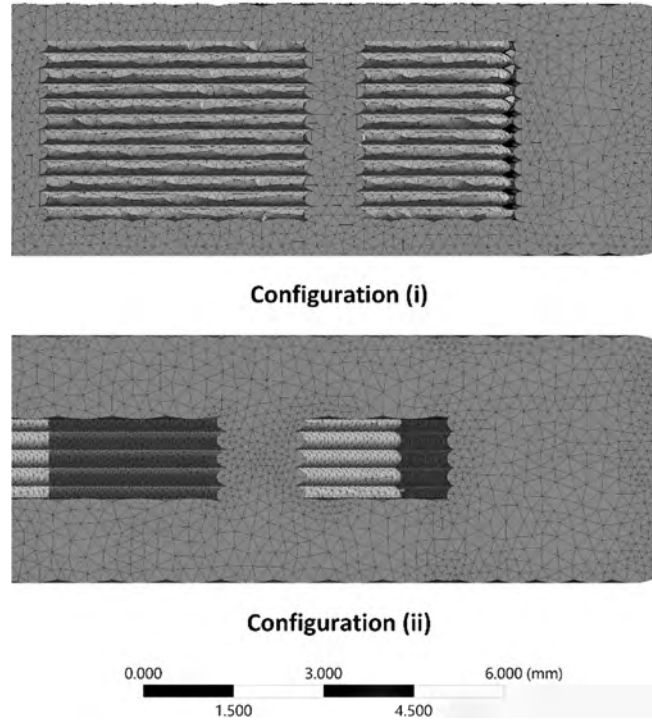


Figure 6-4 Half cross section of the shoulder area showing the meshing of configuration (i) and (ii)

Based on these material properties and the process parameters, an experimental study was conducted which will be used for validation purposes. Five tensile test specimen replicates were manufactured per each configuration and material using a Stratasys Fortus 900mc FDM printer. With a 1 mm/min strain rate, the tensile test was performed on an MTS 810 tensile testing machine according to ISO 527-1. The uncertainty in results ranges between 0.46% and 3.2 %, with a mean of 0.96% and the standard deviation of 0.93%. The average force-displacement curve for each specimen is shown in Figure 6-5 (a). The experimental results are compared to the FEA results for the range of 1 mm, which cover the linear elastic zone of the part, and the comparison is depicted in Figure 6-5 (b).

The boundary conditions used in the FEA are fundamental, where one end of the test specimen was fixed in the x-axis direction and allowed to translate symmetrically around the centerlines of the cross section in the Y and Z axes directions. Then, a four step displacement from 0 to 1 mm with 0.25 increments, was applied to the opposite end to tension the specimen in the positive x-axis direction. The 1 mm range was chosen based on our goal to simulate only the linear elastic zone of the FDM parts. Since the yield strength of plastics is difficult to determine from curves, the simulation zone was determined by plotting the tangent modulus line (dotted lines) between the points corresponding to 0.05% and 0.25% strain as shown in Figure 6-5 (a) according to ISO



527-1. It was observed that the material behaves linearly until about 1mm of the full tested displacement.

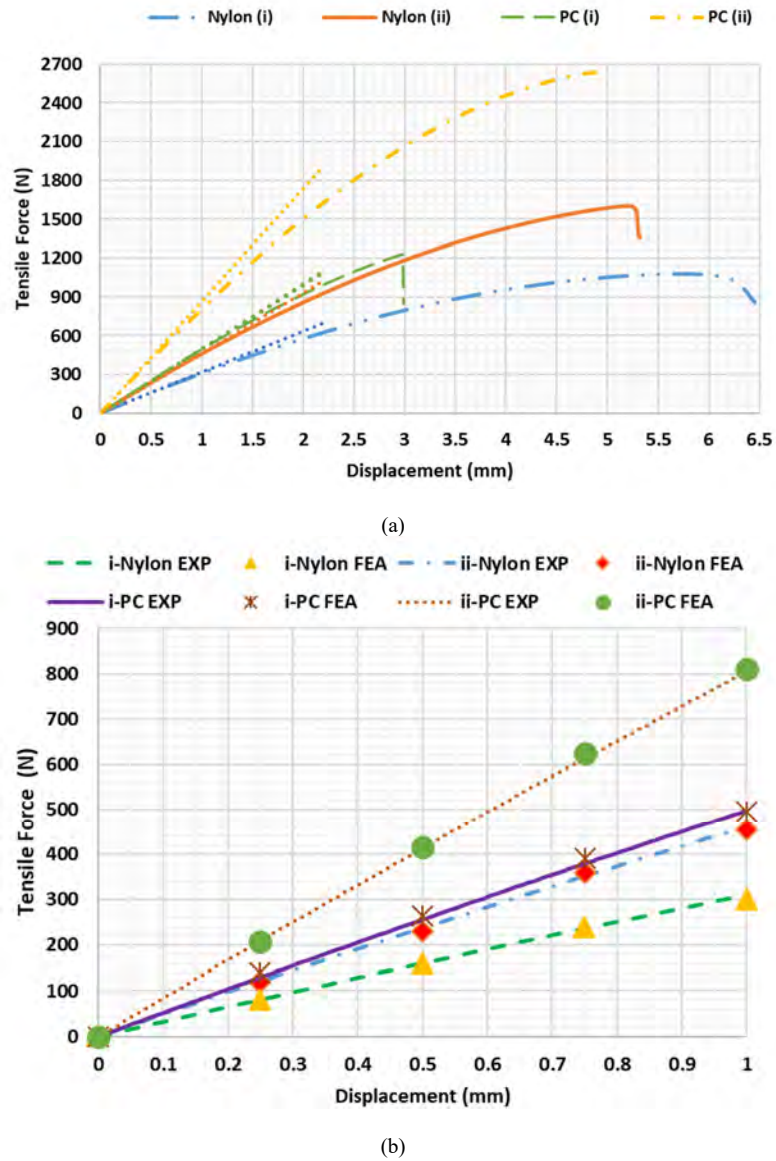


Figure 6-5 (a) Mechanical test results of both Nylon-12 and PC with printing configuration i and ii  
(b) Results up to 1 mm displacement compared to the FEA prediction

ANSYS Workbench Academic was used in this study to conduct the FEA. The von Mises stress results of the Nylon specimen manufactured with the configuration (i) and (ii) are shown in Figure 6-6, where the stresses are presented on the top surface and throughout a longitudinal section. To validate the results, the reaction force at the fixed end was evaluated for each displacement step, as this can be easily compared to the raw mechanical tensile test results. The



FEA analysis was also used to evaluate the stresses and the reaction tensile force for the same two configurations of PC material, while only the Nylon-12 results are shown in Figure 6-6. The FEA results using reverse CAD model are in good agreement with the experimental results with a maximum of 5.74% error. The FEA of the original CAD is also performed to show the deviation compared to the experimental results. Based on these results, the Reverse CAD approach proves to accurately analyze the imposed anisotropic mechanical behavior of the FDM printed parts of any isotropic material within the linear elastic range and in the perpendicular direction to the printing. The limitation to the current version of the reverse CAD model is that it cannot predict the mechanical properties in the printing direction as the extruded ellipse geometries are combined together as one part only at their intersection zones.

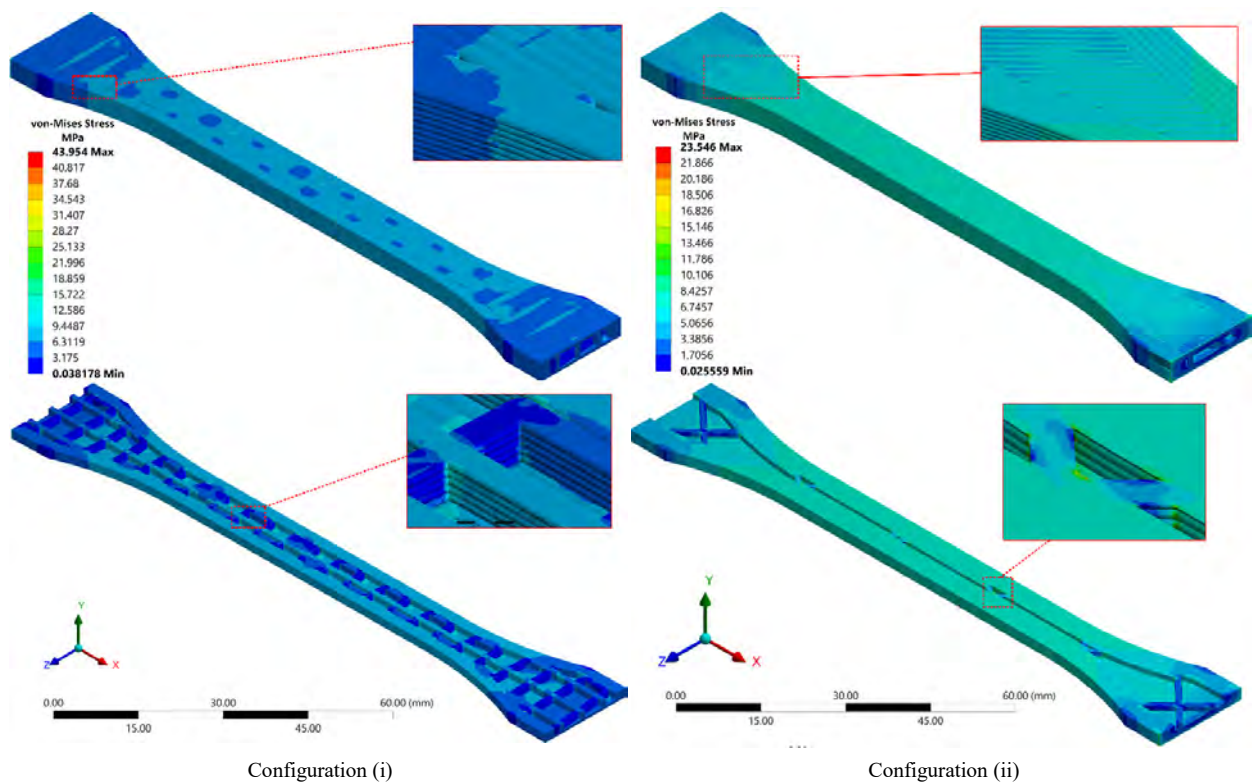


Figure 6-6 von Mises stress FEA results for Configuration (i) and (ii) made of Nylon-12. Corresponding section views are shown to depict infills

## 6.4 Conclusion

In the era of AM, novel simulation methods are needed to reduce the design and production time further and to enable engineering the part with required properties through CAD/CAM tools. This chapter proposes an innovative tool for simulating the geometric and mechanical properties while using the current generation of open-source/commercially available CAD/CAM software.

This is based on a Reverse CAD algorithm, which reconstructs a CAD model from the sliced file. The Reverse CAD model is the virtual replica of the part to be printed with specific printer and machine parameters, e.g., layer thickness and infill density. The algorithm facilitates accurate modelling and analysis of the FDM printed part behaviour. The application and efficiency of the algorithm are validated by qualitative analysis mass comparison, mechanical behaviour analysis using different process parameters and printers.

The limitation of the algorithm as of now is the computation speed. As the number of features increases in the CAD model, the computational speed decreases. However, the computational speed increases simultaneously to layer thickness since it takes fewer loops to cover the same volume. Currently, the Reverse CAD algorithm is further developed to reduce computation speed, make it more robust, and also to simulate the support structures to understand the effect of supports on the output properties and to optimize it. The future analysis work will be implementing the plasticity and fracture models in FEA while using the reverse CAD model and using specimen parts inspired by applications.

## **7 Dual Graded Lattice Structures: Generation Framework and Mechanical Properties Characterization\***

Additive manufacturing enables the production of complex structured parts with tailored properties. Instead of manufacturing parts as fully solid, they can be infilled with lattice structures to optimize mechanical, thermal, and other functional properties. A lattice structure is formed by the repetition of a particular unit cell using a certain defined pattern. The unit cell's geometry, relative density, and size dictate the lattice structure's properties. Functionally graded lattice structure allows for further part optimization, where certain domains of the part require denser infill compared to other domains. This chapter consists of two main parts. In the first section, the dual graded lattice structure (DGLS) generation framework is discussed. This framework can grade both the size and the relative density or porosity of standard and custom unit cells simultaneously as a function of the structure spatial coordinates. Popular benchmark parts from different fields were used to test the framework's efficiency against different unit cell types and grading equations. In the second part, we investigated the effect of lattice structure dual grading on mechanical properties. It was found that combining both relative density and size grading enhances compressive strength, modulus of elasticity, absorbed energy, and fracture behaviour of the lattice structure at the same part weight.

This chapter approaches the thesis research question by providing a 3D modelling tool to tune mechanical properties beyond the process parameter optimization limits, for example like improving toughness, strain, and ultimate tensile strength. Dual grading can achieve similar mechanical behaviour with less materials.

### **7.1 Introduction**

Lattice structures are a type of cellular material characterized by open porosity and can be arranged in a stochastic or non-stochastic unit cell order [123]. Non-stochastic lattice structures are constructed by the periodic repetition of an elementary unit, called a unit cell, within a given domain along the principal axes [124]. A unit cell's geometry is classified into four major groups:

---

\*This chapter is published in “Mostafa, K.G.; Momesso, G.A.; Li, X.; Nobes, D.S.; Qureshi, A.J. Dual Graded Lattice Structures: Generation Framework and Mechanical Properties Characterization. *Polymers* 2021, 13, 1528. <https://doi.org/10.3390/polym13091528>”

strut-based, triply periodic minimal surfaces (TPMS), topology optimized (TO), nature-inspired, and custom-designed. Several strut-based unit cells are based on the geometry of the Archimedean solid, for example, the simple cube, body center cubic (BCC), diamond, and octet truss, as shown in Figure 7-1 (a) to (d). The TPMS are implicit surfaces with a zero mean curvature [125], for example, Schoen IWP, Schwartz D, Gyroid, and Schwartz P, as shown in Figure 7-1 (e) to (h). Topology optimized unit cells (TO) are generated using a finite element method-based optimization to minimize or maximize a specific mechanical property [126].

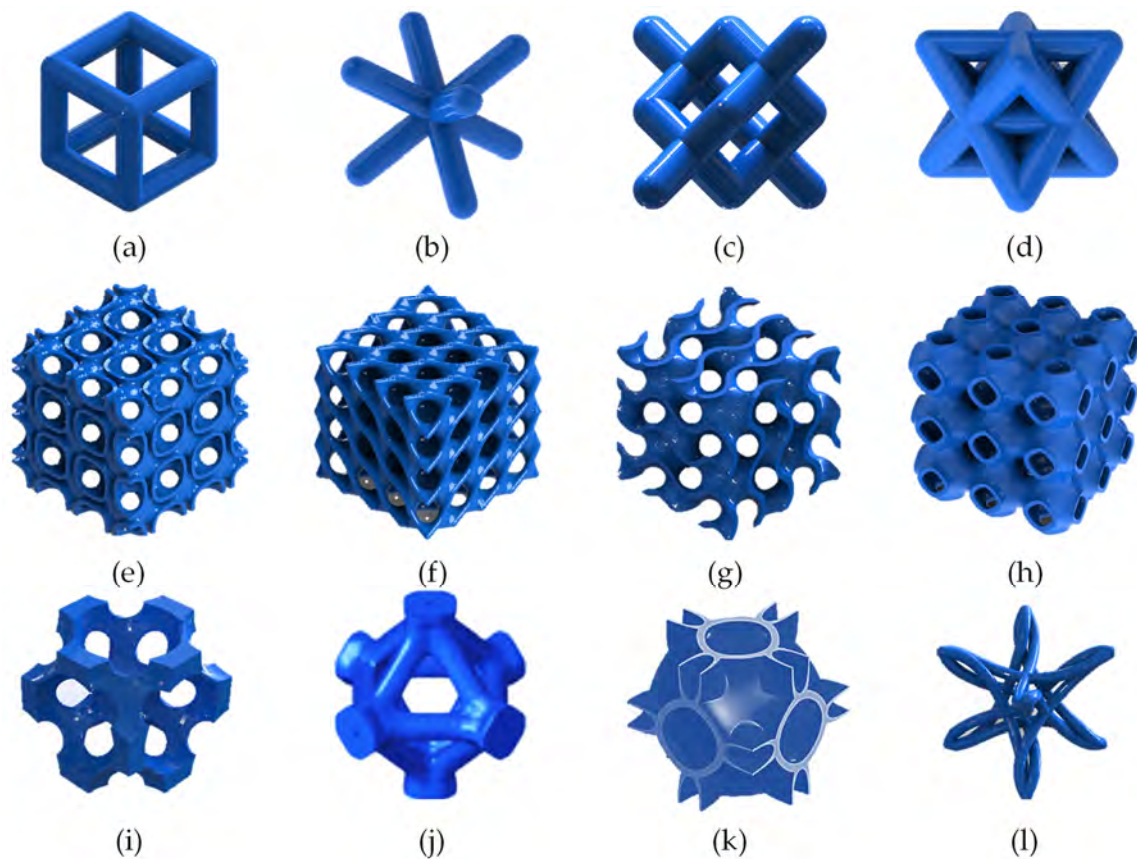


Figure 7-1 Different unit cells types and shapes: (a) simple cube, (b) back-centred cubic BCC, (c) diamond, (d) octet-truss, (e) IWP Schoen, (f) Schwartz diamond, (g) Gyroid, (h) Schwartz primitive, (i) and (j) topology optimized face-centred cubic cells, (k) hybrid (Neovius+Schwartz P), and (l) custom artistically designed unit cell

There are several TO units developed recently; some of the famous designs are face-centred cubic (FCC) and reverse FCC unit cell [127], as shown in Figure 7-1 (i) and (j). Some unit cells are inspired by structures found in nature like honeycombs, plants, bubbles[128], and human and animal bones [129–131]. The last group is the custom-designed lattices, such as hybrid unit cells

that achieve cross-performance of two different unit cells [132], as shown in Figure 7-1 (k). Custom cells also include auxetic unit cells, which achieve negative Poisson's ratio [133] or negative thermal expansion coefficient [134]. There are also aesthetics-designed unit cells [135], as shown in Figure 7-1 (l). Lattice structure utilization has enhanced several applications like improving the oxygen permeability, mechanical properties, and biodegradability of biomedical implants [136–138]. It was also used to improve antennas and acoustic devices' performance while maintaining a lightweight and compact design [139,140].

The lattice structures' mechanical properties can be predicted as a function of their unit cell geometry, relative density, size, porosity, shell or strut dimensions, and spatial orientation [141–144]. A minor modification in any unit cell parameters significantly affects the whole lattice structure's mechanical behaviour [145]. Most lattice structures are stretching-dominant structures while undergoing tensile or compressive stresses and provide a stiff structure. However, some lattice structures are bending-dominant structures with higher energy absorption capacity [146–148]. TPMS unit cells have an above-average surface area with low stress generated during static loadings as well as better handling of angular loads as a result of the better load distribution compared to strut-based design strut-based lattices [149,150]. Topology optimized lattices possess higher stiffness at lower relative density than TPMS and strut-based lattices [151]. In general, the unit cell's relative density is the most significant parameter in determining the overall stiffness and the ultimate tensile strength [149,151]. Unit cell size, however, has a crucial role in determining the failure mechanism of the structure. Smaller cell size improves the low strain structural failure due to a localized fracture [152] and enhances the buckling resistance [153]. As the cell size increases, energy absorption decreases [154]. The stress-strain curve's compressive plateau value and the strain value at which the plateau occurs are controlled by the unit cell's relative density and size combined. As the unit cell's relative density increases and its size decreases, the unit cells' self-contact occurs and gets closer to densification, which decreases the strain required to reach the plateau and also produces a smoother curve with minimal stress fluctuation [146,149].

Another advantage of additive manufacturing is the functional grading of the lattice structures, materials, and microstructures [123]. Functionally graded structures offer part optimization and property tailoring over the part domain, such as tuning a part's natural frequency [155] or thermal conductivity [156] while maintaining the part strength. Moderate relative density grading was found to improve the stiffness of the part significantly [157]. Size grading has improved energy

absorption in some loading directions and did not affect the other directions. Relative density grading was confirmed with another study to be the most significant parameter to control the part stiffness and energy absorption [158,159]. The grading equation was shown to affect the part's behavior, for example, linear or harmonic grading [160].

Lattice structure generation requires two main processes: unit cell modeling and unit cell propagation. The unit cell is modeled and represented, currently, by three main methods. The unit cell is represented as an implicit function, voxel logical array, or CAD file, usually a surface mesh representation [124,128,161]. Implicit modeling allows the control of the relative density and the size of the unit cell. However, it requires computational power to compute the surface for each point in the part domain. The voxel logical array and the STL file can only scale the cell size without controlling the unit cell relative density.

The unit cell propagation methods are classified into conformal or direct patterning [148,162]. Conformal patterning allows unit cells to conform and orient with respect to the domain boundary and space. In contrast, direct patterning uses the domain's boundary to trim the uniformly tessellated unit cells all over the domain space. The integrity of the cells in conformal patterning methods is better compared to direct patterning. However, the unit cell size, orientation, and aspect ratio are dependent on the domain geometry, which might affect the part's intended mechanical properties. Direct patterning allows propagating the cells with independent parameters from the part geometry, facilitating tailoring the part properties. A solution to the trimmed direct patterned lattice structure integrity is to use a solid or a conformal designed shell on the part boundary [124]. Propagation of implicitly represented unit cells allows for a smoother transition between different density grading, which decreases the stress concentration [163] compared to the voxel and the CAD representation method, which requires extra processing steps to fill the gaps [164].

The implicit grading of the cell type, relative density, and size of the TPMS can be performed using MS lattice software based on a user-defined grading function; however, it does not achieve a dual graded lattice structure [158,161]. The implicit unit cell generation method can provide relative density grading while manipulating unit cell distortion (size, skewness, and rotation) to follow stress contours generated in different bodies [165]. Several available commercial software provides lattice structure modeling and topology optimization, for example, Netfabb [166], K3DSurf [167], Altair [168], ANSYS [169], 3-Matic STL [170], ParaMatters [171], and n-Topology [172].

One of the research gaps in the literature found is that the effect of applying two simultaneously varying properties of the unit cells within the lattice structure on mechanical properties is not investigated. This type of grading is called dual grading. The grading function and grading direction have not been sufficiently studied, and the grading direction, whether relative density or size grading, is unidirectional and symmetric around one axis only. Also, the effect of the unit cell's aspect ratio grading on the mechanical properties was not sufficiently studied experimentally. This chapter presents a framework that allows for dual graded lattice structure generation. The user can simultaneously achieve both size and relative density grading while propagating various custom unit cell types within the different part's domains. The dual grading designs allow harnessing the benefits of both types of grading. With the continuous development of new unit cell geometries, there is a need for a generic framework that can adopt the new unit cell quickly. The currently available commercial and open-source software limits the unit cell types used to generate a lattice structure to pre-defined unit cells. The dual graded lattice structure generation framework (DGLS) allows the users to input any custom unit cell. The DGLS manipulates the size and the relative density grading independently based on a user's custom input mathematical functions in terms of the unit cell's spatial position.

The first part of the chapter describes and discusses the algorithm and the software developed to achieve a dual graded lattice structure using several case studies. The second part of this chapter experimentally investigates dual grading, grading functions, and grading direction effects on the tuning of mechanical properties. Contrary to the unilateral and non-symmetrical graded test specimen found in the literature, this chapter investigates bilateral and fully symmetrical grading around the test specimens' geometrical center. The lattice specimens' deformation was monitored and analyzed using digital image correlation (DIC), and the fracture shape was captured.

## **7.2 Dual Grading Generation Algorithm**

The dual graded lattice structure framework is developed to allow the user to vary/grade two properties of the unit cells simultaneously while generating the lattice structure. The DGLS algorithm consists of five main processes, as shown in Figure 7-2:

1. Input of computer graphics parameters (Process I)
2. Input of DGLS GUI parameters (Process II)
3. Performing of lattice structure (Process III)
4. Performing of shell operations (Process IV)

## 5. Exporting final part (Process V)

Each process has different options or sub-processes that determine the final output geometry. Each process requires specific user inputs, either numerical equations, constants, or STL files. After the user provides the required inputs, the Lattice structure and shell operations start. The processing time varies based on the resolution of the STL files, the size of the unit cells compared to the base part, and if the shell operations are required or not. The user can export the lattice structure, perforated shell, or the merged shell and lattice structure as the final part STL file.

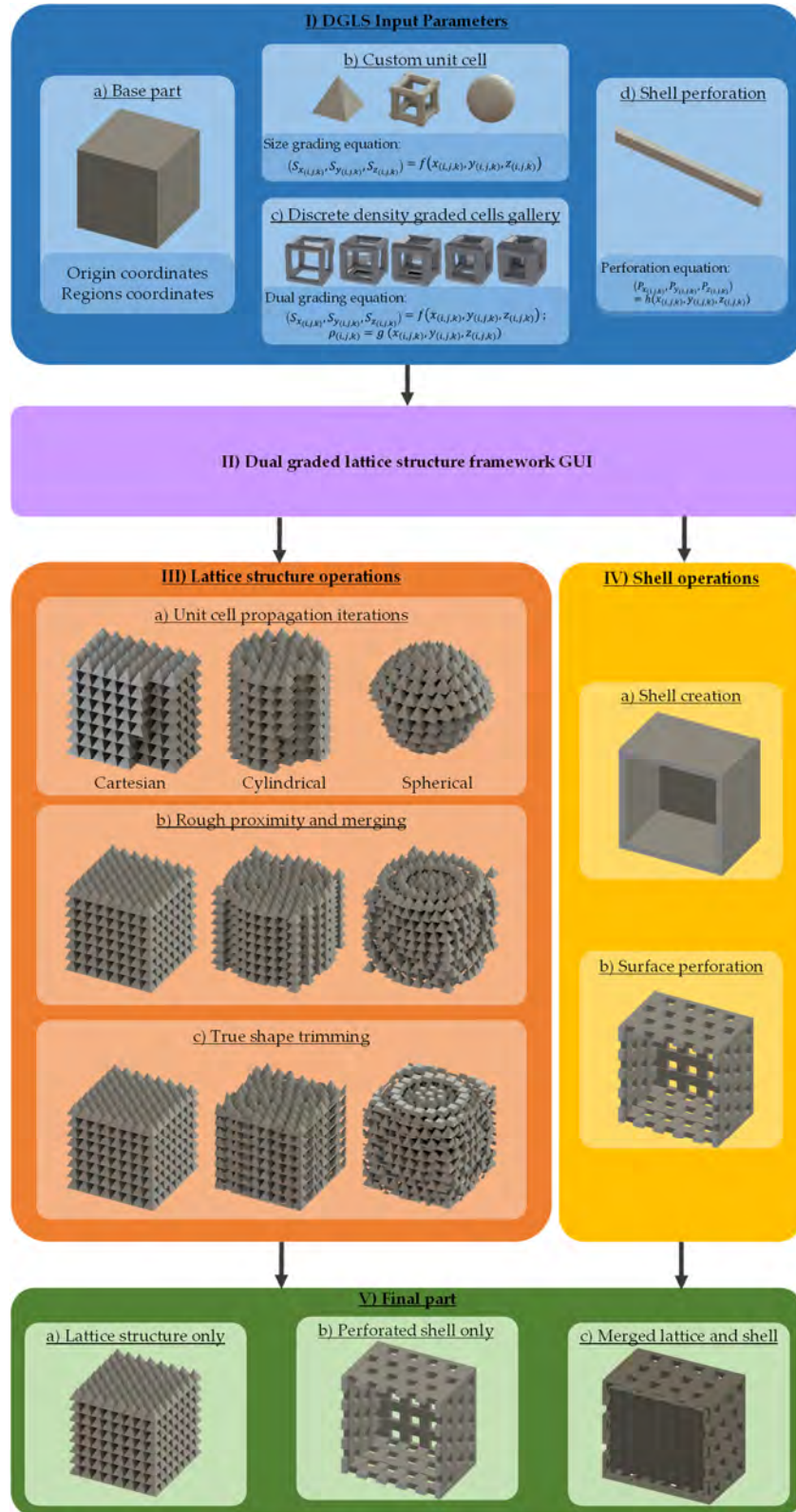
### 7.2.1 Development Environment

The DGLS framework was developed in a C++ environment with a basic graphical user interface (GUI) built in the Qt framework. This environment can take advantage of the powerful graphics and mathematical libraries available in open-source formats. Some examples include the geometry processing library (LIBIGL) [173], computational geometry algorithms library (CGAL) [174], OpenGL Mathematics (GLM) [175], Cork Boolean library (CORK) [176], the matrix and linear algebra library EIGEN [177], and the mathematics expression parser and compiler TINYEXPR [178].

### 7.2.2 DGLS Input Parameters

As shown in Figure 7-2, the first input parameter is the base part (I-a), a binary STL file, to be infilled with the lattice structure. After that, the user either accepts the current part origin point, which by default is set to the part geometric center, or assigns a new origin relative to the original one. Afterwards, the user has to define the different part domains/regions. Each domain can have its unique unit cell geometry, grading equations, coordinate system type, and sub-origin point. The part can be divided into an unlimited number of domains. For each domain, the user has to input the appropriate STL file for the lattice structure's unit cell. The user can then configure the domain boundary shape and size.





**III) Lattice structure operations**

**a) Unit cell propagation iterations**





Cartesian      Cylindrical      Spherical

**b) Rough proximity and merging**





**c) True shape trimming**





**IV) Shell operations**

**a) Shell creation**



**b) Surface perforation**



**a) Lattice structure only**



**b) Perforated shell only**



**c) Merged lattice and shell**



Figure 7-2 Dual grading generation framework

In the case of size graded or non-graded lattice structure, one STL file for the unit cell (I-b) is required per each part domain. However, for relative density, porosity, or dual graded lattice structure, a discretized gallery (I-c) of at least two different relative density unit cells needs to be input along with their relative density numerical values. The unit cell size is manipulated independently in the unit cell's three main axes: the  $S_{x(i,j,k)}$ ,  $S_{y(i,j,k)}$ , and  $S_{z(i,j,k)}$ , where  $(i, j, k)$  is the position index of the unit cell in a lattice structure. This allows the aspect ratio of the unit cells to change throughout the lattice structure. The user has to define three equations to describe the size as a function of the unit cell's three-dimensional position relative to the origin of the corresponding part's domain.

For relative density grading, the user has to provide one equation describing the relative density grading,  $\rho_{(i,j,k)}$ , as a function of the unit cell's three-dimensional spatial position relative to the domain's origin. For dual grading, both the size and relative density equations are required. The spatial position used in defining the grading equations can follow either a Cartesian, a cylindrical, or a spherical coordinate system. The coordinate system dictates the unit cells' propagation directions. Equations can contain a wide range of mathematical functions from linear and polynomial to periodic and logarithmic functions.

The shell operations require the user to input the shell thickness, perforation pattern tool STL file (I-d), and a user-defined equation to describe the perforations' in-plane position as a function of in-plane coordinates. The user has to set an overlap value percentage, which describes the amount of the overlapping distance between any two cells in any axis as a function of the current unit cell size. The overlap percentage is evaluated for each propagation iteration. The overlap is set to ensure the lattice structure's integrity.

### 7.2.3 Lattice structure operations

The lattice structure operations (III) consist of three sub-processes: the unit cell propagation (III-a), the rough proximity and merging (III-b), and the true shape trimming (III-C), as shown in Figure 7-2. If the part is portioned in several domains, the cell propagation process is performed independently for each part domain using the domain's origin. Otherwise, it propagates through the whole part and uses the whole body's origin. The propagation process (III-a) has three different iterators; each one is dedicated to a particular coordinate system. The propagation direction follows

the coordinate system that was chosen for the domain or the whole body. All iterators set the first cell at the origin point (0,0,0) regardless of the coordinate system.

The first iterator is dedicated to Cartesian coordinates. The Cartesian iterator reads the input size equations and evaluates the unit cell's size at the origin, then sets the first unit cell at the domain's origin. The iterator then evaluates and updates the new  $z$ -position based on the current unit cell size in the  $z$ -direction ( $S_{z(i,j,k)}$ ) at position index of  $(i, j, k)$  and the overlap value ( $\delta$ ), as represented by (7-6). Subsequently, it evaluates the new cell three-dimensional size ( $S_x, S_y, S_z$ ) at the new evaluated position  $(x_{(i,j,k+1)}, y_{(i,j,k+1)}, z_{(i,j,k+1)})$  and adds the new cell at the newly evaluated  $z$ -position. After the iterator continues the propagation in the  $z$ -direction till the unit cells reach the rough proximity boundary of the domain or the part, it sets the  $z$ -position to zero again. The iterator evaluates the new  $y$ -axis position based on the current unit cell size in the  $y$ -direction ( $S_{y(i,j,k)}$ ) and the overlap value ( $\delta$ ), as shown in (7-5). Then the iteration in the  $z$ -direction is repeated. The iteration in the  $y$ -direction continues until the unit cells reach the part's or the domain's rough proximity boundary. Then it sets the  $y$ -position to zero again. Then the iterator evaluates the new  $x$ -position based on the current unit cell size in the  $x$ -direction ( $S_{x(i,j,k)}$ ) and the overlap percentage. Subsequently, the iteration in the  $y$ -direction is repeated. It is similar to nested loops with the iterations in the  $x$ -direction being on the outer loop, while  $y$ -direction being in the middle loop, and  $z$ -direction being the innermost loop.

For the relative density grading or dual grading required by the user, the iterator initially reads the relative density grading equation and the discretized unit cell gallery. Then the relative density is evaluated in the  $z$  loop iterations for each cell. The relative density value is rounded to the nearest available unit cell from the discretized unit cell gallery inputted by the user. The evaluated cell size is applied to the chosen unit cell from the gallery before adding it to the lattice structure. If the part has multiple domains, the  $x$ ,  $y$ , and  $z$  iterations are applied to each domain independently in the ascending order in which the domains were defined.

For the size grading, the DGLS framework was developed to have one independent size axis, and the other two size axes can either be set to be the independent or dependent axis. In the case of the Cartesian iterator, the  $S_{x(i,j,k)}$  can be only a function of the  $x$ -axis location as follow:

$$S_{x(i,j,k)} = f_x(x_{(i,j,k)}). \quad (7-1)$$

The  $S_{y(i,j,k)}$  can also be a function of  $y$ -axis location only or both  $x$  and  $y$ -axis locations, as follow:

$$S_{y(i,j,k)} = f_y(x_{(i,j,k)}, y_{(i,j,k)}). \quad (7-2)$$

The  $S_{z(i,j,k)}$  can either be a function of the  $z$ -axis location only or all the three axes locations as follow:

$$S_{z(i,j,k)} = f_z(x_{(i,j,k)}, y_{(i,j,k)}, z_{(i,j,k)}). \quad (7-3)$$

The new cell location in each iterator is calculated using the current cell location, the size of the current cell, and the overlap value as follow:

$$x_{(i+1,j,k)} = x_{(i,j,k)} + S_{x(i,j,k)} - \delta/2 \quad (7-4)$$

$$y_{(i,j+1,k)} = y_{(i,j,k)} + S_{y(i,j,k)} - \delta/2 \quad (7-5)$$

$$z_{(i,j,k+1)} = z_{(i,j,k)} + S_{z(i,j,k)} - \delta/2 \quad (7-6)$$

These constraints assure that most of the size grading equations lead to a successful lattice structure where all the unit cell nodes are attached to the neighbouring unit cells' corresponding nodes. The axis dependency is further discussed in the case studies section. The relative density grading can be a function of any of the axes or all the axes together.

The cylindrical and spherical iterators are similar to the Cartesian iterator algorithm, in which a nested loops structure was used. The only difference is the axes' names and the propagation directions. For the cylindrical iterator, the unit cell propagation starts in the  $z$ -axis direction, then the iterator shifts the polar direction,  $\theta$ . After the  $\theta$  iterations reach  $180^\circ$ , the iterator shifts the  $r$ -position in the radial direction. Therefore the outer loop controls the propagation in the radial direction, the middle loop controls the polar direction, while the inner loop controls the  $z$ -direction. The spherical iterator's outer loop controls the propagation in the radial direction. The middle loop controls propagation in the polar direction, and the inner loop controls the azimuthal direction,  $\phi$ . The size dependency on the coordinate axes for the cylindrical iterator is described by:

$$(S_{x(i,j,k)}, S_{y(i,j,k)}, S_{z(i,j,k)}) = (f_x(r_{(i,j,k)}), f_y(r_{(i,j,k)}, \theta_{(i,j,k)}), f_z(r_{(i,j,k)}, \theta_{(i,j,k)}, z_{(i,j,k)})). \quad (7-7)$$

while the size dependency on the coordinate axes for the spherical iterator is described by:

$$(S_{x(i,j,k)}, S_{y(i,j,k)}, S_{z(i,j,k)}) = (f_x(r_{(i,j,k)}), f_y(r_{(i,j,k)}, \theta_{(i,j,k)}), f_z(r_{(i,j,k)}, \theta_{(i,j,k)}, \phi_{(i,j,k)})). \quad (7-8)$$

It is worth noting that the DGLS currently does not support the unit cell rotation during the propagation; therefore, the unit cell's angular orientation is set by the original STL file orientation.

The second sub-process in the lattice structure operations is the merging of unit cells (III-b). This process takes place directly after the unit cell is propagated to fill roughly every domain. The unit cells within each domain are merged using Boolean operations. Two options are available for the domain's rough-shaped lattice. It can be trimmed with the true shape of the domain boundary, or the roughly shaped lattice gets merged with the surrounding untrimmed domains. The second option ensures that the lattice structure is one connected part.

The last process is the true shape trimming of the whole part (III-c). After all the domains are merged, the semi-finished lattice structure is trimmed with the base part's true boundary if no shell is required. Otherwise, the semi-finished lattice structure is trimmed with the offset boundary surface of the shell generated.

#### 7.2.4 Shell operations and part finishing

The user can create a shell out of the base part using the shell operations process (IV), as shown in Figure 7-2. The shell is created using operation (IV-a) by offsetting the base part's external surface inwards by a distance equal to the shell thickness, then subtracting the newly formed part from the original base part using Boolean operations. Several issues such as global loops and the self-intersecting local loops may arise depending on the part geometry and the shell thickness value. The DGLS framework utilizes the bi-arcs fitting algorithm [179] to detect and solve global or local loops.

The user can choose to perforate the created shell using operation (IV-b), which requires the custom patterning tool STL file (I-d). The patterning tool is replicated over the three principal planes:  $x$ - $y$ ,  $x$ - $z$ , and  $y$ - $z$ . A user-defined position function governs each replication position in terms of the in-plane Cartesian coordinates. Afterwards, the pattern replication over each plane is projected on the body and subtracted using Boolean operations. Currently, the DGLS is using a Cartesian coordinates system in the shell perforation. The user can choose to export the resultant final part (V) as a lattice structure without the shell (V-a), a hollow perforated shell without any

lattice structure inside (V-b), or a merged lattice structure with a generated shell (V-c). The output part is exported as an STL file.

### 7.2.5 Case Studies

Several test scenarios were designed to assess the DGLS framework's performance. The test scenarios included the generation of a constant size lattice structure, size graded, and dual graded lattice structure. For each scenario, a different unit cell type and geometry are used.

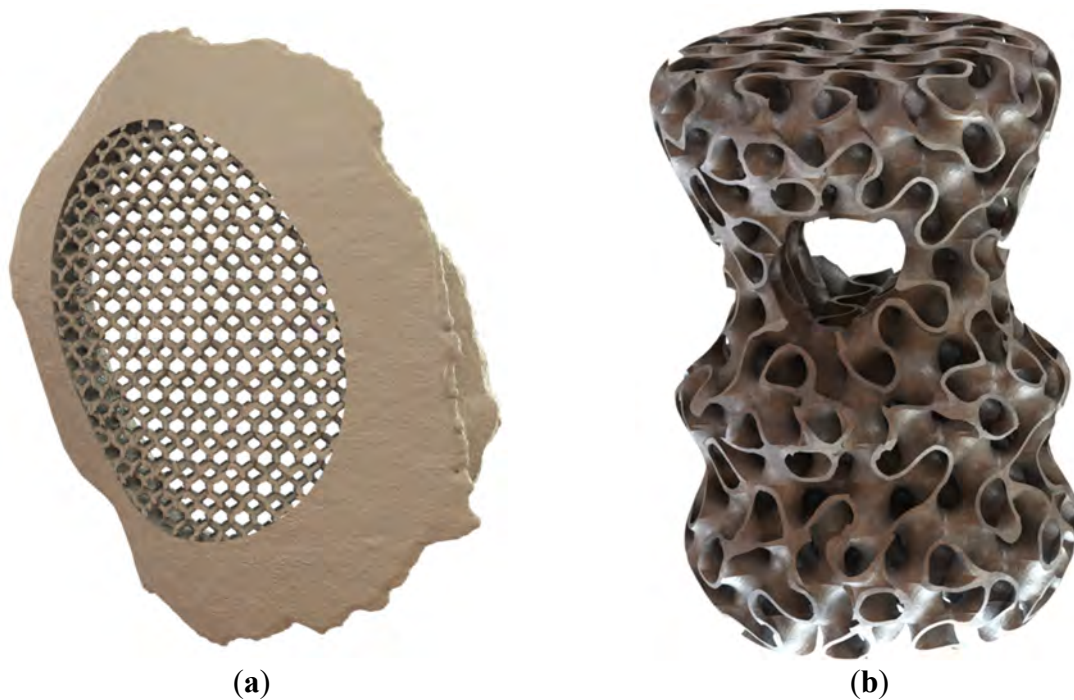


Figure 7-3 Constant size and relative density generated lattice structure for (a) skull implant partially filled with a cubic diamond lattice structure, and (b) spline-based revolved artifact filled gyroid

For the constant lattice structure generation, two scenarios were envisaged. The first one uses a cubic diamond unit cell, which belongs to the strut-based unit cells, to fill an ellipse-shaped domain within a skull implant base part, as shown in Figure 7-3(a). The second scenario uses the gyroid unit cell, which belongs to the TPMS unit cells, to fill a whole artifact base part shaped as a revolved spline with an ellipse cut-out, as shown in Figure 7-3 (b). The size equations for both scenarios were set to constant values, and the coordinate system was set to Cartesian. The output parts were digitally examined, and the output mesh was qualitatively evaluated to locate any



orphan meshes and mesh discontinuity. Both parts showed a successfully generated lattice structure.

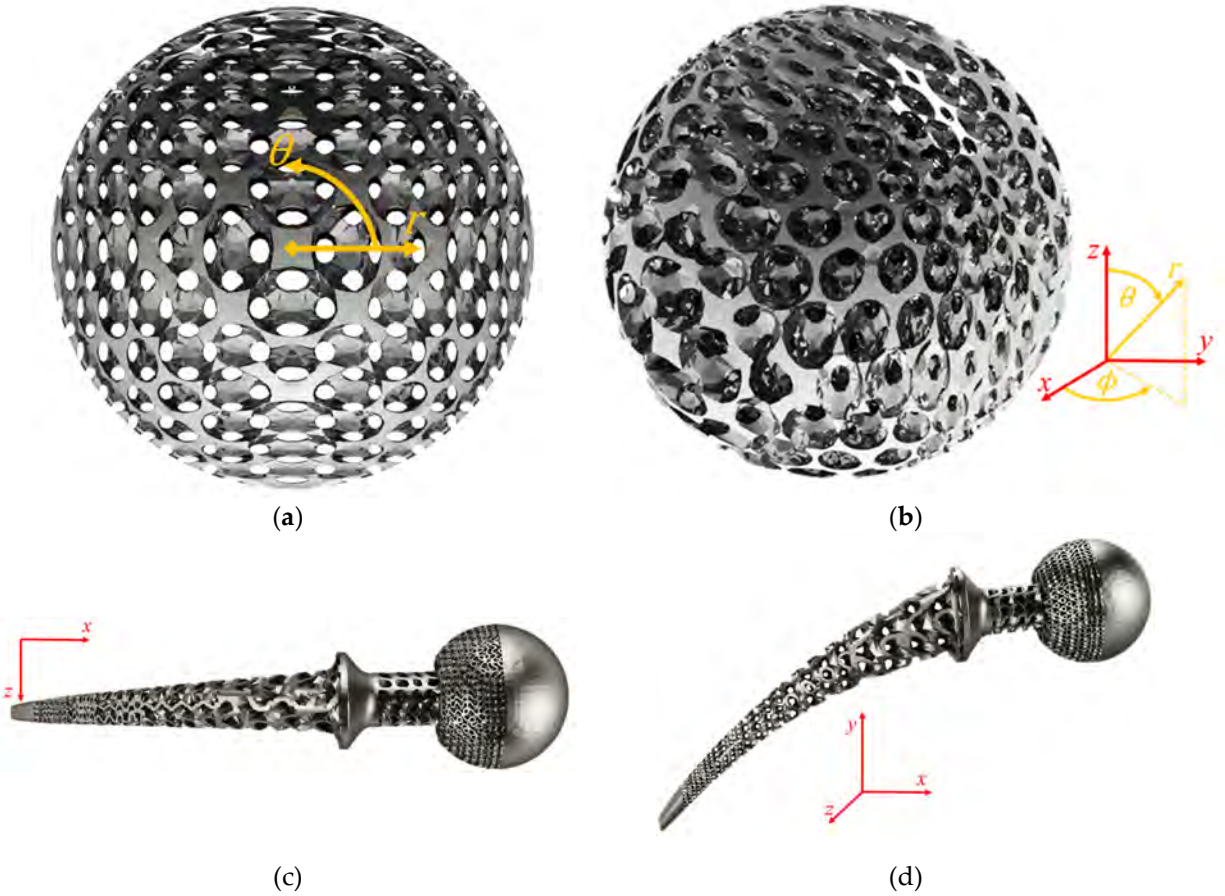


Figure 7-4 Size graded lattice structures: (a) side view and (b) isometric view of a sphere filled with TO FCC unit cell, and (c) top view and (d) isometric view of multi-domain hip joint implant partially filled with Schwartz D unit cell

For size grading, the first testing scenario is to fill a sphere base part with a size graded topology optimized FCC unit cell using a spherical coordinates system, as shown in Figure 7-4 (a) and (b). Each of the size grading governing equations dependent on one unique coordinate axis only. This design allows for a spatially graded unit cell size with a varying aspect ratio while constraining each unit cell's nodes to meet all neighboring unit cells. The origin of the coordinate system was set to be in the center of the sphere. The unit cells'  $S_x$  varies linearly in the radial direction with the largest value at the center and decreases towards the sphere circumference. Simultaneously, the  $S_y$  is slightly varying in the polar direction in a sinusoidal behavior as a function of the polar coordinate. The  $S_z$  was set to vary sinusoidally in the azimuthal direction. The

second scenario is to partially infill a hip joint implant with a size varying Schwartz D, which belongs to the TPMS unit cells using Cartesian coordinates, as shown in Figure 7-4 (c) and (d). The part was divided into six domains, some of the domains were left solid, and the others are infilled with the Schwartz D unit cell either with a size graded or constant unit cells. The three size equations are dependent on the  $x$ -axis only. This design allows for a fixed aspect ratio while applying the size grading.

For the dual grading, two test scenarios were designed to test DGLS ability to handle dual grading for strut-based and TPMS unit cells, and linear and non-linear grading. The first testing scenario is to infill a sinusoidal revolve shape with a simple cubic unit cell using Cartesian coordinates, as shown in Figure 7-5 (a) and (b). The origin was set to the center of the shape. The discretized relative density graded unit cell gallery used consists of five different relative densities. The size followed a sinusoidal grading function for the three size equations, with the largest unit cell size in the center of the part and a size decrease towards the part external surface. The  $S_x$  was only a function of the  $x$ -axis, the  $S_y$  was interdependent on both the  $x$  and the  $y$  axis, and the  $S_z$  was interdependent on all three axes. The size interdependency on multiple axes was successful with the framed unit cells, while for the nodal-based unit cell, it produced gaps between the neighboring nodes. The relative density grading followed a sinusoidal grading function as a function of the  $x$ -axis only. The densest unit cells are on the edges, and the relative density decreases towards the center of the part.

The second scenario for the dual grading is to fill the well-known GE bracket artifact with a varying porosity IWP Schoen unit cell using a Cartesian coordinate system, as shown in Figure 7-5 (c) and (d). The part was partitioned into five domains. The middle domain consists of a non-graded octet truss lattice structure; next to it from both sides is a complete solid domain, and surrounded by the dual graded IWP Schoen lattice structure. The discrete unit cell gallery consists of three unit cells with a varying ISO-value ranging from 0.3 to 0.9. Size grading follows a linear function and varies only along the  $x$ -axis for the three size equations. It starts with a small unit cell size near the part's edges and increases towards the center. The porosity grading also followed a linear function, and it varies in the orthogonal direction along the  $z$ -axis. It starts with a smaller pore size at the center of the part, and the pore size increases towards the outer edges. The dual grading algorithm was successful with both the strut-based and the TPMS based unit cells. It was



observed that the size of the discretized gallery and the slope of the grading function affect the smoothness of the transition between different relative density cells.

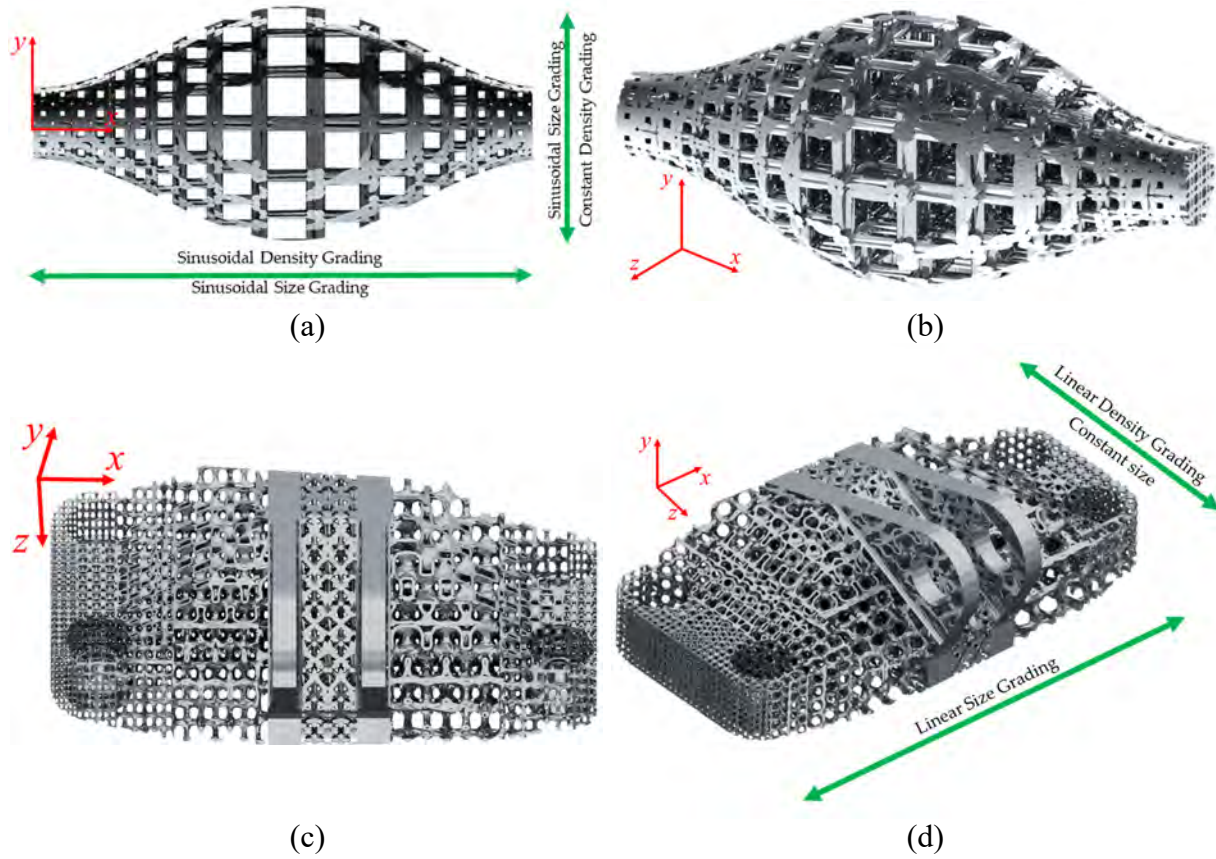


Figure 7-5 Dual graded lattice structure: (a) Front view and (b) Isometric view of a sinusoidal-based revolved parts filled with a cubic unit cell, and (c) Top-down view and (d) Isometric view of GE bracket filled with IWP Schoen unit cell

The shell perforation and integration were tested using a simple cube as the base part, while its patterning tool is a diamond shape. The shell is merged with a lattice structure based on an artistically designed unit cell shown in Figure 7-1 (l). The final output part is shown in Figure 7-6 (a). The second test generates a shell for a spline-based revolved part with different curvature radii along its contour. The generated shell to be perforated with a circular-shaped patterning tool. This part allowed the testing of the global and local loop resolving algorithm implemented in the DGLS. The shell is then integrated with a multi-domain size graded lattice structure, as shown in Figure 7-6 (b). In both scenarios, the patterning position followed a linear function. In the cube scenario, the patterning was projected from the three planes, while in the spline-revolved part, the patterns were projected from two planes only.

The DGLS can generate a two-step size graded shell, which is achieved by generating a shell from the base part without applying any perforation then propagating a size graded unit cell through the shell. An example of a size-graded gyroid shell was generated for the sinusoidal revolved part with no infill inside, as shown in Figure 7-6 (c). The shell offsetting showed success in producing a shell without local or global loops as shown in Figure 7-6 (b). However, the patterning tool did not produce a good pattern with highly curved parts. A conformal patterning algorithm would be more suitable for highly curved shapes. The two-step shell was successful with the TPMS shells compared to the strut-based unit cells. Using a relatively thick shell compared to the unit cell size used is essential to produce a continuously connected two-step shell.

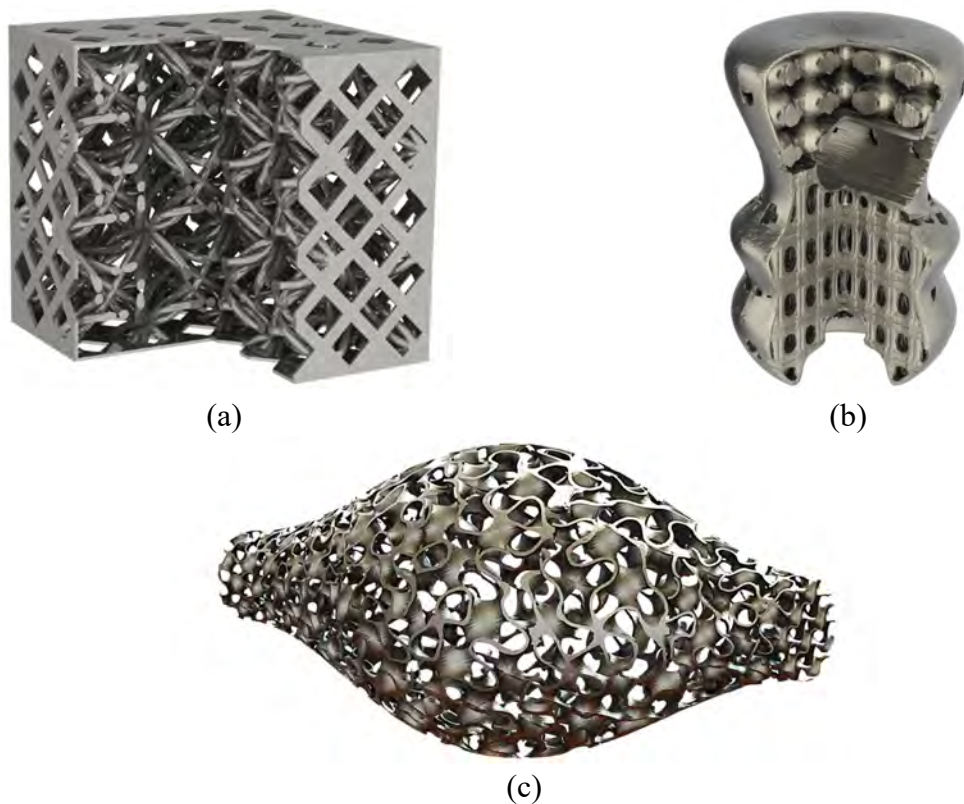


Figure 7-6 Shell generation and perforation: (a) Cubic shell perforated with a diamond pattern and filled with the artistic unit cell, (b) spline-based revolved Shell perforated with a circular pattern and filled with multi-domain sized graded unit cells, and (c) two-step size graded gyroid shell for a sinusoidal revolved shape

### 7.3 Dual Grading Experimental Investigation

Two experiments were designed to understand the effect of size grading, relative density grading, and dual grading on the modulus of elasticity, compressive strength, absorbed energy,

and failure shapes. The first experiment is intended to investigate the lattice structure designs developed using the upper and lower limits of the grading parameters without grading. The second experiment investigates several grading designs using different size and relative density grading equations. The designed specimens were additively manufactured using stereolithography (SLA). A digital image correlation system was used to analyze each specimen's developed strain under compression testing and capture the failure shape.

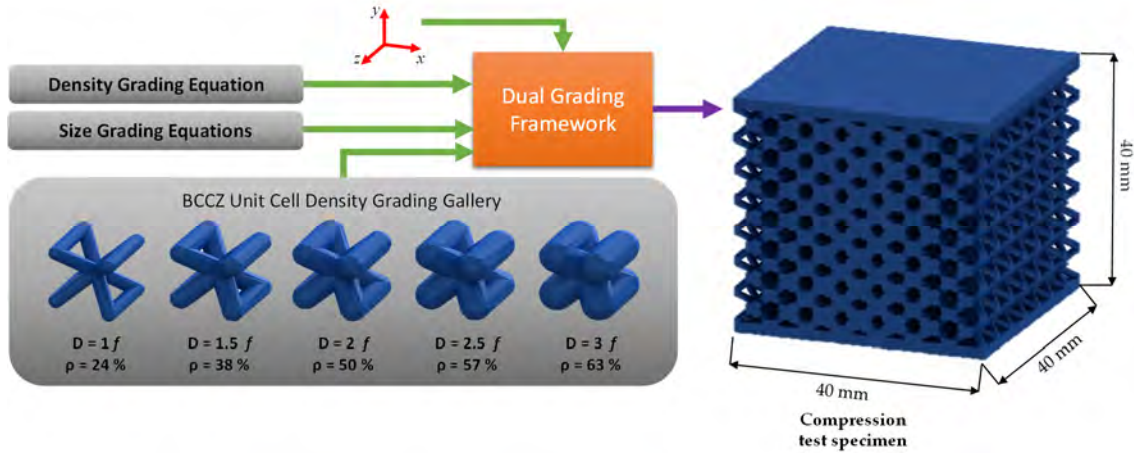


Figure 7-7 Generation of the dual graded lattice structure using a BCCZ grading gallery for compression test specimens

### 7.3.1 Lattice Structure Design

The unit cell selected for the two experiments is the BCCZ unit cell. A discretized gallery consists of five BCCZ unit cells with different relative densities input to the dual grading framework and the spatial equations governing the cell and density grading, as shown in Figure 7-7. The dual graded experiment's design envelope is defined by the selected upper and lower bounds of both the unit cell size and the unit cell relative density. The minimum relative density available in the gallery is 24%, with a strut diameter of  $1f$ , in which  $f$  is a scaling factor based on the cell size. The highest relative density is 63%, with a strut diameter of  $3f$ . Therefore, at a fixed cell size, the densest cell has a strut diameter of three times the lowest relative density cell. The cell size is continuously varied using the size governing equations (S1) to (S5) with a lower limit for any cell dimension, out of the three dimensions, is set to 3.5 mm, and the upper limit is set to 6.5 mm. The compression test specimen is a  $40 \times 40 \times 40 \text{ mm}^3$  cube including a 2 mm thick shell at the top and the bottom of the designed lattice specimens, as shown in Figure 7-7, which follows

the criteria specified in ISO 844:2014(E)[180]. The unit cells were propagated across the compression specimen domain with the orientation shown in Figure 7-7, in which the horizontal traverse strut is parallel to the top and bottom skin.

The first experiment studies the effect of the unit cell's size and relative density on the whole lattice structure's mechanical properties. This experiment is considered as a control experiment for the design domain boundary; the mechanical property values evaluated in this experiment are expected not to be exceeded by all the dual graded designs within the mentioned design envelop. The specimens in this experiment have a constant relative density and constant cell size unit cells. This experiment consists of four lattice structure designs using the upper and lower values of the relative density and size used in this investigation, as shown in Figure 7-8. The first boundary design has a 3.5 mm cell size and 24% relative density, which means that this design uses the smallest unit cell size (SS) and the lowest cell relative density (LD) of all the values used in this investigation. The second boundary design has the largest cell size (LS), of 6.5 mm, while having the lowest cell relative density (LD) used in this investigation. The third has the smallest cell size and the highest cell relative density (HD) of 63%. The fourth design has the largest cell size (LS) and the highest relative density (HD).

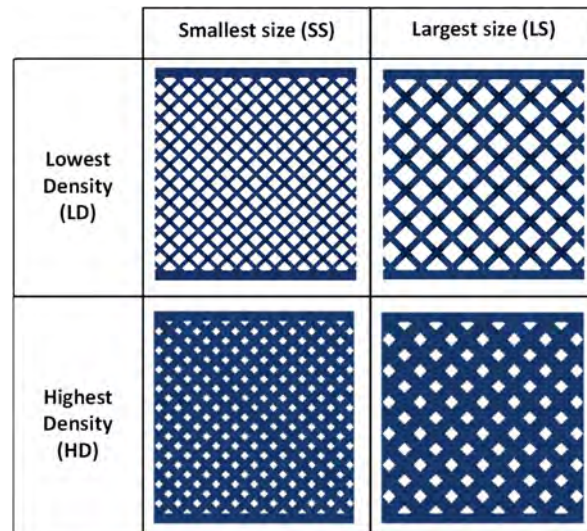


Figure 7-8 Front views of the boundary lattice structure designs for compression test specimen

The second experiment consists of fifteen unique lattice structure designs based on a full factorial experimental design, as shown in Figure 7-9. The experiment has two parameters. The first one represents the size grading governing equation, and the second one represents the relative



density grading governing equation. The size grading parameter has five levels or grading equations as follows:

$$S_{x(i,j,k)} = C_S; S_{y(i,j,k)} = C_S; S_{z(i,j,k)} = C_S, \quad (S1)$$

where the first set of size grading equations (S1) have a constant size unit cell distribution across the domain with the  $C_S$  value that equals 5.5 mm. This value was chosen based on the average cell size used in other graded lattice structure designs. The origin of the Cartesian coordinate system is defined at the center of the mass of the cube.

The second set of size grading equations (S2),

$$S_{x(i,j,k)} = 6.5 - 0.185x_{(i,j,k)}; S_{y(i,j,k)} = C_S; S_{z(i,j,k)} = 6.5 - 0.185z_{(i,j,k)}, \quad (S2)$$

describe a size grading design with the largest unit cell around the origin and the unit cell width decreases along the  $x$  and  $z$  axes towards the cube edges while the cell height is kept constant at the value  $C_S$  along the  $y$ -axis. This size grading design allows the cell aspect ratio to vary between 1:1 to 1:1.5 along the  $x$  and  $z$  axes.

The third grading equation set (S3),

$$S_{x(i,j,k)} = 0.3x_{(i,j,k)} + 3.5; S_{y(i,j,k)} = C_S; S_{z(i,j,k)} = 0.3z_{(i,j,k)} + 3.5, \quad (S3)$$

has the opposite grading direction of (S2). The cell width starts with the smallest values at the middle of the cube and increases towards the cube edges along the  $x$  and  $z$  axes. Equations set (S3) also reverse the aspect ratio variation done by (S2).

The fourth and fifth equation sets, (S4) and (S5),

$$S_{x(i,j,k)} = 6.5 - 0.185x_{(i,j,k)}; S_{y(i,j,k)} = 6.5 - 0.185y_{(i,j,k)}; \quad (S4)$$

$$S_{z(i,j,k)} = 6.5 - 0.185z_{(i,j,k)}$$

$$S_{x(i,j,k)} = 0.3x_{(i,j,k)} + 3.5; S_{y(i,j,k)} = 0.3y_{(i,j,k)} + 3.5; S_{z(i,j,k)} = 0.3z_{(i,j,k)} + 3.5, \quad (S5)$$

describe a three-dimensional size grading spatially. The (S4) design starts with a large unit cell size in the middle of the cube, and it decreases towards the cube edges along the  $x$ ,  $y$ , and  $z$  axes. While (S5) has the smallest unit cell in the middle of the cube, its size increases along the three axes towards the edges. The aspect ratio of both the (S4) and (S5) designs vary along the three axes. However, the cells along the planar and spatial diagonals have a 1:1 aspect ratio. The

geometry produced by the different size grading equation sets can be seen independently of any relative density grading in the first column of Figure 7-9.

The relative density grading has three grading governing equations. The first equation (D1),

$$\rho_{(i,j,k)} = C_D, \quad (D1)$$

represents a constant relative density across the specimen domain with a value of  $C_D$ ; which equals 38% relative density. The second equation (D2),

$$\rho_{(i,j,k)} = -0.0485x_{(i,j,k)}^2 - 0.7044x_{(i,j,k)} + 63, \quad (D2)$$

represents a relative density grading with a quadratic distribution. The highest relative density is in the middle of the cube and decreasing along the  $x$ -axis towards the edges. The third equation (D3),

$$\rho_{(i,j,k)} = -0.0496x_{(i,j,k)}^2 + 2.8545x_{(i,j,k)} + 24, \quad (D3)$$

represents a relative density grading along the  $x$ -axis, starting with the lowest relative density in the middle of the cube and increasing towards the cube edges. The geometries produced by grading the relative density independently of the cell size grading are shown in the first row of Figure 7-9. The remaining designs in Figure 7-9 are the combination between the size and the relative density grading equations. All the lattice designs are fully symmetric about the three principal axes, with the center of the cube's coinciding with the intersection point of all the symmetry planes.

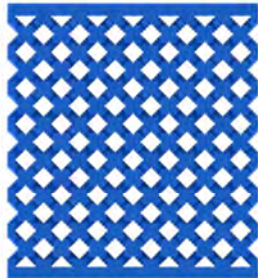
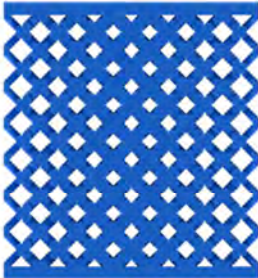
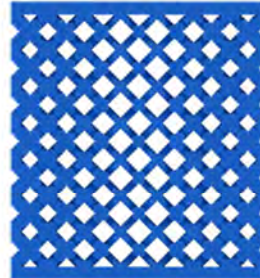
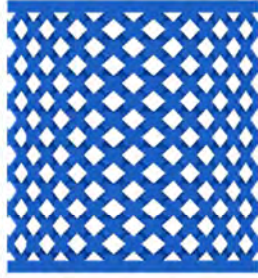

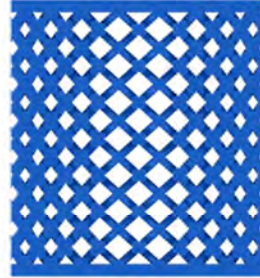
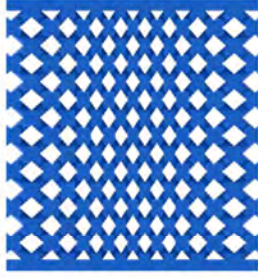
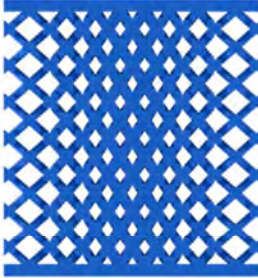
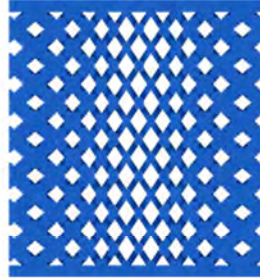

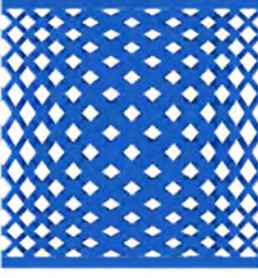
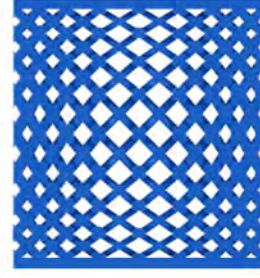

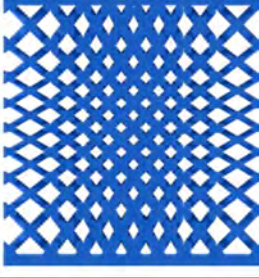

	Constant Density (D1)	Graded Density (D2)	Graded Density (D3)
Constant Size (S1)			
Size Graded (S2)			
Size Graded (S3)			
Size Graded (S4)			
Size Graded (S5)			

Figure 7-9 Front view of the dual graded lattice structure designs for compression test specimens

### **7.3.2 Specimen Manufacturing**

The specimens were manufactured using a Form 2 3D printer by Formlabs, a Stereolithography (SLA) desktop 3D printer. The material used is Clear resin by Formlabs. The manufacturing parameters were chosen based on the recommended optimum parameters to produce high strength with moderate ultimate strain, as concluded by Garcia et al. [181]. Post curing was found to be the most significant parameter, with one hour as the optimum level. The test specimens were manufactured at 100  $\mu\text{m}$  layer thickness and oriented with the side face of the lattice specimen facing down, and the skin is parallel to the manufacturing direction. The specimens were washed with isopropyl alcohol for 10 minutes and left to dry for one hour in a dark area. The total post-curing duration was one hour, distributed equally on all the lateral faces. Two replicates were manufactured for each lattice design to establish confidence while investigating a wide range of grading designs with nineteen unique lattice designs.

### **7.3.3 Compression test and digital image correlation**

Compression tests were carried out using INSTRON 5966 universal testing systems for most specimens except six designs that exceeded 10 kN loading force. These were tested on an MTS 810 with 100 kN loading force capacity. The compression test was run at a loading speed of 1 mm/min without preloading, as recommended by ISO 604:2002(E)[182]. The compressive strength and the elastic modulus were determined based on the ISO standard criteria for rigid cellular plastic materials, ISO 844:2014(E)[180]. The compressive strength value equals the maximum compressive stress occurring before 10% compressive strain. Otherwise, it is equal to the stress corresponding to 10% compressive strain. The absorbed energy is not described in the previous standard. However, the ISO standard for cellular metal material, ISO 13314:2011(E) [183], describes it. The absorbed energy was calculated as the area under the stress-strain curve till the densification or 50% compressive strain. A failure is considered if the stress dropped 40% within a short time or after the compressive strain reaches 40%.

A stereo digital image correlation system (DIC) was used to capture and analyze the different lattice structure designs' deformation during compression testing. The system consists of two Pike F421b cameras manufactured by Allied Vision Technology with a 2048 $\times$ 2048 pixels CCD sensor. Each camera is equipped with Nikon 28-85mm AF macro zoom lens with adjustable aperture,



zoom, and focus separately. Before testing each specimen, the three lens parameters were adjusted so that the specimen was in focus and with balanced lighting across the specimen. The magnification range across all the specimens was between 9 to 14 pixels/mm. The angle between the two cameras was set to  $25^\circ$ , with one of the cameras looking perpendicular to the specimen's front face. Testing was captured at one frame per second, which means that each frame was capturing a compressive displacement of around 20  $\mu\text{m}$  based on the loading rate of 1 mm/min. The specimens were sprayed with black and white spray paint to create a scattered speckle pattern on the lattice specimen's front face. Before each test, a DIC calibration process was carried out by capturing a calibration pattern consisting of  $8 \times 8$  circular dots with a 4 mm diameter at several spatial rotations. Both the calibration and the test images were captured using VIC-Snap software by Correlated Solutions. While the image processing and data analysis were performed using VIC-3D software by Correlated Solutions. The average calibration score was around 0.06, with a maximum value of 0.08 and a minimum value of 0.04. The subset was tuned for each specimen to minimize the projection error; the maximum subset value was  $67 \times 67$  pixels, and the minimum value was  $35 \times 35$  pixels. The step value was set to 11 pixels. The average projection error equals 0.1, with a maximum value of 0.46 and a minimum value of 0.021.

### **7.3.4 Results**

#### **7.3.4.1 Mechanical properties**

The boundary lattice structure design experimental results are presented in Table 7-17. The relative density of the unit cell has the most significant influence on the compressive strength. The increase in the unit cell relative density from 24% and 63% leads to double the increase in the whole specimen volume ratio, which is the ratio between the lattice structure volume and the occupied solid volume domain. The average strength and modulus of elasticity increased over 20 times. The stress-strain curves for the boundary-designed lattice structure using the lowest and highest unit cell relative density are shown in Figure 7-10 (a) and (b), respectively. Comparing these two figures, as the cell size increases at the same relative density, the compressive strength and the modulus of elasticity increase. The increase in the mechanical properties values is comparatively high at lower unit cell relative density. However, at higher relative densities, the mechanical properties values do not increase significantly. On the other hand, as cell size increases

at both the low and high relative density, the compressive strain decreases to be less than 10%. Small cell size resulted in a smooth and steady compressive stress-strain curve without sudden stress drops for either the LD or HD designs. While the large cell size resulted in a significant stress drop just after a 10% compressive strain, and in the case of the LD design, densification occurred, and the stress increased with frequent stress drops. In contrast, in the HD design case, a complete failure occurred during the first stress drop. The lowest modulus of elasticity and compressive strength in the boundary designs belongs to the LDSS lattice structure and equals 10.53 MPa and 0.42 MPa, respectively. While the highest modulus of elasticity and compressive strength were 368.40 MPa with 13.52 MPa, respectively, and it was for the HDLS lattice. The absorbed energy had a reversed response at the low and high relative density designs. As the cell size increases, so the absorbed energy increases at the LD designs. However, in the HD designs, as the cell size increases, the absorbed energy decreases. The LDSS lattice has the lowest energy absorption found, and it is equal to 0.12 MJ/ m<sup>3</sup>, while the HDSS has the highest is for and equals 3.94 MJ/ m<sup>3</sup>.

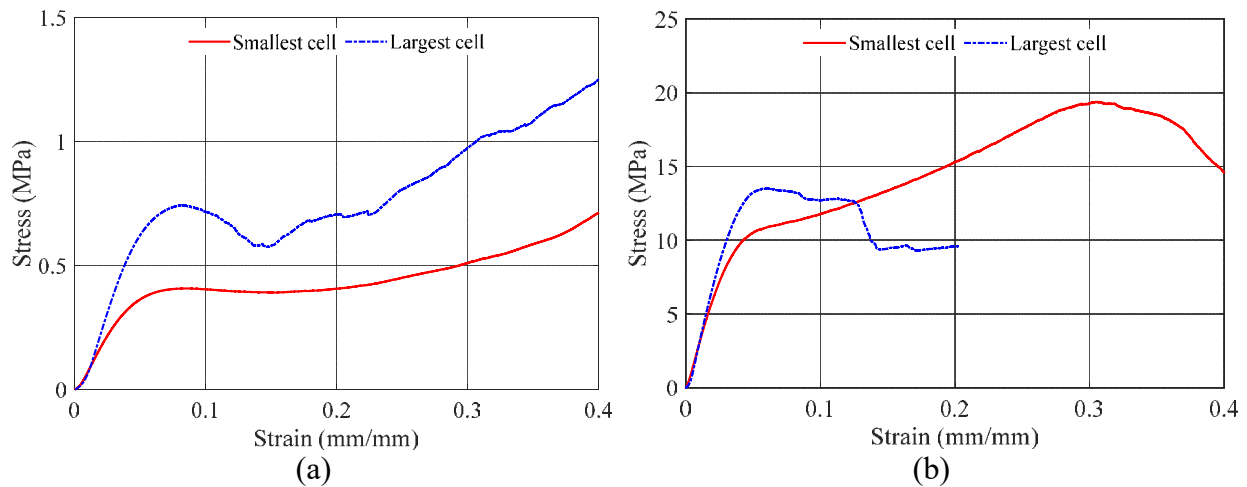


Figure 7-10 Stress-strain curves for (a) different cell size at LD, (b) different cell size at HD

Table 7-17 Average mechanical properties result for boundary lattice structure designs

Design Configurations		Modulus of Elasticity (MPa)	Compressive Strength (MPa)	Compressive Strain (%)	Absorbed Energy (MJ/m <sup>3</sup> )	Volume Ratio
LD	SS	10.50± 1.90	0.40 ±0.05	10	0.12 ± 0.08	0.36
	LS	18.70 ± 3.40	0.80 ± 0.03	8	0.20 ± 0.12	0.36
HD	SS	330.30 ± 22.30	11.70± 1.30	10	3.90 ± 0.20	0.73
	LS	369.60 ± 28.70	13.50± 1.60	5.5	1.50 ± 0.13	0.71

In the dual graded design experiment, the stress-strain curves' general profiles and the mechanical properties values of these lattices are classified into three main groups based on their relative density grading function group. The mechanical properties values, compressive plateaus, and volume ratios vary within each group's specific range. For the first group, D1, which has a constant relative density, the size grading did not affect the volume ratio of the test specimen, which is constant for all the size graded designs with a value of 0.53, as shown in Table 7-2. By observing the stress-strain curves shown in Figure 7-11 (a), all the size graded designs have a similar trend, which after the maximum stress value is reached, a small stress drop occurs. The stress starts to increase except for design S3, which ultimately fails after reaching the maximum stress value. This group's modulus of elasticity ranges between 51.60 MPa (S1) to 86.10 MPa (S2), while the compressive strength is almost 3.1 MPa for all the specimens except S1. The compressive strain is set to 10% from all samples except S2 and S3, which occurs around 7%. The energy absorption is the only parameter with a significant variation by changing the size grading as it ranges between 0.27 MJ/m<sup>3</sup> (S3) to 0.80 MJ/m<sup>3</sup> (S5). In this group, the size grading significantly controlled the absorbed energy and the modulus of elasticity. It was shown that design S3 is a brittle design. However, it has high strength and elasticity. The S1, which has no grading in size or relative density, shows the lowest modulus of elasticity and compressive strength and average energy absorption. S4 and S5 designs have the highest energy absorption.

Table 7-2 Average mechanical properties results for dual graded lattice structure designs

Design Configurations	Modulus of Elasticity (MPa)	Compressive Strength (MPa)	Compressive Strain (%)	Absorbed Energy (MJ/m <sup>3</sup> )	Volume Ratio	
D1	S1	51.60 ± 7.80	2.30 ± 0.60	10	0.64 ± 0.13	0.53
	S2	86.10 ± 14.70	3.10± 0.10	8	0.73± 0.12	0.53
	S3	81.50 ± 9.60	3.00 ± 0.70	6	0.27 ±0.08	0.53
	S4	52.90 ± 11.10	3.10 ± 0.80	10	0.76 ±0.13	0.53
	S5	67.50 ± 8.60	3.10± 0.06	10	0.80 ±0.09	0.53
D2	S1	139.30 ± 12.40	5.50± 0.30	10	1.55 ±0.30	0.60
	S2	169.20± 14.70	8.10± 0.40	10	2.54 ±0.27	0.60
	S3	139.70 ±12.20	5.70 ± 0.60	5	1.00 ± 0.12	0.55
	S4	150.00 ± 15.80	7.80 ± 0.30	10	2.27 ±0.26	0.60
	S5	138.50 ± 13.60	5.90 ± 1.30	10	1.52 ±0.20	0.55
D3	S1	126.50 ± 7.90	4.70 ± 0.30	10	0.43 ±0.17	0.55
	S2	131.80 ± 6.80	4.70 ± 0.80	6	0.23 ±0.14	0.55
	S3	199.60 ± 20.00	5.80 ± 1.10	5	0.47 ±0.10	0.60
	S4	121.20 ± 8.30	4.50 ± 0.70	7	0.70 ±0.13	0.55

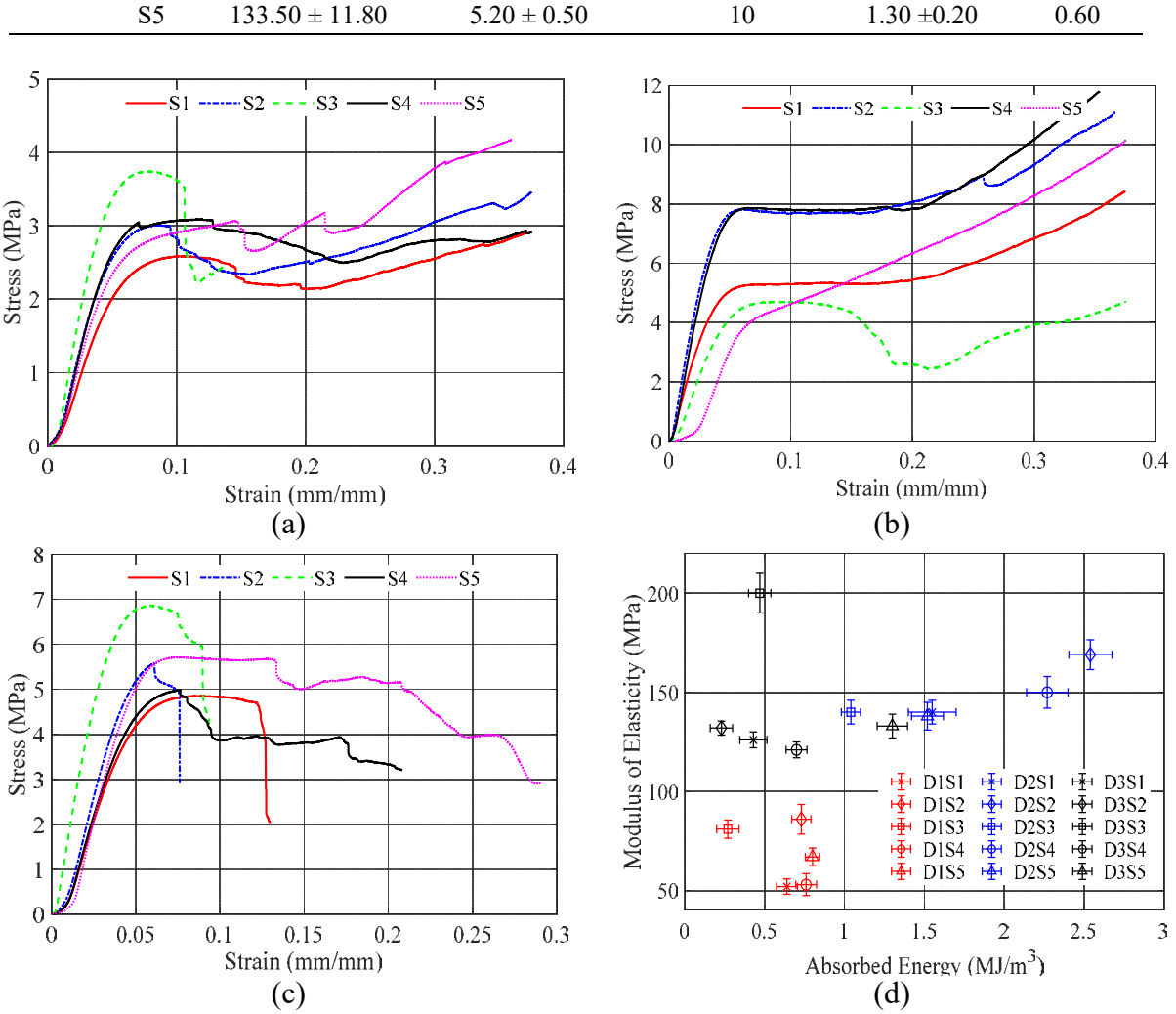


Figure 7-11 Stress-strain curves for (a) Different cell size grading designs at D1, (b) Different cell size grading designs at D2, (c) Different cell size grading designs at D3, and (d) Modulus of elasticity and absorbed energy versus the 15 graded lattice designs

The stress-strain curves of the second-relative density graded group D2, shown in Figure 7-11 (b), are generally smoother curves with steady compressive plateaus and no stress drops. This group's average compressive strength is higher than the two other groups, with a maximum of 8.10 MPa (S2) and a minimum of 5.40 MPa (S1). The modulus of elasticity is around 140 MPa for most samples except S2, which has the highest value of 169.20 MPa. Only the S3 design reached the compressive strain at 5%, and a significant stress drop occurred afterwards. Almost all the samples had a compressive plateau after reaching the maximum stress value. These plateaus occurred between 10% to 15% strain, except for S5, which started to increase directly after the elastic zone region. The average energy absorption is higher for all the D2 groups than the two other groups,

with the highest at  $2.54 \text{ MJ/m}^3$  (S2) and the lowest at  $1 \text{ MJ/m}^3$  (S3). The volume ratio is around 0.6 except for S3 and S5, which are at 0.55. S2 and S4 designs pose the highest material properties in the D2 group. Within this group, the size grading designs noticeably affect the mechanical properties.

The last group is D3, which has a generally brittle profile with low elasticity. As shown in Figure 12 (c), the stress-strain curves have a significant stress drop with a complete failure after reaching the maximum stress value. Only two sizes graded designs, S1 and S5, reached a compressive plateau after reaching the maximum stress value before complete failure; S5 showed a better stress-strain curve than S1 as it is the only specimen the failed at 30% strain. The D3 group has higher average compressive strength and modulus of elasticity than the D1 group but is still lower than the D2 group. However, the average energy absorption of this group is lower than the D1 group and D2 group. The volume ratio of this group for most of the specimens is 0.55. The modulus of elasticity is 199.6 MPa for S3, and the lowest is 121.2 MPa for S4. The compressive strength variation due to size grading was not substantial as the highest compressive strength is 5.70 MPa for S3 while the lowest is 4.70 MPa for both S1 and S2. Most of the specimens in this group reached the maximum stress at around 6% strain, except S1 and S5 achieved that at 10%. S5 design achieved the highest absorbed energy with a value of  $1.3 \text{ MJ/m}^3$ , and the lowest value was  $0.23 \text{ MJ/m}^3$  for the S2 design.

By looking at Figure 7-11 (d), it can be easily noticed that each density grading design has its region defined by the modulus of elasticity and the amount of absorbed energy. The first region occupied by the red marker is for the D1 designs, the second region is occupied by the blue markers and is for the D2 design, and the third region is occupied by the black markers and is for the D3 design, which indicates the significance of the density grading on both parameters. D2 design is the highest obtained values for all the mechanical properties compared to the D1 and D3. Within each relative density grading group, the unit cell size grading can fine-tune and maximize the mechanical properties and improve the stress-strain curve. Also, there is an interaction between both density grading designs and the size grading designs. S2 design maximized the modulus of elasticity and the compressive strength in both D1 and D2 design groups. S4 and S5 designs maximized the energy absorption within D1 and D3 design groups. While S2 and S4 maximized the energy absorption within the D2 group. S3 design produced a brittle mechanical performance with a complete failure under a small amount of strain for all three design groups. D2S2 design is

considered the best design followed by D2S4 to achieve the highest absorbed energy and ultimate tensile strength.

#### 7.3.4.2 Deformation behavior

Digital image correlation was used to understand each lattice deformation behavior. The deformation was evaluated for the specimen front surface only. All of the distributions are rendered at the compressive strength and strain. The DIC results are stable within a range of deformation of 10% strain value. Above 10% strain, the strain analysis either fails to evaluate the distribution or produces high error renders. The vertical direction's engineering strain has two distinctive distribution patterns, as shown in Figure 7-12 (a) and (b). Pattern (a) has the maximum strain at the top of the specimen and decreases towards the specimen's base. Pattern (b) has concentric strain distribution with maximum value in the center, and it decreases towards the edges of the specimen. Pattern (b) is the dominant distribution for most specimens, while distribution (a) occurred in specimen LDLS, D3S2, D3S3, D3S4, and D1S3. Pattern (a) occurred three times in group D3 and two times in group S3.

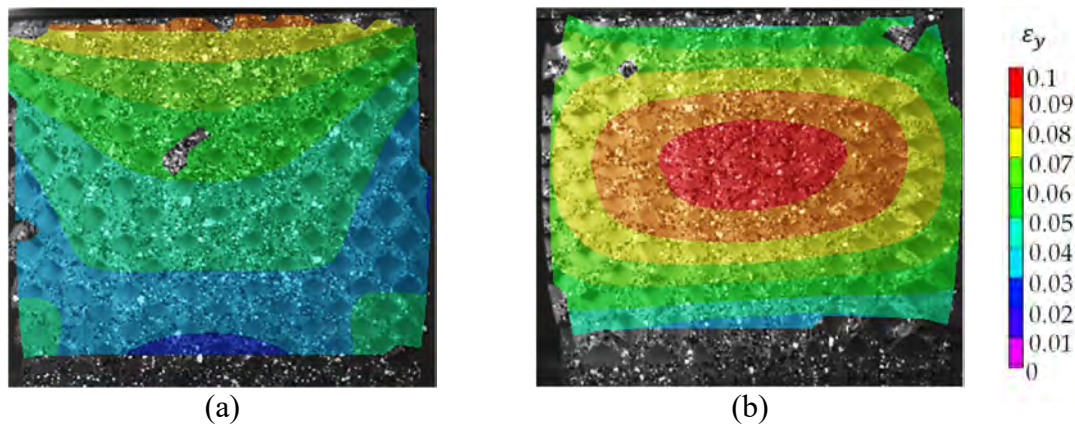


Figure 7-12 Digital Image Correlation (DIC) results depicting the two common engineering strain distribution patterns in the vertical direction at 10% compressive strain (a) unidirectional and (b) concentric strain distributions pattern

Engineering strain in the horizontal direction is evaluated for each design to investigate the different designs' deformation behavior. For the low relative density (LD) boundary designs, at 10% compressive strain, the horizontal engineering strain distribution is symmetric for both the LDSS and the LDLS, as shown in Figure 7-13 (a) and (b), respectively. The LDLS tends to have a concentric distribution with a high engineering strain in the middle and decreases towards the

edges. The LDSS has a hyperbolic distribution. The LDLS had a unidirectional compressive strain shown in Figure 7-12 (a) and had a noticeable stress drop after the maximum stress value shown in the stress strain curve Figure 7-10 (a). By analyzing the deformation of the part beyond 10% strain, it was observed that there was a 45° initiated crack from the right-top corner as shown in Figure 7-14 (b), and unit cells were compressed along that line. For the LDSS design, the cells were squeezed in the middle horizontally, as shown in Figure 7-14 (a). At the end of the test, the LDSS design retrieved most of its original height and width, while the LDLS was fractured and remained in its compressed state as shown in Figure 7-14 (e) and (f), respectively.

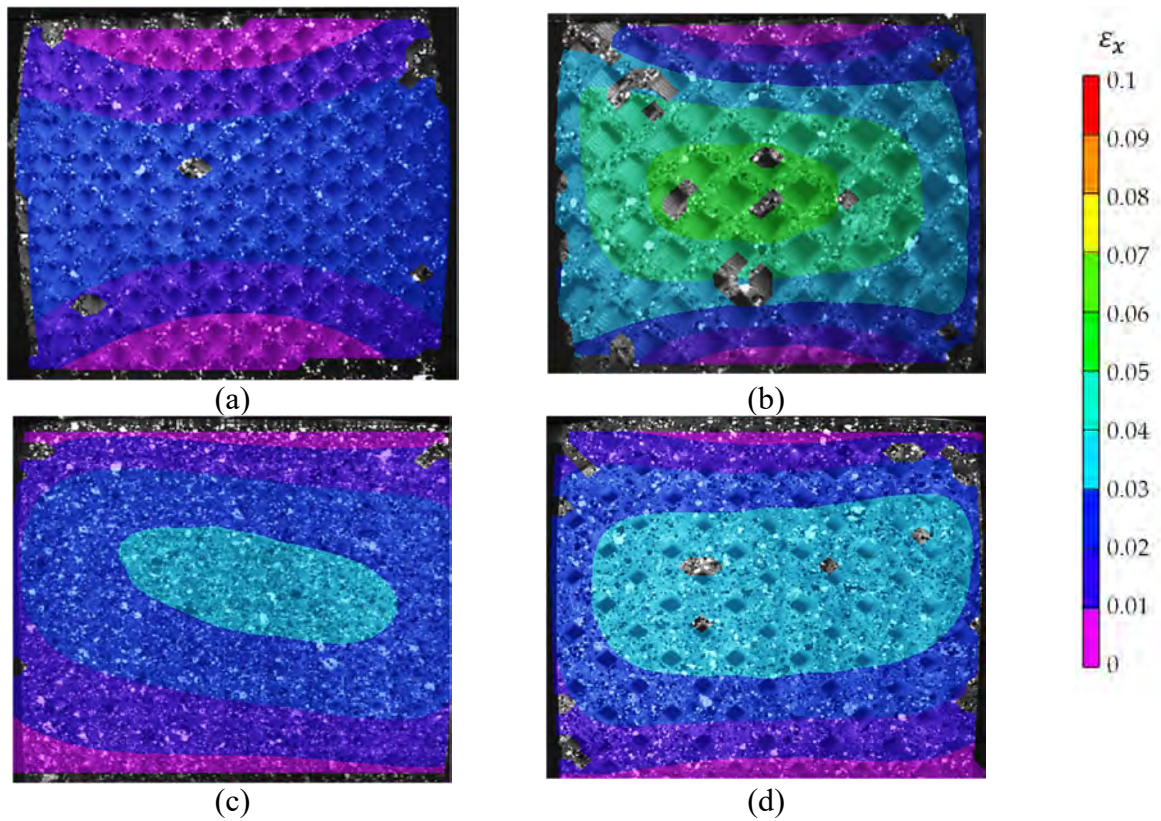


Figure 7-13 Digital Image Correlation (DIC) results of the boundary lattice designs depicting the engineering strain distribution in the horizontal direction at 10% compressive strain for (a) LDSS, (b) LDLS, (c) HDSS, and (d) HDLS boundary designs



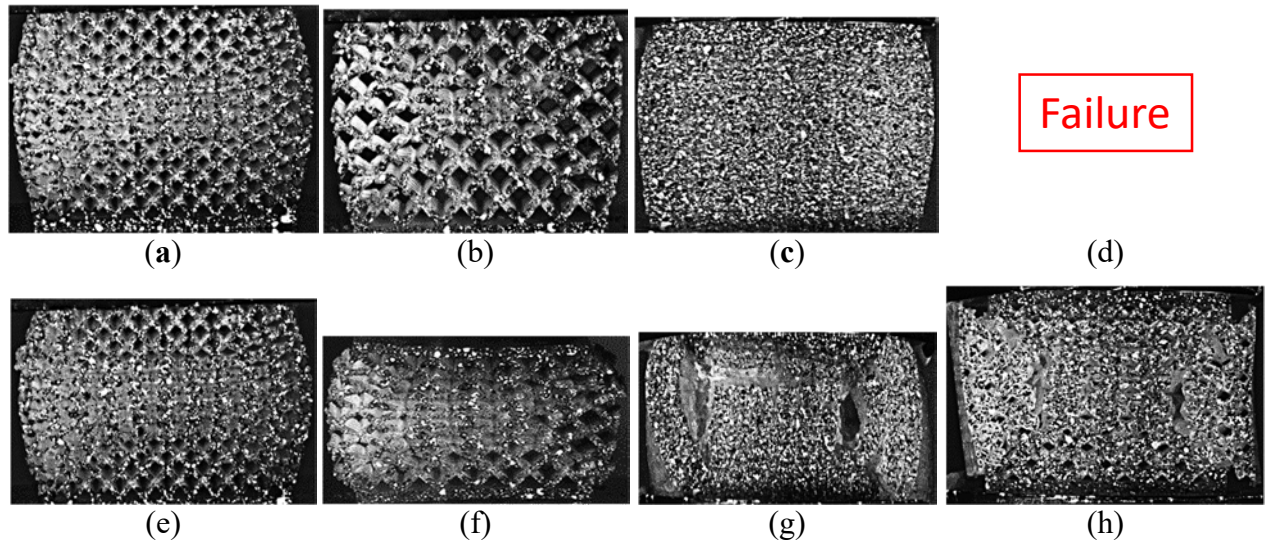


Figure 7-14 Deformation of the boundary lattice designs: (a) LDSS at 30%, (b) LDLS at 30%, (c) HDSS at 30%, (d) HDLS failed before reaching 30%, (e) LDSS after test ended, (f) LDLS after test ended, (g) HDSS after test ended, and (h) HDLS after test ended

The vertical and horizontal engineering strain distribution shows a concentric pattern for the high relative density boundary designs, as shown in Figure 7-13 (c) and (d). The HDSS specimen was observed to be intact with slight buckling at 30% strain, as shown in Figure 7-14 (c). Both HD designs were fractured entirely at the end of the test, with a complete separation of the sidewalls and large vertical cavities appearing in the middle of the part, as shown in Figure 7-14 (g) and (h).

For the dual graded designs, at 10% compressive strain, most of the designs followed a concentric distribution for the vertical strain distribution. However, six designs had a unidirectional distribution, namely, D1S3, D3S3, D3S2, D2S4, D3S4, and D1S5. For the horizontal strain distribution obtained at 10% compressive strain, two main patterns were found. The first pattern is the concentric pattern, and the second pattern follows a hyperbolic distribution, as shown in Figure 7-15. Most of the dual graded lattice designs followed a hyperbolic distribution, while only the D1S3, D2S3, D1S5, and D2S5 had a concentric distribution. The peak strain is in the center within the concentric distribution. The average peak value at 10% compressive strain was 0.4, while the maximum engineering strain recorded was 0.7 and belonged to the D2S3. On the other hand, the hyperbolic distribution has its peak engineering strain at the side edges of the specimen, and the average peak value was 0.45, and the highest was 0.85 and belonged to the D2S4.



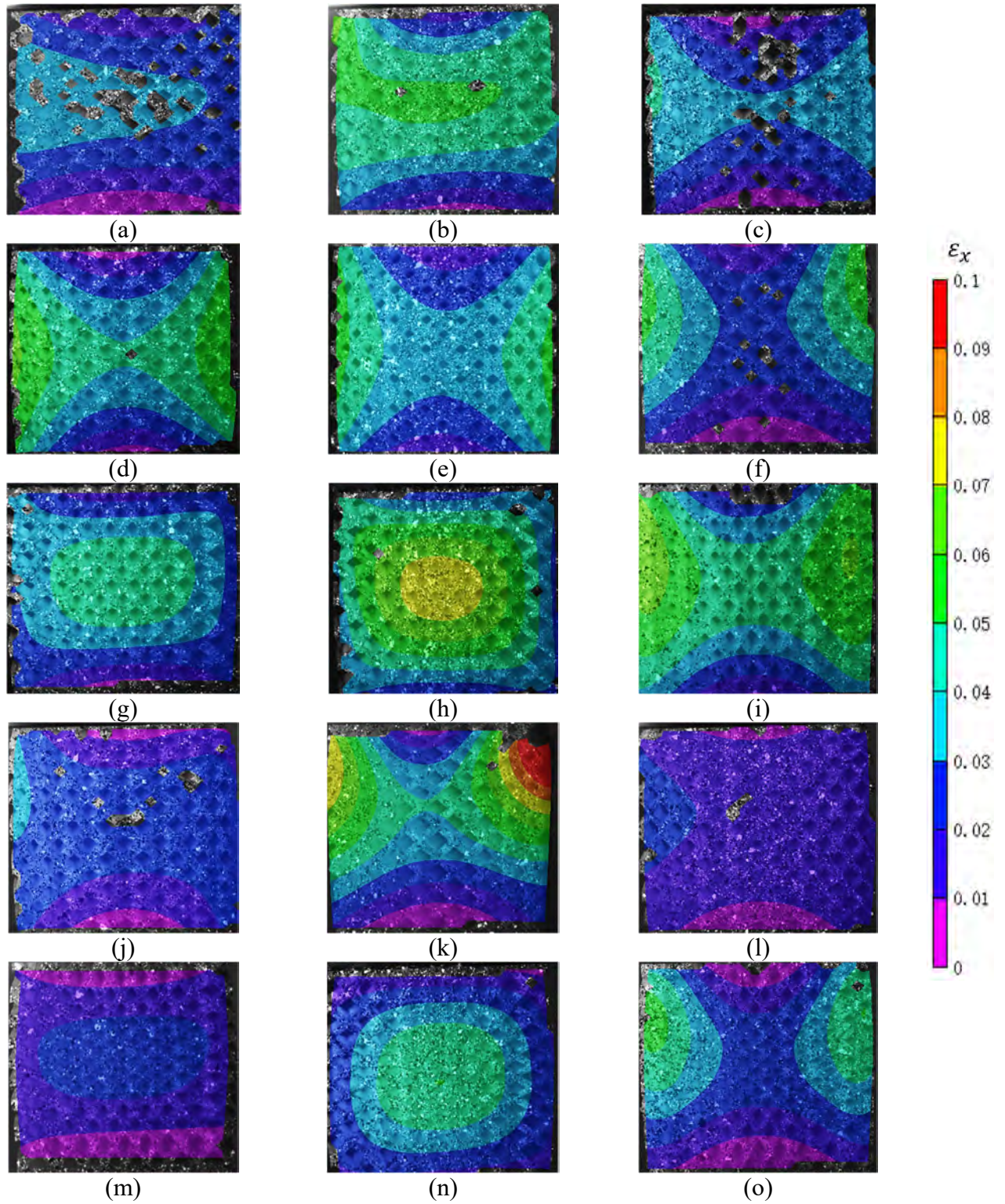


Figure 7-15 Digital Image Correlation (DIC) results of the functionally graded lattice designs depicting the strain distribution in the horizontal direction at 10% compressive strain: (a) D1S1, (b) D2S1, (c) D3S1, (d) D1S2, (e) D2S2, (f) D3S2, (g) D1S3, (h) D2S3, (i) D3S3, (j) D1S4, (k) D2S4, (l) D3S4, (m) D1S5, (n) D2S5, and (o) D3S5



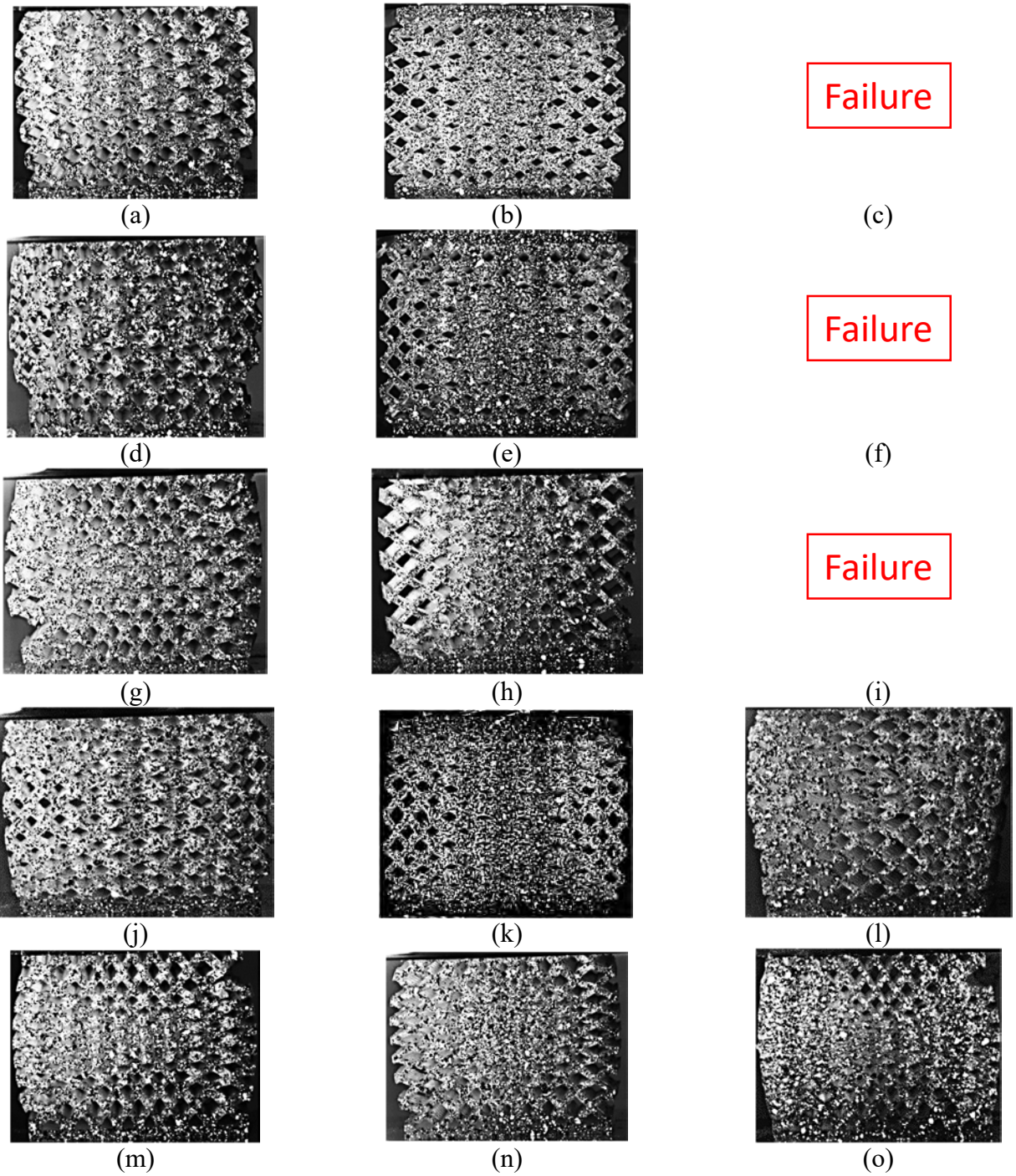


Figure 7-16 Deformation of the dual graded lattice designs at 30% compressive strain: (a) D1S1, (b) D2S1, (c) D3S1 failed before 30%, (d) D1S2, (e) D2S2, (f) D3S2 failed before 30%, (g) D1S3, (h) D2S3, (i) D3S3 failed before 30%, (j) D1S4, (k) D2S4, (l) D3S4, (m) D1S5, (n) D2S5, and (o) D3S5

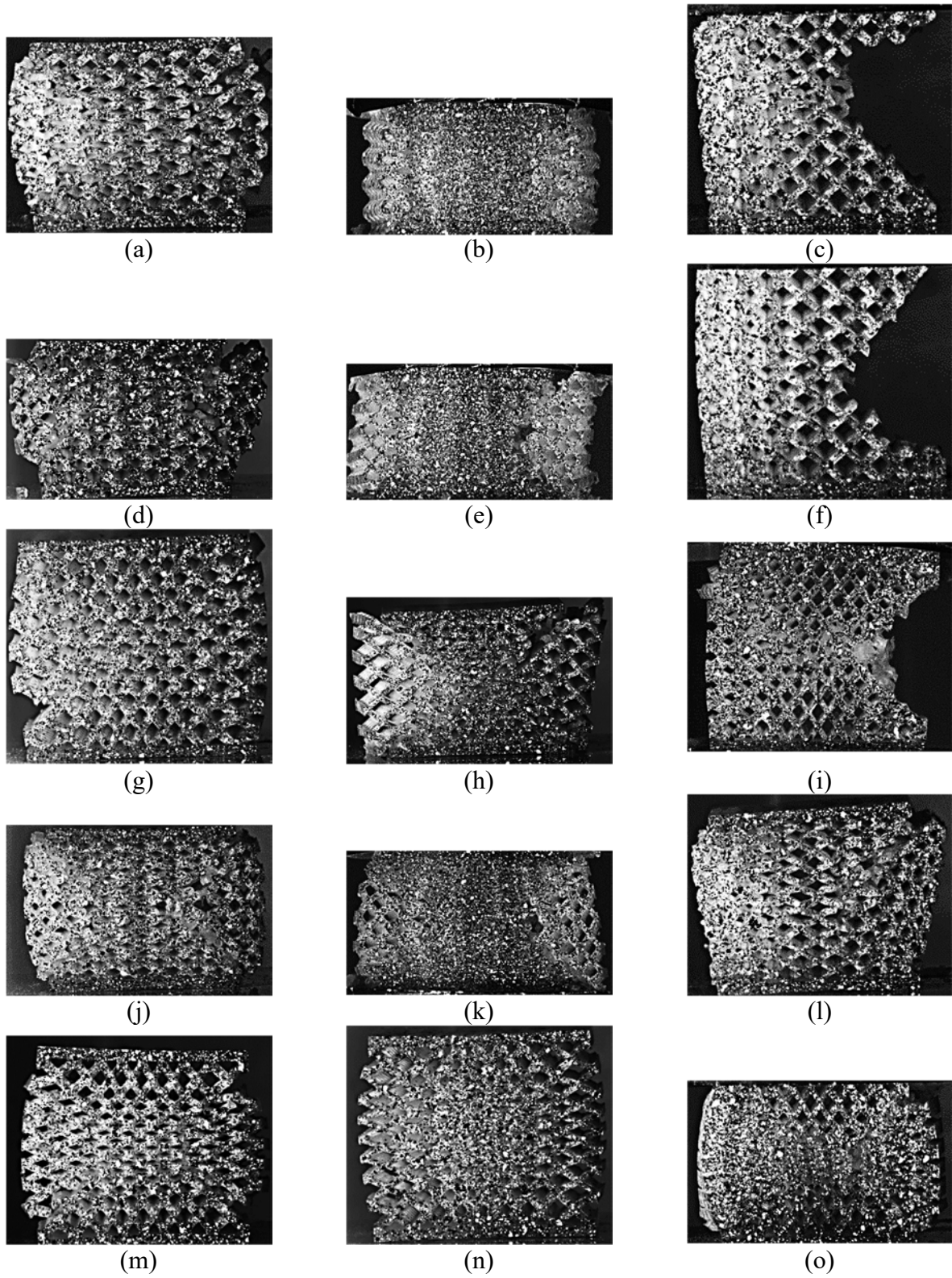


Figure 7-17 DGLS Deformation at the end of test: (a) D1S1, (b) D2S1, (c) D3S1, (d) D1S2, (e) D2S2, (f) D3S2, (g) D1S3, (h) D2S3, (i) D3S3, (j) D1S4, (k) D2S4, (l) D3S4, (m) D1S5, (n) D2S5, and (o) D3S5



The deformation shape at 30% compressive strain was captured and presented in

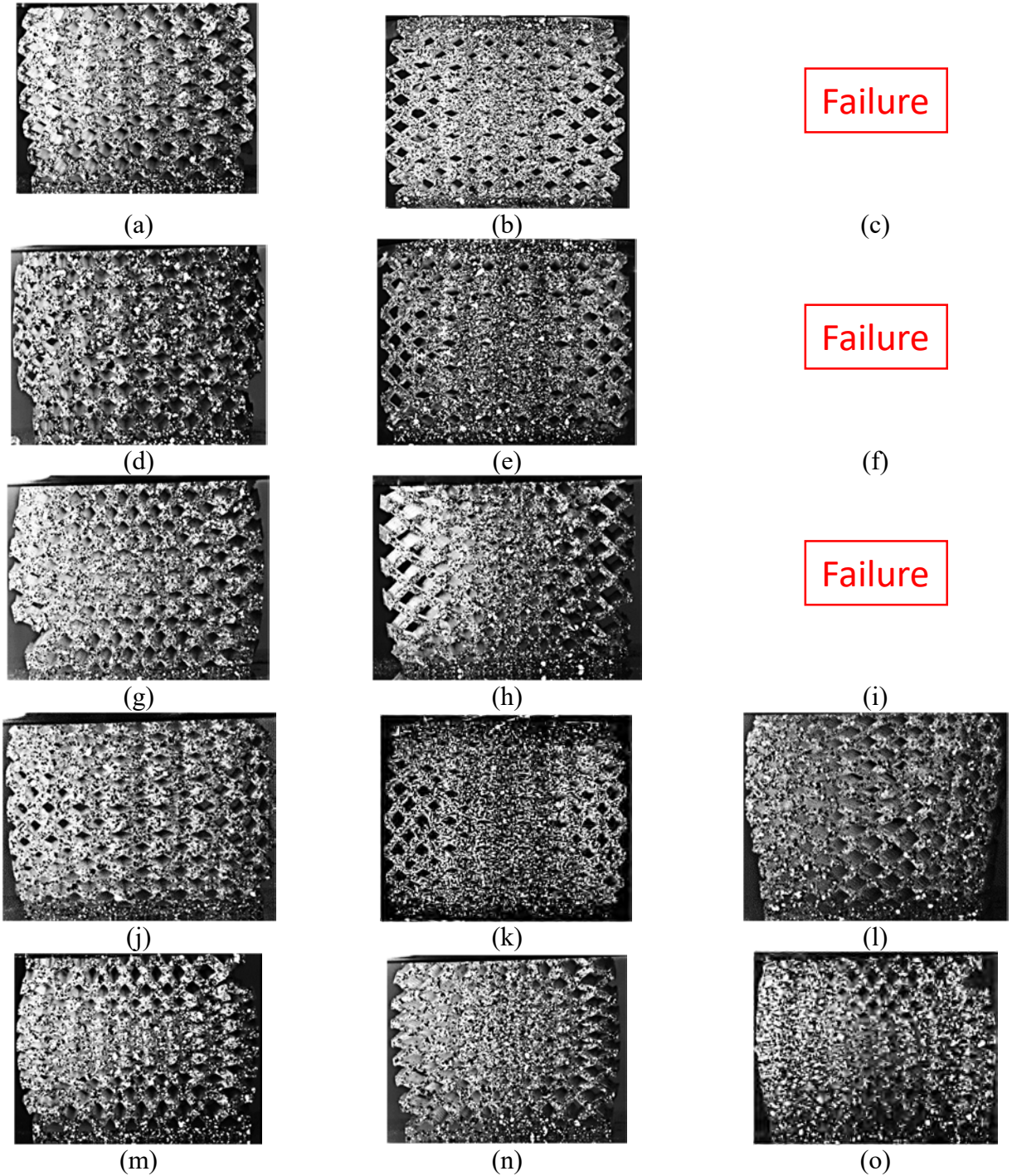


Figure 7-16 Deformation of the dual graded lattice designs at 30% compressive strain: (a) D1S1, (b) D2S1, (c) D3S1 failed before 30%, (d) D1S2, (e) D2S2, (f) D3S2 failed before 30%, (g) D1S3, (h) D2S3, (i) D3S3 failed before 30%, (j) D1S4, (k) D2S4, (l) D3S4, (m) D1S5, (n) D2S5, and (o) D3S5

, but the DIC analysis failed at this large deformation. The first three size grading designs at the third relative density grading design (D3) failed before reaching the 30% compressive strain.

Three designs showed partial fracture D1S3, D1S5, D2S1, and D3S5. A visible crack initiated from the corners of D1S5 and D2S1. Most of the buckling shapes found were round, with the highest displacement in the mid of the buckling curvature. Only two designs, D1S2 and D3S4, showed a different buckling shape where the buckling displacement was larger at the top of the lattice than the lower part. The D2 designs showed higher densification in the middle of the lattice specimen than all the other lattices.

After the specimen was released from the testing machine at the test end, the failure and fracture shapes were captured and presented in **Error! Reference source not found..** For the D1 designs, the S2 design showed the most crack growth, and the crack was initiated diagonally from two orthogonal directions. Both S1 and S4 were fractured diagonally across the whole lattice, and the struts were broken. Both S3 and S5 showed a minor fracture from the side surfaces, and they retained a significant portion of their original height afterwards. For the D2 designs, the failure shapes show complete specimen densification. The crack initiated near the lattice's edges, with the middle part of the lattice still intact. The S5 design did not show any signs of significant cracks, and it restored a significant portion of its original height. The first three size grading designs for the D3 designs have a common fracture pattern. The fracture shape is a large triangular segment of around 20% to 35% of the lattice volume. The triangular segment was ultimately separated and flew away forcefully from the part. The 2D size grading seems to improve the fracture behaviour and the elongation in S4 and S5 designs. The S5 designs seem to improve the lattice's overall integrity despite the relative density grading design used.

## 7.4 Conclusion

In this chapter, a dual graded lattice structure generation framework is introduced. The developed framework was tested against several unit cell lattice types like strut-based, triply periodic minimal surfaces, topology optimized, and artistically designed unit cells and showed a promising performance. Several size grading and dual grading equations and their axes dependency were investigated. The framework utilized a discrete unit cell grading gallery to efficiently manipulate the unit cells' relative density and porosity while grading the unit cells' size. The effect of cell size, relative density, and the dual grading on the mechanical properties, deformation behaviour, and fracture shape was investigated experimentally

For non-graded lattices, as the unit cell size increases, the compressive strain decreases. As the unit cell size decreases, the stress-strain curve becomes smooth and steady with a higher

compressive strain. A small increase in the unit cell's relative density increases the compressive strength and the absorbed energy significantly. As the unit cell relative density decreases, the resistance to fracture increases and the part's ability to restore its original shape increases.

The relative density grading function sets the average values for the compressive strength, modulus of elasticity, and the absorbed energy for the dual graded lattices. In contrast, the unit cell's size grading function would fine-tune the mechanical properties and stress-strain curve. By comparing the average compressive strength values achieved by the three relative density grading functions used in this study, it was found that the constant relative density has the lowest average compressive strength of 2.9 MPa at an average volume ratio of 0.53. The second relative density grading function achieves the highest average compressive strength of 6.8 MPa at an average volume ratio of 0.58. In contrast, the third relative density grading function has an average compressive strength of 5 MPa at an average volume ratio of 0.57. Even at normalizing the compressive strength values using the corresponding volume ratio, the normalized compressive strength values are 5.4 MPa, 11.7 MPa, and 8.7 MPa for the first (D1), second (D2), and third (D3) relative density grading functions, respectively. The relative density grading function affects the stress-strain curve significantly. The D2 lattices have a steady and smooth stress-strain curve, in which the stress value increases after reaching the compressive strength value without any sudden stress drops compared to the D1. While D3 lattices have a general brittle behavior and break right after reaching the compressive strength with compressive strain below 10%. The D2 lattices have the highest average normalized absorbed energy (divided by the volume ratio) of 3 MJ/m<sup>3</sup> compared to D1 and D3 lattices with around 1.2 MJ/m<sup>3</sup>.

The size grading functions fine-tune the absorbed energy value and the deformation and fracture behavior. The size grading did not affect the compressive strength in the constant relative density lattices (D1) and the graded density lattices (D3) significantly; however, its tuning effect was significant in the D2 relative density graded lattices. For the D2 relative density graded lattices, the size grading function S2 increased the compressive strength to 8 MPa from the 5.4 MPa achieved by S1 lattice, which has constant unit cell size; both designs have the same volume ratio of 0.6. The absorbed energy also increased to 2.54 MJ/m<sup>3</sup> achieved by the S2 lattice from the 1.04 MJ/m<sup>3</sup> achieved by the S3 lattice. The S3 size grading function generally introduces brittleness irrespective of the density grading function. However, the S5 size grading function increases the lattice's fracture resistance and allows the lattice to endure higher compressive strains

without showing significant fractures. It was also noticed that the S5 lattices would return to roughly their original height after the compression test compared to other size-graded lattices. The dual grading combination that produced the highest compressive strength and absorbed energy is the D2S2 design. The D2S5 design has the highest fracture resistance among all designs. The D3S3 has the highest elastic modulus and the lowest compressive strain.

The dual graded lattice structure framework (DGLS) currently has some limitations. One of the limitations is that the unit cell's spatial rotation is fixed throughout the lattice structure. Also, the DGLS can vary the relative density along one axis only. The future suggested upgrades are to implement the conformal algorithm to allow the cell orientation to improve the trimming of the cells at the part boundary; this will also allow for conformal perforation of the surface. The relative density should be graded as a function of the three axes and not just one.

## 8 Conclusions

The promised advantages of AM will not get realized, and the results can be significantly costly unless not only the new rules for DfAM are used but also new design strategies must be incorporated to overcome the inherent limitation of the used AM processes. Efficient part design, process parameters, and path planning are required to produce cost-effective and successful functional parts that must be carefully designed and optimized to overcome the inherent tradeoffs of the selected process. The ultimate goal of DfAM is to produce parts with “as-built” geometrical measurements and mechanical performance that match the “as designed” CAD part design specifications. The challenges facing design for polymer additive manufacturing process outcomes are coupled, process parameters are interdependent, commercially promised resolution is different from manufacturing resolution, and lack of simulation, modeling and optimization tools. The research domain of this thesis includes two subdomains. The first subdomain is the process parameter optimization, and the second domain is part design optimization to improve mechanical properties, geometrical accuracy and minimize cost and weight. Two polymer additive manufacturing processes are used in this thesis to apply and investigate the different challenges, namely Projection stereolithography (PSLA) and fused deposition modelling (FDM).

Chapter 2 provides a comprehensive analytical and experimental investigation on the projection stereolithography additive manufacturing process. They study the effect of the process parameters on process outcomes. A novel multilayer vertical energy accumulation model is presented, which considers the difference between the light absorbance through the liquid prepolymer resin and the solid cured polymer. This model is used to explain why a part manufactured with 10  $\mu\text{m}$  layer thickness has double or more strength compared to a 50  $\mu\text{m}$  layer thickness for the same exposure time and LED power. An original terminology called the Irradiance affected zone (IAZ) is introduced, which defines the number of layers affected by the projected irradiance for a particular exposure time and is a function of the process parameters and the material working curve constants. The IAZ sets a limit on the number of layers considered in calculating the accumulated energy for each of the previously cured layers and also defines the minimum feasible size of horizontal channels to be manufactured for a specific material at a process parameter. A horizontal curing model is discussed and used to assess the minimum feasible



size for different geometrical results and also to show that as the exposure time increases, the diameters of the channels decrease, and the diameters of solid bars increase.

For the material properties, the layer thickness was found to be the most significant parameter controlling the process outcomes followed by the exposure time, and the LED power was the least significant process parameter. It is crucial to select the proper process parameter to achieve the geometrical dimensions required while having enough green strength for the part to hold itself against its weight, separation force, and post-processing. A novel definition of the critical amount of energy required to start developing the different material properties is introduced.

A surface roughness model is developed as a function of the layer thickness and the exposure time based on the curing models developed in chapter 2. The prediction results were compared to the experimental results obtained from parts manufactured with a different combination of process parameters. The surface profile angle was predicted with a maximum error of 2°, and the average surface roughness was predicted with an error of 2.7 microns.

Chapter 3 provides a reliable novel irradiance characterization technique is proposed using the irradiance-induced fluorescence technique. The irradiance profile projected from individual micromirrors is analyzed, and the average Gaussian profile was found to be 52  $\mu\text{m}$ . The overall irradiance map was characterized, and the maximum and minimum irradiance was found to be 24.5 and 14  $\text{mW}/\text{cm}^2$ . It was found that the maximum error due to manufacturing location is 0.237 mm. However, the grayscale technique has proved its efficiency in controlling the dimensions of the 8mm cylinders by manipulating the layer thickness and exposure time with it. Three sets of grayscale configurations were used, which was able to adjust the mean diameter of the 8 mm cylinder to be within the normal IT fitting tolerance grade.

Chapter 4 provided tools to model and optimize the geometry produced by the PSLA process. It was shown that the 3D prediction algorithm is capable of predicting geometries using sliced images. The algorithm showed distorted shapes and dimensions, which came in agreement with the measured values in chapter 2. The algorithm was also able to predict the distinctive surface roughness, which also came into agreement with the measured results in chapter 2. A three-stage geometry optimization algorithm was proposed. The algorithm utilizes the concept of irradiance affected zone to minimize the number of pixels to tune. The algorithm was able to improve the circularity of vertical cylinders and enhance the dimensions of horizontal holes. The algorithm was

able to account for the irradiance map irregularities while not interfering with other optimization steps.

In chapter 5, the effect of seven-part design parameters was studied on the ultimate tensile and flexure strength, tensile and flexure modulus of elasticity, building time and volume of 3D printed Nylon 12 using Taguchi's L18 orthogonal array. The infill density was shown to be the most significant parameter for all responses, except the building time for which the infill density ranks second after the layer thickness. The number of contours is the second most significant parameter for all the responses except for building time, for which it ranks third after the infill density. The layer thickness ranks the third for most of the parameters except for the time it ranks the sixth. The number of shells is the fourth significant parameter for most of the parameters. The raster pattern has the lowest significance of all parameters, while the volume ranks sixth. The first four significant parameters control about 80% of the response value. The cost is calculated based on the volume, time, and current price rates in the Canadian market, and then the strength to cost ratio is evaluated. The optimum level for each parameter was determined using the mean effects plot, and the response at the optimum levels was estimated using Taguchi's response prediction method.

In chapter 6 proposes an innovative tool for simulating the geometric and mechanical properties based on the G-code machine input file. This algorithm reconstructs a CAD model from the sliced file. The Reverse CAD model is the virtual replica of the part to be printed with specific printer and machine parameters, e.g., layer thickness and infill density. The algorithm facilitates accurate modelling and analysis of the FDM printed part behaviour. The application and efficiency of the algorithm are validated by qualitative analysis mass comparison, mechanical behaviour analysis using different process parameters and printers.

In the last chapter, a dual graded lattice structure generation framework is introduced. The developed framework was tested against several types of unit cells and showed a promising performance. Several size grading and dual grading equations and their axes dependency were investigated. The framework utilized a discrete unit cell grading gallery to efficiently manipulate the unit cells' relative density and porosity while grading the unit cells' size. The effect of cell size, relative density, and the dual grading on the mechanical properties, deformation behaviour, and fracture shape was investigated experimentally. It was found that the relative density grading function sets the average values for the compressive strength, modulus of elasticity, and the

absorbed energy for the dual graded lattices. In contrast, the unit cell's size grading function would fine-tune the mechanical properties and stress-strain curve. The relative density grading function affects the stress-strain curve significantly. Some lattices design had a steady and smooth stress-strain curve, in which the stress value increases after reaching the compressive strength value without any sudden stress drops compared to other designs. The size grading functions fine-tune the absorbed energy value and the deformation and fracture behaviour. The dual grading combination that produced the highest compressive strength and absorbed energy is the D2S2 design. While D2S5 design has the highest fracture resistance among all designs, and D3S3 has the highest elastic modulus and the lowest compressive strain.

### **8.1 Research Work Limitations**

For chapter 4, the optimization algorithm was not able to improve the horizontal dimensions significantly. The pixel blending algorithm was efficient in improving the shape form but not the dimension; therefore, a more rigorous optimization algorithm should be developed to improve horizontal dimensions. The proposed methodology did not integrate the surface roughness optimization algorithms, and it should be the extent of this work in the future.

For chapter 5, one of the limitations is that the measured properties correspond to the strength of the specific test specimens, which can be altered if the specimen is scaled in the width or thickness directions. The FDM products are highly orthotropic materials; therefore, for each printing configuration, the modulus of elasticity, Poisson's ratio, and shear modulus for the three-main axis are entirely different. This issue is addressed in the next chapter. The cost model used in this study is limited, in which the printed material and machine costs are only considered, while the support material, pre-processing, and post-processing costs were not included in the model.

For chapter 6, the limitation of reverse CAD the algorithm as of now is the computation speed; as the number of features increases in the CAD model, the computational speed decreases. However, the computational speed increases simultaneously to layer thickness since it takes fewer loops to cover the same volume. Currently, the Reverse CAD algorithm is further developed to reduce computation speed, make it more robust, and also to simulate the support structures to understand the effect of supports on the output properties and to optimize it. The future analysis work will be implementing the plasticity and fracture models in FEA while using the reverse CAD model and using specimen parts inspired by applications.

For chapter 7, the dual graded lattice structure framework (DGLS) currently has some limitations. One of the limitations is that the unit cell's spatial rotation is fixed throughout the lattice structure. Also, the DGLS can vary the relative density along one axis only. The future suggested upgrades are to implement the conformal algorithm to allow the cell orientation to improve the trimming of the cells at the part boundary; this will also allow for conformal perforation of the surface. The relative density should be graded as a function of the three axes and not just one.

## **8.2 Future work scope**

1. The use of a reinforced machine learning algorithm as a replacement to the 3-stages algorithm is one of the important future work scopes. This algorithm will combine convolution neural networks, recursive neural networks, and long-short term memories to simulate and optimize 3d geometries. A preliminary study was done on this area to investigate it was showing promising results with faster computational time.
2. The dual graded algorithm should be able to read the results from finite elements and automatically grade lattice structures based on the stress fields.

•

## References

- [1] International Standard Organization (ISO), 2015, *ISO/ASTM 52900:2015(E) Additive Manufacturing — General Principles — Terminology*, Geneva, Switzerland.
- [2] Jacobs, P. F., 1992, *Rapid Prototyping & Manufacturing: Fundamentals of StereoLithography*, Society of Manufacturing Engineers (SME), USA.
- [3] Bandyopadhyay, A., 2019, *Additive Manufacturing*, CRC Press.
- [4] Eufrazio Aguilera, A. F., Nagarajan, B., Fleck, B. A., and Qureshi, A. J., 2019, “Ferromagnetic Particle Structuring in Material Jetting - Manufacturing Control System and Software Development,” *Procedia Manufacturing*, Elsevier B.V., pp. 545–551.
- [5] Gibson, I., Rosen, D., and Stucker, B., 2015, *Additive Manufacturing Technologies*, Springer New York, New York, NY.
- [6] Hertefeld, E., Zhang, C., Jin, Z., Jakub, A., Russell, K., Lakehal, Y., Andreyeva, K., Bangalore, S. N., Mezquita, J., Blutinger, J., and Lipson, H., 2019, “Multi-Material Three-Dimensional Food Printing with Simultaneous Infrared Cooking,” *3D Print. Addit. Manuf.*, **6**(1), pp. 13–19.
- [7] Singhal, T., Khare, A., Gupta, N., and Gandhi, T. K., 2018, “3D-Printed Sole with Variable Density Using Foot Plantar Pressure Measurements,” *2018 IEEE 8th International Advance Computing Conference (IACC)*, IEEE, pp. 136–141.
- [8] Omiyale, B. O., and Kayode Farayibi, P., 2020, “Additive Manufacturing in the Oil and Gas Industries,” *Rev. Fac. Eng. analecta Tech. Szeged.*, **14**(1), pp. 9–18.
- [9] Paolini, A., Kollmannsberger, S., and Rank, E., 2019, “Additive Manufacturing in Construction: A Review on Processes, Applications, and Digital Planning Methods,” *Addit. Manuf.*, **30**, p. 100894.
- [10] Rupal, B. S., Anwer, N., Secanell, M., and Qureshi, A. J., 2020, “Geometric Tolerance and Manufacturing Assemblability Estimation of Metal Additive Manufacturing (AM) Processes,” *Mater. Des.*, **194**, p. 108842.
- [11] Rupal, B. S., Mostafa, K. G., Wang, Y., and Qureshi, A. J., 2019, “A Reverse CAD Approach for Estimating Geometric and Mechanical Behavior of FDM Printed Parts,” *Procedia Manuf.*, **34**, pp. 535–544.
- [12] Mostafa, K., Qureshi, A. J., and Montemagno, C., 2017, “Tolerance Control Using Subvoxel Gray-Scale DLP 3D Printing,” *ASME Adv. Manuf.*, **2**, p. V002T02A035.
- [13] Mostafa, K. G., Arshad, M., Ullah, A., Nobes, D. S., and Qureshi, A. J., 2020, “Concurrent Modelling and Experimental Investigation of Material Properties and Geometries Produced by Projection Microstereolithography,” *Polymers (Basel).*, **12**(3), p. 506.
- [14] Blanco, I., 2020, “The Use of Composite Materials in 3D Printing,” *J. Compos. Sci.*, **4**(2), p. 42.
- [15] Gibson, I., 2017, “The Changing Face of Additive Manufacturing,” *J. Manuf. Technol. Manag.*, **28**(1), pp. 10–17.
- [16] Helou, M., and Kara, S., 2018, “Design, Analysis and Manufacturing of Lattice Structures: An Overview,” *Int. J. Comput. Integr. Manuf.*, **31**(3), pp. 243–261.
- [17] Tosto, C., Saitta, L., Pergolizzi, E., Blanco, I., Celano, G., and Cicala, G., 2020, “Methods for the Characterization of Polyetherimide Based Materials Processed by Fused Deposition Modelling,” *Appl. Sci.*, **10**(9), p. 3195.
- [18] Cicala, G., Giordano, D., Tosto, C., Filippone, G., Recca, A., and Blanco, I., 2018, “Polylactide (PLA) Filaments a Biobased Solution for Additive Manufacturing: Correlating

- Rheology and Thermomechanical Properties with Printing Quality,” *Materials* (Basel), **11**(7), p. 1191.
- [19] Mao, M., He, J., Li, X., Zhang, B., Lei, Q., Liu, Y., and Li, D., 2017, “The Emerging Frontiers and Applications of High-Resolution 3D Printing,” *Micromachines*, **8**(4), p. 113.
  - [20] Ahmadian, A., Adam, Y., William, P., and Tammy, W., 2016, “3D Printing : An Emerging Tool for Novel Microfluidics and Lab - on - a - Chip Applications,” *Microfluid. Nanofluidics*, **20**(3), pp. 1–18.
  - [21] Raman, R., and Bashir, R., 2015, *Stereolithographic 3D Bioprinting for Biomedical Applications*, Elsevier Inc.
  - [22] Choi, J.-W., Wicker, R., Lee, S.-H., Choi, K.-H., Ha, C.-S., and Chung, I., 2009, “Fabrication of 3D Biocompatible/Biodegradable Micro-Scaffolds Using Dynamic Mask Projection Microstereolithography,” *J. Mater. Process. Technol.*, **209**(15–16), pp. 5494–5503.
  - [23] Schuster, M., Turecek, C., Kaiser, B., Stampfl, J., Liska, R., and Varga, F., 2007, “Evaluation of Biocompatible Photopolymers I: Photoreactivity and Mechanical Properties of Reactive Diluents,” *J. Macromol. Sci. Part A*, **44**(5), pp. 547–557.
  - [24] Melchels, F. P. W., Domingos, M. A. N., Klein, T. J., Malda, J., Bartolo, P. J., and Huttmacher, D. W., 2012, “Additive Manufacturing of Tissues and Organs,” *Prog. Polym. Sci.*, **37**(8), pp. 1079–1104.
  - [25] Ligon, S. C., Liska, R., Stampfl, J., Gurr, M., and Mülhaupt, R., 2017, “Polymers for 3D Printing and Customized Additive Manufacturing,” *Chem. Rev.*, **117**(15), pp. 10212–10290.
  - [26] Bártolo, P. J., 2011, *Stereolithography*, Springer US, Boston, MA.
  - [27] Pan, Y., Zhou, C., and Chen, Y., 2012, “A Fast Mask Projection Stereolithography Process for Fabricating Digital Models in Minutes,” *J. Manuf. Sci. Eng.*, **134**(5), p. 051011.
  - [28] Rupal, B. S., Garcia, E. A., Ayranci, C., and Qureshi, A. J., 2019, “3D Printed 3D-Microfluidics: Recent Developments and Design Challenges,” *J. Integr. Des. Process Sci.*, **22**(1), pp. 5–20.
  - [29] Hornbeck, L. J., 1997, “Digital Light Processing for High-Brightness High-Resolution Applications,” *SPIE Proj. Displays III*, **3013**(May 1997), pp. 27–40.
  - [30] Dudley, D., Duncan, W. M., and Slaughter, J., 2003, “Emerging Digital Micromirror Device (DMD) Applications,” *SPIE*, H. Urey, ed., p. 14.
  - [31] Gritsenko, D., Ahmadian Yazdi, A., Lin, Y., Hovorka, V., Pan, Y., and Xu, J., 2017, “On Characterization of Separation Force for Resin Replenishment Enhancement in 3D Printing,” *Addit. Manuf.*, **17**, pp. 151–156.
  - [32] Mostafa, K., Qureshi, A. J., and Montemagno, C., 2017, “Tolerance Control Using Subvoxel Gray-Scale DLP 3D Printing,” *Proceedings of the ASME 2017 International Mechanical Engineering Congress and Exposition. Volume 2: Advanced Manufacturing*, American Society of Mechanical Engineers, Tampa, Florida, USA, p. V002T02A035.
  - [33] Choi, J. W., Ha, Y. M., Lee, S. H., and Choi, K. H., 2006, “Design of Microstereolithography System Based on Dynamic Image Projection for Fabrication of Three-Dimensional Microstructures,” *J. Mech. Sci. Technol.*, **20**(12), pp. 2094–2104.
  - [34] Lambert, P. M., Campaigne, E. a., and Williams, C. B., 2013, “Design Considerations for Mask Projection Microstereolithography Systems,” *Solid Free. Fabr. Symp.*, pp. 111–130.
  - [35] Hutchison, D., 2005, “The Smoothpicture Algorithm: An Overview.”
  - [36] Liu, Y. Q., Zhang, G. Q., Ding, X. L., and ..., 2010, “3-Dimension Video Processing for

- Diamond DMD Based On FPGA,” ... Manag. Serv. ..., pp. 259–265.
- [37] Gutttag, K., 2012, “Texas Instrument DLP ‘Diamond’ Pixel” [Online]. Available: <http://www.kgutttag.com/2012/02/09/ti-dlp-diamond-pixel/>.
  - [38] Gong, H., Beauchamp, M., Perry, S., Woolley, A. T., and Nordin, G. P., 2015, “Optical Approach to Resin Formulation for 3D Printed Microfluidics,” *RSC Adv.*, **5**(129), pp. 106621–106632.
  - [39] Instructables, 2017, “Ember Printer: Using Pattern Mode for Finer Details,” **1**, pp. 1–12.
  - [40] Steyrer, B., Neubauer, P., Liska, R., and Stampfl, J., 2017, “Visible Light Photoinitiator for 3D-Printing of Tough Methacrylate Resins,” *Materials (Basel)*, **10**(12), pp. 1–11.
  - [41] Lin, J., Cheng, D., Chen, K., and Liu, H., 2019, “Dual-Wavelength (UV and Blue) Controlled Photopolymerization Confinement for 3D-Printing: Modeling and Analysis of Measurements,” *Polymers (Basel)*, **11**(11), p. 1819.
  - [42] JAKUBIAK, J., and RABEK, J. F., 2000, “Three-Dimensional (3D) Photopolymerization in Stereolithography. Part I. Fundamentals of 3D Photopolymerization,” *Polimery*, **45**(11/12), pp. 759–770.
  - [43] Wu, J., Zhao, Z., Hamel, C. M., Mu, X., Kuang, X., Guo, Z., and Qi, H. J., 2018, “Evolution of Material Properties during Free Radical Photopolymerization,” *J. Mech. Phys. Solids*, **112**, pp. 25–49.
  - [44] Bertsch, A., Jézéquel, J. Y., and André, J. C., 1997, “Study of the Spatial Resolution of a New 3D Microfabrication Process: The Microstereophotolithography Using a Dynamic Mask-Generator Technique,” *J. Photochem. Photobiol. A Chem.*, **107**(1–3), pp. 275–281.
  - [45] Bertana, V., De Pasquale, G., Ferrero, S., Scaltrito, L., Catania, F., Nicosia, C., Marasso, S. L., Cocuzza, M., and Perrucci, F., 2019, “3D Printing with the Commercial UV-Curable Standard Blend Resin: Optimized Process Parameters towards the Fabrication of Tiny Functional Parts,” *Polymers (Basel)*, **11**(2).
  - [46] Aznarte, E., Ayranci, C., and Qureshi, A. J., 2017, “Digital Light Processing (DLP): Anisotropic Tensile Considerations,” *28th Annual International Solid Freeform Fabrication Symposium*, pp. 413–425.
  - [47] Aznarte Garcia, E., Qureshi, A. J., and Ayranci, C., 2018, “A Study on Material-Process Interaction and Optimization for VAT-Photopolymerization Processes,” *Rapid Prototyp. J.*, **24**(9), pp. 1479–1485.
  - [48] Ryan, J., Dizon, C., Espera, A. H., Chen, Q., and Advincula, R. C., 2018, “Mechanical Characterization of 3D-Printed Polymers,” *Addit. Manuf.*, **20**, pp. 44–67.
  - [49] Chockalingam, K., Jawahar, N., Ramanathan, K. N., and Banerjee, P. S., 2006, “Optimization of Stereolithography Process Parameters for Part Strength Using Design of Experiments,” *Int. J. Adv. Manuf. Technol.*, **29**(1–2), pp. 79–88.
  - [50] Monzón, M., Ortega, Z., Hernández, A., Paz, R., and Ortega, F., 2017, “Anisotropy of Photopolymer Parts Made by Digital Light Processing,” *Materials (Basel)*, **10**(1), pp. 1–15.
  - [51] Zheng, X., Deotte, J., Alonso, M. P., Farquar, G. R., Weisgraber, T. H., Gemberling, S., Lee, H., Fang, N., and Spadaccini, C. M., 2012, “Design and Optimization of a Light-Emitting Diode Projection Micro-Stereolithography Three-Dimensional Manufacturing System,” *Rev. Sci. Instrum.*, **83**(12).
  - [52] Warburg, F., Ribo, M. M., Luongo, A., Danielak, A. H., and Pedersen, D. B., 2018, “Intensity Mapping for Mask Projection Based Photopolymerization,” *2018 ASPE and Euspen Summer Topical Meeting*, Berkeley.
  - [53] Yang, Y., Li, L., and Zhao, J., 2019, “Mechanical Property Modeling of Photosensitive

- Liquid Resin in Stereolithography Additive Manufacturing : Bridging Degree of Cure with Tensile Strength and Hardness,” *Mater. Des.*, **162**, pp. 418–428.
- [54] Zhou, C., Chen, Y., and Waltz, R. A., 2009, “Optimized Mask Image Projection for Solid Freeform Fabrication,” *J. Manuf. Sci. Eng.*, **131**(6), p. 061004.
  - [55] Zhou, C., and Chen, Y., 2012, “Additive Manufacturing Based on Optimized Mask Video Projection for Improved Accuracy and Resolution,” *J. Manuf. Process.*, **14**(2), pp. 107–118.
  - [56] Mitteramskogler, G., Gmeiner, R., Felzmann, R., Gruber, S., Hofstetter, C., Stampfl, J., Ebert, J., Wachter, W., and Laubersheimer, J., 2014, “Light Curing Strategies for Lithography-Based Additive Manufacturing of Customized Ceramics,” *Addit. Manuf.*, **1**, pp. 110–118.
  - [57] Gong, H., Bickham, B. P., Woolley, A. T., and Nordin, G. P., 2017, “Custom 3D Printer and Resin for 18 Mm × 20 Mm Microfluidic Flow Channels,” *Lab Chip*, **17**(17), pp. 2899–2909.
  - [58] O’Neill, P. F., Kent, N., and Brabazon, D., 2017, “Mitigation and Control of the Overcuring Effect in Mask Projection Micro-Stereolithography,” *AIP Conference Proceedings*, p. 200012.
  - [59] Hofstetter, C., Orman, S., Baudis, S., and Stampfl, J., 2018, “Combining Cure Depth and Cure Degree , a New Way to Fully Characterize Novel Photopolymers,” *Addit. Manuf.*, **24**(September), pp. 166–172.
  - [60] Wang, Z., Martin, N., Hini, D., Mills, B., and Kim, K., 2017, “Rapid Fabrication of Multilayer Microfluidic Devices Using the Liquid Crystal Display-Based Stereolithography 3D Printing System,” *3D Print. Addit. Manuf.*, **4**(3), pp. 156–164.
  - [61] Kowsari, K., Zhang, B., Panjwani, S., Chen, Z., Hingorani, H., Akbari, S., Fang, N. X., and Ge, Q., 2018, “Photopolymer Formulation to Minimize Feature Size, Surface Roughness, and Stair-Stepping in Digital Light Processing-Based Three-Dimensional Printing,” *Addit. Manuf.*, **24**, pp. 627–638.
  - [62] Giannatsis, J., and Dedoussis, V., 2007, “Decision Support Tool for Selecting Fabrication Parameters in Stereolithography,” *Int. J. Adv. Manuf. Technol.*, **33**(7–8), pp. 706–718.
  - [63] Onuh, S. O., and Hon, K. K. B., 1998, “OPTIMISING BUILD PARAMETERS FOR IMPROVED SURFACE FINISH IN STEREOLITHOGRAPHY,” **38**(4).
  - [64] Ahn, D., Kim, H., and Lee, S., 2007, “Fabrication Direction Optimization to Minimize Post-Machining in Layered Manufacturing,” *Int. J. Mach. Tools Manuf.*, **47**(3–4), pp. 593–606.
  - [65] Ahn, D., Kim, H., and Lee, S., 2009, “Surface Roughness Prediction Using Measured Data and Interpolation in Layered Manufacturing,” *J. Mater. Process. Technol.*, **209**(2), pp. 664–671.
  - [66] Pandey, P. M., Reddy, N. V., and Dhande, S. G., 2003, “Improvement of Surface Finish by Staircase Machining in Fused Deposition Modeling,” *J. Mater. Process. Technol.*, **132**(1–3), pp. 323–331.
  - [67] Shankar Limaye, A., and Rosen, D. W., 2006, “Compensation Zone Approach to Avoid Print-through Errors in Mask Projection Stereolithography Builds,” *Rapid Prototyp. J.*, **12**(5), pp. 283–291.
  - [68] Pan, Y., and Chen, Y., 2016, “Meniscus Process Optimization for Smooth Surface Fabrication in Stereolithography,” *Addit. Manuf.*, **12**, pp. 321–333.
  - [69] Kumar, K., and Kumar, G. S., 2015, “An Experimental and Theoretical Investigation of Surface Roughness of Poly-Jet Printed Parts,” *Virtual Phys. Prototyp.*, **10**(1), pp. 23–34.
  - [70] Huang, Y.-M., Jeng, J.-Y., and Jiang, C.-P., 2003, “Increased Accuracy by Using Dynamic



- Finite Element Method in the Constrain-Surface Stereolithography System,” J. Mater. Process. Technol., **140**, pp. 191–196.
- [71] Sun, C., Fang, N., Wu, D. M., and Zhang, X., 2005, “Projection Micro-Stereolithography Using Digital Micro-Mirror Dynamic Mask,” Sensors Actuators, A Phys., **121**(1), pp. 113–120.
  - [72] Limaye, A. S., and Rosen, D. W., 2007, “Process Planning Method for Mask Projection Micro-Stereolithography,” Rapid Prototyp. J., **13**(2), pp. 76–84.
  - [73] Pan, Y., Zhao, X., Zhou, C., and Chen, Y., 2012, “Smooth Surface Fabrication in Mask Projection Based Stereolithography,” J. Manuf. Process., **14**(4), pp. 460–470.
  - [74] ASME B46.1, 2009, “Surface Texture: Surface Roughness, Waviness and Lay, An: American National Standard,” **2009**.
  - [75] Autodesk, 2015, *Autodesk Standard Clear Prototyping Resin (PR48)*.
  - [76] “How to Take a Working Curve Measurement and Create Exposure Settings From It : 9 Steps (with Pictures) - Instructables” [Online]. Available: <https://www.instructables.com/id/How-to-Take-a-Working-Curve-Measurement-and-Create/>. [Accessed: 21-Jan-2020].
  - [77] International Standard Organization (ISO), 2013, *International Standard Plastics — Determination of Tensile Properties Part 1: General Principles, ISO 527-1:2012(E)*, Geneva, Switzerland.
  - [78] International Standard Organization (ISO), 2013, *International Standard Plastics — Determination of Tensile Properties Part 2: Test Conditions for Moulding and Extrusion Plastics, ISO 527-2:2012(E)*, Geneva, Switzerland.
  - [79] Puebla, K., Arcaute, K., Quintana, R., and Wicker, R. B., 2012, “Effects of Environmental Conditions, Aging, and Build Orientations on the Mechanical Properties of ASTM Type I Specimens Manufactured via Stereolithography,” Rapid Prototyp. J., **18**(5), pp. 374–388.
  - [80] Rupal, B. S., Ahmad, R., and Qureshi, A. J., 2018, “Feature-Based Methodology for Design of Geometric Benchmark Test Artifacts for Additive Manufacturing Processes,” Procedia CIRP, **70**(May), pp. 84–89.
  - [81] de Pastre, M.-A., Thompson, A., Quinsat, Y., Albajez, J. A., Senin, N., and Leach, R. K., 2019, “Polymer Powder Bed Fusion Surface Texture Measurement,” Meas. Sci. Technol., (December).
  - [82] Leach, R. K., Bourell, D., Carmignato, S., Donmez, A., Senin, N., and Dewulf, W., 2019, “Geometrical Metrology for Metal Additive Manufacturing,” CIRP Ann., **68**(2), pp. 677–700.
  - [83] Zhou, C., and Chen, Y., 2009, “Calibrating Large-Area Mask Projection Stereolithography for Its Accuracy and Resolution Improvements,” Proc. 20th Annu. Solid Free. Fabr. Symp., (Dmd), pp. 82–97.
  - [84] Emami, M. M., and Rosen, D. W., 2020, “Modeling of Light Field Effect in Deep Vat Polymerization for Grayscale Lithography Application,” Addit. Manuf., (April), p. 101595.
  - [85] Deng, T., Liu, W., Xie, W., Huang, J., and Tang, A., 2021, “Mask Image Grayscale Regulation for Projection Stereolithography in Tissue Engineering.”
  - [86] Torres, L. A., Fleck, B. A., Wilson, D. J., and Nobes, D. S., 2013, “Calibration of a Planar Laser Induced Fluorescence Technique for Use in Large Scale Water Facilities,” Meas. J. Int. Meas. Confed., **46**(8), pp. 2597–2607.
  - [87] Mandal, S., Bhattacharyya, S., Borovkov, V., and Patra, A., 2012, “Photophysical Properties, Self-Assembly Behavior, and Energy Transfer of Porphyrin-Based Functional

- Nanoparticles,” J. Phys. Chem. C, **116**(20), pp. 11401–11407.
- [88] Huang, Y.-M., and Jiang, C.-P., 2003, “Curl Distortion Analysis during Photopolymerisation of Stereolithography Using Dynamic Finite Element Method,” Int. J. Adv. Manuf. Technol., **21**(8), pp. 586–595.
  - [89] Zhou, C., Chen, Y., and Waltz, R. A., 2009, “Optimized Mask Image Projection for Solid Freeform Fabrication,” J. Manuf. Sci. Eng., **131**(6), p. 061004.
  - [90] Kang, H. W., Park, J. H., and Cho, D. W., 2012, “A Pixel Based Solidification Model for Projection Based Stereolithography Technology,” Sensors Actuators, A Phys., **178**, pp. 223–229.
  - [91] Ding, X.-Y., Ren, Y.-X., Gong, L., Fang, Z.-X., and Lu, R.-D., 2014, “Microscopic Lithography with Pixelate Diffraction of a Digital Micro-Mirror Device for Micro-Lens Fabrication,” Appl. Opt., **53**(24), p. 5307.
  - [92] Huang, Y. M., Kuriyama, S., and Jiang, C. P., 2004, “Fundamental Study and Theoretical Analysis in a Constrained-Surface Stereolithography System,” Int. J. Adv. Manuf. Technol., **24**(5–6), pp. 361–369.
  - [93] Zheng, X., Deotte, J., Alonso, M. P., Farquar, G. R., Weisgraber, T. H., Gemberling, S., Lee, H., Fang, N., and Spadaccini, C. M., 2012, “Design and Optimization of a Light-Emitting Diode Projection Micro-Stereolithography Three-Dimensional Manufacturing System,” Rev. Sci. Instrum., **83**(12), p. 125001.
  - [94] Kara, T., Ekmekci, E., and Apan, M., 2008, “Determining the Uniformity Coefficient and Water Distribution Characteristics of Some Sprinklers,” Pakistan J. Biol. Sci. PJBS, **11**(2), pp. 214–9.
  - [95] Montero, M., Roundy, S., and Odell, D., 2001, “Material Characterization of Fused Deposition Modeling (FDM) ABS by Designed Experiments,” Proc. Rapid Prototyp. Manuf. Conf., pp. 1–21.
  - [96] Ziemian, C. W., and Iii, P. M. C., 2001, “Computer Aided Decision Support for Fused Deposition Modeling,” Rapid Prototyp. J., **7**(3), pp. 138–147.
  - [97] . J. L., . Z. A. K., and . S. Y. K., 2006, “Optimizing Flexible Behaviour of Bow Prototype Using Taguchi Approach,” J. Appl. Sci., **6**(3), pp. 622–630.
  - [98] Masood, S. H., Mau, K., and Song, W. Q., 2010, “Tensile Properties of Processed FDM Polycarbonate Material,” Mater. Sci. Forum, **654–656**, pp. 2556–2559.
  - [99] Ziemian, C., Sharma, M., and Ziemi, S., 2012, “Anisotropic Mechanical Properties of ABS Parts Fabricated by Fused Deposition Modelling,” *Mechanical Engineering*, InTech, pp. 159–180.
  - [100] Rayegani, F., and Onwubolu, G. C., 2014, “Fused Deposition Modelling (FDM) Process Parameter Prediction and Optimization Using Group Method for Data Handling (GMDH) and Differential Evolution (DE),” Int. J. Adv. Manuf. Technol., **73**(1–4), pp. 509–519.
  - [101] Singh, H., Rayegani, F., and Onwubolu, G., 2014, “Cost Optimization of FDM Additive Manufactured Parts,” *Volume 2A: Advanced Manufacturing*, ASME, p. V02AT02A005.
  - [102] Qureshi, A. ., Mahmood, S., Wong, W. L. ., and Talamona, D., 2015, “Design for Scalability and Strength Optimisation for Components Created through FDM Process,” Iced 2015, (October), pp. 1–12.
  - [103] Wu, W., Geng, P., Li, G., Zhao, D., Zhang, H., and Zhao, J., 2015, “Influence of Layer Thickness and Raster Angle on the Mechanical Properties of 3D-Printed PEEK and a Comparative Mechanical Study between PEEK and ABS,” Materials (Basel), **8**(9), pp. 5834–5846.

- [104] Fernandez-Vicente, M., Calle, W., Ferrandiz, S., and Conejero, A., 2016, "Effect of Infill Parameters on Tensile Mechanical Behavior in Desktop 3D Printing," *3D Print. Addit. Manuf.*, **3**(3), pp. 183–192.
- [105] Cantrell, J., Rohde, S., Damiani, D., Gurnani, R., Disandro, L., Anton, J., Young, A., Jerez, A., Steinbach, D., Kroese, C., and Ifju, P., 2011, "Experimental Characterization of the Mechanical Properties of 3D-Printed ABS and Polycarbonate Parts," Univ. Florida.
- [106] Srivastava, M., Maheshwari, S., Kundra, T. K., and Rathee, S., 2017, "Multi-Response Optimization of Fused Deposition Modelling Process Parameters of ABS Using Response Surface Methodology ( RSM ) -Based Desirability Analysis," *Mater. Today Proc.*, **4**(2), pp. 1972–1977.
- [107] Kumar, S., Ranjeet, P., and Sahu, K., 2017, "Optimization of Fused Deposition Modeling Process Parameters Using a Fuzzy Inference System Coupled with Taguchi Philosophy," *Adv. Manuf.*, **5**(3), pp. 231–242.
- [108] Rathee, S., Srivastava, M., Maheshwari, S., and Noor, A., 2017, "Effect of Varying Spatial Orientations on Build Time Requirements for FDM Process : A Case Study," *Def. Technol.*, **13**(2), pp. 92–100.
- [109] Chacón, J. M., Caminero, M. A., García-plaza, E., and Núñez, P. J., 2017, "Additive Manufacturing of PLA Structures Using Fused Deposition Modelling : Effect of Process Parameters on Mechanical Properties and Their Optimal Selection," *Mater. Des.*, **124**, pp. 143–157.
- [110] Singh, R., and Garg, H. K., 2016, "Fused Deposition Modeling – A State of Art Review and Future Applications," *Reference Module in Materials Science and Materials Engineering*, Elsevier, pp. 1–21.
- [111] Stratasys, 2008, *FDM Nylon 12 Mechanical Properties*.
- [112] Roy, R. K., 2010, *A Primer on the Taguchi Method*, Society of Manufacturing Engineers (SME), Southfield, MI, USA.
- [113] Ahn, S., Montero, M., Odell, D., Roundy, S., and Wright, P. K., 2002, "Anisotropic Material Properties of Fused Deposition Modeling ABS," *Rapid Prototyp. J.*, **8**(4), pp. 248–257.
- [114] Bertoldi, M., Yardimci, M.A., Pistor, C.M., Gucer, S.I. and Sala, G., 1998, "Mechanical Characterization of Parts Processed via Fused Deposition," *Solid Freeform Fabrication Proceedings*, Austin, Texas, pp. 557–565.
- [115] Gurralla, P.K. and Regalla, S. P., "Part Strength Evolution with Bonding between Filaments in Fused Deposition Modelling: This Paper Studies How Coalescence of Filaments Contributes to the Strength of Final FDM Part," *Virtual Phys. Prototyp.*, (9(3)), pp. 141–149.
- [116] Croccolo, D., De Agostinis, M., and Olmi, G., 2013, "Experimental Characterization and Analytical Modelling of the Mechanical Behaviour of Fused Deposition Processed Parts Made of ABS-M30," *Comput. Mater. Sci.*, **79**, pp. 506–518.
- [117] Durgun I, E. R., 2014, "Experimental Investigation of FDM Process for Improvement of Mechanical Properties and Production Cost," *Rapid Prototyp. J.*, **20**(3), pp. 228–35.
- [118] Domingo-Espin, M., Puigoriol-Forcada, J.M., Garcia-Granada, A.A., Lluma, J., Borros, S. and Reyes, G., 83AD, "Mechanical Property Characterization and Simulation of Fused Deposition Modeling Polycarbonate Parts," *Mater. Des.*, p. pp.670-677.
- [119] Rezayat, H., Zhou, W., Siriruk, A., Penumadu, D. and Babu, S. ., 2015, "Structure–Mechanical Property Relationship in Fused Deposition Modelling," *Mater. Sci. Technol.*, **31**(8), pp. 895–903.

- [120] Garg, A. and B., “An Insight to the Failure of FDM Parts under Tensile Loading: Finite Element Analysis and Experimental Study,” *Int. J. Mech. Sci.*, (120), pp. 225–236.
- [121] Urbanic, R.J., Hedrick, R.W. and Burford, C. G., 2017, “A Process Planning Framework and Virtual Representation for Bead-Based Additive Manufacturing Processes,” *Int. J. Adv. Manuf. Technol.*, **90**(1–4), pp. 361–376.
- [122] Mostafa, K. G., Montemagno, C., and Qureshi, A. J., 2018, “Strength to Cost Ratio Analysis of FDM Nylon 12 3D Printed Parts,” *Procedia Manuf.*, **26**, pp. 753–762.
- [123] Mahmoud, D., and Elbestawi, M., 2017, “Lattice Structures and Functionally Graded Materials Applications in Additive Manufacturing of Orthopedic Implants: A Review,” *J. Manuf. Mater. Process.*, **1**(2), p. 13.
- [124] Aremu, A. O., Brennan-Craddock, J. P. J., Panesar, A., Ashcroft, I. A., Hague, R. J. M., Wildman, R. D., and Tuck, C., 2017, “A Voxel-Based Method of Constructing and Skinning Conformal and Functionally Graded Lattice Structures Suitable for Additive Manufacturing,” *Addit. Manuf.*, **13**, pp. 1–13.
- [125] Feng, J., Fu, J., Shang, C., Lin, Z., Niu, X., and Li, B., 2020, “Efficient Generation Strategy for Hierarchical Porous Scaffolds with Freeform External Geometries,” *Addit. Manuf.*, **31**, p. 100943.
- [126] Yang, C., Xu, K., and Xie, S., 2020, “Comparative Study on the Uniaxial Behaviour of Topology-Optimised and Crystal-Inspired Lattice Materials,” *Metals (Basel)*, **10**(4), p. 491.
- [127] Bonatti, C., and Mohr, D., 2019, “Mechanical Performance of Additively-Manufactured Anisotropic and Isotropic Smooth Shell-Lattice Materials: Simulations & Experiments,” *J. Mech. Phys. Solids*, **122**, pp. 1–26.
- [128] Nazir, A., Abate, K. M., Kumar, A., and Jeng, J.-Y., 2019, “A State-of-the-Art Review on Types, Design, Optimization, and Additive Manufacturing of Cellular Structures,” *Int. J. Adv. Manuf. Technol.*, **104**(9–12), pp. 3489–3510.
- [129] Kumar, S., Tan, S., Zheng, L., and Kochmann, D. M., 2020, “Inverse-Designed Spinodoid Metamaterials,” *npj Comput. Mater.*, **6**(1), p. 73.
- [130] Wu, J., Aage, N., Westermann, R., and Sigmund, O., 2018, “Infill Optimization for Additive Manufacturing—Approaching Bone-Like Porous Structures,” *IEEE Trans. Vis. Comput. Graph.*, **24**(2), pp. 1127–1140.
- [131] Rana, U. A., Koon, T. W., Mostafa, K., Baqai, A. A., and Qureshi, A. J., 2017, “Characterization of Cuttlebone for Adaptive Infills,” 2017 8th Int. Conf. Mech. Aerosp. Eng., pp. 591–595.
- [132] Chen, Z., Xie, Y. M., Wu, X., Wang, Z., Li, Q., and Zhou, S., 2019, “On Hybrid Cellular Materials Based on Triply Periodic Minimal Surfaces with Extreme Mechanical Properties,” *Mater. Des.*, **183**, p. 108109.
- [133] Xue, Y., Wang, X., Wang, W., Zhong, X., and Han, F., 2018, “Compressive Property of Al-Based Auxetic Lattice Structures Fabricated by 3-D Printing Combined with Investment Casting,” *Mater. Sci. Eng. A*, **722**, pp. 255–262.
- [134] Liu, J., Gaynor, A. T., Chen, S., Kang, Z., Suresh, K., Takezawa, A., Li, L., Kato, J., Tang, J., Wang, C. C. L., Cheng, L., Liang, X., and To, A. C., 2018, “Current and Future Trends in Topology Optimization for Additive Manufacturing,” *Struct. Multidiscip. Optim.*, **57**(6), pp. 2457–2483.
- [135] Piper, S., “From the Lab: Auxetic Smart Structures - PIPER3DP” [Online]. Available: <http://www.piper3dp.com/blogs/from-the-lab-auxetic-smart-structures/>. [Accessed: 19-Nov-2020].

- [136] Rahmani, R., Antonov, M., Kollo, L., Holovenko, Y., and Prashanth, K. G., 2019, "Mechanical Behavior of Ti6Al4V Scaffolds Filled with CaSiO<sub>3</sub> for Implant Applications," *Appl. Sci.*, **9**(18), p. 3844.
- [137] Qin, Y., Wen, P., Guo, H., Xia, D., Zheng, Y., Jauer, L., Poprawe, R., Voshage, M., and Schleifenbaum, J. H., 2019, "Additive Manufacturing of Biodegradable Metals: Current Research Status and Future Perspectives," *Acta Biomater.*, **98**, pp. 3–22.
- [138] Zadpoor, A. A., 2019, "Mechanical Performance of Additively Manufactured Meta-Biomaterials," *Acta Biomater.*, **85**, pp. 41–59.
- [139] Espin-Lopez, P. F., and Pasian, M., 2018, "Compact 3D-Printed Variable-Infill Antenna for Snow Cover Monitoring," *12th European Conference on Antennas and Propagation (EuCAP 2018)*, Institution of Engineering and Technology, pp. 325 (4 pp.)-325 (4 pp.).
- [140] Thompson, M. K., Moroni, G., Vaneker, T., Fadel, G., Campbell, R. I., Gibson, I., Bernard, A., Schulz, J., Graf, P., Ahuja, B., and Martina, F., 2016, "Design for Additive Manufacturing: Trends, Opportunities, Considerations, and Constraints," *CIRP Ann.*, **65**(2), pp. 737–760.
- [141] Dumas, M., Terriault, P., and Brailovski, V., 2017, "Modelling and Characterization of a Porosity Graded Lattice Structure for Additively Manufactured Biomaterials," *Mater. Des.*, **121**, pp. 383–392.
- [142] de Aquino, D. A., Maskery, I., Longhitano, G. A., Jardini, A. L., and del Conte, E. G., 2020, "Investigation of Load Direction on the Compressive Strength of Additively Manufactured Triply Periodic Minimal Surface Scaffolds," *Int. J. Adv. Manuf. Technol.*, **109**(3–4), pp. 771–779.
- [143] Cutolo, A., Engelen, B., Desmet, W., and Van Hooreweder, B., 2020, "Mechanical Properties of Diamond Lattice Ti–6Al–4V Structures Produced by Laser Powder Bed Fusion: On the Effect of the Load Direction," *J. Mech. Behav. Biomed. Mater.*, **104**, p. 103656.
- [144] Liu, L., Kamm, P., García-Moreno, F., Banhart, J., and Pasini, D., 2017, "Elastic and Failure Response of Imperfect Three-Dimensional Metallic Lattices: The Role of Geometric Defects Induced by Selective Laser Melting," *J. Mech. Phys. Solids*, **107**, pp. 160–184.
- [145] Maconachie, T., Leary, M., Lozanovski, B., Zhang, X., Qian, M., Faruque, O., and Brandt, M., 2019, "SLM Lattice Structures: Properties, Performance, Applications and Challenges," *Mater. Des.*, **183**, p. 108137.
- [146] Abou-Ali, A. M., Al-Ketan, O., Lee, D.-W., Rowshan, R., and Abu Al-Rub, R. K., 2020, "Mechanical Behavior of Polymeric Selective Laser Sintered Ligament and Sheet Based Lattices of Triply Periodic Minimal Surface Architectures," *Mater. Des.*, **196**, p. 109100.
- [147] Nagesha, B. K., Dhinakaran, V., Varsha Shree, M., Manoj Kumar, K. P., Chalawadi, D., and Sathish, T., 2020, "Review on Characterization and Impacts of the Lattice Structure in Additive Manufacturing," *Mater. Today Proc.*, **21**, pp. 916–919.
- [148] Tao, W., and Leu, M. C., 2016, "Design of Lattice Structure for Additive Manufacturing," *2016 International Symposium on Flexible Automation (ISFA)*, IEEE, pp. 325–332.
- [149] Plessis, A. du, Yadroitsava, I., Yadroitsev, I., Roux, S. G. le, and Blaine, D. C., 2018, "Numerical Comparison of Lattice Unit Cell Designs for Medical Implants by Additive Manufacturing," *Virtual Phys. Prototyp.*, **13**(4), pp. 266–281.
- [150] Marschall, D., Rippl, H., Ehrhart, F., and Schagerl, M., 2020, "Boundary Conformal Design of Laser Sintered Sandwich Cores and Simulation of Graded Lattice Cells Using a Forward Homogenization Approach," *Mater. Des.*, **190**, p. 108539.

- [151] Teimouri, M., and Asgari, M., 2020, “Mechanical Performance of Additively Manufactured Uniform and Graded Porous Structures Based on Topology-Optimized Unit Cells,” *Proc. Inst. Mech. Eng. Part C J. Mech. Eng. Sci.*, pp. 1–26.
- [152] Maskery, I., Aboulkhair, N. T., Aremu, A. O., Tuck, C. J., and Ashcroft, I. A., 2017, “Compressive Failure Modes and Energy Absorption in Additively Manufactured Double Gyroid Lattices,” *Addit. Manuf.*, **16**, pp. 24–29.
- [153] Kumar, A., Collini, L., Daurel, A., and Jeng, J.-Y., 2020, “Design and Additive Manufacturing of Closed Cells from Supportless Lattice Structure,” *Addit. Manuf.*, **33**, p. 101168.
- [154] Yang, L., Han, C., Wu, H., Hao, L., Wei, Q., Yan, C., and Shi, Y., 2020, “Insights into Unit Cell Size Effect on Mechanical Responses and Energy Absorption Capability of Titanium Graded Porous Structures Manufactured by Laser Powder Bed Fusion,” *J. Mech. Behav. Biomed. Mater.*, **109**, p. 103843.
- [155] Cheng, L., Liang, X., Belski, E., Wang, X., Sietins, J. M., Ludwick, S., and To, A., 2018, “Natural Frequency Optimization of Variable-Density Additive Manufactured Lattice Structure: Theory and Experimental Validation,” *J. Manuf. Sci. Eng.*, **140**(10), pp. 1–16.
- [156] Vantighem, G., De Corte, W., Steeman, M., and Boel, V., 2019, “Density-Based Topology Optimization for {3D}-Printable Building Structures,” *Struct. Multidiscip. Optim.*, **60**(6), pp. 2391–2403.
- [157] Plocher, J., and Panesar, A., 2020, “Effect of Density and Unit Cell Size Grading on the Stiffness and Energy Absorption of Short Fibre-Reinforced Functionally Graded Lattice Structures,” *Addit. Manuf.*, **33**, p. 101171.
- [158] Al-Ketan, O., Lee, D.-W., Rowshan, R., and Abu Al-Rub, R. K., 2020, “Functionally Graded and Multi-Morphology Sheet TPMS Lattices: Design, Manufacturing, and Mechanical Properties,” *J. Mech. Behav. Biomed. Mater.*, **102**, p. 103520.
- [159] Singh, G., and Pandey, P. M., 2019, “Uniform and Graded Copper Open Cell Ordered Foams Fabricated by Rapid Manufacturing: Surface Morphology, Mechanical Properties and Energy Absorption Capacity,” *Mater. Sci. Eng. A*, **761**, p. 138035.
- [160] Maskery, I., Aremu, A. O., Parry, L., Wildman, R. D., Tuck, C. J., and Ashcroft, I. A., 2018, “Effective Design and Simulation of Surface-Based Lattice Structures Featuring Volume Fraction and Cell Type Grading,” *Mater. Des.*, **155**, pp. 220–232.
- [161] Al-Ketan, O., and Abu Al-Rub, R. K., 2020, “MSLattice: A Free Software for Generating Uniform and Graded Lattices Based on Triply Periodic Minimal Surfaces,” *Mater. Des. Process. Commun.*, (September), pp. 1–10.
- [162] Dong, G., Tang, Y., and Zhao, Y. F., 2017, “A Survey of Modeling of Lattice Structures Fabricated by Additive Manufacturing,” *J. Mech. Des.*, **139**(10), pp. 1–13.
- [163] Montoya-Zapata, D., Moreno, A., Pareja-Corcho, J., Posada, J., and Ruiz-Salguero, O., 2019, “Density-Sensitive Implicit Functions Using Sub-Voxel Sampling in Additive Manufacturing,” *Metals (Basel)*, **9**(12), p. 1293.
- [164] Chougrani, L., Pernot, J. P., Véron, P., and Abed, S., 2017, “Lattice Structure Lightweight Triangulation for Additive Manufacturing,” *CAD Comput. Aided Des.*, **90**, pp. 95–104.
- [165] Xue, D., Zhu, Y., and Guo, X., 2020, “Generation of Smoothly-Varying Infill Configurations from a Continuous Menu of Cell Patterns and the Asymptotic Analysis of Its Mechanical Behaviour,” *Comput. Methods Appl. Mech. Eng.*, **366**, p. 113037.
- [166] “Autodesk NETFABB” [Online]. Available: <https://www.autodesk.com/products/netfabb/>.
- [167] “K3DSurfle” [Online]. Available: <http://k3dsurf.sourceforge.net/>.

- [168] “Altair” [Online]. Available: <https://www.altair.com/additive-manufacturing/>.
- [169] “Ansys Spaceclaim” [Online]. Available: <https://www.ansys.com/products/3d-design/ansys-spaceclaim>.
- [170] “Materialize 3-Matic” [Online]. Available: <https://www.materialise.com/en/software/3-matic>.
- [171] “ParaMatters” [Online]. Available: <https://paramatters.com/>.
- [172] Garber, T., Goldenberg, J., Libai, B., and Muller, E., 2004, “Design and Analysis of a Mask Projection Micro- Stereolithography System,” *Mark. Sci.*, **23**(3), pp. 419–428.
- [173] Jacobson, A., and Panozzo, D., 2018, “A Simple C++ Geometry Processing Library” [Online]. Available: <https://github.com/libigl/libigl>. [Accessed: 15-Dec-2020].
- [174] Fabri, A., and Pion, S., 2009, “CGAL - The Computational Geometry Algorithms Library: Demo Paper,” *GIS: Proceedings of the ACM International Symposium on Advances in Geographic Information Systems*, ACM Press, New York, New York, USA, pp. 538–539.
- [175] G-Truc Creation, 2005, “OpenGL Mathematics (GLM)” [Online]. Available: <https://glm.g-truc.net>. [Accessed: 15-Jun-2020].
- [176] Bernstein, G., 2013, “Cork Boolean Library” [Online]. Available: <https://github.com/gilbo/cork>. [Accessed: 15-Dec-2020].
- [177] Guennebaud, G., and Jacob, B., 2010, “Eigen v3: Linear Algebra Library,” 2 [Online]. Available: <http://eigen.tuxfamily.org>. [Accessed: 15-Dec-2020].
- [178] Winkle, L. Van, 2009, “Tiny Recursive Descent Expression Parser, Compiler, and Evaluation Engine for Math Expressions” [Online]. Available: <https://codeplea.com/tinyexpr>. [Accessed: 15-Dec-2020].
- [179] Koc, B., and Lee, Y.-S., 2002, “Non-Uniform Offsetting and Hollowing Objects by Using Biarc Fitting for Rapid Prototyping Processes,” *Comput. Ind.*, **47**(1), pp. 1–23.
- [180] International Organization for Standardization, 2014, “Rigid Cellular Plastics — Determination of Compression Properties,” ISO 8442:2014(E), (Sixth edition).
- [181] Garcia, E. A., Ayranci, C., and Qureshi, A. J., 2020, “Material Property-Manufacturing Process Optimization for Form 2 Vat-Photo Polymerization 3D Printers,” *J. Manuf. Mater. Process.*, **4**(1), p. 12.
- [182] International Organization for Standardization, 2002, “Plastics — Determination of Compressive Properties,” ISO 6042:2002(E), (Third edition).
- [183] International Standardization Organization (ISO), 2011, *Mechanical Testing of Metals — Ductility Testing — Compression Test for Porous and Cellular Metals ISO 13314:2011(E)*, Geneva, Switzerland.